NORTHWESTERN UNIVERSITY

Effects of Confinement and Interfaces on Stress Relaxation and Stiffness in Polymer Films and

Nanocomposites Characterized by Novel Fluorescence Techniques

A DISSERTATION

SUBMITTED TO THE GRADUATE SCHOOL

IN PARTIAL FULFILLMENT OF THE REQUIREMENTS

for the degree

DOCTOR OF PHILOSOPHY

Field of Chemical Engineering

By

Shadid Askar

EVANSTON, ILLINOIS

March 2017

ABSTRACT

Effects of Confinement and Interfaces on Stress Relaxation and Stiffness in

Polymer Films and Nanocomposites Characterized by Novel Fluorescence Techniques

Shadid Askar

Advancements in nanotechnology have led to the production of devices with components with sub-100 nm size scales. Studies have investigated how properties of polymers change when confined to nanoscale dimensions. However, stiffness-confinement studies have reported increases, decreases, and invariance with confinement for different polymer/substrate pairs, making it difficult to obtain general trends in such behavior. The major focus of this dissertation is to develop a fundamental understanding of stiffness-confinement effects.

A novel fluorescence technique is developed to study stress relaxation and stiffness in PS films and nanocomposites. It is shown that stress relaxation occurs over hours despite the films being tens of degrees above T_g. Stiffness-confinement studies demonstrate that single-layer films stiffen with confinement with stronger effects in the rubbery state. Bilayer film studies show that stiffness is enhanced near a substrate and reduced near a free surface. The fluorescence/trilayer technique is used to directly characterize stiffness gradients enabling the first comparison of stiffness gradient length scales obtained using two different techniques – fluorescence and atomic force microscopy (AFM). Both show agreement that stiffness gradients depend on whether the model nanocomposites are confined or bulk. Fluorescence demonstrates that thermal history impacts magnitudes and length scales associated with stiffness perturbations in model nanocomposites at room temperature. It is demonstrated that PS is more susceptible to substrate perturbations in the rubbery state and more susceptible to surface perturbations in the glassy state. The tunability of stiffness-confinement behavior is shown in PS films containing a plasticizer. The fluorescence approach is extended by using a broader class of vibronic coupling

dyes to characterize stress relaxation and T_g. These studies help identify trends in stiffness-confinement behavior and help to provide consensus among various reports.

This dissertation provides an understanding of T_g-confinement behavior of PS in complex geometries such as polymer brushes and supported nanorods. In brushes grown from nanoparticles, T_g and fragility decrease with sufficiently low molecular weight while T_g breadth increases. In PS nanorods, intermediate molecular weight PS exhibited no change in T_g with reduced rod diameter. However, high molecular weight PS exhibited reductions in T_g with decreasing rod diameter due to intrinsic size effects.

ACKNOWLEDGMENTS

To my advisor, John Torkelson, thank you for dedicating yourself to my professional and personal development. You have played an enormous role in making me the scientist that I am today. This work would not be possible without your guidance and support.

To my wife, Samina Qureshi, you cannot know how important you are to me. I deeply appreciate your love and support. This process has often frustrated me (and maybe you), but you always manage to make me feel better and that has made graduate school easier. I cannot imagine life without you, and I am excited about the journey that we will share together side-by-side.

To my mother, Yasmeen Ali, thank you for your unending love. You continue to remind me to take life's challenges in stride and to enjoy myself. To my father, Tahsin Askar, thank you for the advice and support you have given me. You have instilled in me the values and hard work ethic necessary to be successful. Without the sacrifices that both of you and my grandparents have made, I would not be where I am today.

To my friends, Nick, Perry, Alex, Ashty, James, George, Ridwan, and Sam, thanks for reminding me that there is a life outside of graduate school. You guys keep me humble, whether I ask for it or not.

Thank you to former Polymer Crew group members that I have had the pleasure of working with: Chris E., Stephen M., Phil B., Mirian D., Emily L., Krishnan I., Anthony T., Lawrence C., and Tian L. The mentorship you have provided me has proven to be useful.

Finally, thank you to current Polymer Crew group members: Liz D., Lan Z., Kailong J., Goliath B., Lingqiao L., Tong W., Mingxiao L., and Xi C. I have truly enjoyed working with all of you over the years and hope that our paths cross in the future.

TABLE OF CONTENTS

LIST OF FIGURES

LIST OF TABLES

I. INTRODUCTION AND BACKGROUND

CHAPTER 1

Introduction

Measuring the properties of polymers confined to the nanoscale has been an intense area of research over the past two decades. The effects of confinement on polymers have been characterized for a range of properties including glass transition temperature (T_g), physical aging, diffusion, fragility, and modulus or stiffness, and the vast majority of studies have focused on thin polymer films supported on a range of substrates. Significantly less investigated are polymer nanocomposites, which are composed of nanofillers dispersed within a polymer matrix. This thesis contributes towards a fundamental understanding of confinement effects on stiffness and T_g through the study of new systems and new techniques.

The interest in the effects of nanoconfinement on polymer properties is technologically important as many polymeric applications seek to utilize devices featuring size scales less than 100 nm. Various applications include lithographically designed polymers (Mundra 2007a, Delcambre 2010), thin film transistors (Kim 2007), filtration membranes (Huang 2006), and others. Nanocomposites are used widely as lightweight, yet mechanically robust materials in aerospace (Wardle 2008, Gibson 2010), solar cell (Xin 2008, Small 2012), and medical applications (Dong 2005, Monteiro 2009). Different applications employ polymers that have a range of polymer-substrate, polymer-nanofiller, or polymer-air interfaces, which can impact performance. For instance, polymer nanobeams that are designed to have high aspect ratios can suffer from beam collapse due to perturbations from free-surface interfaces (Delcambre 2010). Understanding such stiffness-confinement behavior has significant financial value.

Academic interest in nanoconfinement is driven by a need to fundamentally understand the origins of confinement-induced perturbations to polymer properties. It has been demonstrated that polymer dynamics associated with T_g are perturbed within several tens of nanometers from a free-surface interface (Ellison 2003). Such length scales are beyond what would be predicted from length scales associated with cooperatively rearranging regions ($\sim 1 - 4$ nm) (Tracht 1998).

Understanding perturbation length scales associated with T_g and other properties such as stiffness have important ramifications for various polymer systems including thin films and polymer nanocomposites.

The seminal studies in the field of polymer nanoconfinement were conducted by Keddie *et al*. who demonstrated that supported films of polystyrene (PS) and poly(methyl methacrylate) (PMMA) exhibit reductions in T_g in the absence of attractive polymer-substrate interactions (Keddie 1994a, Keddie 1994b). They hypothesized that the presence of a liquid-like surface layer at the polymer-air interface impacts the dynamics of the film to an increasing extent as film thickness is reduced. Experimental evidence for a higher-mobility surface layer was provided by Ellison and Torkelson in 2003, who demonstrated via a fluorescence/multilayer technique that T_g of the top 14 nm of a PS film is reduced by 32 °C. They found that perturbations near the surface extend tens of nanometers towards the interior of the films. The use of trilayer films to characterize polymers near the surface, interior, and substrate has also been extended to characterize gradient length scales associated with physical aging (Priestley 2005b).

Related research into confinement effects on other polymer properties such as modulus or stiffness have also been investigated for the past two decades (Lee 1996, Briscoe 1998, Forrest 1998, Soles 2002, Hartschuh 2004, Stafford 2004, Hartschuh 2005, Inoue 2005, O'Connell 2005, Yoshimoto 2005, Inoue 2006, Stafford 2006, Cheng 2007, Tweedie 2007, Stoykovich 2008, Gomopoulos 2009, Delcambre 2010, Gomopoulos 2010, Xu 2010, Arinstein 2011, Watcharotone 2011, Batistakis 2012, Evans 2012a, Torres 2012, Batistakis 2014, Chung 2014, Askar 2015, Cheng 2015, Chung 2015, Li 2015c, Liu 2015, Xia 2015c, Xia 2015b, Ye 2015, Askar 2016, Brune 2016, Chung 2016, Nguyen 2016, Xia 2016). Film-wrinkling, ultrathin film tensile testing, and nanobeam bending experiments report decreases in modulus with confinement, whereas Brillouin light scattering, neutron scattering, nanoindentation, and nanobubble inflation report increases in modulus with confinement. Yet other studies employing picosecond acoustics indicate that stiffness is invariant with confinement. Among these reports, a

variety of polymer-substrate pairs are investigated at a range of temperatures. The research community has historically viewed the different sets of reports on stiffness-confinement behavior as opposing or contradictory.

A major motivation of this dissertation is to understand the physical origins of stiffness-confinement behavior in polymers and to provide clarity to the apparent disparities in research literature. This is achieved by employing a fluorescence technique, which can interrogate polymer properties in ways that other techniques cannot. Fluorescence has been employed for decades to probe local environmental changes caused by changes in polarity (Kalyanasundaram 1977, Dong 1984, Nakashima 1993), micelle formation (Kalyanasundaram 1977, Nakashima 1993), and glass formation (Frank 1975, Ellison 2002a, Ellison 2002b, Ellison 2003, Ellison 2004a, Ellison 2004b, Mundra 2007b, Priestley 2007, Kim 2008, Kim 2009, Evans 2011, Kim 2011, Evans 2012b, Evans 2012c). The majority of research in this dissertation utilizes a fluorophore, pyrene, which exhibits changes in its spectral emission depending on its local environment. In seminal studies by Kalyanasundaram and Thomas as well as Dong and Winnik, it was demonstrated that the ratio of peak intensities I_1/I_3 increases with increasing polarity (Kalyanasundaram 1977, Dong 1984). Pyrene has since been utilized to characterize changes in T_g. In this dissertation, the use of pyrene is extended to characterize stress relaxation and stiffness. The fluorescence technique is non-contact, non-destructive, and provides the ability to characterize length scales associated with stiffness-confinement effects.

In Section I, after the Introduction, Chapter 2 provides the background information required for understanding the research presented in this dissertation. Background on glass transition temperature, fragility, as well as modulus of polymers is presented. Also provided is background on the basics of fluorescence spectroscopy and how it can be used to understand polymer dynamics associated with T_g and stiffness.

Section II (Chapters 3 – 9) focuses on developing an understanding of stiffness-confinement effects in polymer films and polymer model nanocomposites. Chapter 3

demonstrates for the first time that stress relaxation can be characterized using a non-contact fluorescence approach in supported, bulk PS films. Previous fluorescence studies have utilized pyrene to sense changes in local polarity and T_g. We show that pyrene sensitivity to local polarity and T_g is part of a more general phenomenon of molecular caging. We demonstrate that pyrene is sensitive to changes in local rigidity and thus stress relaxation and stiffness.

Chapter 4 focuses on characterizing average stiffness-confinement effects and demonstrating that fluorescence can be used to characterize perturbations to stiffness associated with substrate and free-surface interfaces. Results are obtained using single-layer and bilayer PS films labeled with pyrene. We advance knowledge of confinement effects by characterizing perturbations to stiffness above, near, and below bulk T_g. We also demonstrate that substrate and free-surface interfaces perturb the polymer in different ways. Results from this chapter reveal that there are trends associated with stiffness-confinement behavior and provide general consensus to the apparently disparate research in the community.

Chapter 5 provides a deeper understanding of stiffness-confinement effects by characterizing stiffness gradient length scale using both fluorescence and nanoindentation via atomic force microscopy (AFM). Stiffness gradients are characterized near a polymer-substrate interface with the use of trilayer model nanocomposites, which provide a means for directly characterizing stiffness length scales using fluorescence. Reasons for conducting experiments on room-temperature model nanocomposites are two-fold: to gain an understanding of stiffness-confinement length scales in real nanocomposites as well as to compare results with AFM. We find that fluorescence and nanoindentation exhibit good qualitative and quantitative agreement regarding stiffness gradient length scales near a polymer-substrate interface.

Chapter 6 introduces the concept that thermal history effects can impact length scales associated with stiffness gradients. Comparisons are made at the same temperature between model nanocomposites that have been subject to two different thermal history conditions. It is observed that thermal history impacts both the magnitude and length scale associated with

stiffness perturbations near a rigid substrate interface. These results indicate that comparisons between reports in the research literature require careful consideration of the thermal history conditions.

Chapter 7 extends both the utilization of the fluorescence technique and an understanding of stiffness-confinement effects in a number of ways. Trilayer model nanocomposites and trilayer films are utilized to directly characterize stiffness gradients near substrate and free-surface interfaces. We take advantage of the fact that fluorescence can be employed at a range of temperatures to characterize stiffness gradients in the glassy state, near T_g, and in the rubbery state. Results are compared with those from Chapters 4 and 5.

Chapter 8 demonstrates that stiffness-confinement behavior can be tuned via addition of plasticizers. Suppression of stiffness-confinement effects is observed with the addition of dioctyl phthalate as a plasticizer in PS films. Results indicate that plasticizers impact stiffness perturbations associated with substrate interfaces.

In Chapters 3 – 8, pyrene is utilized as the fluorophore to characterize local environmental changes in terms of stress and stiffness. Chapter 9 broadens the fluorescence approach to characterizing stiffness-confinement effects by demonstrating that other fluorophores also show sensitivity to local environmental changes. It is demonstrated that another dye, phenanthrene, has the potential to characterize such properties as well. Phenanthrene and pyrene belong to a class of molecules known as vibronic coupling dyes. Thus, this study opens the possibility to use a broader glass of vibronic coupling dyes to characterize various polymer properties.

In Section III (Chapters 10 & 11), research is focused on characterizing T_g-confinement effects in complex geometries relative to thin polymer films. Measurements are carried out using differential scanning calorimetry (DSC), which represents a gold-standard technique of measuring T_g in both academic and industrial settings. Chapter 10 investigates how both T_g, T_g breadth, and fragility change as a function of molecular weight in dense PS brushes grafted from

silica nanoparticles. We find that the polymer exhibits different properties as a function of distance from the nanofiller interface. Chapter 11 demonstrates the impact of intrinsic size effects in perturbing T_g and fragility for PS nanorods supported in anodized aluminum oxide (AAO) templates. The impacts of intrinsic size effects on T_g and fragility are interrogated by varying the polymer molecular weight.

Section IV (Chapter 12) provides a summary of the research in this dissertation and provides recommendations for future work.

CHAPTER 2

Background

This chapter introduces core concepts that will be discussed throughout this dissertation regarding glass transition temperature, fragility, and modulus or stiffness in polymers. Deviations from bulk behavior in nanoconfined polymer films and nanocomposites will also be introduced in terms of the available research literature. Basic concepts of fluorescence spectroscopy will be discussed to provide physical understanding behind the technique and to justify its use in characterizing polymer properties.

2.1 Bulk Glass Transition Phenomena

2.1.1 The Glass Transition, Cooperativity, and Relaxation Times

A polymer cooled from the rubbery state to the glassy state will experience a temperature at which the time scale for polymer relaxation exceeds the experimental time scale. The temperature at which this occurs is known as the glass transition temperature (T_g). Figure 2-1 shows specific volume or enthalpy as a function of temperature. At T_g, the average relaxation time for a polymer is ~100 s (Bohmer 1993). In addition to the polymer relaxation time associated with segmental motion, polymers undergo large changes in material properties near T_g. For instance, polymers will exhibit several orders of magnitude change in modulus values (Sperling 2006). Despite decades of research on T_g, understanding its physical origins remains one of the biggest challenges in polymer physics (Anderson 1995, Angell 1995, Debenedetti 2001).

The T_g of a polymer is considered to be a kinetic phenomenon that does not exhibit second order phase transition behavior (Schweizer 1989, Chandler 2005, Dyre 2006, Roland 2011). In fact, a mode-coupling theory, which is a purely molecular-kinetics-based model, captures many of the quantitative aspects of T_g (Gotze 1992, Gotze 1998). The kinetic nature of the glass transition is made clear from the $3 - 5$ °C shifts in T_g accompanying an order of magnitude change in cooling rate (Ediger 1996). Faster cooling rates cause polymers to fall out
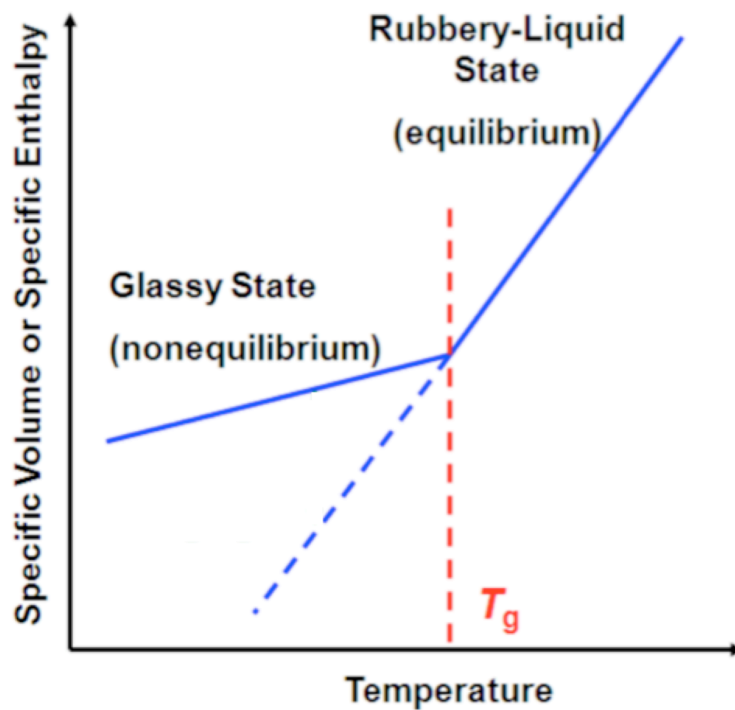
Figure 2-1: Specific volume or enthalpy as a function of temperature. The illustration depicts a polymer undergoing a glass transition at a temperature T_g.

of equilibrium at higher temperatures since the experimental time scale becomes shorter than the polymer relaxation time scale.

The T_g has also been modeled in terms of entropy. Several models relate relaxation time associated with T_g (known as α-relaxation) to configurational entropy. For instance, Adam and Gibbs have proposed a thermodynamic theory that relates the probability of relaxation to the number of configurational states available for relaxation (Adam 1965). The model predicts an ideal glass transition occurring when entropy reaches zero upon cooling. The concept of an ideal T_g is commonly discussed in terms of the Kauzmann paradox (Kauzmann 1948), which indicates that at low temperatures, the entropy of an amorphous liquid is lower than that of its crystalline form at a temperature T_K above 0 K. This implies that if an amorphous liquid were cooled at an infinitely slow rate, the entropy would exhibit negative values at T_K, which is an unphysical result. The glass transition occurs to avoid violating the third law of thermodynamics (Debenedetti 2001).

Polymer motions associated with T_g involve the cooperative segmental mobility of 10s – 100s of repeat units (Schmidt-Rohr 1991, Reinsberg 2001, Merabia 2004), corresponding to a length scale of 1 – 4 nm (Donth 1996, Tracht 1998, Ellison 2005, Cangialosi 2007). This length scale is used to describe a hypothetical volume referred to as a cooperatively rearranging region (CRR) (Adam 1965). In order for one polymer repeat unit to move, surrounding polymer repeat units in a cage around the original unit must also move, which in turn requires other molecules to move, etc. This molecular motion ultimately requires the cooperative mobility of many repeat units. Importantly, differences in mobility from one polymer repeat unit to the next gives rise to a distribution of relaxation times associated with T_g, *i.e.*, α-relaxation time distribution.

The distribution of relaxation times associated with α-relaxation is described by the Kolrausch-Williams-Watts equation. The parameter β (ranging in values from 0 to 1) reflects the breadth of the α-relaxation time distribution (Bohmer 1993, Dhinojwala 1994a, Hall 1997). β values decrease upon cooling towards T_g indicating a broader α-relaxation time distribution

corresponding to the cooperative motion of many repeat units.

2.1.2 Fragility

Above T_g, polymers exhibit α-relaxation times that deviate from Arrhenius temperature dependence and can be modeled by the Williams-Landel-Ferry equation. Near T_g, α-relaxation can undergo many orders of magnitude change because the activation energy required for cooperative segmental motion increases rapidly upon cooling. Figure 2-2 shows the log of relaxation time, τ_α, as a function of T_g/T. The slope of the α-relaxation time evaluated at T_g is a parameter known as the fragility index, m (Angell 1991, Bohmer 1993, Angell 1995, Angell 1997) and can be calculated from the following equation:

$$m = [d(\log(<\tau>))/d(T_g/T)]_{Tg/T}$$

Fragility values of bulk polymers typically range from ~60 to 200 or more, with higher values of m corresponding to polymers that exhibit greater temperature dependence of relaxation time upon cooling towards T_g. Fragility is impacted by the chemical structure of the polymeric materials. For instance, polymers with bulky side groups or rigid backbones have higher m values due to greater requirements for cooperative segmental mobility relative to flexible polymers with small side groups (Kunal 2008) and tend to exhibit less efficient chain packing (Dudowicz 2005a).

Recent research has demonstrated that fragility is a key parameter impacting the strength of T_g-confinement effects (Kunal 2008, Evans 2012c, Evans 2013a, Hayashi 2014, Marvin 2014, Glor 2015, Jin 2016, Lan 2016). In 2013, Evans *et al.* demonstrated in polymer/substrate pairs with non-attractive interactions that the magnitude of T_g-confinement effects increased with increasing m. Others have demonstrated that fragility itself is subject to confinement effects (Fukao 2001, Napolitano 2010, Fukao 2011, Arabeche 2014, Glor 2015, Lan 2016). Outside of thin films, m-confinement effects have seldom been studied in more complex polymer geometries such as polymer brushes grafted from an interface or linear polymers confined within
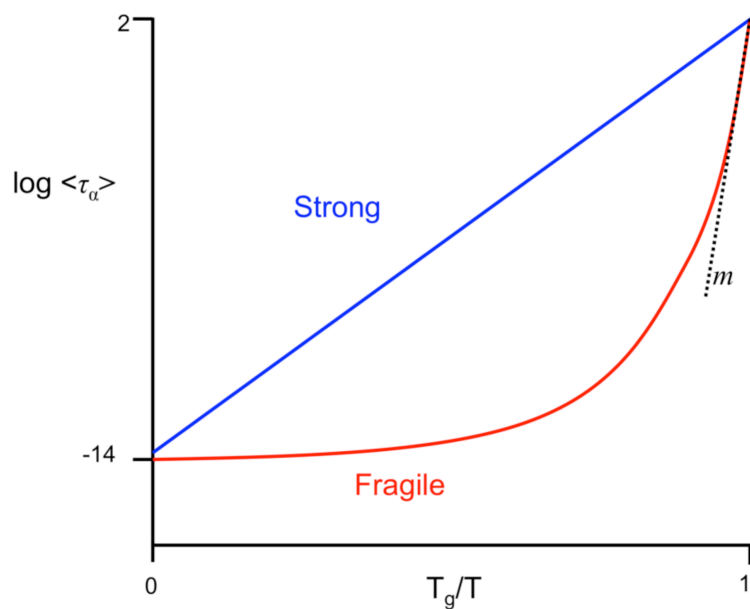
Figure 2-2: Log of α-relaxation time (τ_α) as a function of T_g/T. The blue line depicts a strong glass former with low fragility and the red line depicts a weak glass former with high fragility. Fragility is determined by the slope, m, evaluated at T_g.

cylindrical pores. Some of the studies described in this dissertation will be focused on understanding the impacts of confinement T_g and fragility in complex polymer geometries.

2.2 Glass Transition in Confined Polymers

2.2.1 T_g in Nanoconfined Polymer Films

The effects of nanoscale confinement on polymer T_g have been studied extensively over the past two decades (Keddie 1994b, Forrest 1997a, Grohens 1998, Fukao 2000, Kim 2000, Mattsson 2000, Dalnoki-Veress 2001, Kawana 2001, Tsui 2001, Grohens 2002, Xie 2002, Ellison 2003, Sharp 2003, Ellison 2005, Fakhraai 2005, Roth 2006, Seemann 2006, Mundra 2007b, Rittigstein 2007, Roth 2007a, Roth 2007c, Torres 2009, Dion 2010, Glynos 2011, Kim 2011, Baeumchen 2012, Evans 2013a, Gao 2013, Zhang 2013a, Lan 2014, Vignaud 2014, Baglay 2015, Evans 2015, Geng 2015, Glor 2015, Glynos 2015, Kanaya 2015, Kawaguchi 2015, Li 2015a, Priestley 2015, Zhang 2015, Geng 2016, Jin 2016, Lan 2016, Liu 2016, Shin 2016, Tan 2016). In 1994, Keddie *et al*. (Keddie 1994a, Keddie 1994b) demonstrated that the T_g of nanoconfined polymer films decreased relative to bulk values. In particular, PS films supported on silicon exhibited reductions in T_g when thickness was at or below ~40 nm. They postulated that T_g reductions were observed due to the presence of a mobile, liquid-like surface layer that impacted the polymer to a greater extent with decreasing film thickness. Support for this idea came from Sharp and Forrest (Sharp 2003) who demonstrated that the presence or absence of T_g-confinement effects in PS films could be observed by reversibly uncapping or capping the free-surface interface.

To investigate length scales associated with T_g perturbations near a free-surface interface, Ellison and Torkelson (Ellison 2003) used multilayer films in which dye-labeled polymer layers were placed at various distances from the polymer-air interface. They showed that a 14-nm-thick PS layer located adjacent to the free surface exhibited T_g reduced by 32 °C relative to bulk T_g and that such perturbations to T_g extend tens of nanometers towards the interior of the polymer films.

Such length scales far exceed the $1 - 4$ nm length scale corresponding to a CRR, indicating that interfaces can significantly impact polymer properties.

It has also been demonstrated that T_g increases with decreasing film thickness in the cases of polymer/substrate pairs that have sufficiently large attractive interactions (Keddie 1994a, van Zanten 1996, Ellison 2002b, Park 2004, Mundra 2006, Priestley 2007, Roth 2007a). The fluorescence/multilayer approach was extended to characterize local changes in T_g for a series of poly(n-alkyl methacrylates) and found enhancements near the substrate and reductions near the free surface (Priestley 2007). The enhancement in T_g near the substrate for PMMA or poly(2-vinyl pyridine) (P2VP) can be attributed to hydrogen bonding between the polymer and hydroxyl groups native to the surface of silica substrates. General trends can be observed regarding T_g-confinement effects for sufficiently thin supported polymer films. In the absence of attractive interactions, T_g reductions associated with the free-surface interface and a lack of perturbation to T_g near the substrate interface leads to an overall reduction in film T_g. In the presence of attractive interactions, T_g enhancements near the substrate interface dominate over the T_g reductions near the free-surface interface and leads to an overall enhancement in T_g.

In supported PS films, T_g-confinement effects do not exhibit molecular weight dependence (Keddie 1994b, Kawana 2001, Ellison 2003, Ellison 2005, Seemann 2006, Lan 2014, Zhang 2015). This is in sharp contrast to free-standing PS films that exhibit molecular weight (MW) dependence of T_g-confinement effects (Forrest 1997a, Mattsson 2000, Dalnoki-Veress 2001, Kim 2011). For instance, the strength of T_g-confinement effects increases when molecular weight exceeds ~350 kg/mol for PS (Dalnoki-Veress 2001). The presence of molecular weight dependence to T_g-confinement behavior in free-standing PS and the absence in supported PS films remains an unanswered question in the research field. To address this question, de Gennes (de Gennes 2000) proposed that if loops of a polymer chain can reach the free-surface interfaces in free-standing films, excess free volume will be introduced in the polymers causing reductions in T_g. This theoretical picture was shown to be incorrect by Kim

and Torkelson (Kim 2011) who used a fluorescence/multilayer technique in free-standing films. It was demonstrated that a dye-labeled middle layer exhibited dramatic T_g reductions, despite not being in contact with either free-surface interface. Investigating geometries other than thin polymer films could provide greater clarity regarding the role of molecular weight on T_g-confinement behavior.

2.2.2 T_g in Polymer Nanocomposites

T_g-confinement behavior has also been investigated in polymer nanocomposites (Starr 2001, Ash 2002b, Berriot 2002, Savin 2002a, Starr 2002, Arrighi 2003, Blum 2003, Wang 2003, Bansal 2005, Ramanathan 2005, Bansal 2006, Hong 2006, Rittigstein 2006, Kropka 2007, Lee 2007, Rittigstein 2007, Ramanathan 2008, Ding 2009 Kropka 2008, Fang 2010, Harton 2010, Parker 2010, Pryamitsyn 2010, Mizuno 2011, Moll 2012, Ndoro 2012, Fotiadou 2013, Holt 2013, Zhu 2013, Chandran 2014, Kim 2015b, Casalini 2016, Mangal 2016). Molecular dynamics simulations have indicated that T_g of polymer nanocomposites can be enhanced or reduced by tuning polymer-nanofiller interactions, and that the effects are analogous to free-surface or attractive polymer-substrate interactions observed in thin polymer films (Starr 2001).

Interfacial interactions between a polymer and a nanofiller dictate the properties of the nanocomposite as a whole and therefore significant nanoparticle aggregation may hinder property enhancements associated with the presence of nanofillers. One approach to improve particle dispersion involves utilizing polymer-grafted nanoparticles or hairy nanoparticles, which can exhibit enhanced compatibility with the surrounding polymer matrix (Savin 2002b, Rong 2006, Akcora 2009b, Pietrasik 2011, Voudouris 2011, Dang 2013, Fernandes 2013, Fernandes 2014, Kim 2015a, Koerner 2016). But in order to understand the properties of the nanocomposite as a whole, it is important to first understand the T_g behavior of the grafted-nanofillers themselves. Few studies have investigated such properties. Savin *et al*. (Savin 2002b) reported reductions in T_g of polystyrene-grafted silica nanoparticles (Si-PS) with decreasing graft molecular weight (MW). Dang *et al*. (Dang 2013) also reported reductions in T_g with reductions

in graft MW from ~200 kg/mol to ~10 kg/mol, respectively. Kim *et al.* (Kim 2015a) investigated the T_g behavior of *cis*-1,4-polyisoprene-grafted silica nanoparticles (Si-PI) and observed MW dependence. This dissertation describes research conducted on PS-grafted silica nanoparticles aimed towards understanding the MW-dependence of T_g-confinement behavior.

2.3 Bulk Polymer Stiffness and Modulus

2.3.1 Modulus and the Five Regions of Viscoelasticity

The ability of a material to resist deformation is quantified by its modulus. Deformation can be applied in a number of ways including by stretching, compressing, shearing, etc. to yield different modulus values such as Young's modulus, shear modulus, and bulk modulus. For instance, Young's modulus is equal to the ratio of tensile stress to tensile strain in the limit of zero strain and is a "fundamental measure of stiffness of a material" (Sperling 2006).

Polymers are viscoelastic materials that exhibit a combination of elastic and viscous behavior depending on temperature. Figure 2-3 shows the log of Young's modulus as a function of temperature. There are five regions of viscoelastic behavior that can be used to describe polymer properties. In the glassy region (1), polymers exhibit Young's modulus values that are roughly constant with temperature. For high molecular weight PS, typical glassy modulus values are around 3 GPa or 3000 MPa. In the region below T_g, molecular motions are most commonly limited to rotational or vibrational motions. The relationships between modulus and short time-scale vibrational motions will be discussed in Section 2.3.2.

Upon heating through the glass transition region (2), *i.e.*, near T_g, polymers will generally exhibit reductions in modulus by about three orders of magnitude over a 20 – 30 °C temperature range (Sperling 2006) and polymers in this region can be described as leathery. Polymers will exhibit cooperative segmental mobility in this region as described in Section 2.2. Upon heating further, amorphous polymers will enter the rubbery plateau region (3). Depending on whether the polymer is cross-linked or linear, the modulus will exhibit differing behavior. If the polymer is
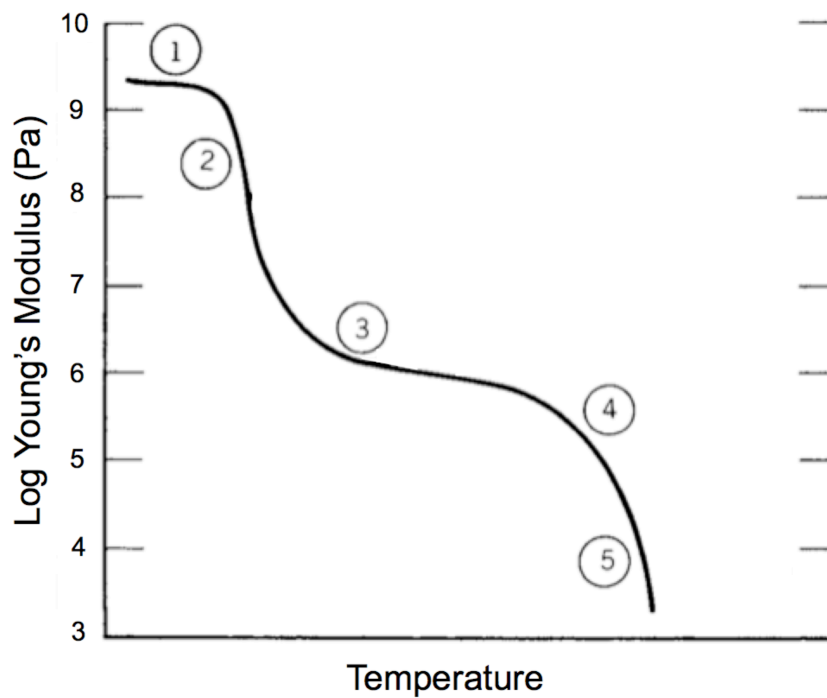
Figure 2-3: Log of Young's Modulus as a function of temperature for a polymer. The numbers correspond to the different regions of viscoelastic behavior: (1) glassy region, (2) glass transition region, (3) rubbery plateau, (4) rubbery flow, and (5) liquid flow. (Plot adapted from Sperling, *Introduction to Physical Polymer Science*. Copyright 2006 John Wiley & Sons Inc.)

cross-linked, modulus values will increase linearly with temperature, whereas if the polymer is linear, modulus values will decrease slowly with increasing temperature. Modulus values in the rubbery plateau region are ~2 MPa. In terms of linear polymer, molecular motions in the rubbery plateau region correspond to snake-like motions of polymer chains associated with the reptation model (de Gennes 1971). The majority of this thesis will focus on the stiffness of PS in the first three regions of viscoelastic behavior.

At even higher temperatures polymers will enter the rubbery flow (4) and liquid flow (5) regions in which the polymers will behave like liquids (Sperling 2006). Polymers will exhibit significant mobility such that chains can slide past one another and flow as individual molecules.

2.3.2 Polymer Vibrational Dynamics

Stiffness or modulus can be related to short time scale (~nanosecond) vibrations or mobility in materials (Sperling 2006). For instance, experimental characterizations of boson peak or mean-squared displacement (MSD), $<u^2>$, demonstrate the connection between such parameters and modulus. The boson peak is associated with collective vibrational modes with frequencies in excess of what is predicted by the Debye model of acoustic modes (Soles 2001). It has been demonstrated via Brillouin light scattering that the boson peak energy correlates with the velocity of acoustic waves traveling through polymer. The velocity of acoustic waves is proportional to the square root of the bulk modulus. Dynamics associated with MSD have been correlated to the modulus of polymers in a number of studies using incoherent neutron scattering (Soles 2002, Inoue 2005, Ye 2015). The MSD is inversely proportional to the harmonic force constant (Soles 2002, Inoue 2005) or spring constant (Ye 2015) (at sufficiently low temperatures). Inoue *et al*. state that the force constant determined in PS films corresponds to "those for torsion of the C-C bond in the main chain and/or the force constant for the interaction potential between nonbonded atoms" (Inoue 2005). These force or spring constants scale roughly with the polymer modulus (Soles 2002, Inoue 2005, Ye 2015). Therefore, properties such as boson peak and MSD, which describe vibrational dynamics, are correlated with modulus.

A deeper physical understanding of how MSD is tuned or altered can be rationalized according to a "caging" mechanism. Reductions in MSD (enhancements in harmonic force constant) correspond to environments in which the atoms are "caged" and trapped in deep potential energy minima (Soles 2002). In a stiff or "caged" environment, vibrations associated with MSD are suppressed. Similarly, in stressed or stiff environments, atoms are trapped in potential energy minima. The relaxation of stresses or reductions in stress leads to reductions in the force constant as atoms are less trapped in potential energy minima, or less "caged" by their environment. Experimental techniques capable of characterizing molecular caging have the potential to characterize stiffness in polymers (Simmons 2016).

2.4 Stiffness in Confined Polymers

2.4.1 Stiffness in Nanoconfined Polymer Films

Modulus- or stiffness-confinement behavior of polymers have been studied nearly as long as T_g-confinement behavior (Lee 1996, Briscoe 1998, Forrest 1998, Soles 2002, Hartschuh 2004, Stafford 2004, Hartschuh 2005, Inoue 2005, O'Connell 2005, Yoshimoto 2005, Inoue 2006, Stafford 2006, Cheng 2007, Tweedie 2007, Stoykovich 2008, Gomopoulos 2009, Delcambre 2010, Gomopoulos 2010, Xu 2010, Arinstein 2011, Watcharotone 2011, Batistakis 2012, Evans 2012a, Torres 2012, Batistakis 2014, Chung 2014, Askar 2015, Cheng 2015, Chung 2015, Li 2015c, Liu 2015, Xia 2015c, Xia 2015b, Ye 2015, Askar 2016, Brune 2016, Chung 2016, Nguyen 2016, Xia 2016). However, various reports have indicated that stiffness increases, decreases, or remains invariant with confinement.

Reports on polymer films supported on rigid substrates have most commonly indicated invariance or enhancement in modulus with decreasing film thickness. Using Brillouin light scattering (BLS), Gomopoulos *et al*. (Gomopoulos 2009) and Cheng *et al*. (Cheng 2007) measured the modulus of supported PS films as a function of thickness at room temperature. PS films exhibited invariance in modulus down to thicknesses of 40 nm. However, neither BLS

study investigated films with thicknesses below 40 nm. A study using picosecond acoustics invariance in the wave velocity with thickness down to 40 nm in PMMA single-layer films supported on aluminum. Closer inspection of their data indicates that wave velocity and thus stiffness are enhanced in films with thicknesses below 40 nm. Although data were not explicitly provided Lee *et al*. stated that similar enhancements in wave velocity and thus stiffness were observed for ultrathin PS films. Inoue *et al*. (Inoue 2006) used incoherent neutron scattering to measure changes in $<u^2>$. Relative to bulk response in glassy-state PS films at 40 °C, $<u^2>$ decreased slightly in 100-nm-thick films and more significantly in 40-nm-thick films. Larger percentage reductions from bulk response were observed in the rubbery state at 135 °C in these nanoconfined films.

When a rigid substrate is replaced by a soft substrate or a free surface, experimental studies have most commonly reported a reduction in stiffness with confinement. In PDMS-supported polymer films, studies using a film wrinkling technique have reported reductions in modulus with decreasing thickness (Stafford 2004, Stafford 2006, Torres 2012). Stafford *et al*. (Stafford 2006) reported that PDMS-supported PS films exhibit reductions in room-temperature modulus with decreasing thickness at ~40 nm and below. Liu *et al*. (Liu 2015) investigated stiffness-confinement effects in room-temperature, free-standing PS films via the stress-strain response of stretched films floating on water. They reported that the modulus decreased precipitously below thicknesses of ~25 nm (Liu 2015). Other studies (Stoykovich 2008, Delcambre 2010) that have utilized beam-bending in nanopatterned PMMA structures at room temperature observed structural collapse as beam width was reduced below 100 nm (Stoykovich 2008) and 50 nm (Delcambre 2010). It can be rationalized that with decreasing width, free-surface effects dominate and cause nanobeam collapse. In contrast, nanobubble inflation studies of free-standing polymer films exhibit differences compared to ultrathin film tensile testing and beam-bending studies; in a $10 - 15$ °C temperature range above and below T_g, these studies have reported stiffening with decreasing thickness below ~200 nm (O'Connell 2005, Xu 2010, Li

2015c).

Several simulation studies have focused on characterizing the impacts of confinement on supported polymer films with no free surfaces (Batistakis 2012, Batistakis 2014), supported polymer films with one free surface (Xia 2015b), and free-standing polymer films (Yoshimoto 2005, Xia 2015c). Simulations are in general qualitative agreement with many experimental reports that the presence of a rigid substrate increases stiffness (Batistakis 2012, Batistakis 2014, Xia 2015b), the presence of a free surface reduces stiffness (Yoshimoto 2005, Xia 2015c, Xia 2015b), and free-standing polymer films exhibit reduced stiffness with reduced thickness (Yoshimoto 2005, Xia 2015c). Specifically, Xia and Keten (Xia 2015b) simulated stiffness behavior of 5-, 10-, and 19-nm-thick supported PMMA films. They reported that $<u^2>$ decreases and stiffness increases within ~2 nm of the substrate interface and that stiffness decreases within a comparable length scale of the free surface, but did not comment on the impact of overall film thickness on stiffness gradients.

The sets of results described for average stiffness-confinement effects in polymers have historically been viewed as contradictory to one another. However, many factors must be considered that could impact stiffness-confinement behavior such as the polymer species, whether the polymer is supported, temperature, thermal history, etc. To understand average stiffness-confinement behavior, it is necessary to characterize length scales of stiffness perturbations near interfaces. Whereas the majority of reports in literature have focused on average stiffness-confinement effects, relatively little research has been done characterizing stiffness gradient as a function of distance from substrate and free surface interfaces. Outside of the research described in this dissertation there are only two experimental reports characterizing stiffness gradients. Both studies have used nanoindentation via atomic force microscopy to show that stiffness increases with decreasing distance from a rigid substrate interface. The room-temperature stiffness gradient length scales were observed to extend ~100 nm or ~170 nm in PMMA supported on silica or alumina (Cheng 2015) as well as ~40 nm for styrene-butadiene

rubber supported on silica (Brune 2016). A major focus of this dissertation is to provide clarity regarding stiffness gradient length scales in terms of substrate and free-surface interfaces and whether such gradients are tunable.

2.4.2 Stiffness in Polymer Nanocomposites

Stiffness-confinement behavior in polymer nanocomposites has also been investigated in a range of polymer/nanofiller systems (Rharbi 1999, Tsukruk 2001, Ash 2002a, Kader 2006, Mijovic 2006, Shen 2006, Kontou 2007, Chen 2008, Fang 2009, Ramorino 2009, Geiser 2010, Pramoda 2011, Froltsov 2012, Madkour 2012, Wang 2012, Giesa 2013, Natarajan 2013, Diez-Pascual 2014, Mujtaba 2014, Yang 2014, Shao 2015, Simmons 2016, Wang 2016b, Weir 2016, Zachariah 2016). Enhancements in mechanical properties are strongly impacted by interfacial interactions between the nanofiller and polymer matrix. For instance, Ash *et al*. (Ash 2002a) found decreases in modulus for PMMA-alumina nanocomposites. In particular, addition of 5 wt% alumina led to 15 % reductions in modulus. This report did not comment on the potential formation of free surfaces between the polymer and nanofiller that may have led to these peculiar results. A study by Kontou and Anthoulis (Kontou 2007) found an optimum modulus enhancement when 4 wt% silica is dispersed in a PS matrix. The reason for the optimum modulus enhancement was attributed to substantial particle aggregation above 4 wt% that negated any potential modulus enhancement due to the formation of free surfaces between polymer and nanofiller.

Grafted nanoparticles may be employed that can improve compatibility between nanofiller and matrix. Studies of polymer-grafted nanoparticles reveal more information regarding stiffness-confinement effects in nanocomposites. Natarajan *et al*. (Natarajan 2013) found that the modulus of the PS-silica nanocomposites increased with increasing content up to 40 wt% silica. They attributed this behavior to the effective dispersion achieved with PS-grafted nanoparticles. An investigation on PS-grafted silica nanoparticles dispersed in a PS matrix by Maillard *et al*. (Maillard 2012) found that whereas the modulus increases with increasing silica

content, other properties may suffer such as the failure-to-strain or yield stress. They reported optimum property enhancements at about 5 wt% PS-grafted silica depending on the graft chain length and density.

In order to understand average stiffness-confinement behavior in real nanocomposites, it is necessary to understand how polymers are perturbed near interfaces. In addition, information regarding stiffness gradient length scales could aid in tailoring nanocomposites to have desired mechanical properties. In real nanocomposites, characterizing stiffness perturbations is a technological challenge since there is a distribution of interparticle spacing between nanofiller. Model polymer nanocomposites provide an alternative geometry with which to gain an understanding of confinement effects in real nanocomposites. Model polymer nanocomposites are essentially polymer films supported on both sides with substrates (Rittigstein 2007, Schadler 2007a, Killgore 2011). The distance between two substrates, *i.e.*, thickness is related to average interparticle spacing within real nanocomposites. Model nanocomposites are used in this dissertation to gather information regarding length scales associated with stiffness-confinement behavior in real nanocomposites. Similar experiments have been conducted relating T_g-confinement effects in model and real nanocomposites (Rittigstein 2007).

2.5 Fluorescence Spectroscopy

2.5.1 Basics of Fluorescence

The process of fluorescence begins with the excitation of electrons of a fluorophore from the ground state to the vibrational levels of the excited states. The electrons can then return back to the vibrational levels of the ground state by either non-radiative means (vibrations, rotations, etc.) or radiative means (fluorescence). This process is illustrated in a Jablonski diagram (Figure 2-4). In Figure 2-4, the bands correspond to various degenerate vibrational levels associated with the ground and excited states (Valeur 2001, Lakowicz 2006). Electrons can be excited from the ground state S_0 to one of the vibrational levels of the first excited singlet state S_1. The electron
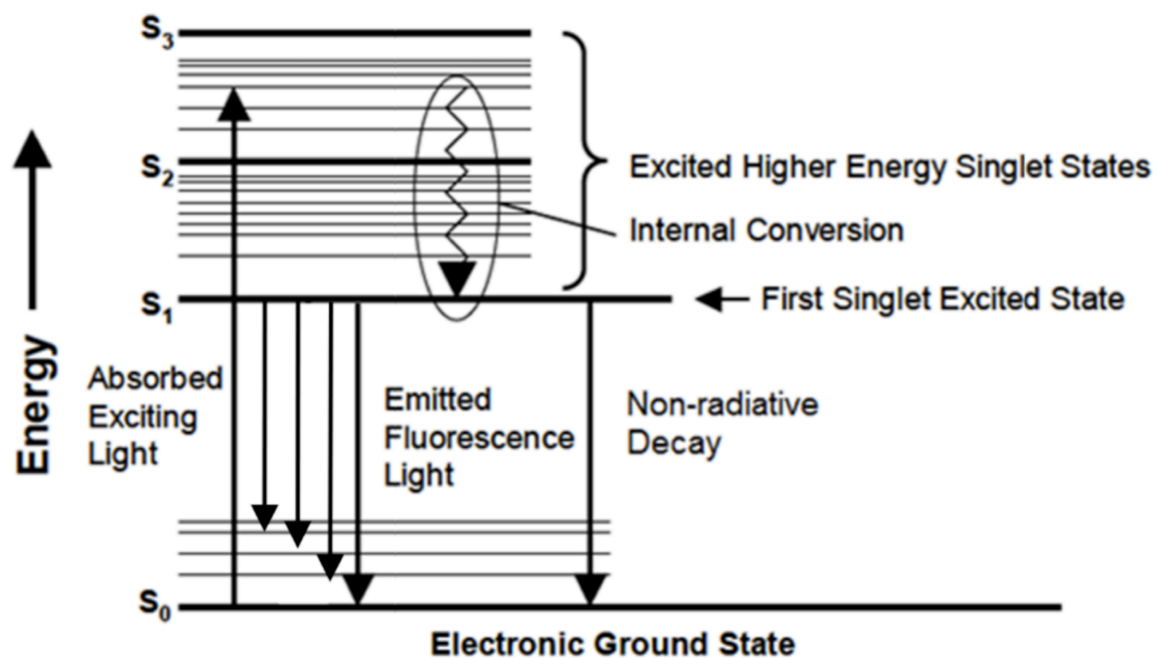
Figure 2-4: Jablonski diagram depicting the process of fluorescence. Bold horizontal lines correspond to energy states and thin horizontal lines correspond to degenerate energy levels (vibronic bands) with in the energy states. Vertical arrows depict electronic transitions. (Reproduced from Lakowicz. *J. Principles of Fluorescence Spectroscopy*. Copyright 1999 Plenum.)

can then return to a lower vibrational degenerate level associated with S_1 via internal conversion on the time scale of 10^{-12} s. The electrons can eventually return to the ground state on the time scale of $\sim 10^{-9} – 10^{-8}$ s (Valeur 2001). Such a time scale is similar to those of vibrational dynamics associated with stiffness or modulus ($\sim 10^{-9}$ s) (Sperling 2006).

Because of internal conversion processes, the energies of photons emitted during fluorescence are lower than those of the photons absorbed. For this reason, fluorescence spectra are shifted towards lower energy (higher wavelengths) relative to the absorption spectra. Important parameters related to fluorescence are the intensity of emitted lights and the quantum yield, which is the ratio of emitted photons to absorbed photons. Both intensity and quantum yield are impacted by local environmental changes and the ability for non-radiative energy decay pathways to be accessed (Valeur 2001).

Different fluorophores have different fluorescence emission spectra. For instance, the fluorescence spectrum for pyrene has five distinct peak intensities, and each one corresponds to a particular electronic transition. For instance, in pyrene the peak associated with the highest-energy (lowest wavelength) emission corresponds to the $S_1 \rightarrow S_0$ transition and is denoted as I_1 for the first vibronic band peak intensity (Kalyanasundaram 1977, Karpovich 1995). The other four peaks correspond to lower-energy (higher wavelength) vibronic transitions.

2.5.2 Sensitivity of Dyes to Local Environment

The dye that has received the most attention for its sensitivity to environmental changes is pyrene. In particular, seminal studies on pyrene fluorescence have demonstrated that the spectral shape of pyrene fluorescence emission changes depending on local solvent polarity (Kalyanasundaram 1977, Dong 1984). Kalyanasundaram and Thomas showed that the ratio of vibronic band peak intensities I_1/I_3 increases with increasing solvent polarity (Figure 2-5). This sensitivity was more fully developed into what is known as the Py scale of solvent polarity (Kalyanasundaram 1977, Dong 1984). As mentioned in Section 2.5.1, the peak intensities correspond to particular electronic transitions, and the wavelength associated with each intensity
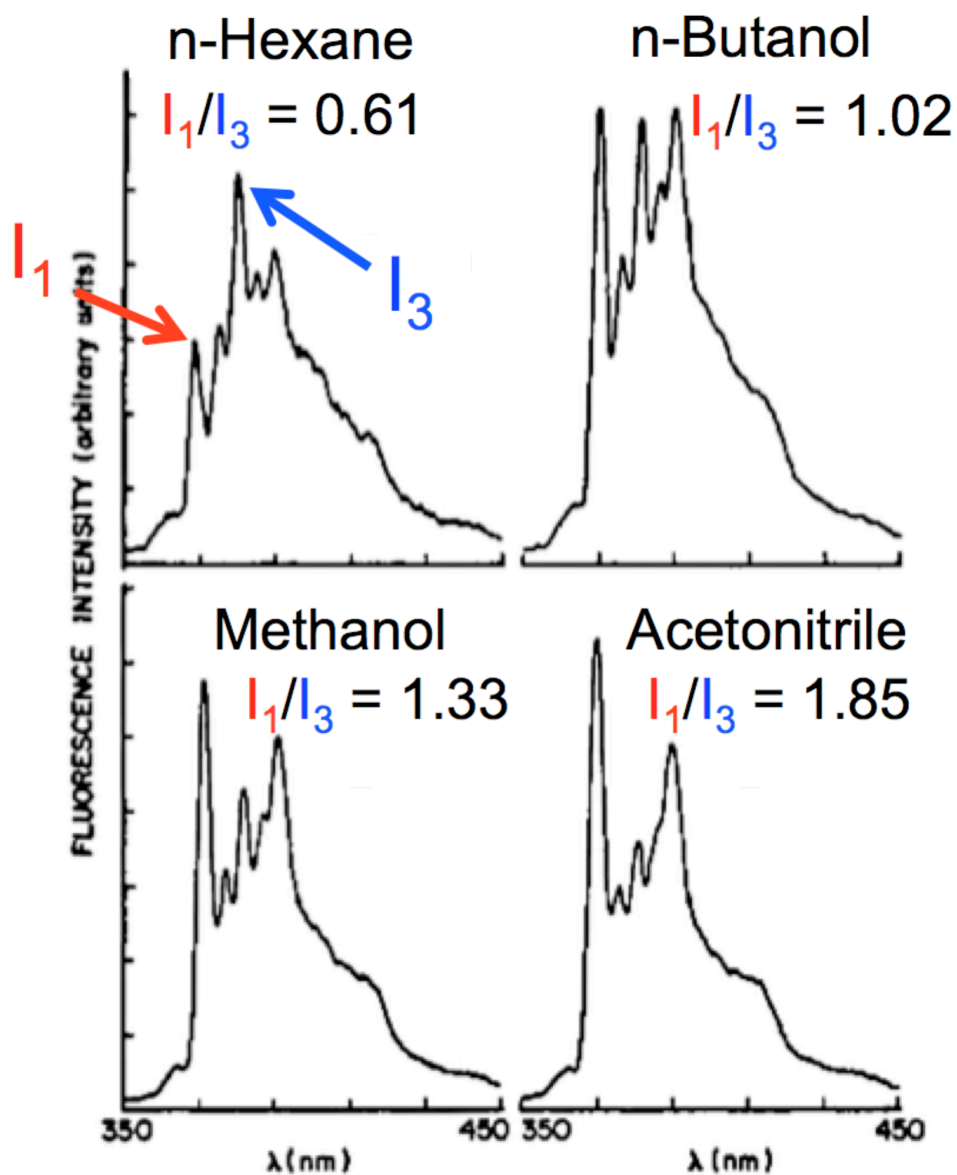
Figure 2-5: Pyrene fluorescence emission spectra in four solvents with increasing polarity from n-hexane, n-butanol, methanol, and acetonitrile. The ratio of the first vibronic band peak intensity to the third vibronic band peak intensity (I_1/I_3) increases with increasing polarity. (Reproduced from Kalyanasundaram and Thomas. *J. Am. Chem. Soc*. **1977**, 99, 2039. Copyright 1977 American Chemical Society.)

peak indicates the corresponding energy of the electronic transition. Thus, an enhancement in I_1/I_3 indicates a shift towards higher-energy electronic transitions. The shift towards higher-energy electronic transitions has been attributed to induced dipole-dipole coupling interactions between excited-state pyrene molecules and surrounding solvent molecules (Kalyanasundaram 1977, Dong 1984, Karpovich 1995, Valeur 2001). Upon excitation via UV light, electrons undergo a transition from a symmetrical distribution in the ground state to an asymmetrical distribution in the excited state, thereby inducing a dipole moment in excited-state pyrene. Depending on the polarity of surrounding solvent molecules, they will orient around the poles of excited-state pyrene via coupling (Karpovich 1995, Valeur 2001). With greater polarity, there is greater dipole-dipole coupling, which suppresses non-radiative energy decay pathways and consequently enhances high-energy fluorescence pathways. This ultimately causes enhancements in I_1 at the expense of other peaks, with the strongest effects being observed relative to I_3 (Kalyanasundaram 1977).

Not all fluorophores exhibit similar sensitivity to polarity like pyrene. In 1995, Karpovich and Blanchard have demonstrated that the sensitivity to polarity originates from the fact that pyrene belongs to a class of dyes known as vibronic coupling dyes. Electrons of vibronic coupling dyes like pyrene generally exhibit very weak transitions of electrons from the ground state (S_0) to the first excited singlet state (S_1) and strong transitions to the second excited singlet state (S_2) or others (Karpovich 1995, Valeur 2001). In essence, $S_0 \Leftrightarrow S_1$ is weak and $S_0 \Leftrightarrow S_2$ is strong. This is because vibronic coupling dyes have overlapping excited-state energy levels. In high-polarity environments, the induced dipole-dipole coupling mediates or separates the overlapping exhibited-state energy levels and allows for stronger $S_0 \Leftrightarrow S_1$ transitions. This is manifested as enhancements in I_1 relative to other peaks (Kalyanasundaram 1977, Karpovich 1995). Non-vibronic coupling dyes do not exhibit this type of sensitivity.

2.5.3 Characterization of T_g in Polymers Using Fluorescence

In 1975, Frank was the first to characterize T_g in polymers using fluorescence, by

monitoring excimer fluorescence of poly(2-vinyl naphthalene) doped into PS films (Frank 1975). Loutfy (Loutfy 1981, Loutfy 1986) developed a range of rotor probes to characterize T_g via the temperature dependence of fluorescence emission intensity. Some pyrenyl dyes can be used to measure T_g by the integrated intensity and also by the intensity ratio (I_1/I_3) (Ellison 2002a, Ellison 2002b, Ellison 2003, Ellison 2004a, Ellison 2004b, Mundra 2007b, Priestley 2007, Kim 2008, Kim 2009, Evans 2011, Kim 2011, Evans 2012b, Evans 2012c, Askar 2015, Askar 2016). T_g is measured by identifying a transition in the temperature dependences of overall intensity or of I_1/I_3 in the rubbery and glassy states.

2.5.4 Characterization of Stiffness in Polymers Using Fluorescence

The ability to use pyrenyl dyes to measure T_g and polarity as has been described in Section 2.5.3 suggests that the sensitivity to local environments originates from a more general phenomenon of "molecular caging." Densification upon cooling through T_g and induced dipole-dipole coupling mechanisms are two examples of molecular caging that can impact pyrene fluorescence. In this dissertation we utilize this general sensitivity to characterize other polymer properties such as stress and stiffness. The majority of research is conducted using 1-pyrenylmethyl methacrylate (MPy) as a pyrenyl label attached to PS chains. (Compared to MPy labels, 1-pyrenylbutyl methacrylate (BPy) labels exhibit significantly reduced sensitivity of I_1/I_3 to local rigidity. The reduction in sensitivity with increasing linkage distance (butyl vs. methyl) has been noted previously (Kim 2008, Evans 2012b).) In stressed or stiff environments, excited-state pyrene is caged to a greater extent. This leads to suppression of non-radiative forms of energy decay and enhancements in high-energy transitions of electrons from the excited state to the ground state. Thus, I_1/I_3 increases with increasing stiffness and stress (Askar 2015, Askar 2016, Zhang 2017). The time scale associated with pyrene fluorescence, from absorption to emission, is ~200 nanoseconds (Mundra 2007b), similar to the time scale associated with $<u^2>$ measurements. Furthermore, the ability to use fluorescence to characterize the Debye-Waller factor (related to $<u^2>$) as a surrogate to incoherent neutron scattering experiments, as done by

Cicerone *et al*. (Cicerone 2011), suggests that the caging mechanism is common to both incoherent neutron scattering and selective fluorescence studies. In this dissertation, we demonstrate the first use of fluorescence to characterize stress stiffness in polymers and use the technique as a tool to investigate stiffness-confinement behavior in ways that other techniques cannot.

II. CHARACTERIZING STIFFNESS-CONFINEMENT EFFECTS IN POLYMER FILMS AND MODEL NANOCOMPOSITES VIA FLUORESCENCE SPECTROSCOPY

CHAPTER 3

Residual Stress Relaxation and Stiffness in Spin-Coated Polymer Films:

Characterization by Ellipsometry and Fluorescence

As described in Chapter 2, pyrene fluorescence is sensitive to its local environment via changes in molecular caging. In this chapter, pyrene fluorescence sensitivity is utilized to characterize stress relaxation in spin-coated PS films. The results are compared against a more widely used ellipsometry approach to demonstrate significant agreement. Also discussed is the physical basis (and proof-of-concept experiments) for how stiffness in polymers can also be characterized as will be discussed in later chapters in this dissertation.

3.1 Introduction

Residual stresses in polymer films are a function of processing method, *e.g.*, spin-coating resulting in non-equilibrium local chain conformations, and of thermal history, *e.g.*, heating or cooling which leads to stresses arising from different thermal expansion coefficients of the film and its substrate (Prest 1979, Prest 1980, Cohen 1981, Lin 1993, Ree 1994, Frank 1996, Ree 1997, Walheim 1997, Reiter 2001, Mundra 2006, Chung 2009, Thomas 2011a). Residual stresses remain in the films until sufficient thermal annealing is done to relax the stresses. Unrelaxed residual stresses in thin polymer films have been observed to induce crack formation (Francis 2002), delamination from substrates (Francis 2002), and dewetting (Reiter 1992, Reiter 1993), all of which are critical considerations for the fabrication of nanoconfined polymeric devices.

Approaches to characterize residual stresses include the curvature method (Croll 1978, Croll 1979), cylindrical punch (Ju 2007), blister method (Guo 2005), surface wrinkling (Chung 2009), cantilever bending method (Thomas 2011b), dewetting (Reiter 1994, Richardson 2003, Reiter 2005, Damman 2007, Reiter 2013), and intrinsic excimer fluorescence (Mundra 2006). With curvature measurements, sensitivity to residual stresses decreases for ultrathin films since it is difficult to resolve small changes in curvature (Tang 2007, Chung 2009). Contact methods that perturb polymer chains such as cylindrical punch, blister, and cantilever bending techniques

involve imparting external stresses on polymer samples which may convolute stress relaxation measurements (Chung 2009). Optical methods may be used to avoid such issues arising from contact methods. Nearly ten years ago, Mundra *et al.* (Mundra 2006) demonstrated that intrinsic excimer fluorescence of styrene-containing polymer systems could be used to sense stress relaxation via small changes in local chain conformation that lead to changes in the ratio of excimer to monomer fluorescence (Mundra 2006). However, this approach is limited to polymers and copolymers that contain sufficient levels of styrene-styrene dyads along a chain to exhibit substantial excimer fluorescence.

Here, we demonstrate that non-contact, non-destructive optical methods involving ellipsometry and a self-referencing fluorescence method, which exhibits sensitivity of the shape of the pyrenyl dye fluorescence emission spectrum to local molecular caging (see Section 3.2 below), can be used to monitor and characterize residual stress relaxation in polymer films. Ellipsometry provides sensitivity to residual stress relaxation via time- and temperature-dependent changes in thickness of films that have been spin-coated onto Si/SiO_x substrates and subjected to a variety of thermal history conditions. As shown below, depending on thermal history and measurement temperature, stress relaxation in polystyrene (PS) films may be accompanied by small but measurable decreases or increases in thickness, with residual stress relaxation characterized by ellipsometry occurring over periods of hours in the rubbery state. With fluorescence, we monitor the time- and temperature-dependent changes in an intensity ratio associated the emission spectrum of pyrenyl dyes covalently attached at trace levels to the polymer. Previous studies have used the temperature dependence of such an intensity ratio to characterize the glass transition temperature (T_g) of homopolymers, as supported and free-standing thin and ultrathin films, and polymer blends (Kim 2008, Evans 2011, Kim 2011, Evans 2012b, Evans 2012c, Jin 2015). With the present study, we extend this approach to characterize stress relaxation and to provide sensitivity to stiffness in thin films. In agreement with ellipsometry measurements, fluorescence shows that residual stress relaxation occurs over

periods of hours in the rubbery state and that stress relaxation has no effect on film T_g. Fluorescence characterization also provides evidence that the mechanism underlying stress relaxation is β-relaxation and that ultrathin, free surface layers of bulk films are less stiff than ultrathin substrate layers. With 20- to 400-nm-thick PS films, fluorescence characterization at 60 °C indicates that film stiffness is a significant function of the substrate character, with stiffness increasing as follows: free-standing (no substrate) films < films supported on a very soft polymer substrate < films supported on a rigid glass substrate.

3.2 Rationale for Using the Spectral Shape of Pyrene Fluorescence Emission to Characterize Polymer Stress Relaxation and Stiffness

As mentioned in the Background, pyrene fluorescence can be used to characterize polymer properties such as stress relaxation and stiffness. Here, we provide the physical background behind the technique and how it is used to characterize polymer stiffness. Stiffness or modulus can be related to short time scale (~nanosecond) vibrations or mobility in materials (Sperling 2006). Experimental connections have been drawn between dynamics associated with the boson peak and mean-squared displacement (MSD), $<u^2>$, and polymer modulus. The boson peak is associated with collective vibrational modes with frequencies in excess of what is predicted by the Debye model of acoustic modes (Soles 2001). Soles *et al*. used Brillouin light scattering to demonstrate that the boson peak energy correlates with the velocity of acoustic waves traveling through polymer. In turn, the velocity of acoustic waves is proportional to the square root of bulk modulus (Soles 2001). In addition to the boson peak, vibrational dynamics associated with the $<u^2>$ have been correlated with polymer modulus via incoherent neutron scattering (INS) (Soles 2002, Inoue 2005, Ye 2015). At sufficiently low temperature, the $<u^2>$ is inversely proportional to the harmonic force constant (Soles 2002, Inoue 2005) or spring constant (Ye 2015). Inoue *et al*. state that the force constant in PS films corresponds to "those for torsion of the C-C bond in the main chain and/or the force constant for the interaction potential

between nonbonded atoms." The force or spring constants scale roughly with polymer modulus, and INS experiments find that supported polymer films stiffen upon confinement (Soles 2002, Inoue 2005, Ye 2015). Similar conclusions have recently been reached using atomistically informed coarse-grained molecular dynamics simulation (Xia 2015c, Xia 2015b).

Mean-squared displacement effects can be rationalized via a "caging" mechanism. Decreases in $<u^2>$ (increases in harmonic force constant) correspond to environments in which atoms are "caged" and trapped in deep potential energy minima (Soles 2002). In a stiff or caged environment, vibrations associated with $<u^2>$ are suppressed. Similarly, in stressed environments, atoms are trapped in potential energy minima. Stress relaxation decreases the force constant as atoms are less trapped in potential energy minima, or less caged.

The caging mechanism underlies the sensitivity of the spectral shape of pyrenyl dye fluorescence to stress relaxation and stiffness. The time scale associated with fluorescence, from absorption to emission, is some nanoseconds (Mundra 2007b), similar to the time scale associated with $<u^2>$ measurements. Furthermore, the ability to use fluorescence to characterize the Debye-Waller factor (related to $<u^2>$) as a surrogate to INS experiments, as done by Cicerone *et al.* (Cicerone 2011), suggests that the caging mechanism is common to both INS and selective fluorescence studies. We exploit the sensitivity of pyrene fluorescence spectral shape to caging to characterize stress relaxation and stiffness in pyrene dye-labeled PS films. We find that as stresses relax, or as stiffness decreases, reduced caging results in corresponding changes in the pyrene fluorescence emission spectrum. Specifically, the ratio the fluorescence intensity of the first and third vibronic band peaks, I_1/I_3, decreases as caging decreases and thus as stress is relaxed in the polymer sample.

Experimental support for the caging mechanism comes from the sensitivity of pyrene fluorescence spectral shape to local solvent polarity. Originally reported by Kalyanasundaram and Thomas (Kalyanasundaram 1977), the sensitivity was attributed to an induced dipole-dipole coupling mechanism between pyrene and surrounding solvent molecules. In the ground state,

pyrene electrons are symmetrically distributed. However, upon excitation by UV light, the electrons become asymmetric in distribution, which induces a dipole moment in pyrene. Depending on solvent polarity, solvent molecules re-orient and cage the excited-state pyrene molecules. In a high-polarity solvent, this caging is stronger and suppresses non-radiative forms of energy decay and enhancements of high-energy transitions of electrons from the excited state to the ground state. With pyrene fluorescence, the intensity of the first vibronic band peak, I_1, is associated with high-energy transitions to the ground state and the intensity of the third vibronic band peak, I_3, is associated with low-energy transitions. The ratio I_1/I_3 increases with increasing solvent polarity due to greater caging that suppresses non-radiative pathways of energy decay (Kalyanasundaram 1977, Dong 1984). The changes in I_1/I_3 with stress relaxation or stiffness are qualitatively consistent with the I_1/I_3 dependence on solvent polarity (Kalyanasundaram 1977, Dong 1984), which indicates that caging is the underlying mechanism for the sensitivity of fluorescence emission spectral shape of pyrene to its local environment.

3.3 Experimental Methods

3.3.1 Materials

Polystyrene (Pressure Chemical, made by anionic polymerization) with number-average molecular weight (M_n) of 160 kg/mol and dispersity = 1.06 was used as received. Using azobisisobutyronitrile (Aldrich, under the name 2,2'-azobis(2-methylproprionitrile)) as initiator, 1-pyrenylmethyl methacrylate (MPy) (Toronto Research Chemicals) was copolymerized at very low levels with styrene (SigmaAldrich) at 70 °C via bulk free radical polymerization to yield two MPy-labeled polystyrene (MPy-PS) samples. The MPy-PS samples were washed by dissolving in toluene and precipitating in methanol seven times to remove any residual MPy or styrene monomer and were placed in a vacuum oven at 105 °C for 3 days prior to use. As determined by gel permeation chromatography (Waters 2410, calibrated with PS standards in tetrahydrofuran, refractive index detector), the two washed MPy-PS samples had M_n values of 200 and 800

kg/mol, each with a dispersity of 1.3. As determined by UV-Vis absorbance spectroscopy

(Perkin Elmer Lambda 35) following the approach of Gebert and Torkelson (Gebert 1990), the

200 and 800 kg/mol MPy-PS samples contained 1.2 and 1.1 mol% MPy as fluorescence label.

Bulk T_gs were determined by differential scanning calorimetry (Mettler Toledo DSC822e,

second-heat T_g onset method at 10 °C/min heating rate): T_gs were 100 °C for 160 kg/mol PS, 101

°C for 200 kg/mol MPy-PS, and 103 °C for 800 kg/mol MPy-PS.

3.3.2 Spin-Coated Films

 Films of PS or MPy-PS were spin-coated onto glass slides from toluene (SigmaAldrich)

solutions containing 0.5 to 7.0 wt% polymer with spin speeds ranging from 1500 to 3000 rpm.

Glass slides were thoroughly cleaned by etching in 1.0 M hydrochloric acid, rinsed with water,

and dried prior to submerging in base solution (10 wt% sodium hydroxide/20 wt% water/70 wt%

ethanol). Substrates were then rinsed with water and dried prior to use. With multilayer films,

samples were spun onto freshly cleaved mica and annealed under vacuum at $T_{g,bulk}$ + 20 °C for 2

h. (As shown in detail by Zhang *et al.* (Zhang 2010), no residual solvent remains in PS films

made by spin coating from toluene solution.) After annealing, mica-supported films were

transferred at room temperature onto glass-substrate supported films by a water transfer

technique (Forrest 1997b). Residual water evaporated overnight under ambient conditions prior

to annealing the multilayer film in the vacuum oven at 120 °C for 3 h before fluorescence

measurement. These annealing conditions were chosen to ensure that the multiple layers welded

into a consolidated film but did not allow for substantial interdiffusion between layers (Ellison

2003, Kim 2011). Polydimethylsiloxane (PDMS) substrates were prepared from Dow Corning

Sylgaard 184 at a base to catalyst ratio of 10:1 and cured at ambient conditions overnight prior to

heating in an oven at 100 °C. Thin MPy-PS layers were floated off mica and placed onto PDMS

substrates prior to measurement. For free-standing films, MPy-PS films were floated onto nylon

washers (Kim 2008, Kim 2011) after 120 °C annealing for 2 h before floating.

3.3.3 Ellipsometry

Spectrocopic ellipsometry (J. A. Woollam Co. M-2000D over a range of wavelengths from 400 to 1000 nm) was used to measure ellipsometric angles (ψ and Δ) of incident light reflected off silica-supported PS or MPy-PS films. Using a Cauchy layer model, ellipsometric angles were fitted to determine film thickness. The Cauchy layer model included a PS layer atop a silicon substrate containing a 2-nm-thick silicon oxide surface layer. Thickness values were determined by fitting ψ and Δ to the PS layer in the model. To determine thickness of films or layers used in fluorescence studies, PS and MPy-PS films were spin-coated at the same time from the same solutions with the same spin speeds onto silicon slides with a native silicon oxide surface layer and measured via ellipsometry. Thicknesses were determined at room temperature.

To investigate the relaxation of residual stresses in bulk-like PS films by ellipsometry, the thickness of two 800-nm-thick PS films was monitored during 300 min of isothermal annealing at $T_{g,bulk} + 40\,°C$. Prior to annealing at $T_{g,bulk} + 40\,°C$, one film was placed in a vacuum oven overnight at 60 °C and the other at 110 °C. Following that, the films were placed on a pre-heated Instec heating element at $T_{g,bulk} + 40\,°C$ (sample transfer time of ~30 s) for time-resolved thickness measurements. To reduce the noise associated with measuring thickness, reported thickness values are the averages of seven data points taken over a period of 2 min.

Ellipsometry was also used to measure T_g before and after annealing at $T_{g,bulk} + 40\,°C$. Once spin-coated, a bulk-like PS film was annealed overnight in a vacuum oven at 60 °C. The film was then placed on a heater pre-heated to 140 °C for 5 min prior to monitoring thickness during cooling from 140 to 60 °C at a rate of 1 °C /min. After the first cooling cycle, the sample was re-heated to 140 °C to monitor the change in isothermal thickness over 1 h as residual stresses relaxed. The thickness response to cooling at a rate of 1 °C /min was then monitored during a second cooling cycle using the same film. The T_g was determined by the intersection of lines fitted to the temperature-dependent rubbery and glassy thickness responses (Keddie 1994a).

3.3.4 Fluorescence Spectroscopy

Fluorescence was used to measure T_g and characterize residual stress relaxation of MPy-PS films. After spin-coating and annealing films overnight at 60 °C under vacuum, emission spectra were collected (Photon Technology International fluorimeter in front-face geometry) at wavelengths from 370 to 405 nm (0.5 nm increment, 1 s integration), with excitation at 324 nm. Excitation and emission slit widths were 0.5 mm (1 nm bandpass). Spectra were used to determine the ratio of the first vibronic band peak intensity to the third vibronic band peak intensity (I_1/I_3) of the pyrene-labeled polymer. Peak intensities were calculated from an average of five data points spanning a 2 nm window: I_1 was an average of five points between 376 to 378 nm and I_3 an average of five data points between 387 to 389 nm.

Fluorescence was also used to characterize the effect of spin speed on I_1/I_3. MPy-PS films were spin coated from toluene solution containing 4 to 6 wt% polymer and spin speeds of 1500 to 3000 rpm. The four 680-nm-thick films were annealed overnight in a vacuum oven at 60 °C and then placed on a heater to collect emission spectra at 25, 60, and 120 °C.

To characterize residual stress relaxation, bulk MPy-PS films (annealed under vacuum at 60 °C overnight) were placed on a heater pre-heated to anneal temperatures ranging from 110 to 140 °C (sample transfer time of ~1 min). Samples were held isothermally at the respective annealing temperatures for 12 h with spectra collected every 1 h.

To determine T_g via fluorescence, a 650-nm-thick single-layer PS film (annealed at 60 °C for 12 h under vacuum) was placed on an Instec heater pre-heated to 140 °C and held for 10 min. Emission spectra were collected upon cooling from 140 to 60 °C in 5 °C decrements. Before spectral measurement, the sample was held for 5 min to ensure equilibration to the temperature of the heating element. After the first cooling cycle, the sample was re-heated to 140 °C and held for 1 h to relax residual stresses. The cooling cycle was then repeated to collect emission spectra a second time. The T_g was determined by the intersection of lines fit to the temperature-dependent rubbery and glassy responses of I_1/I_3 (Kim 2008, Kim 2011).

An investigation of T_g and stiffness on bilayer films and a single 30-nm-thick MPy-PS film supported on glass was conducted in a different manner. Prior to fluorescence measurements, films were annealed under vacuum at 120 °C for 3 h to weld the layers while avoiding significant interdiffusion of polymer between layers. After annealing, films were placed on the Instec heater pre-heated to 140 °C for 10 min prior to cooling from 140 to 60 °C in 5 °C decrements and were cooled through one or two cooling cycles. Fluorescence measurements needed to address the effects of confinement on T_g and I_1/I_3 values in MPy-PS films supported on glass or on cross-linked PDMS or as free-standing films were done in a manner similar to that for the 30-nm-thick MPy-PS film but using only a single cooling cycle.

3.4 Results and Discussion

This section is divided into three parts. The first describes ellipsometry measurements of thickness to characterize residual stress relaxation in bulk PS films under various thermal history conditions and a study on whether stress relaxation affects the film T_g. The second describes a fluorescence study that characterizes stress relaxation in bulk, dye-labeled PS films under similar thermal history conditions as those in the ellipsometry study and a proof-of-concept experiment demonstrating the sensitivity of fluorescence to stiffness in PS films. The third involves using fluorescence to compare T_g- and stiffness-confinement effects in MPy-PS as films supported on glass and cross-linked PDMS substrates and as free-standing films.

3.4.1 Ellipsometry Characterization of Residual Stress Relaxation in Supported PS Films

Spectroscopic ellipsometry was used to determine the effect, if any, of residual stress relaxation on thickness in rubbery-state bulk PS films (M_n = 160 kg/mol). Prior to measurement, two 800-nm-thick PS films were annealed under vacuum at 60 or 110 °C for 12 h. After annealing, each film was placed on a heater pre-heated to 140 °C (T_g + 40 °C) and held isothermally for 300 min as thickness was characterized via ellipsometry. Figure 3-1 shows that the thicknesses for the two PS films decrease by slightly less or slightly more than 2 parts per
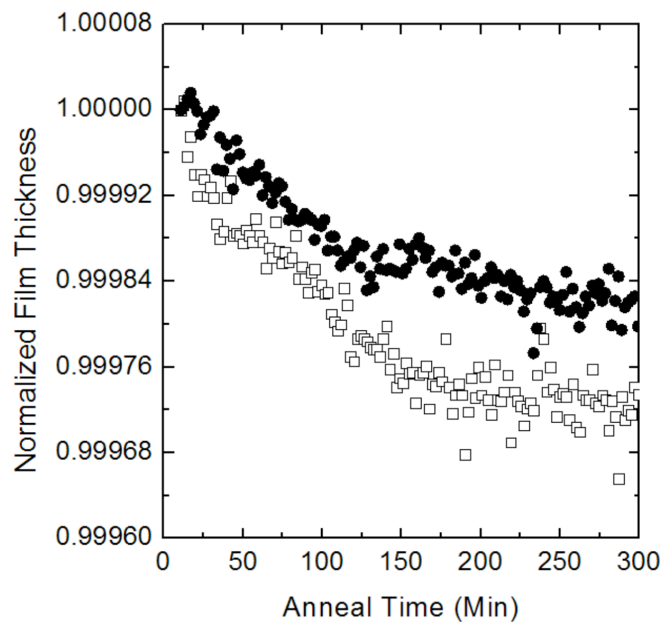
Figure 3-1: Normalized thickness of two 800-nm-thick PS films as a function of anneal time at 140 °C. Prior to annealing at 140 °C, one film was annealed at 110 °C for 12 h under vacuum (closed circles) and the other at 60 °C (open squares). Thickness was monitored isothermally at 140 °C for 300 min for both films. Each data point represents the average of seven thickness measurements collected over a period of 2 min to smooth the data.

10000 over the 300 min of heating isothermally at 140 °C. Since residual toluene is not present in spin-cast PS films made from toluene solutions (Zhang 2010), the decrease in thickness is not related to solvent loss upon exposure to elevated temperature (T) but instead is related to residual stress relaxation. The thickness of the film annealed overnight at 60 °C prior to ellipsometry measurements decreased more than that of the film annealed overnight at 110 °C.

This difference in thickness reduction during isothermal heating at 140 °C can be attributed to two factors. First, prior to ellipsometry measurement, the film annealed for 12 h at 110 °C underwent greater stress relaxation than the film annealed for 12 h at 60 °C. Second, the film annealed at 60 °C prior to thickness measurements at 140 °C was subjected to a greater step change in T (+ 80 °C) compared to the film annealed at 110 °C (+ 30 °C). The larger step change in T associated with the film annealed at 60 °C likely imparted greater thermal stresses on that film (the film is supported on silica, which has a much smaller thermal expansion coefficient than rubbery-state polymer). The relaxation of the additional stresses is manifested as larger thickness changes during the subsequent isothermal heating of the film at 140 °C. Figure 3-1 shows that bulk PS films with these thermal histories are not in equilibrium as determined via thickness (or, equivalently, specific volume) measurements even though they are at T_g + 40 °C and that residual stress relaxation at T_g + 40 °C occurs over a period of hours.

Ellipsometry was also used to investigate whether the presence of residual stresses perturbs T_g in bulk, spin-coated PS (M_n = 160 kg/mol) films. Thermal expansivity is greater above T_g than below T_g, and T_g can be determined by the intersection of lines fitted through the rubbery and glassy T-dependences of thickness. Figure 3-2 shows the thickness of a PS film (annealed 12 h under vacuum at 60 °C prior to ellipsometry) upon cooling from 140 to 60 °C at a rate of 1 °C/min (closed squares); these data yield T_g = 101 °C.

After the first cooling cycle, the film was heated rapidly from 60 to 140 °C and held for 1 h annealing time at 140 °C prior to measuring T_g during a second cooling cycle (open squares). As shown in Figure 3-3, the thickness increased by ~0.15 nm during the annealing for 1 h (data
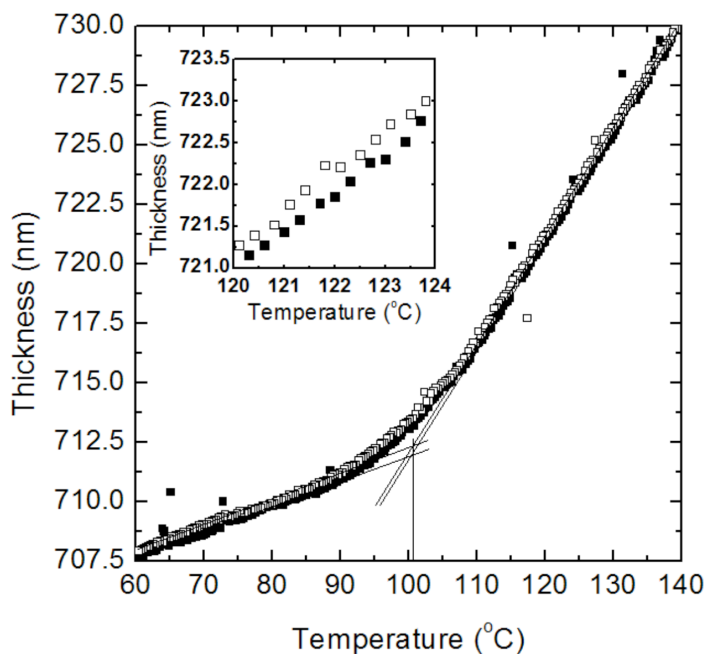
Figure 3-2: Thickness measurements as a function of temperature of a bulk PS film on cooling from 140 °C to 60 °C at a rate of 1 °C/min. Prior to ellipsometry measurements, the film was spin-coated and annealed under vacuum at 60 °C for 12 h and placed on a heater pre-heated to 140 °C. Closed squares show the thickness during the first cooling cycle. After completion, the sample was re-heated to 140 °C and annealed for 1 h. Open squares show the thickness measurements during the second cooling cycle. Inset shows data over a 4 °C temperature range to demonstrate thickness increase after isothermal annealing at 140 °C. A T_g of 101 °C was determined by the intersection of the lines fitted through the rubbery and glassy responses of thickness to temperature.
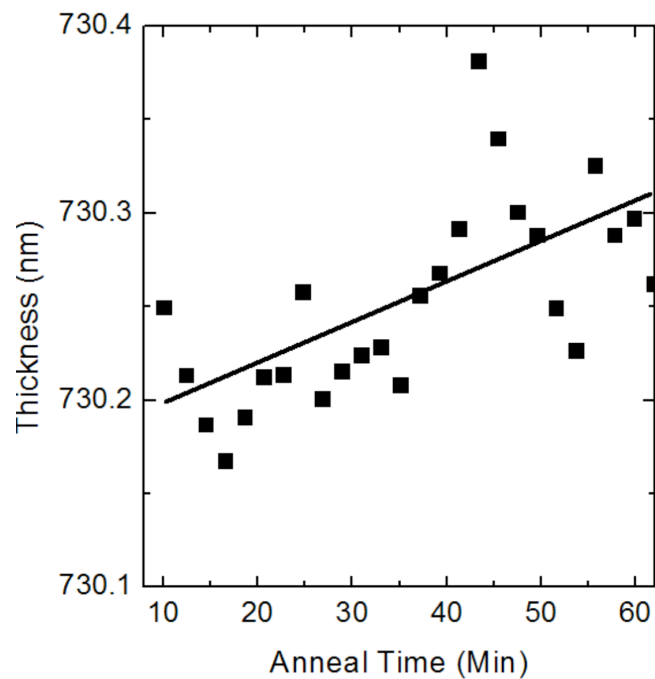
Figure 3-3: Ellipsometry measurements of thickness as a function of anneal time (1 h) at 140 °C for the same film used in Figure 3-2. Upon completion of the first cooling cycle (from 140 °C to 60 °C at 1 °C/min), the sample was re-heated to 140 °C, and thickness was monitored as a function of isothermal annealing at 140 °C. Each black square represents the average of seven thickness measurements collected over a period of 2 min. A best-fit line demonstrates that the thickness increases with increasing anneal time at 140 °C.

from 10 to 60 min) at 140 °C during which time some stress relaxation occurs. Thus, relaxation of residual stress in bulk, supported PS films can result in either a thickness decrease (Figure 3-1) or a thickness increase (Figure 3-3) depending on thermal history. The complex thermal history for the film in Figure 3-3 likely introduced additional thermal stresses from thermal expansivity mismatches between the film and substrate (Zoetelief 1996). In spite of the slightly greater thickness of the film during the second cooling cycle as compared to the first cooling cycle, as shown in Figure 3-2 the film T_g measured from the second cooling was 101 °C, identical to that from the first cycle. This result is consistent with neutron reflectivity studies of film thickness by Kanaya *et al*. (Kanaya 2003), who concluded that the T_g of a polymer film measured upon cooling from the rubbery state is independent of thermal history. Since T_g was the same before and after annealing for 1 h at 140 °C, residual stress relaxation does not alter the T_g of spin-coated polymer films even though the specific volume of the films may be affected by the relaxation.

3.4.2 Novel Fluorescence Characterization of Residual Stress Relaxation in Supported PS Films

Fluorescence measurements were done using PS (M_n = 200 kg/mol) containing 1.2 mol% MPy as comonomer in order to characterize residual stress relaxation for PS films supported on glass. The fluorescence technique involves interpreting changes in the shape of the pyrenyl dye fluorescence emission spectrum in response to local changes in molecular caging, which is related to polymer stiffness (see Section 3.2).

Figure 3-4 compares emission spectra for a 680-nm-thick film of PS (M_n = 160 kg/mol) doped with 0.2 wt% pyrene as free dye (Figure 3-4A) and a 650-nm-thick film of MPy-PS (M_n = 200 kg/mol) (Figure 3-4B) at 60 °C. In Figure 3-4A, arrows point to peaks corresponding to the first through fifth vibronic band intensities for the pyrene emission spectrum. Figure 3-4B shows that upon covalent attachment of pyrenyl dye to PS in MPy-PS, the emission spectrum changes such that only the first and third vibronic band peak intensities I_1 and I_3 are distinguishable,
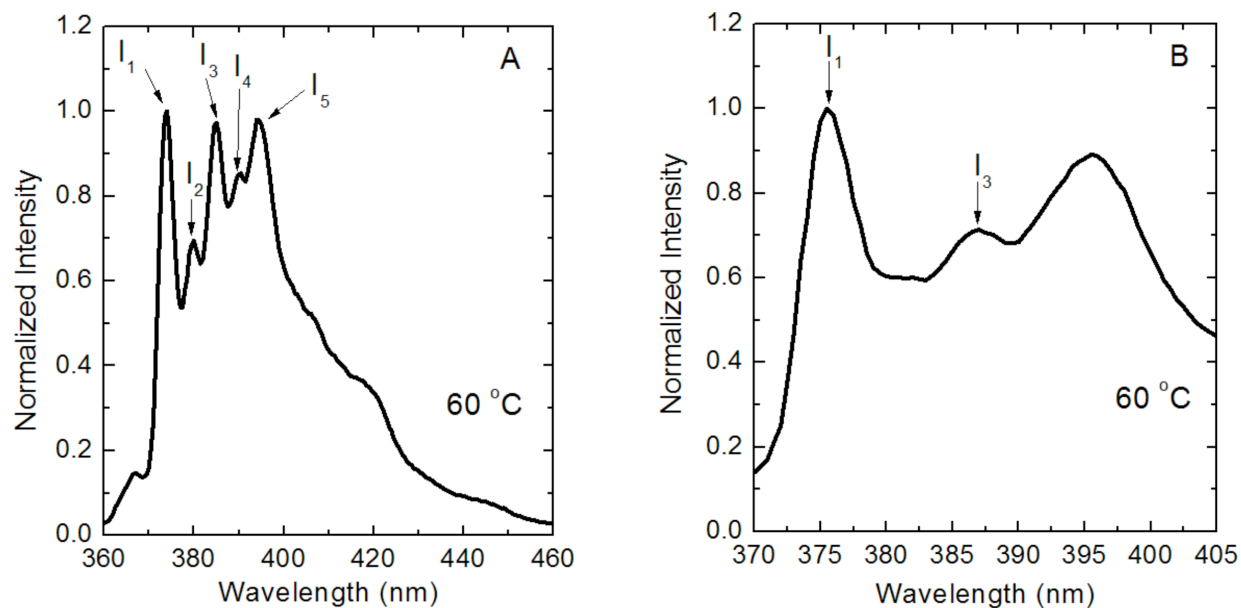
Figure 3-4: A: Fluorescence spectrum of a 680-nm-thick PS film doped with 0.2 wt. % pyrene at 60 °C. After spin coating, fluorescence emission spectra were collected after 2 h anneal time in a vacuum oven at 60 °C. Arrows indicate locations of the first through fifth vibronic band peak intensities ($I_1 \rightarrow I_5$). B: Typical fluorescence spectrum of a 650-nm-thick MPy-PS film at 60 °C. Arrows indicate locations of the first and third vibronic band peak intensities in B.

whereas the second vibronic band is nearly invisible and the fourth and fifth bands merge.
Covalent attachment of pyrenyl dye to PS also shifts peak wavelengths by a few nanometers
(Ellison 2004a). Changes in the intensity ratio of the first vibronic band peak to the third vibronic
band peak, I_1/I_3, were used to characterize the stress state of films as described in Section 3.2
above. I_1/I_3 is expected to increase in a more caged environment, such as one in which stress or
stiffness is elevated.

As shown in Figure 3-5, the spin speed used in preparing spin-coated PS films was varied
to study its effect on I_1/I_3. 680-nm-thick MPy-PS films were spin-coated from 4 to 6 wt%
solutions in toluene onto glass slides at spin speeds from 1500 to 3000 rpm. (This range of spin
speeds matched that used to make all films in this study.) After spin-coating, films were annealed
for 12 h at 60 °C under vacuum and were then placed on a heater pre-heated to 25, 60, or 120 °C
to collect emission spectra. Within experimental error, the results from Figure 3-5 indicate that
the spin speed in the range of 1500 to 3000 rpm does not affect I_1/I_3 values for bulk MPy-PS
films over a wide range of T above and below T_g. This result implies that, as measured by
fluorescence, the stress state of the films is independent of spin speed over the range studied.

The effect of isothermal heating on stress relaxation of bulk MPy-PS films was also
studied by fluorescence. Figure 3-6 shows the evolution of I_1/I_3 over 12 h of isothermal heating
over a T range of 110 to 140 °C. Prior to high-T heating, the 680-nm-thick films were annealed
at 60 °C for 12 h in a vacuum oven and then transferred to a heater pre-heated to the respective
heating T. The thermal histories of samples in Figure 3-6 are similar to those of samples in
Figure 3-1 (open squares). For annealing at 110 °C, I_1/I_3 remained constant, indicating a lack of
stress relaxation at T_g + ~10 °C as measured by fluorescence. For annealing Ts ranging from 115
to 140 °C, I_1/I_3 decreased with annealing time and then reached apparent steady-state values,
consistent with stress relaxation. Relaxation times were obtained from the intersection of lines
corresponding to the decreasing and steady regimes (see dashed drop lines in Figure 3-6). At 115
°C, relaxation occurred over ~8 h, whereas at 140 °C relaxation occurred over ~1 h. (We note
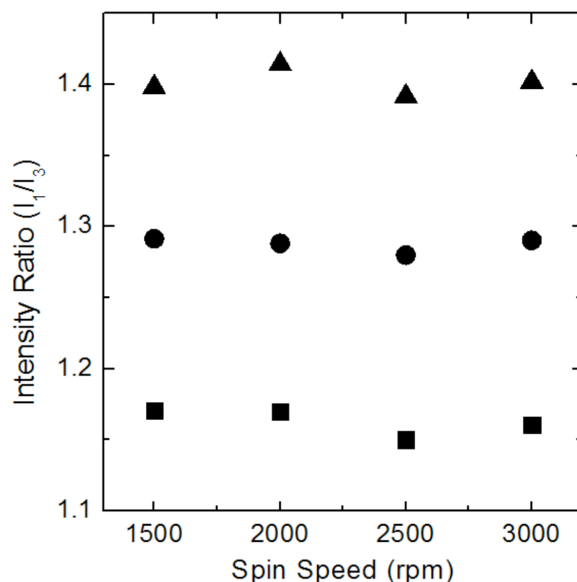
Figure 3-5: Intensity ratio as a function of spin speed for 680-nm-thick MPy-PS films prepared by spin-coating 4-6 wt% solutions of PS in toluene. Prior to fluorescence measurements, films were annealed at 60 °C for 12 h. Intensity ratios were acquired at 25 °C (triangles), 60 °C (circles), and 120 °C (squares). (Background noise was subtracted.)
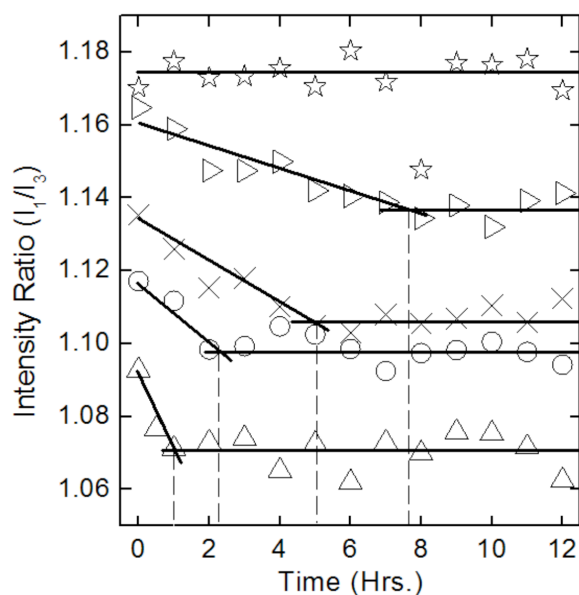
Figure 3-6: Intensity ratios for 680-nm-thick MPy-PS films monitored over 12 h of annealing time at 110 °C (stars), 115 °C (triangles pointing right), 120 °C (X's), 130 °C (circles), and 140 °C (triangles pointing up). Lines were drawn to indicate the change in the direction of I_1/I_3 values as a function of anneal time. Prior to fluorescence measurements at the respective anneal temperatures, samples were spin-coated and then annealed under vacuum at 60 °C for 12 h.

that residual stress relaxation times are expected to be even shorter for temperatures above 140 °C, but the measurements are particularly challenging for two reasons. First, it is difficult to distinguish between the sample temperature equilibration to the heater and decreases in I_1/I_3 due to residual stress relaxation. Second, prolonged exposure to high temperatures could result in PS to permanently adhering to the surface of the substrate through the formation of Guiselin brushes (Napolitano 2011) which could convolute the results.) Similar results to those in Figure 3-6 were obtained for films that were made and processed like those in Figure 3-6 with the exception that they were not annealed under vacuum at 60 °C for 12 h after spin-coating and prior to fluorescence measurements.

After 12 h annealing, samples were placed at 120 °C for 10 min to compare I_1/I_3 values at a common T. For films annealed for 12 h at 115 to 140 °C, I_1/I_3 at 120 °C was 1.11 ± 0.02, indicating that the films reached a common final stress state. For the film annealed at 110 °C, the I_1/I_3 value after 10 min at 120 °C was 1.16. This difference is consistent with the conclusion that isothermal annealing for 12 h at 110 °C (T_g + ~10 °C) was insufficient to relax residual stresses in bulk PS films.

A 1960 viscoelastic shear stress relaxation study by Tobolsky and Murakami (Tobolsky 1960) provides further support that data in Figure 3-6 are associated with stress relaxation. They found that the shear stress relaxation time for PS (M_w = 200 kg/mol) at 115 °C is 8.4 h. Although the method in the present study differs from that by Tobolsky and Murakami, the time required for stress relaxation as measured by fluorescence (~8 h at 115 °C) agrees well with that measured by shear stress relaxation.

Residual stress relaxation times determined from I_1/I_3 values in Figure 3-6 exhibit significant T dependence. Although the apparent relaxation responses in the present study are not exponential decay functions which are often associated with stress relaxation (Tobolsky 1960), we note that the relaxation times obtained at 115 to 140 °C from the data in Figure 3-6 exhibit Arrhenius behavior; see Figure 3-7. (Figure 3-7 includes a relaxation time at 135 °C from data
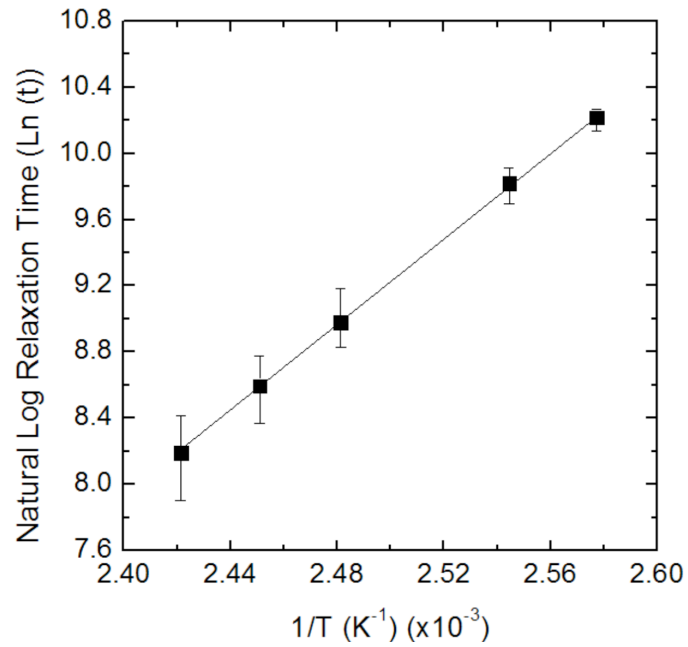
Figure 3-7: Natural logarithm of residual stress relaxation times obtained from Figure 3-6 plotted against 1/T. Error bars represent the plausible range of times based on the fit lines in Figure 3-6.

not shown in Figure 3-6.) Using the slope of the best-fit line in Figure 3-7, an activation

energy (E_a) of ~110 kJ/mol was obtained for residual stress relaxation over the T range from T_g +

~15 °C to T_g + ~40 °C.

The Arrhenius T-dependence associated with the stress relaxation times above T_g is

consistent with β-relaxation processes and inconsistent with α-relaxation, the latter of which

follows the Williams-Landel-Ferry (WLF) equation or Vogel-Fulcher-Tammann (VFT)

equation. Although the WLF equation does not follow an Arrhenius T-dependence, it is possible

to calculate apparent activation energies using WLF fit parameters at a particular T (Ferry

1980).[56] Depending on WLF fit parameters for bulk PS (Adam 1965, Plazek 1965, Pschorn 1991,

Dhinojwala 1994b, Patel 2004), apparent activation energies vary from 430 to 550 kJ/mol at 115

°C and 260 to 320 kJ/mol at 140 °C. The E_a value of 110 kJ/mol determined in this study via

pyrenyl dye fluorescence over the same T range is much lower than the apparent E_a values

associated with α-relaxation. In contrast, the E_a value of 110 kJ/mol is in reasonable accordance

with E_a values of 120 to 140 kJ/mol reported for β-relaxation in bulk PS (Yano 1971, Sperling

2006). Thus, in agreement with other reports (Tobolsky 1956, Prest 1981, Chowdhury 2012), our

fluorescence results are consistent with β-relaxation being the underlying mechanism of residual

stress relaxation in polymers.

The effects of stress relaxation on overall intensity and T_g were also studied. Figure 3-8

shows emission spectra for a 650-nm-thick MPy-PS film subjected to thermal history conditions

similar to those for the film characterized by ellipsometry in Figure 3-2. After spin-coating and

annealing under vacuum at 60 °C for 12 h, the film was placed on a heater pre-heated to 140 °C,

and spectra were collected upon cooling from 140 to 60 °C in 5 °C decrements after waiting 5

min at each T to allow for thermal equilibration between measurements (red upper curves). After

the first cooling cycle, the film was re-heated to 140 °C and annealed for 1 h prior to a second

cooling cycle (black lower curves). The intensity increased with decreasing T for both data sets.

Part of the reason for the T dependence of intensity is that at elevated T, greater thermal
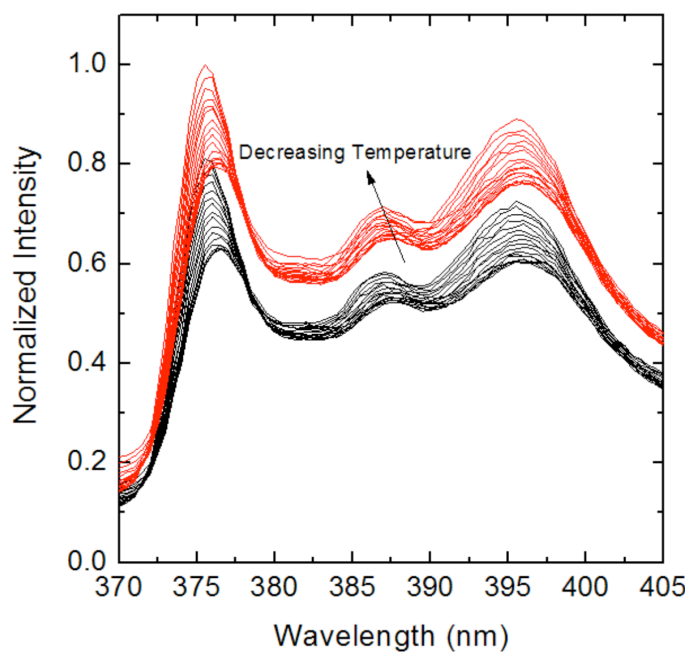
Figure 3-8: Fluorescence emission spectra of a single 650-nm-thick MPy-PS film cooled from 140 °C to 60 °C in 5 °C decrements. Red upper curves are spectra collected during the first cooling cycle. After the first cooling cycle, the sample was re-heated to 140 °C and annealed for 1 h to relax residual stresses. Fluorescence emission spectra were then collected during a second cooling cycle (black lower curves). Prior to the first set of fluorescence measurements, the film was annealed under vacuum at 60 °C for 12 h. The arrow indicates that the intensities of fluorescence emission spectra increase during cooling. (Background noise was subtracted.)

energy in the environment enhances pathways (increased vibrations) for non-radiative decay

of excited-state pyrenyl dyes. Another part of the T dependence of intensity is related to

molecular caging. Upon cooling, the increasingly rigid environment surrounding the dyes

suppresses pathways for non-radiative decay via caging and increases the intensity of the emitted

light with greater increases in I_1 relative to I_3. The results also show that after annealing for 1 h at

140 °C, fluorescence intensities decreased at all Ts (second cooling cycle compared to first

cycle). The decrease in intensities after annealing at 140 °C is consistent with enhancements in

pathways for non-radiative decay of the excited-state pyrenyl dye after stress relaxation during

the 1 h annealing at 140 °C (indicative of reduced caging).

Figure 3-9 shows the determination of T_g from the T dependence of I_1/I_3 from data in

Figure 3-8. Previous research (Kim 2008, Evans 2011, Kim 2011, Evans 2012b, Evans 2013a,

Evans 2013b) has shown that self-referencing intensity ratios can be used to characterize T_g of a

film via the intersection of lines fitted through the rubbery and glassy T dependences. (Several

fluorescence studies used the ratio I_3/I_1 to measure T_g in MPy-labeled polymers, whereas here we

use the inverse, I_1/I_3.). The red circles in Figure 3-9 correspond to I_1/I_3 values (from the red upper

curves in Figure 3-8) during a cooling cycle from 140 to 60 °C. The sample was then re-heated

to 140 °C and annealed for 1 h. The black triangles in Figure 3-9 correspond to I_1/I_3 values (from

the black lower curves in Figure 3-8) during the second cooling cycle. Although the I_1/I_3 values

are lower during the second cooling cycle than in the first (due to stress relaxation), the T_g of the

film, 101 °C (± 2 °C), was invariant within error, consistent with ellipsometry results in Figure 3-

2. Thus, both ellipsometry and fluorescence sense residual stress relaxation of unrelaxed PS

films during high-T annealing and indicate that T_g is independent of stress relaxation.

Besides providing quantitative characterization of T_g, the data in Figure 3-9 also indicate

the relaxation of residual stresses in bulk MPy-PS films. Because of stress relaxation during the

140 °C annealing step for 1 h between the first and second cooling cycles, I_1/I_3 values at a given

T decrease by 0.03 to 0.05 between the first and second cycles. This result is consistent in two

70
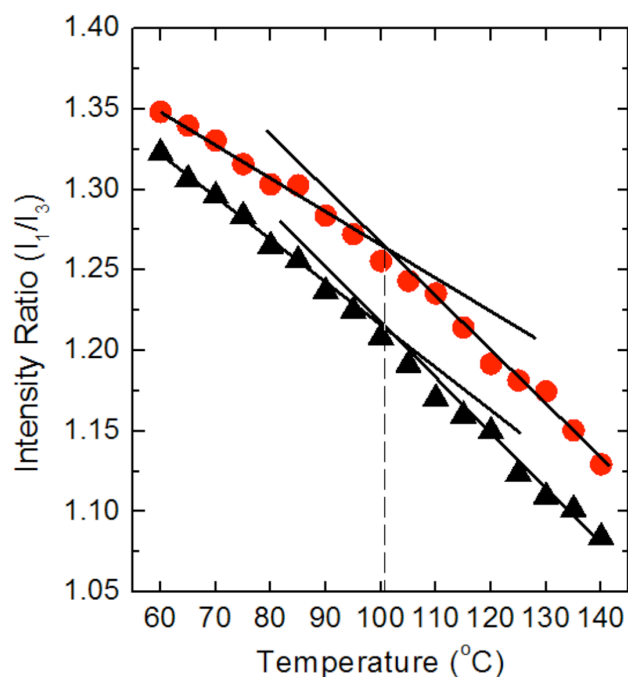
Figure 3-9: Fluorescence intensity ratio values (I_1/I_3) for the same 650-nm-thick MPy-PS film in Figure 3-8 as a function of temperature upon cooling from 140 °C to 60 °C in 5 °C decrements. Red circles represent I_1/I_3 values during the first cooling cycle calculated from the red upper curves in Figure 3-5. Black triangles represent I_1/I_3 values measured during a second cooling cycle calculated from the black lower curves in Figure 3-8. The T_g value of 101 °C, measured from the intersection of the rubbery- and glassy-state T dependence of I_1/I_3, is identical for the two cooling cycles. (The thermal history of this film closely matches the thermal history of the film used for Figure 3-2. Background noise was subtracted.)

ways with a reduction in caging around excited-state pyrenyl dyes and thus a decrease in stiffness of the polymer films. First, the intensity ratios are lower when the polymer is in the rubbery state, and higher when the polymer is cooled to the rigid, glassy state, which is consistent with I_1/I_3 values being reduced in less caged or less stiff environments. Second, upon exposure to high T, the chains have enough thermal energy to relax towards a less stressed or caged state, thereby decreasing the stiffness in the second cycle relative to the first cycle.

Figure 3-10 shows results from a proof-of-concept experiment in which selective placement of the MPy-labeled PS layer in bilayer and single-layer films was used to study the influence of the polymer-substrate and polymer-air interfaces on film stiffness. Shown are data for three films supported on glass substrates. The first data set is for a bilayer film consisting of a 30-nm-thick MPy-PS substrate layer capped by a 620-nm-thick PS layer. Within 30 nm of the substrate interface $T_g = 100$ °C, within error equal to bulk T_g, and the I_1/I_3 values are the highest of the three cases. The latter point indicates that the 30-nm layer nearest the substrate is the stiffest, which is consistent with results from a coarse-grained molecular dynamics simulation study (Xia 2015b).

In contrast, Figure 3-10 also shows that when a 30-nm-thick MPy-PS layer is placed atop a 610-nm-thick PS layer, the I_1/I_3 values are the lowest, which indicates that the layer nearest the free surface is the least stiff. This conclusion is also consistent with results from a coarse-grained molecular dynamics simulation study (Xia 2015c). In agreement with previous experimental results (Ellison 2003), the T_g for a 30-nm-thick free-surface layer on bulk PS is 90 °C, reduced by ~10 °C from bulk PS T_g.

The final data set in Figure 3-10 is that of a single-layer 30-nm-thick MPy-PS film. Both the free surface and substrate interface influence the film stiffness, and the I_1/I_3 values are intermediate to those of the free surface and substrate layers in the two bulk bilayer films. Additionally, the T_g is reduced from bulk T_g to 90 °C due to free surface effects (Ellison 2003). This proof-of-concept study demonstrates that it is possible to employ a fluorescence/multilayer
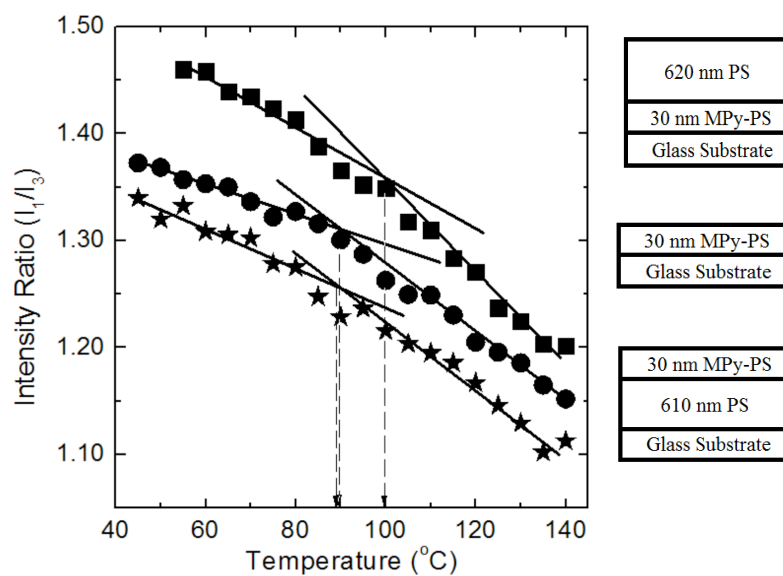
Figure 3-10: I_1/I_3 values as a function of temperature upon cooling in 5 °C decrements for single and bilayer films. Data are shown for a 30-nm-thick MPy-PS layer capped with a 620-nm-thick unlabeled PS layer (squares), a single 30-nm-thick MPy-PS film (circles), and a 30-nm-thick MPy-PS layer atop a 610-nm-thick supported unlabeled PS layer (stars). (Background noise was subtracted.)

approach to interrogate the influence of the polymer-air and polymer-substrate interfaces on the stiffness of confined polymer films as long as the fluorescence measurable is sensitive to stiffness. The next few chapters in this dissertation characterize gradients in caging and hence stiffness as a function of distance from a free surface or substrate interface in polymer films.

3.4.3 Fluorescence Approach to Investigate Effects of Confinement on T_g and Stiffness of Free-Standing and Supported PS Films on Soft (PDMS) and Hard (Glass) Substrates

As shown above, an advantage of the self-referencing pyrene fluorescence technique using I_1/I_3 values lies in its ability to obtain T_g and provide sensitivity to stiffness from the same experiment. Using a protocol similar to that for the 30-nm-thick MPy-PS film in Figure 3-10, T_gs were determined for MPy-PS ($M_n = 800$ kg/mol) as free-standing films as well as films supported on PDMS and glass substrates. (A very high molecular weight PS sample was used in this section because of challenges in preparing free-standing PS films of lower molecular weight that would not develop holes during the fluorescence measurements taken upon cooling from well above T_g.)

Figure 3-11 shows that all films with thickness exceeding 100 nm have $T_g = 100$ °C or slightly higher and that T_g-confinement effects are evident for nanoconfined films. In agreement with previous studies (Forrest 1998, Kim 2008, Kim 2011), free-standing PS films exhibit a much greater T_g-confinement effect than the substrate-supported films. (The three data points in Figure 3-11 showing T_g-confinement effects in free-standing PS films are in good agreement with data summarized in Figure 3-2 of Forrest 1998 that compare T_gs as a function of molecular weight in nanoconfined, free-standing PS films.) Figure 3-11 also shows that PS exhibits substantially similar T_g reductions with confinement when supported on glass or on PDMS. This latter result is in disagreement with past fluorescence studies showing that nanoconfined free-surface layers of PS atop bulk layers of other polymers may exhibit significant perturbations to T_g based on the polymer species making up the underlying layer (Roth 2007a). We hypothesize that the substantial lack of effect observed with a PDMS substrate is related to the extraordinarily
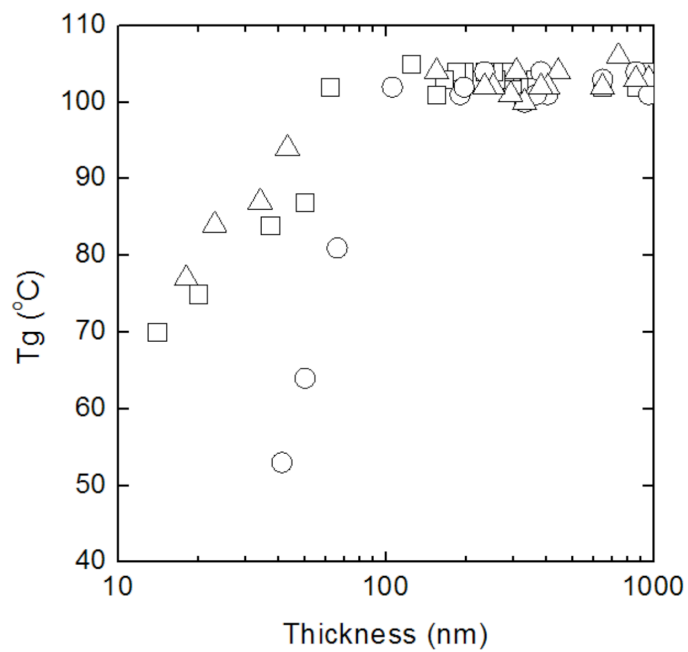
Figure 3-11: Effect of substrate on the *T*g-confinement for MPy-PS films: supported on PDMS (squares), supported on glass (triangles), free-standing MPy-PS films (circles).

large difference in the dynamics exhibited by PS and PDMS at 60 °C, which implies that no significant T_g perturbation occurs when the neighboring polymer layers have essentially totally uncoupled dynamics.

For the same films used in Figure 3-11, Figure 3-12 shows I_1/I_3 values of MPy-PS films at 60 °C (results are from the data sets obtained upon cooling to measure T_g) which make evident that the stiffness-confinement response is qualitatively and quantitatively different from the T_g-confinement response. Background counts (due to thermal noise associated with the photomultiplier tube) were subtracted from MPy-PS emission spectra prior to determination of I_1/I_3 values reported for all films in Figures 3-5, 3-6, 3-9 and 3-10. This background subtraction was almost totally negligible for bulk films as it did not significantly alter the intensity ratio values for bulk films nor did it affect the reported T_g values. For ultrathin film or layer study in Figure 3-10, the background spectrum was collected by spin-coating a 30-nm-thick unlabeled PS film onto glass and measuring the emission. Such background subtraction has a larger effect on the I_1/I_3 values for an ultrathin MPy-PS film than for a bulk MPy-PS film. Background emission counts were subtracted from all fluorescence data except Figures 3-11 & 3-12. We also note that the T_g results (Figure 3-11) will be unaffected by the lack of background subtraction. Although background subtraction would affect the particular I_1/I_3 values in Figure 3-12, the trends indicated by the data are still valid—I_1/I_3 values for thin films deviate from their bulk values.) In particular, PS films supported on glass or cross-linked PDMS exhibit increases in I_1/I_3 values upon confinement at ~400 nm thickness, which is much larger than the onset thickness for T_g-confinement effects. Furthermore, whereas T_g decreases with confinement, caging, as measured by I_1/I_3 values, and thus stiffness increase with confinement in substrate-supported PS films. A stiffening effect with confinement has been previously reported for polymer films on a hard substrate (like glass or Si) via coarse-grained dynamics simulations (Xia 2015b) as well as nanoindentation experiments (Watcharotone 2011, Cheng 2015), INS characterization of MSD (Soles 2002, Inoue 2005), and surface capillary wave studies by X-ray photon correlation
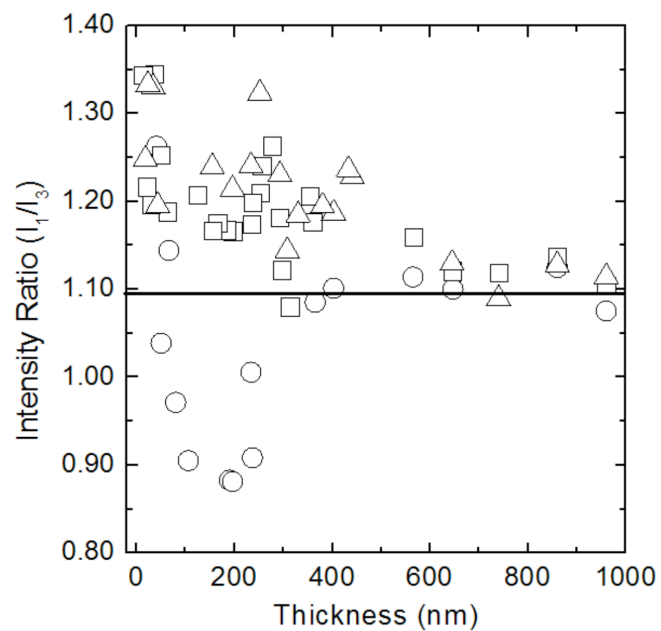
Figure 3-12: Intensity ratio as a function of thickness at 60 °C for MPy-PS films supported on PDMS (squares), and on glass (triangles), and for free-standing MPy-PS films (circles). Horizontal line corresponds to bulk intensity ratio value for MPy-PS. (Background noise was not subtracted.)

spectroscopy (Evans 2012a) (the length scales at which stiffness-confinement effects are observed are smaller in several of those studies.) Different results indicating a reduction in modulus with confinement have been obtained via wrinkling experiments of glassy polymer on cross-linked PDMS (Stafford 2004, Stafford 2006).

Upon decreasing thickness from ~400 nm down to ~20 nm, the MPy-PS films supported on the harder, glass substrate exhibit somewhat higher I_1/I_3 values and thus greater caging and stiffness compared to films supported on the softer, PDMS substrate. Related effects of PS film stiffness have been reported for Si and cross-linked PDMS substrates via surface capillary wave studies (Evans 2012a). Furthermore, the free-standing films in this thickness range exhibit substantially lower I_1/I_3 values than the substrate-supported films, which indicates that the free-standing films are the least stiff. These results show the importance of substrate and substrate hardness in affecting the stiffness of confined PS films and are qualitatively consistent with predictions from coarse-grained dynamics simulation studies (Xia 2015c).

With free-standing MPy-PS films, Figure 3-12 shows a major reduction in I_1/I_3 values with decreasing thickness from ~400 nm to ~200 nm corresponding to a reduction in caging and stiffness. Below a thickness of ~200 nm, the free-standing films exhibit a major increase in I_1/I_3 values with decreasing thickness, consistent with an increase in stiffness. The stiffening effect with decreasing thickness below 200 nm in the free-standing films is unanticipated based on the fact that both fluorescence results associated with bilayer films in section 3.4.2 above and coarse-grained dynamics simulations (Xia 2015c, Xia 2015b) indicate that PS free surface layers exhibit a substantial reduction in caging and thus stiffness relative to bulk PS. However, the free-standing film results below a thickness of ~200 nm are consistent with results of a microbubble inflation study that showed stiffening of glassy-state, free-standing PS films with decreasing thickness and below 112 nm (O'Connell 2008). In the ultrathin regime at ~20 nm thickness, all three supported and free-standing PS film systems exhibit the same I_1/I_3 value, consistent with similar caging and stiffness in the various supported and free-standing films. While unusual, the

stiffness-confinement behavior exhibited by free-standing PS films is no more unusual than the molecular-weight dependent T_g-confinement effect behavior in PS films reported in the literature (Forrest 1998, Kim 2008, Kim 2011).

3.5 Conclusions

Ellipsometry and fluorescence are used in novel ways to characterize and investigate residual stress relaxation in bulk PS films. With ellipsometry, stress relaxation is characterized by the film thickness response to several thermal history conditions. Depending on thermal history, stress relaxation can manifest as either small thickness increases or decreases in bulk PS films, with the evolution in thickness occurring over periods of hours at $T_g + 40$ °C. Nevertheless, as measured by ellipsometry, stress relaxation has no effect on the T_g of PS films.

A self-referencing fluorescence method based on the I_1/I_3 intensity ratio of the pyrene dye emission spectrum (and its sensitivity to molecular caging, which is related to stiffness or modulus) is also used for the first time to study stress relaxation. In agreement with ellipsometry results, residual stress relaxation as measured by fluorescence occurs in the rubbery state over periods of hours. The rubbery-state stress relaxation times obtained via fluorescence exhibit an Arrhenius T dependence with an activation energy of ~110 kJ/mol which is consistent with β-relaxation. Also in agreement with ellipsometry results, fluorescence measurements show that the T_g of bulk PS films is unaffected by residual stress relaxation.

The special ability of fluorescence to investigate behavior within one layer of a multilayer film was exploited to compare the effects of confinement on stiffness near a free surface and a substrate interface. Bilayer bulk film studies reveal that 30-nm-thick free-surface layers are less stiff and 30-nm-thick substrate layers are stiffer than bulk PS films and 30-nm-thick PS films supported on glass. The effect of confinement on the stiffness of films was further studied as a function of relative stiffness of the substrate (glass vs. cross-linked PDMS) and in free-standing films lacking a substrate. The studies revealed that the effects of confinement on T_g

and stiffness are qualitatively and quantitatively different and that in confined films between 20 and 400 nm in thickness, the PS films exhibited increasing I_1/I_3 values and hence stiffness in the following order: free-standing films < PDMS-supported films < glass-supported films.

ACKNOWLEDGMENTS

CHAPTER 4

Stiffness of Thin, Supported Polystyrene Films: Free-Surface, Substrate, and

Confinement Effects Characterized via Self-Referencing Fluorescence

4.1 Introduction

The vast majority of studies investigating confinement effects on glass transition

temperature (T_g) (Keddie 1994b, Keddie 1994a, Forrest 1997b, Herminghaus 2002, Ellison 2003,

Liu 2003, Fakhraai 2005, Mundra 2006, Priestley 2007, Roth 2007b, Kim 2008, Yang 2010,

Glynos 2011, Inoue 2011, Kim 2011, Inoue 2013, Lang 2013, Xia 2013, Forrest 2014, Hayashi

2014, Lang 2014, Yoon 2014, Evans 2015, Kanaya 2015, DeFelice 2016) of linear polymers

show qualitative and often quantitative agreement for particular polymer-substrate pairs or free-

standing polymer films. As mentioned in the Background (Chapter 2), general trends regarding

stiffness-confinement behavior are less clear (Lee 1996, Briscoe 1998, Forrest 1998, Soles 2002,

Hartschuh 2004, Stafford 2004, Hartschuh 2005, Inoue 2005, O'Connell 2005, Yoshimoto 2005,

Inoue 2006, Stafford 2006, Cheng 2007, Tweedie 2007, Stoykovich 2008, Gomopoulos 2009,

Delcambre 2010, Gomopoulos 2010, Xu 2010, Arinstein 2011, Watcharotone 2011, Batistakis

2012, Evans 2012a, Torres 2012, Batistakis 2014, Chung 2014, Askar 2015, Cheng 2015, Chung

2015, Li 2015c, Liu 2015, Xia 2015c, Xia 2015b, Ye 2015, Askar 2016, Brune 2016, Chung

2016, Nguyen 2016, Xia 2016). In this chapter, greater detail is provided with regard to the

studies in the field. Such details are necessary to ascertain general trends.

Using Brillouin light scattering (BLS), Gomopoulos *et al*. (Gomopoulos 2009) and

Cheng *et al*. (Cheng 2007) measured the modulus of supported PS films as a function of

thickness at room temperature. Polystyrene (PS) films exhibited invariance in modulus down to

thicknesses of 40 nm. Neither BLS study investigated films with thicknesses below 40 nm. Lee

et al. (Lee 1996) used picosecond acoustics to measure changes in longitudinal wave velocity

(the square of which is proportional to through-film elastic modulus) in supported poly(methyl

methacrylate) (PMMA) films as a function of overall thickness. They reported invariance in the

wave velocity with thickness down to 40 nm in PMMA single-layer films supported on aluminum. Enhancements in the wave velocity and thus stiffness were reported in films with decreasing thickness below 40 nm. Although data were not explicitly given, Lee *et al*. (Lee 1996) stated that similar enhancements in wave velocity and thus stiffness were observed for ultrathin PS films. Inoue *et al*. (Inoue 2006) used incoherent neutron scattering to measure changes in mean-squared displacement, $<u^2>$, (which is related to the Debye-Waller factor) in supported PS films with thicknesses of 100,000, 100, and 40 nm at 40 °C and 135 °C. (The relationship between $<u^2>$ and stiffness has been described recently in several reports (van Zanten 2000, Soles 2001, Soles 2002, Inoue 2005, Yang 2011, Xia 2015b, Ye 2015, Simmons 2016), with several references (van Zanten 2000, Soles 2001, Yang 2011, Xia 2015b, Simmons 2016) indicating that local stiffness $\sim 1/<u^2>$.) Relative to bulk response in glassy-state PS films at 40 °C, $<u^2>$ decreased slightly in 100-nm-thick films and more significantly in 40-nm-thick films. Larger percentage reductions from bulk response were observed in the rubbery state at 135 °C in these nanoconfined films.

When a rigid substrate is replaced by a soft substrate or a free surface, experimental studies have most commonly reported a reduction in stiffness with confinement. Studies using a film wrinkling technique on poly(dimethyl siloxane) (PDMS)-supported polymer films reported reductions in modulus with decreasing thickness (Stafford 2004, Stafford 2006, Torres 2012). Stafford *et al*. (Stafford 2006) reported that PDMS-supported PS films exhibit reductions in room-temperature modulus with decreasing thickness at ~40 nm and below. Using ultrathin film tensile testing, Liu *et al*. (Liu 2015) investigated stiffness-confinement effects in room-temperature, free-standing PS films via the stress-strain response of stretched films floating on water. They reported that the modulus decreased precipitously below thicknesses of ~25 nm (Liu 2015). Other studies (Stoykovich 2008, Delcambre 2010) that have utilized beam-bending in nanopatterned PMMA structures at room temperature observed structural collapse as beam width was reduced below 100 nm (Stoykovich 2008) and 50 nm (Delcambre 2010). It can be

rationalized that with decreasing width, free-surface effects dominate and cause nanobeam collapse. In contrast, nanobubble inflation studies of free-standing polymer films exhibit differences compared to ultrathin film tensile testing and beam-bending studies; in a $10 - 15$ °C temperature range above and below T_g, these studies have reported stiffening with decreasing thickness below ~200 nm (O'Connell 2005, Xu 2010, Li 2015c).

Several simulation studies have focused on characterizing the impacts of confinement on supported polymer films with no free surfaces (Batistakis 2012, Batistakis 2014), supported polymer films with one free surface (Xia 2015b), and free-standing polymer films (Yoshimoto 2005, Xia 2015c). Simulations are in general qualitative agreement with many experimental reports that the presence of a rigid substrate increases stiffness (Batistakis 2012, Batistakis 2014, Xia 2015b), the presence of a free surface reduces stiffness (Yoshimoto 2005, Xia 2015c, Xia 2015b), and free-standing polymer films exhibit reduced stiffness with reduced thickness (Yoshimoto 2005, Xia 2015c). Specifically, Xia and Keten (Xia 2015b) simulated stiffness behavior of 5-, 10-, and 19-nm-thick supported PMMA films. They reported that $<u^2>$ decreases and stiffness increases within ~2 nm of the substrate interface and that stiffness decreases within a comparable length scale of the free surface. Xia and Keten (Xia 2015b) did not comment on the impact of overall film thickness on the length scales associated with stiffness perturbations near the substrate and free-surface interfaces, *i.e.*, whether the length scales are limited to ~2 nm because of the extreme confinement of film thickness.

Excluding the studies described in this dissertation there are only two experimental reports characterizing stiffness gradients in supported polymers (Cheng 2015, Brune 2016) on stiffness gradients in supported, bulk polymer films. Both studies used nanoindentation to determine the extent to which substrates impact the room-temperature modulus of polymer films as a function of distance from the interface. This was achieved by indenting the polymer parallel to the substrate. Cheng *et al*. (Cheng 2015) reported that PMMA films exhibited greater stiffness near a silica substrate, with gradients extending up to ~100 nm or ~170 nm towards the interior

of films supported on silica or alumina substrates, respectively. Brune *et al*. (Brune 2016) reported that films of bound PS-butadiene rubber exhibit stiffening near a silica substrate interface, with gradients extending ~40 nm towards the interior of the films. Outside of the research described in this dissertation, there is no experimental report of stiffness gradients as a function of distance from a free-surface interface.

Here, fluorescence is used to characterize effects of confinement on average stiffness across a film as well as stiffness gradients near the substrate and free-surface interfaces. Average stiffness-confinement effects are investigated by characterizing silica-supported, single-layer PS films as a function of overall thickness. The effects of confinement on interfacial perturbations are investigated using ultrathin bilayer films, and the length scales associated with interfacial perturbations are investigated using bulk bilayer films. The bulk bilayer film results represent the first experimental characterization of caging or stiffness gradients near a free surface in polymer films. This chapter also provides the first comparison of the length scales associated with stiffness perturbations near the substrate and free-surface interfaces among published work.

Stiffness gradients in bilayer polymer films are characterized via the sensitivity of pyrenyl dye-label fluorescence to its local environment. As described in Chapter 2, fluorescence of vibronic coupling dyes (such as some pyrenyl dyes) is sensitive to polymer stiffness via a caging mechanism. The caging mechanism is described in detail in both the Background and Chapter 3. In short, a pyrene fluorescence measurable I_1/I_3 increases in stiff environments.

There are several key advantages associated with this fluorescence technique. For instance, by incorporating dye-labeled layers in bilayer films, gradients may be characterized near free-surface and substrate interfaces. Other advantages include the ability to characterize polymer stiffness several tens of degrees above T_g and many tens of degrees below T_g, as well as the non-contact nature of the technique, which eliminates issues inherent to contact-based approaches that may perturb polymers during measurement. (Given the ~200 ns excited-state lifetime of the pyrenyl dye (Mundra 2007b), yielding a response that is akin to a high frequency

measurement, we interpret that the stiffness being probed by the fluorescence method is related to a glassy, high frequency modulus even at temperatures some tens of degrees above T_g.) Similar self-referencing fluorescence approaches have been used in a range of studies including those measuring T_g (Lenhart 2001, Kim 2008, Kim 2011, Evans 2012b), residual stress relaxation (Mundra 2006, Askar 2015), aggregate and micelle formation (Kalyanasundaram 1977, Wilhelm 1991, Kim 2002), and polarity in heterogeneous polymeric systems (Prado 2000, Tedeschi 2001) and solvents (Kalyanasundaram 1977, Dong 1984).

4.2 Experimental Methods

4.2.1 Materials

Polystyrene (Pressure Chemical, synthesized by anionic polymerization) with nominal molecular weight of 400 kg/mol and dispersity = 1.06 was used as received. Using azobisisobutyronitrile (Aldrich, under the name 2,2'-azobis(2-methylproprionitrile)) as initiator, 1-pyrenylmethyl methacrylate (MPy) (Toronto Research Chemicals) was copolymerized at very low levels with styrene (SigmaAldrich) at 70 °C via bulk free radical polymerization to yield MPy-labeled polystyrene (MPy-PS). The MPy-PS product was dissolved in toluene and precipitated in methanol seven times to remove any residual MPy or styrene monomer. The washed polymer was placed in a vacuum oven at 105 °C for 3 days prior to use. As determined by gel permeation chromatography (Waters 2410, calibrated with PS standards in tetrahydrofuran, refractive index detector), the washed MPy-PS sample had M_n = 370 kg/mol, with dispersity = 1.7. As determined by UV-vis absorbance spectroscopy (Perkin Elmer Lambda 35), MPy-PS contains 0.6 mol% pyrene label. Bulk T_g was determined via differential scanning calorimetry (Mettler Toledo DSC822e, second-heat T_g onset method at 10 °C/min heating rate): T_gs were 102 °C for 400 kg/mol PS and 101 °C for 370 kg/mol MPy-PS.

4.2.2 Film Preparation

Films were spin-coated onto green glass slides from toluene (SigmaAldrich) solutions

containing 0.5 to 7.0 wt% PS or MPy-PS with spin speeds ranging from 1500 to 3000 rpm. Glass slides were thoroughly cleaned by etching in 1.0 M hydrochloric acid, rinsing with water, and drying prior to submerging in base solution (10 wt% sodium hydroxide/20 wt% water/70 wt% ethanol). Substrates were then rinsed with water and dried prior to use. With bilayer films, samples were spun onto freshly cleaved mica and annealed under vacuum at $T_{g,bulk}$ + 20 °C for 2 h. After annealing, mica-supported films were transferred at room temperature onto glass-substrate supported films by a water transfer technique (Forrest 1997b). Residual water was evaporated overnight under ambient conditions prior to annealing the bilayer film in a vacuum oven at 120 °C for 3 h before fluorescence measurement. These annealing conditions ensured that the bilayers healed into a consolidated film without substantial interlayer diffusion (Whitlow 1991, Ellison 2003, Kim 2011).

4.2.3 Ellipsometry

To measure film thickness, PS and MPy-PS were first spin-coated onto silicon slides with a native silicon oxide layer from the same solutions with the same spin speeds at the same time as the films spin-coated onto the glass slides. Measurements were performed at room temperature using spectroscopic ellipsometry (J. A. Woollam Co. M-2000D over a range of wavelengths from 400 to 1000 nm). The ellipsometric angles (ψ and Δ) of incident light reflected off silica-supported PS or MPy-PS films were measured and fitted to a Cauchy layer model to determine thickness. The Cauchy layer model included a PS layer atop a silicon substrate containing a 2-nm-thick silicon oxide surface layer. Film thickness was determined by fitting ψ and Δ to the PS layer in the Cauchy model.

4.2.4 Fluorescence Measurements

Fluorescence was used to characterize I_1/I_3 values, which reflect molecular caging and hence are related to stiffness, of MPy-PS films or layers as a function of temperature; these measurements also yield characterization of T_g (Kim 2008, Kim 2011, Askar 2015, Evans 2015). After spin-coating and annealing films (see Section 4.2.2), emission spectra were collected

(Photon Technology International fluorimeter in front-face geometry) at wavelengths from 370 to 405 nm (0.5 nm increment, 1 s integration), with excitation at 324 nm. Excitation and emission slit widths were 0.5 mm (1 nm bandpass). Spectra were used to determine the ratio of the first vibronic band peak intensity to the third vibronic band peak intensity (I_1/I_3) of the pyrene-labeled polymer. Peak intensities were calculated from an average of five data points spanning a 2 nm window: I_1 was an average of points between 376 and 378 nm and I_3 an average of points between 387 and 389 nm.

Fluorescence spectra were collected from 140 °C to 60 °C in 5 °C decrements. Before collecting an emission spectrum, films were held for 5 min at each temperature to enable temperature equilibration. Once spectra were collected, background noise was measured by acquiring the spectra of unlabeled PS films of thickness similar to the MPy-PS films. Values of I_1/I_3 at particular temperatures were used to gather stiffness information for each film in the rubbery and glassy states and near T_g. After plotting I_1/I_3 as a function of temperature, lines were fit to the rubbery and glassy temperature dependences to determine T_g (Kim 2008, Kim 2011, Askar 2015, Evans 2015).

4.3 Results and Discussion

4.3.1 Average Stiffness-Confinement Effects in Supported Single-Layer PS films

Figure 4-1A shows typical fluorescence emission spectra for a 935-nm-thick 1-pyrenylmethyl methacrylate-labeled PS film supported on silica at 140 °C, 100 °C, and 60 °C (bottom to top). Fluorescence intensity increases substantially with decreasing temperature but non-uniformly as a function of emission wavelength. Upon cooling, non-radiative pathways of energy decay for excited-state pyrenyl electrons are suppressed and fluorescence is enhanced. Figure 4-1A also shows the locations of the first and third vibronic band peaks. The intensities of these peaks were used to determine the I_1/I_3 ratio. (The second vibronic band peak is almost invisible; covalently attaching pyrene to PS chains slightly alters the spectral shape compared to
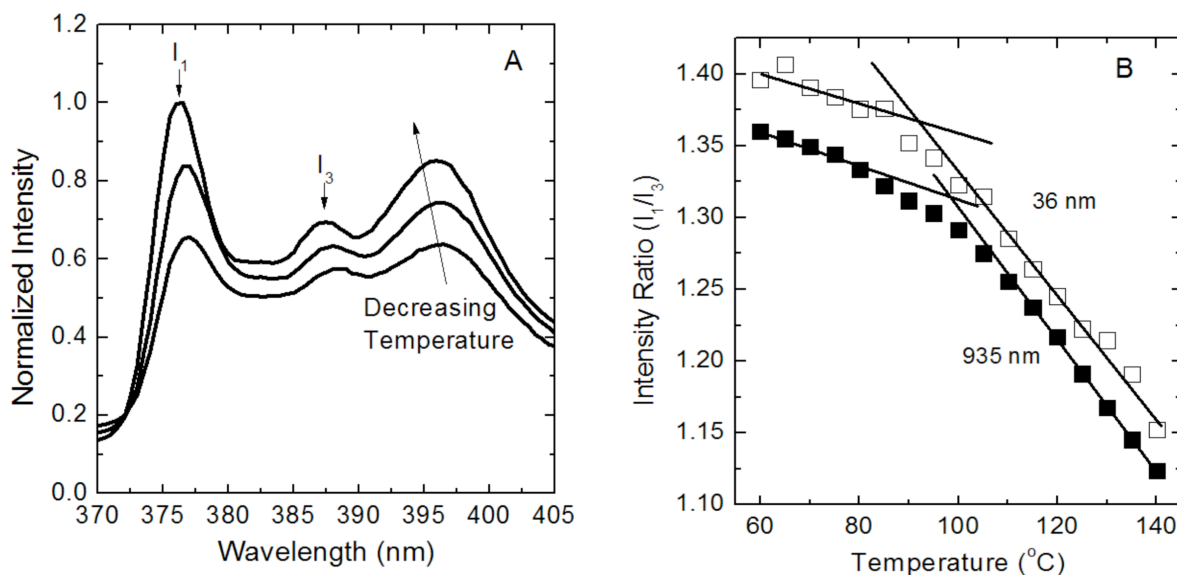
Figure 4-1: A: Normalized fluorescence emission intensity spectra for a 935-nm-thick 1-pyrenylmethyl-labeled PS film. Spectra are shown for 140 °C, 100 °C, and 60 °C (from bottom to top). Arrows indicate emission peak intensity values (I_1 and I_3). B: Intensity ratio (I_1/I_3) values as a function of temperature for 935- and 36-nm-thick films. Both films are supported on silica. (Background noise was subtracted from all spectra in this work.)

doped pyrene (Kim 2008, Askar 2015).) With decreasing sample temperature, I_1 increases

more significantly than I_3. This trend is consistent with the sensitivity of I_1/I_3 to molecular caging

and hence stiffness (Askar 2015). As excited-state pyrenyl dye labels experience greater

molecular caging from the surrounding local environment upon cooling, I_1/I_3 values increase.

Figure 4-1B shows I_1/I_3 values as a function of temperature for two silica-supported

single-layer MPy-PS films. Data are shown for a 935-nm-thick, bulk, single-layer film (black

squares) and a 36-nm-thick single-layer film (open squares). While not the focus of this study, T_g

values may be determined using the intensity ratio method by the intersection of lines fitted to

the rubbery and glassy temperature dependences of I_1/I_3 (Kim 2008, Kim 2011, Askar 2015,

Evans 2015). The single-layer bulk PS film exhibits $T_g = 100 \pm 1$ °C, in reasonable agreement

with DSC measurements. Relative to bulk T_g, there is a reduction in T_g to 92 ± 2 °C for the 36-

nm-thick film; this reduction is due to the free surface perturbing T_g from its bulk value, with

perturbations propagating into the film interior (Ellison 2003, Priestley 2007, Roth 2007b, Inoue

2011, Kim 2011, Baeumchen 2012). Importantly, despite the fact that the 36-nm-thick supported

PS film exhibits a significant reduction in T_g relative to bulk, as evidenced by higher I_1/I_3 values

the confined film exhibits enhanced molecular caging and thus stiffness relative to bulk response

at all temperatures.

Figure 4-2 shows I_1/I_3 values of single-layer MPy-PS films as a function of logarithmic

film thickness at 60 °C, 100 °C, and 140 °C. The dotted lines in the plots correspond to I_1/I_3

values determined for the bulk, 935-nm-thick, single-layer MPy-PS film. For single-layer films

at 60 °C and 100 °C, I_1/I_3 remains invariant (within error) with decreasing thickness down to 63

nm and exhibits increasing values (outside error) at 36 nm and below. In 16-nm-thick films, I_1/I_3

values increase relative to bulk response by ~0.04 at 60 °C and ~0.05 at 100 °C. For single-layer

films at 140 °C, I_1/I_3 remains invariant (within error) with decreasing thickness down to 240 nm

and exhibits increasing values (outside error) at 165 nm and below. In 16-nm-thick films, I_1/I_3

increases relative to bulk response by ~0.04 at 140 °C. The increases in I_1/I_3 values indicate an
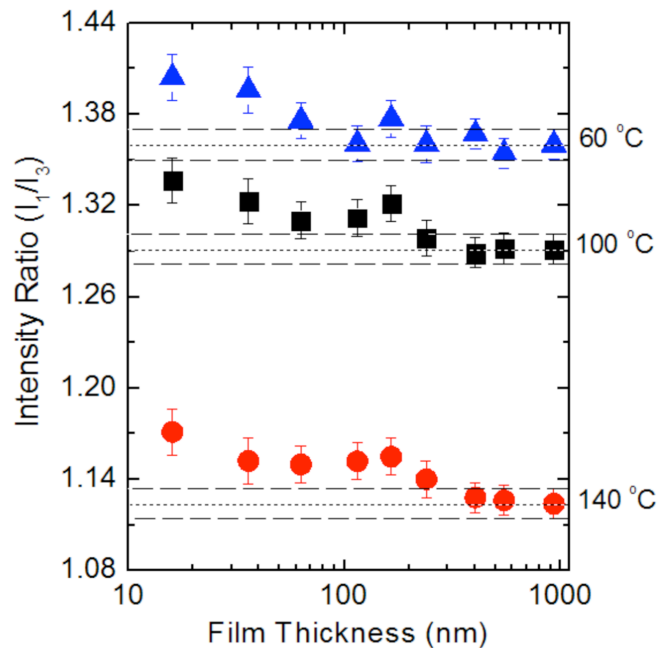
Figure 4-2: Intensity ratio (I_1/I_3) values as a function of film thickness for single-layer films supported on silica at 60 °C (blue triangles), 100 °C (black squares), and 140 °C (red circles). The dotted lines represent the I_1/I_3 values for a 935-nm-thick film at the various temperatures. Error bars and dashed lines indicate the variation in I_1/I_3 associated with slight position changes in the film.

enhancement in caging and thus average stiffness across sufficiently thin films.

The results on glassy-state (60 °C) and near T_g (100 °C) single-layer, supported PS films shown in Figure 4-2 are in major agreement with results from BLS studies of single-layer, supported PS films that reported invariance in stiffness with decreasing thickness for PS films down to 40 nm (Cheng 2007, Gomopoulos 2009). (Related BLS studies that do not allow for direct comparison with results in Figure 4-2 have revealed invariance in stiffness with decreasing thickness down to the smallest measured thickness: down to 100 nm in supported polyimide films (Gomopoulos 2010) and with decreasing ridge width in PS nanostructures with widths as small as 88 nm (Hartschuh 2005) and 80 nm (Hartschuh 2004).) A picosecond acoustic study (Lee 1996) that measured longitudinal wave velocity in aluminum-supported, single-layer PMMA films reported an invariance with thickness down to 40 nm. Below 40 nm, wave velocity and hence modulus increased with decreasing thickness. Although results were not explicitly given, similar enhancements were reportedly obtained for PS films (Lee 1996). Thus, our fluorescence results for glassy-state, single-layer PS films also agree with results from Lee *et al*.

The results on glassy-state (60 °C) and rubbery-state (140 °C), single-layer, supported PS films shown in Figure 4-2 may be compared with mean-squared displacement results. As stated by Ye *et al*., based on a simple Maxwell model a "reduction in $<u^2>$ is expected…to reflect an enhancement in the local elastic properties of a glass" (Ye 2015) and hence stiffness. This is because reductions in $<u^2>$ correspond to increases in a harmonic spring constant, which is "expected to scale roughly with the high frequency shear modulus." (Ye 2015) Several references have also indicated that stiffness $\sim 1/<u^2>$ (van Zanten 2000, Soles 2001, Yang 2011, Xia 2015b, Simmons 2016). Using incoherent neutron scattering, Inoue *et al*. (Inoue 2006) measured $<u^2>$ for 40-, 100-, and 100,000-nm-thick supported PS films at temperatures ranging from -193 °C to 135 °C. Relative to bulk PS response, at 40 °C, $<u^2>$ decreased substantially (~37%) in a 40-nm-thick film but relatively little (~11%) in a 100-nm-thick film. The relative reductions in $<u^2>$ with confinement increased in the rubbery state at 135 °C, with $<u^2>$

decreasing by ~42% and ~18% in 40- and 100-nm-thick films, respectively. While not providing exact quantitative correspondence with our fluorescence measurements in Figure 4-2, they agree in indicating that the confinement length scale at which substantial stiffening relative to bulk is observed is greater in the rubbery state than in the glassy state.

Thus, the novel fluorescence technique yields results that are in substantial agreement with BLS (Cheng 2007, Gomopoulos 2009) picosecond acoustic (Lee 1996), and incoherent neutron scattering (Inoue 2006) studies that have characterized properties or behavior related to stiffness in single-layer, supported PS films. A particular advantage of our fluorescence technique is the ability to place dye-labeled polymer layers within bilayer films to investigate the impact of both the substrate and free-surface interfaces in perturbing behavior relative to bulk response. Such studies have been reported previously for T_g-confinement effects (Ellison 2003, Priestley 2007, Roth 2007b, Kim 2011) and physical aging-confinement effects (Priestley 2005b) Below, we describe the first study to characterize the roles of free surfaces and substrates in perturbing molecular caging and thus stiffness of polymer films and to provide insight into how temperature relative to T_g can impact the length scales over which such free-surface and substrate perturbations can propagate into films.

4.3.2 Roles of Substrate and Free-Surface Interfaces in Stiffness-Confinement Effects: Bilayer Film Studies

Figure 4-3 shows I_1/I_3 values for MPy-PS layers within single-layer and bilayer films at 140 °C, 100 °C, and 60 °C. MPy-PS layers are depicted in green rectangles, which also contain a number corresponding to the I_1/I_3 value of that layer. Unlabeled PS layers are depicted in open rectangles. The thicknesses of the single-layer and bilayer films are shown via double-headed arrows. For films at 140 °C, the numbers in Figs. 4-3A and 4-3D represent the I_1/I_3 values for 935- and 36-nm-thick single-layer MPy-PS films, respectively. In Figs. 4-3B, 4-3C, 4-3E, and 4-3F, the number within each green layer represents the I_1/I_3 value for a 20-nm-thick MPy-PS layer within bilayer films with overall thicknesses of either 1520 nm (B & C) or 40 nm (E & F).
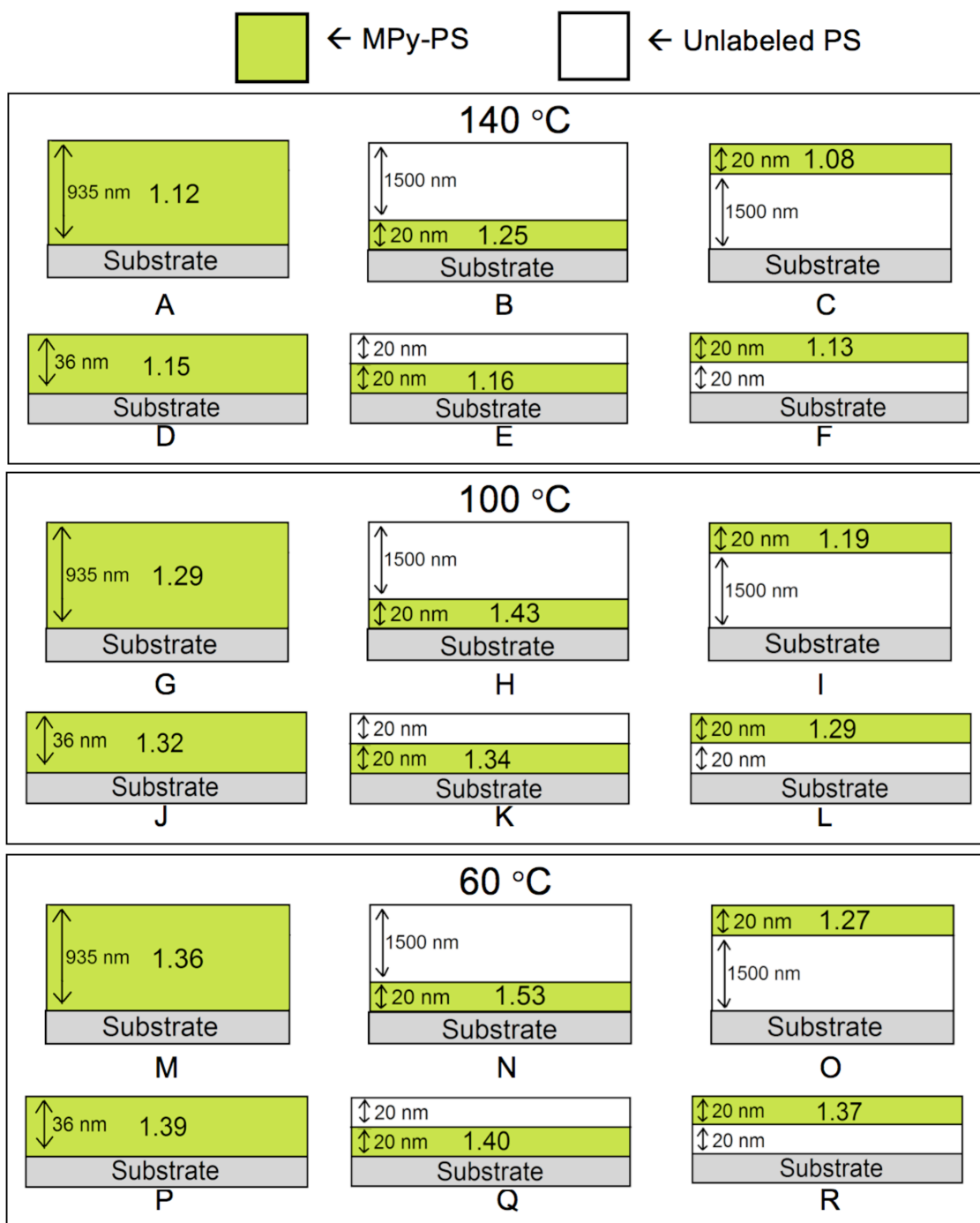
Figure 4-3: Intensity ratio (I_1/I_3) values of single-layer and bilayer films at 140 °C, 100 °C and 60 °C. The numbers in A & D represent I_1/I_3 values for 935- and 36-nm-thick single-layer films at 140 °C. The numbers in the green layers of B & C and E & F represent I_1/I_3 values at 140 °C for 20-nm-thick MPy-PS layers within bilayer films that are either 1500-nm-thick (B & C) or 40-nm-thick (D & E) overall. G-L and M-R represent the I_1/I_3 values at 100 °C and 60 °C for the same films described in A-F.

Figures 4-3A – 4-3C show that, in the rubbery state at 140 °C, 20-nm-thick substrate and free-surface layers in bulk PS bilayer films exhibit substantial differences in I_1/I_3 values relative to average I_1/I_3 values across a bulk film. The value of $I_1/I_3 = 1.25$ in the substrate layer indicates significant enhancement in molecular caging and thus stiffness relative to the average across a bulk film with $I_1/I_3 = 1.12$. As well, the value of $I_1/I_3 = 1.08$ in the free-surface layer indicates a reduction in caging and thus stiffness relative to the bulk average response. Notably, the magnitude of the change in I_1/I_3 relative to bulk response is substantially greater in the substrate layer than in the free-surface layer. This indicates that the perturbation to caging and stiffness caused by an interface is greater for the polymer-substrate interface than for the polymer-air interface. Similar conclusions can be drawn for the bulk single-layer and bilayer films that were characterized near T_g at 100 °C and in the glassy state at 60 °C in Figs. 4-3G – 4-3I and Figs. 4-3M – 4-3O, respectively.

These results and associated conclusions are opposite to what has been observed and concluded regarding T_g-confinement effects in PS films supported on silica (Ellison 2003). Using a related fluorescence method in bilayer PS films with overall thickness yielding bulk T_g ($T_{g,bulk}$) response, Ellison and Torkelson (Ellison 2003) reported that $T_g = T_{g,bulk}$ in a 12-nm-thick dye-labeled layer adjacent to the substrate but $T_g - T_{g,bulk} = -32$ °C in a 14-nm-thick dye-labeled free-surface layer. In other words, the T_g-confinement effect in supported PS films lacking significant attractive polymer-substrate interactions originates at the free surface (and not at the polymer-substrate interface) and, in sufficiently thick films, propagates some tens of nanometers into the film interior.

A comparison of Figs. 4-3D – 4-3F with Figs. 4-3A – 4-3C reveals that, in the rubbery state at 140 °C, the perturbations to caging and stiffness caused by interfaces depend strongly on confinement. The difference in I_1/I_3 values between 20-nm-thick substrate and free-surface layers decreases from 0.17 in 1520-nm-thick bilayer films to 0.03 in 40-nm-thick bilayer films. Thus with sufficient confinement, as in the 40-nm-thick bilayer films, the substrate and free-surface

layers exhibit much more similar molecular caging and stiffness characteristics, which are also very close to that of a single-layer film of a comparable overall thickness (36 nm). Similar conclusions can be drawn for confined single-layer and bilayer films characterized near T_g at 100 °C and in the glassy state at 60 °C.

The effect of confinement in causing free-surface and substrate layers to exhibit more similar responses has also been observed with T_g-confinement effects in PS films supported on silica (Ellison 2003). Using a fluorescence method and bilayer films that varied in overall thickness from several hundred to 24 nm, Ellison and Torkelson (Ellison 2003) reported that when overall bilayer thickness exceeds 60 nm, a 14-nm-thick surface layer exhibits $T_g - T_{g,bulk}$ = -32 °C independent of overall thickness. However, as overall thickness decreases below 60 nm, there is a sharp rise in the surface-layer T_g until overall thickness reaches 25 nm, below which the surface layer simply reports the same T_g as a single-layer film of the overall thickness. Experiments with multilayer films revealed that, unlike films with overall thicknesses exceeding ~60 nm, in 24-nm-thick bilayer films both the 12-nm-thick free-surface and 12-nm-thick substrate layers exhibit the same T_g depression relative to bulk ($T_g - T_{g,bulk}$ = -11 °C) as that reported by a single-layer 24-nm-thick film. In other words, with a sufficiently nanoconfined, supported PS film, the length scale is insufficient to support a substantial, smooth T_g gradient from the free surface to substrate (Ellison 2003).

Ellison and Torkelson (Ellison 2003) concluded that if the total film thickness is below a certain value (~60 nm), then the system adjusts "to satisfy the constraint that the gradient in (T_g) from surface to substrate is not too sharp and abrupt." (Ellison 2003) We hypothesize that a related constraint in caging or stiffness gradient also holds in the current study. In particular, the caging or stiffness represented by I_1/I_3 = 1.53 and 1.27 in 20-nm-thick substrate and free-surface layers, respectively, in 1520-nm-thick bulk films would result in too sharp of a gradient in caging or stiffness if the substrate and free-surface layers were adjacent to each other as in a 40-nm-thick bilayer film.

The major narrowing of the distribution of caging or stiffness response from free surface to substrate with sufficient confinement may also be rationalized as follows. Perturbations to T_g caused by interfaces have been observed to propagate inside a film interior by several tens of nanometers or even greater length scales (Ellison 2003, Priestley 2007, Roth 2007b, Inoue 2011, Kim 2011) We hypothesize that perturbations to caging and hence stiffness caused by interfaces also propagate some substantial distance into a film interior. When the length scale over which an interfacial perturbation propagates inside the film becomes comparable to or greater than one-half of the film thickness, then the behaviors near both interfaces begin to exhibit less difference with sufficient reduction in film thickness. The behaviors very near the free-surface and substrate interfaces should be similar due to the combined propagation of interfacial perturbations across the whole film.

If the free-surface and substrate layers exhibit more similar caging and stiffness effects with increasing overall film confinement, then why is an increase in caging and stiffness evident in sufficiently thin single-layer films at 60 °C, 100 °C, and 140 °C? The apparent stiffening with sufficient confinement results from the fact that at all temperatures studied, the perturbation to caging and stiffness is greater at the substrate interface than at the free surface. Thus, unlike T_g-confinement effects in PS films supported on silica where the T_g reduction originates at the free surface with little or no effect of the substrate interface (Ellison 2003), the effect of the rigid substrate layer on stiffness is greater in magnitude than and thus dominates over the effect of the free-surface layer in sufficiently thin films. In this respect, stiffness-confinement effects in supported PS films are more similar to T_g-confinement effects in supported polymer films that have attractive interactions with the substrate, which result in T_g enhancements with confinement (Priestley 2007).

The length scales associated with free-surface and substrate perturbations are explored further in Figure 4-4. Figure 4-4 shows I_1/I_3 values for MPy-PS layers within bulk bilayer films as a function of MPy-PS layer thickness, h, at 140 °C, 100 °C, and 60 °C; total bilayer film
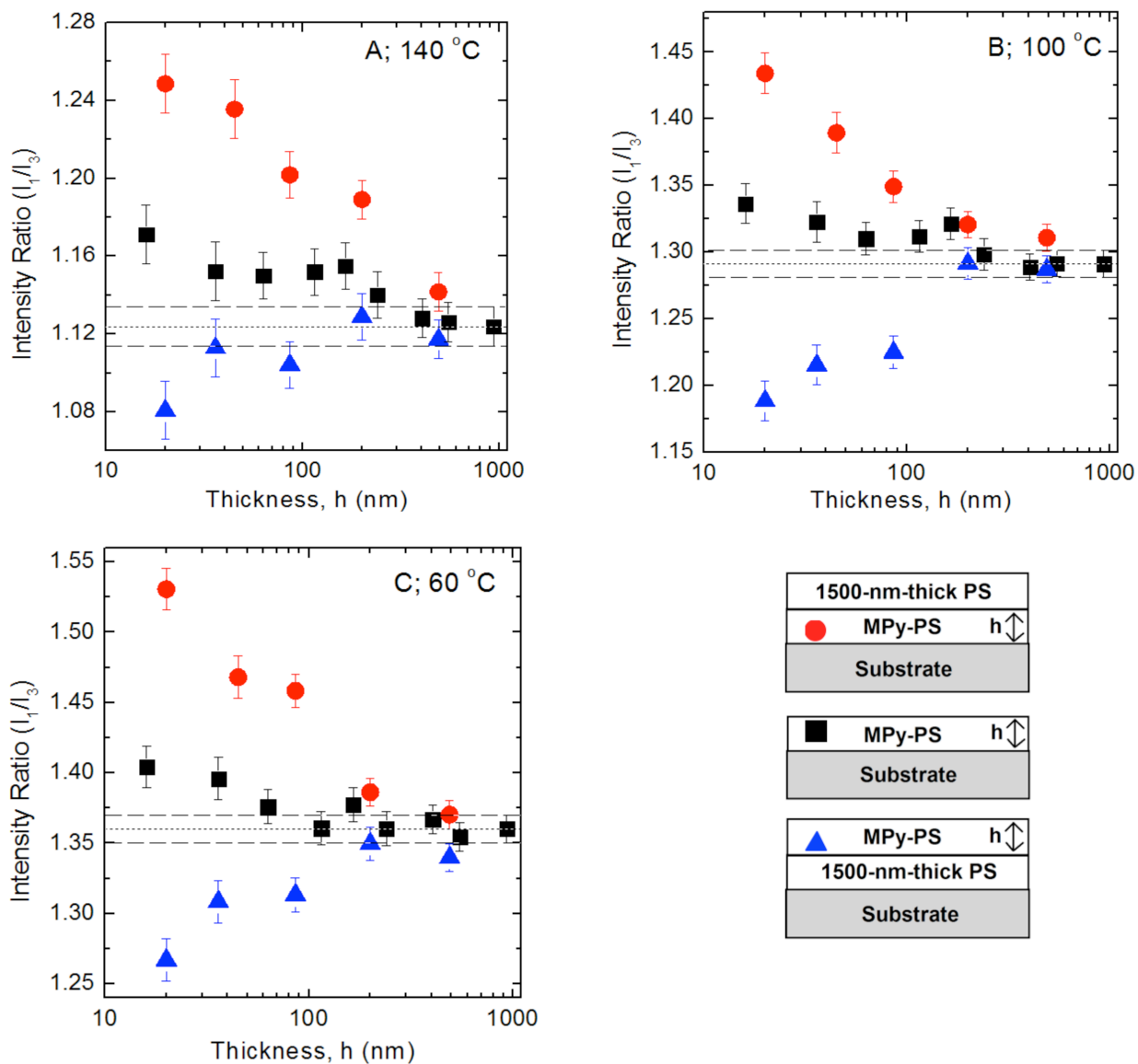
Figure 4-4: I_1/I_3 values as a function of thickness at 140 °C (A), 100 °C (B) and 60 °C (C) for single-layer and bilayer films. I_1/I_3 values are shown for substrate-adjacent MPy-PS layers within bilayer films (red circles), single-layer MPy-PS films (black squares), and free-surface-adjacent MPy-PS layers within bilayer films (blue triangles). Single-layer film data are reproduced from Figure 4-2. The dotted line represents the I_1/I_3 value for a 935-nm-thick single-layer MPy-PS film. Error bars and dashed lines indicate the variation in I_1/I_3 associated with slight position changes in the film.

thickness exceeds 1500 nm. Single-layer film data are reproduced from Figure 4-2.

To investigate the length scales associated with stiffness perturbations near the free surface, the thicknesses of free-surface MPy-PS layers within bulk bilayer films were varied. At 140 °C (Figure 4-4A), I_1/I_3 values decrease from ~1.12 in a 490-nm-thick free-surface layer to ~1.08 in a 20-nm-thick free-surface layer. The plot shows that the 20-nm-thick free-surface layer exhibits reduced I_1/I_3 values relative to bulk response (outside error). However, extending the surface layer thickness to 36 nm yields bulk response within error. These results indicate that while the gradient in caging and hence stiffness extends far enough to perturb the overall response of a 20-nm-thick surface layer, the gradient does not extend far enough to perturb the overall response of a 36-nm-thick surface layer. Thus, the stiffness-gradient length scale propagating from the free surface can be estimated to extend $\lesssim$ 20 nm at 140 °C.

Comparisons may be made to the results from the free surface at 100 °C and 60 °C in Figs. 4-4B and 4-4C, respectively. In contrast to results at 140 °C, in both cases the 36- and 86-nm-thick surface layers exhibit I_1/I_3 values that are reduced relative to bulk response (outside error). Bulk response averaged across the free-surface layer is ultimately achieved when its thickness is 200 nm. These results indicate that the gradient in caging and hence stiffness extends far enough to perturb the overall responses of 36- and 86-nm-thick surface layers but does not extend far enough to perturb the overall response of a 200-nm-thick surface layer. The stiffness gradient propagating from the free surface can be reasonably estimated to extend ~35 – 85 nm at 100 °C and 60 °C. Thus, the length scale over which free-surface perturbations to molecular caging and hence stiffness propagate inside the film at 140 °C is significantly less than those at 100 °C and 60 °C. This result can be explained by the fact that in the rubbery state at 140 °C, bulk PS has a lower modulus (by ~3 orders of magnitude (Sperling 2006)) than glassy-state PS and is thus much less susceptible to perturbations from the free surface relative to PS near T_g at 100 °C or in the glassy state at 60 °C.

To investigate the length scales associated with stiffness perturbations near the substrate,

the thicknesses of substrate MPy-PS layers within bulk bilayer films were varied. At 140 °C (Figure 4-4A), I_1/I_3 values increase from ~1.14 in a 490-nm-thick substrate layer to ~1.25 in a 20-nm-thick substrate layer. The 86- and 200-nm-thick substrate layers exhibit enhanced I_1/I_3 values relative to bulk response (outside error). Bulk response is ultimately achieved when the substrate layer thickness is 490 nm. These results indicate that the caging- and hence stiffness-gradient length scales extend far enough from the substrate to perturb the overall responses of 86- and 200-nm-thick substrate layers but is insufficient to perturb the overall response of a 490-nm-thick substrate layer. Thus, the stiffness-gradient length scale propagating from the substrate can be reasonably estimated to extend ~85 – 200 nm at 140 °C.

A comparison may be made to the results from the substrate at 100 °C and 60 °C in Figs. 4-4B and 4-4C, respectively. At 100 °C and 60 °C, the 45- and 86-nm-thick substrate layers yield I_1/I_3 values that are elevated relative to bulk (outside error). Bulk response is very nearly achieved by extending the substrate layer thickness to 200 nm. Thus, the stiffness-gradient length scale can be estimated to extend ~45 – 85 nm at 100 °C and 60 °C. These results indicate that the caging- and hence stiffness-gradient length scale associated with the polymer-substrate interface is larger at 140 °C relative to those at 100 °C and 60 °C. Thus, in the rubbery state at 140 °C, the much lower-modulus PS is more susceptible to perturbations from the rigid substrate relative to the higher-modulus PS near T_g at 100 °C or in the glassy state at 60 °C.

It is evident from Figure 4-4A at 140 °C that the perturbations from the substrate, both in terms of I_1/I_3 values and gradient length scales, are substantially greater than those from the free surface. As the thickness approaches the length scales associated with stiffness gradients from the interfaces, stiffening is observed for single-layer films with thicknesses of 165 nm and below since substrate effects dominate at 140 °C. However at 100 °C and 60 °C, the length scales associated with substrate and free-surface perturbations are more similar. Therefore, stiffening is only observed for single-layer films with thicknesses of 36 nm and below. These results support the hypothesis that the effects of the propagation of stiffness perturbations from the substrate and

free-surface interfaces are exhibited in the overall response of sufficiently confined PS films.

While bilayer experiments yield information about the approximate length scales associated with stiffness gradients, more definitive determinations of stiffness-gradient length scales may be obtained in trilayer experiments, which involve placing ultrathin dye-labeled layers at particular distances away from the free-surface and substrate interfaces. In this manner, the I_1/I_3 values associated with stiffness perturbations could be determined at specific locations. Similar approaches have been used to characterize T_g and physical aging gradients (Ellison 2003, Priestley 2005b, Kim 2011). Such fluorescence trilayer investigations of stiffness-gradient length scales are provided in Chapter 5 – 7.

The length scales associated with stiffness gradients near the substrate investigated in this study may be compared to the experimental study by Cheng *et al*. (Cheng 2015) who used nanoindentation to characterize PMMA supported on silica or alumina. Stiffness gradients were reported to extend as much as ~100 nm or ~170 nm in PMMA films supported on silica or alumina, respectively. These length scales were equated to the distance at which the normalized modulus exhibited a greater than a very small (~2%) increase relative to bulk response. Substantial changes in modulus ($\geq 10\%$) were reported at distances extending ~50 – 70 nm from a PMMA-silica interface or ~50 – 105 nm from a PMMA-alumina interface. Our fluorescence results indicate that there is stiffening near the PS-silica interface and that stiffness gradients extend ~45 – 85 nm from the substrate. Although PS and PMMA films differ regarding the absence or presence of attractive interactions with the substrates, it is interesting to note that our results regarding length scales over which substrate interfaces perturb stiffness in bulk PS films agree reasonably well with the length scales over which substantial ($\geq 10\%$) enhancements in normalized modulus are reported via nanoindentation studies of PMMA films (Cheng 2015). Direct comparisons between stiffness gradients characterized by fluorescence and AFM on the same samples will be provided in Chapter 5.

Comparisons may also be made with a recent simulation study by Xia and Keten (Xia

2015b) who studied supported PMMA films with thicknesses of 5 to 19 nm. They reported

that stiffness was reduced near the free surface and enhanced near the substrate with perturbation

length scales extending ~2 nm. Based on the results in Figure 4-3 of this study, as film thickness

is reduced to length scales comparable to or less than those associated with interfacial

perturbations, the behavior near each interface becomes more similar. In particular, the stiffness-

gradient length scales near each interface must decrease to adjust to the constraint that the

change in stiffness is not too sharp or abrupt. Taken alone, the stiffness-gradient length scales

characterized in bulk bilayer films in this study (tens of nanometers) may appear to be

inconsistent with those characterized in ultrathin films (~2 nm) in the simulation study (Xia

2015b). However, the gradient length scales may be consistent when comparing films that are

much more highly confined, *e.g.*, the 40-nm-thick bilayer films in which 20-nm-thick substrate

and free-surface layers exhibited little difference within error in I_1/I_3 values and hence stiffness.

These results indicate that care must be taken when comparing stiffness-gradient length scales

from various studies that consider films of very different thicknesses, *i.e.*, the overall film

thickness must be considered because stiffness-gradient length scales are a function of

confinement.

We also note that recent theoretical work by Mirigian and Schweizer (Mirigian 2013,

Mirigian 2015) concerned with activated glassy relaxation and mobility gradients in free-

standing films is particularly relevant to the results of our study. The key, basic idea associated

with their work is that "vapor interfaces speed up barrier hopping in two distinct but coupled

ways by reducing *both* near-surface local caging constraints and spatially long range collective

elastic distortion." (Mirigian 2015) In other words, the energy barrier that impedes relaxation in

glasses is governed by units or particles having to break out of local cages as well as a

contribution resulting from the long-range, high-frequency elastic properties of the glassy matrix

that must dilate to accommodate a unit or particle breaking out of it cage. In their study, they

determined that there are "two *generic dynamical* mechanisms of how a free surface modifies the

spatially nonlocal activated event: (i) a 'direct surface' effect close to the interface mainly associated with the loss of nearest neighbors and its effect on the local cage barrier and (ii) a longer range 'confinement' effect mainly associated with the cutoff of the strain field at the vapor interface which reduces the collective elastic barrier. These two film effects are fundamentally coupled in a spatially heterogeneous manner via gradients of *all* physical properties of the dynamic free energy."(Mirigian 2015) Our experimental results related to gradients from the free surface are in qualitative accord with the theoretical picture developed by Mirigian and Schweizer and may be useful in informing the local modulus used by them as well as the incorporation of long-range effects on elasticity. Related, future theoretical development to address films on solid supports, such as our supported PS films, may also be able to take advantage of our experimental results on gradients from the substrate.

Finally, a comparison between T_g- and stiffness-confinement effects of silica-supported PS films reveals that the two are distinct. This result is evident based on the following reasons. In a report by Ellison and Torkelson (Ellison 2003). T_g gradients were reported to extend tens of nanometers into supported PS films from the free surface and were non-existent within error near the substrate. Fluorescence results indicate that stiffness gradients propagate from both the free surface and the substrate. Even in the absence of T_g-confinement effects near the PS-substrate interface, stiffness gradients extend between ~85 – 200 nm above T_g and between ~45 – 85 nm below and near T_g (Figure 4-4) in bulk bilayer films. Additionally, Figure 4-4 shows that single-layer films exhibit stiffening in sufficiently thin films due to substrate perturbations that dominate over free-surface perturbations. The opposite is true for T_g-confinement effects in silica-supported PS films in which T_g reductions are observed in sufficiently thin PS films due to free-surface perturbations (Ellison 2003). These reasons demonstrate that stiffness-confinement effects and T_g-confinement effects are distinct, in agreement with other reports in literature (Torres 2009, Ye 2015).

4.4 Conclusions

Fluorescence is used to characterize changes in molecular caging and hence stiffness in supported MPy-PS films via the fluorescence measurable I_1/I_3. Single-layer films were used to investigate average stiffness-confinement effects. In the glassy state and near T_g, single-layer, supported PS films exhibit an invariance of caging and hence stiffness down to thicknesses of 63 nm and enhancements for films with thicknesses of 36 nm and below. In the rubbery state, single-layer supported PS films exhibit an invariance of caging and hence stiffness down to thicknesses of 240 nm and enhancements for films with thicknesses of 165 nm and below. The results on single-layer, supported PS films are in good agreement with other experimental reports of single-layer, supported PS films probing properties related to stiffness using BLS (Cheng 2007, Gomopoulos 2009), picosecond acoustics (Lee 1996), and incoherent neutron scattering (Inoue 2006).

Bilayer film experiments were conducted to investigate the role that the substrate and free-surface interfaces play in perturbing stiffness-confinement behavior. In 20-nm-thick substrate or free-surface layers within bulk bilayer films, caging and hence stiffness is substantially enhanced near the substrate and reduced near the free surface with perturbations near the substrate being significantly stronger. However, when the bilayer film thickness is reduced to 40 nm overall, the 20-nm-thick substrate and free-surface layers exhibit more similar responses indicating that the stiffness gradients from interfaces depend on confinement. Bulk bilayer films were used to characterize length scales associated with stiffness gradients near the substrate and free-surface interfaces. In the glassy state and near T_g, stiffness-gradient length scales in bulk PS films are reasonably estimated to extend ~45 – 85 nm from the substrate and ~35 – 85 nm from the free surface. In the rubbery state, the length scales associated with stiffness gradients in bulk PS films are reasonably estimated to extend ~85 – 200 nm from the substrate and $\lesssim$ 20 nm from the free surface. Thus, because confinement modifies stiffness gradients originating from interfaces, bulk polymer films can exhibit stiffness gradients from

interfaces over length scales that equal or substantially exceed the overall thickness at which

average stiffness-confinement effects become evident in nanoconfined films.

CHAPTER 5

Stiffness Gradients in Glassy Polymer Model Nanocomposites:

Comparisons of Quantitative Characterization by

Fluorescence Spectroscopy and Atomic Force Microscopy

5.1 Introduction

Stiffness-confinement effects in polymers have been investigated using a variety of techniques (Lee 1996, Briscoe 1998, Forrest 1998, Soles 2002, Hartschuh 2004, Stafford 2004, Hartschuh 2005, Inoue 2005, O'Connell 2005, Yoshimoto 2005, Inoue 2006, Stafford 2006, Cheng 2007, Tweedie 2007, Stoykovich 2008, Gomopoulos 2009, Delcambre 2010, Gomopoulos 2010, Xu 2010, Arinstein 2011, Watcharotone 2011, Batistakis 2012, Evans 2012a, Torres 2012, Batistakis 2014, Chung 2014, Askar 2015, Cheng 2015, Chung 2015, Li 2015c, Liu 2015, Xia 2015c, Xia 2015b, Ye 2015, Askar 2016, Brune 2016, Chung 2016, Nguyen 2016, Xia 2016). For a range of polymer/substrate pairs, film stiffness has variably been reported to increase, decrease, or remain constant with decreasing film thickness. In Chapter 4 (Askar 2016), we utilized single-layer PS films to characterize average stiffness-confinement effects and bilayer PS films to characterize perturbations to stiffness associated with substrate and free-surface interfaces. Results from our previous study as well as careful consideration of the vast majority of research literature on PS films (Stafford 2004, Inoue 2006, Stafford 2006, Cheng 2007, Gomopoulos 2009, Torres 2012, Askar 2015, Liu 2015, Askar 2016) reveals general trends regarding stiffness-confinement behavior (Askar 2016). We found that, in general, PS supported on rigid substrates exhibits stiffening with sufficient confinement, and PS supported on non-rigid substrates and free-standing PS films exhibit reduced stiffness with confinement (Askar 2016). By characterizing perturbations to stiffness near interfaces, we demonstrated that polymer film stiffness is subject to combined perturbations from the substrate and free-surface interfaces. In sufficiently thin films, substrate perturbations were observed to dominate over free-surface perturbations and hence stiffening was observed in sufficiently nanoconfined PS films supported

on glass (Askar 2016).

Most studies of polymer stiffness-confinement behavior report average stiffness of polymer films across the entire film thickness; length scales associated with stiffness gradients near interfaces have been characterized experimentally in only three published reports (Cheng 2015, Askar 2016, Brune 2016). When fluorescence spectroscopy was used to characterize stiffness in glassy-state, bulk PS bilayer films supported on glass, stiffness gradient length scales were observed to extend ~45 – 85 nm from the substrate interface and ~35 – 85 nm from the free-surface interface at 60 °C and 100 °C (Askar 2016). Nanoindentation via atomic force microscopy (AFM) along with nanostructural modeling involving finite element analysis has also been utilized to characterize stiffness gradients in polymer films (Cheng 2015, Brune 2016) As reported by Cheng *et al.* (Cheng 2015) with stiffening characterized by 2% or greater enhancements relative to bulk modulus, stiffness gradients extended ~100 nm or ~170 nm from the substrate interface in room-temperature, glassy-state PMMA supported on silica or alumina, respectively. Brune *et al*. (Brune 2016) also employed AFM to characterize the interphase length scale associated with an elastomer film covalently attached to a silicon surface. They reported that the interphase determined at room temperature was 40 nm in extent, with tightly bound rubber of thickness below 10 nm exhibiting a shear modulus that was a factor of ~1000 above that of the bulk elastomer and loosely bound rubber of ~30 nm thickness with shear modulus that was a factor of ~25 above that of the bulk elastomer. Given that the three reports of stiffness gradients in polymer films near substrate interfaces considered different polymers and temperature conditions as well as films with chains freely deposited atop the substrate and those with chains covalently bound to the substrate, it is impossible to draw a detailed comparison among the literature reports. However, each study reported an increase in stiffness or modulus over length scales of several to many tens of nanometers from a rigid substrate.

The goal of this study is to provide clarity regarding length scales associated with stiffness perturbations near a substrate interface by providing the first direct comparison of

results on PS model nanocomposites obtained using two complementary techniques – fluorescence spectroscopy and AFM (Askar 2015, Askar 2016). The fluorescence technique relies on a measurable I_1/I_3 that increases in caged and hence stiff environments. Details regarding principles of fluorescence spectroscopy and motivation for its use to characterize stiffness are provided in the Background and Chapter 3.

Stiffness results are also obtained on the same samples using nanoindentation via AFM, which is a contact method yielding quantitative elastic modulus values from the force-displacement data captured during real-time indentation. With this technique, a nanoscale indenter tip interrogates the interfacial region between surface-exposed polymer and substrate to determine changes in Young's modulus values. When the distance from the indentation point to the polymer-substrate interface is comparable to the size of the AFM tip and indentation depth, a stress field discontinuity will modify the measured modulus (Cheng 2015). Under such conditions, careful consideration of adjacent substrate effects and free-surface effects via nanostructural modeling is employed to draw conclusions from this approach.

Here, we characterize stiffness in model nanocomposites to gain an understanding of stiffness-confinement length scales in supported polymer films as well as in nanocomposites. Related experiments were conducted a decade ago comparing T_g-confinement effects in single-layer model polymer nanocomposites (Rittigstein 2007). Our current study has made refinements over our earlier studies (Cheng 2015, Askar 2016) in the use of fluorescence and AFM as techniques for measuring stiffness gradients in polymeric materials. We advance the fluorescence approach for characterizing stiffness by using trilayer samples in which a 20-nm-thick fluorescence dye-labeled layer is located at various distances from a substrate interface. This allows for direct determinations of stiffness gradient length scales. Similar fluorescence/trilayer experiments were previously conducted to characterize gradient length scales in terms of T_g and physical aging in supported and free-standing polymer films (Ellison 2003, Priestley 2005b, Kim 2011). We advance the AFM approach by utilizing more

comprehensive calibration methods and 3D Finite Element Analysis (FEA) simulations to better characterize the influence of the substrate and other factors on stiffness. Such considerations also enable better determinations of the location of the polymer-substrate boundary compared to previous AFM investigations. Under the specific thermal history conditions chosen for this study, we find that fluorescence and AFM yield consistent results indicating that room-temperature PS model nanocomposites exhibit stiffening from a glass substrate interface over length scales of ~80 to 200 nm, with subtle but important differences in length scales over which stiffness is perturbed depending on whether the system is a confined model nanocomposites or a bulk model nanocomposite.

5.2 Experimental Methods

5.2.1 Materials

Polystyrene (Pressure Chemical, synthesized by anionic polymerization) with nominal molecular weight of 400 kg/mol and dispersity = 1.06 was used as received. Using azobisisobutyronitrile (Aldrich, under the name 2,2'-azobis(2-methylpropionitrile)) as initiator, 1-pyrenylmethyl methacrylate (MPy) (Toronto Research Chemicals) was copolymerized at very low levels with styrene (SigmaAldrich) at 70 °C via bulk free radical polymerization to yield MPy-labeled polystyrene (MPy-PS). The resulting MPy-PS was washed by dissolving in toluene and precipitating in methanol seven times to remove unreacted MPy or styrene monomer. The washed polymer was dried in a vacuum oven for 3 days at 105 °C prior to use. Gel permeation chromatography (Waters 2410, calibrated with PS standards in tetrahydrofuran, refractive index detector) was used to determine that the washed MPy-PS sample had M_n = 370 kg/mol, with dispersity = 1.7. UV-vis absorbance spectroscopy (Perkin Elmer Lambda 35) was used to determine that MPy-PS contains 0.6 mol% pyrene label. Bulk T_g was determined via differential scanning calorimetry (Mettler Toledo DSC822e, second-heat T_g onset method at 10 °C/min heating rate): T_gs were 102 °C for 400 kg/mol PS and 101 °C for 370 kg/mol MPy-PS.

5.2.2 Sample Preparation

Single-layer model nanocomposites were used to characterize average stiffness-confinement behavior. Single-layer model nanocomposites were composed of two MPy-PS layers of equal thickness that were healed together into one consolidated single-layer film. This was achieved by spin-coating two MPy-PS layers of equal thickness onto two cover glass slides (FisherBrand) from toluene (SigmaAldrich) solutions containing 0.5 to 7.0 wt% MPy-PS with spin speeds ranging from 1500 to 3000 rpm. After annealing the glass-supported MPy-PS layers under vacuum at 120 °C for 3 h, the layers were brought together such that the MPy-PS layers were supported on both sides with cover glass. The samples were then annealed under vacuum at 120 °C for 3 h to heal the polymer layers into a single-layer model nanocomposite prior to fluorescence measurements.

Trilayer model nanocomposites were utilized in two ways to characterize stiffness gradients. In both types of trilayer model nanocomposites, 20-nm-thick MPy-PS layers were placed between two unlabeled layers. In one case, the 20-nm-thick reporting layer was centered in the middle of the trilayer nanocomposites (referred to as confined model nanocomposites; discussed in subsection 3.2); and in the other case, the 20-nm-thick reporting layer was located at varying distances from one substrate interface (referred to as bulk model nanocomposites; discussed in subsection 3.3). Trilayer model nanocomposites were prepared by first spin-coating two unlabeled PS layers onto cover glass slides. The 20-nm-thick MPy-PS layers were spun onto freshly cleaved mica and annealed under vacuum at 120 °C for 2 h. After annealing, mica-supported films were transferred at room temperature onto one of the glass-substrate supported films by a water transfer technique (Forrest 1997b). Residual water was evaporated overnight under ambient conditions. The cover-glass-supported layers were then brought together to form trilayer model nanocomposites supported on both sides with cover glass. The samples were annealed in a vacuum oven at 120 °C for 3 h before fluorescence measurement. These annealing conditions were used to ensure that the trilayers healed into consolidated layers without

substantial interlayer diffusion (Whitlow 1991, Ellison 2003, Kim 2011).

5.2.3 Ellipsometry

Film thicknesses of PS and MPy-PS films were measured by spin-coating onto silicon slides (with a native silicon oxide layer) from the same solutions with the same spin speeds at the same time as the films spin-coated onto the glass slides. Measurements were performed at room temperature using spectroscopic ellipsometry (J. A. Woollam Co. M-2000D over a range of wavelengths from 400 to 1000 nm). The ellipsometric angles (ψ and Δ) of incident light reflected off silica-supported PS or MPy-PS films were measured and fitted to a Cauchy layer model to determine thickness. The Cauchy layer model included a PS layer atop a silicon substrate containing a 2-nm-thick silicon oxide surface layer. Film thickness was determined by fitting ψ and Δ to the PS layer in the Cauchy model.

5.2.4 Fluorescence

Fluorescence was used to characterize I_1/I_3 values of the pyrenyl dye labels in MPy-PS, which reflect molecular caging and hence stiffness. After spin-coating and annealing films, emission spectra were collected (Photon Technology International fluorimeter in front-face geometry) at wavelengths from 370 to 405 nm (0.5 nm increment, 1 s integration), with excitation at 324 nm. Excitation and emission slit widths were 0.5 mm (1 nm bandpass). Fluorescence spectra were collected at 25 °C after cooling from 140 °C at 1 °C/min. Once spectra were collected, background noise was measured by acquiring the spectra of unlabeled PS films of thickness similar to the MPy-PS films; the background noise was then subtracted from the fluorescence spectra of the MPy-PS films. The resulting spectra were used to determine the ratio of the first vibronic band peak intensity to the third vibronic band peak intensity (I_1/I_3) of the pyrene-labeled polymer. Peak intensities were calculated from an average of five data points spanning a 2 nm window: I_1 was an average of points between ~376 and ~378 nm and I_3 an average of points between ~387 and ~389 nm. Values of I_1/I_3 at 25 °C were used to compare against normalized modulus results from room-temperature AFM experiments.

5.2.5 Ion-milling

After collecting fluorescence data, the model nanocomposite films were cut in the center

of the substrate with a diamond tip cutter exposing the cross-section of interphase region in

preparation for nanoindentation studies. All samples were annealed at 120 °C under vacuum

overnight after cutting to remove thermal history. The cross section of the exposed surface was

treated with Leica TIC3X broad ion beam slope cutter with relatively low voltage at -25 °C to

create extremely flat surfaces over polymer and substrate domains, producing surface roughness

of ~2 nm. Figure 5-A1 in Appendix A depicts the ion-milling procedure used to prepare samples

for nanoindentation experiments.

5.2.6 Nanoindentation via Atomic Force Microscopy

The AFM mechanical mapping (Bruker, USA, 10 nm radius silicon tip) was conducted

on exposed polymer-substrate surfaces under the PeakForce Quantitative Nanomechanical

Mapping mode. The tips were calibrated on the standard samples from Bruker via a multistep

procedure. First, the deflection sensitivity was calibrated via standard sapphire sample. Second,

the spring constant was calculated utilizing the Sader method, where the q-factor was captured

from high-speed data capture. The tip radius was monitored both before and after tests, to

guarantee that the tip radius to remained the same throughout the test. The probe was used to

indent the sample surface at a frequency of 2 kHz. 128 by 128 points of indentation were

executed on a 400 nm^2 or 800 nm^2 area, so raw data as a force vs. Z-displacement curve of each

indent was captured along with maps of modulus, topography, and adhesion.

5.3 Results and Discussion

5.3.1 Description of Experimental Protocols Used to Characterize Stiffness Gradients

Figure 5-1 illustrates the dual approach in this work: to compare stiffness gradient length

scales characterized using fluorescence spectroscopy and AFM. Experiments are conducted on

polymer model nanocomposites, which are polymer films supported on both sides with
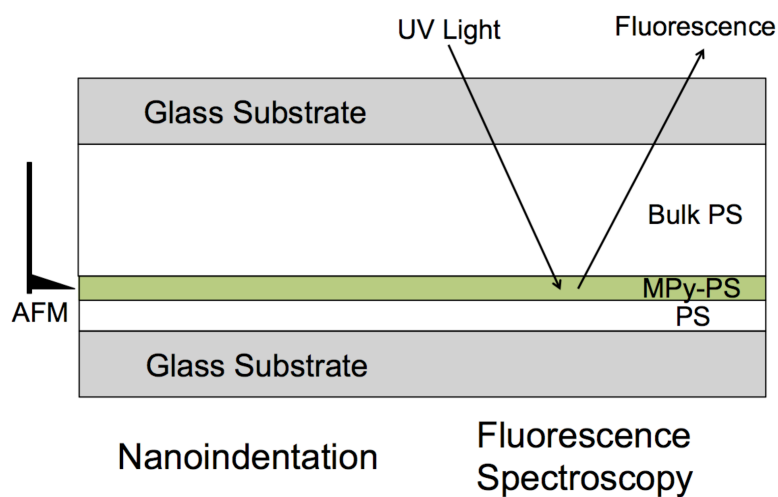
Figure 5-1: Schematic of a model nanocomposite sample depicting the dual approach in this work: to characterize stiffness-confinement effects as a function of overall thickness and as a function of distance from the polymer-substrate interface using AFM and fluorescence on the same samples.

substrates (Rittigstein 2007, Schadler 2007a, Killgore 2011), with the substrate being glass in the current instance. Model nanocomposites are particularly useful samples for basic scientific studies. First, unlike real nanocomposites, model nanocomposites eliminate complications and potential sample-to-sample variations associated with filler aggregates and agglomerates. Second, model nanocomposites provide well-defined interfiller distances with effectively infinite filler surfaces, making model nanocomposites amenable to experimental comparisons done in different laboratories with samples prepared at different times as well as providing relatively simple boundary conditions for comparison with simulations. As demonstrated below, model nanocomposites are also experimentally useful for stiffness gradient characterizations using both fluorescence and AFM on the same samples.

Figures 5-2 and 5-3 illustrate how data are obtained using fluorescence and AFM in this work. Figure 5-2 shows typical fluorescence emission spectra for 20-nm-thick MPy-PS layers within polymer model nanocomposites at 25 °C. Spectra are shown for two model nanocomposites in which the 20-nm-thick MPy-PS layer is located far from the substrate ($h = 1500$ nm) or directly adjacent to the substrate ($h = 10$ nm). Locations of the first and third vibronic band peak intensities are indicated as I_1 and I_3. In Figure 5-2, the spectra are normalized to I_1 for comparisons between the two samples. It has been previously demonstrated that the ratio of intensities I_1/I_3 for MPy-labeled polymer is sensitive to changes in local molecular caging (Askar 2015, Askar 2016) and also allows for determination of T_g values (Kim 2008, Kim 2011, Evans 2012b, Askar 2015, Askar 2016) In particular, I_1/I_3 increases when the excited-state pyrenyl label experiences greater caging in environments that are more stressed or stiff. A comparison of the two spectra reveals that I_3 in the $h = 10$ nm case (with the MPy-PS layer located directly adjacent to the substrate) is lower than I_3 in the $h = 1500$ nm case. Consequently, I_1/I_3 is enhanced at the substrate interface indicating that caging and hence stiffness is enhanced. This result is in agreement with previous single-layer and bilayer fluorescence results in Chapter Chapters 3 and 4 (Askar 2015, Askar 2016). By changing h and maintaining a constant 20-
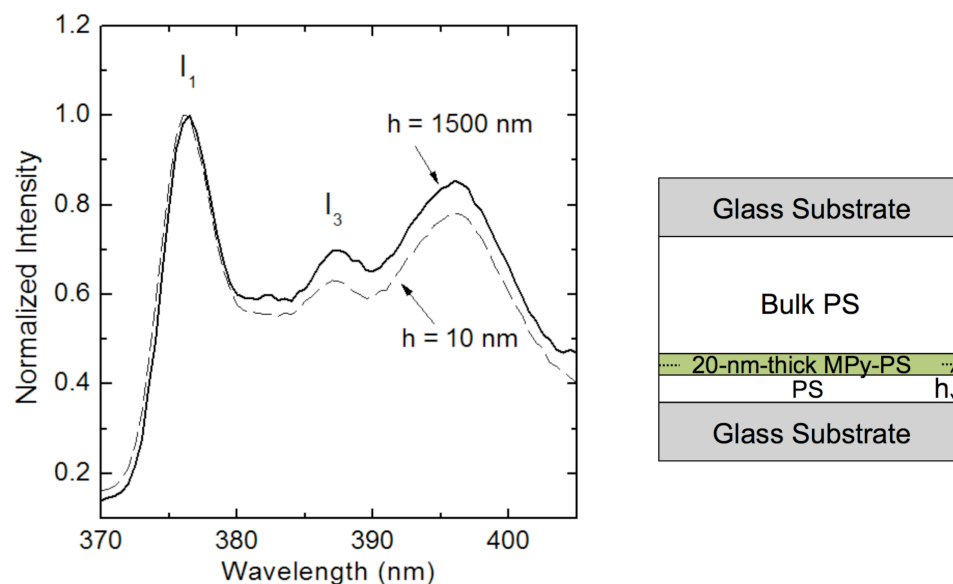
Figure 5-2: Fluorescence emission spectra for model nanocomposites obtained by placing 20-nm-thick MPy-PS layers either 1500 nm from the substrate interface (solid black curve) or directly adjacent to the substrate, *i.e.*, 10 nm from the substrate interface (dashed red curve). Locations of the first and third vibronic band peak intensities, I_1 and I_3, are indicated. Intensities are normalized by the peak intensity associated with I_1. Spectra were collected for samples at 25 °C.
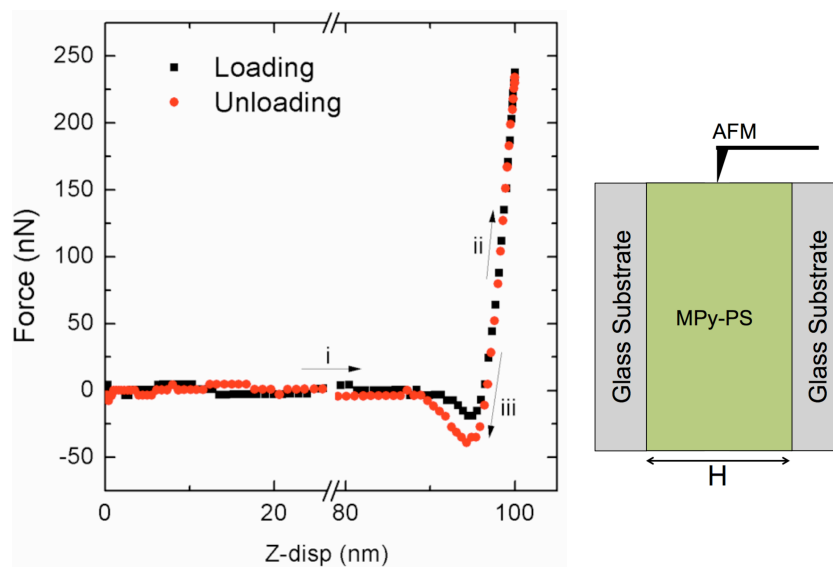
Figure 5-3: A typical force vs. Z-displacement curve from a single indentation cycle. The loading and unloading force-displacement curve presents three scenarios: (i) cantilever approach to sample. (ii) indentation into the sample. (iii) cantilever retracting from the sample surface. Modulus values are determined from the slope of (iii). The schematic depicts how nanoindentation is performed. The sample is situated such that the cantilever moves vertically to interrogate the surface-exposed polymer.

nm-thickness of the MPy-PS layer, stiffness gradients can be characterized in a direct manner using this fluorescence/trilayer technique.

Figure 5-3 shows a typical force vs. Z-displacement curve from a single indentation cycle in AFM quantitative nanomechanical mapping (QNM) nanoindentation. The black squares represent the probe approaching the sample surface from above (i) and then indenting into the sample (ii). The red circles represent the probe retracting from the sample (iii). The small dip where force exhibits negative values is caused by adhesion between the probe and the sample during both snap-in (loading) and separation (unloading). From the force vs. Z-displacement curve of each indent, Derjaguin–Mueller–Toporov models (Eqs. 1 & 2) were used to analyze the AFM data:

$$F - F_{adh} = \frac{4}{3} E_R \sqrt{R(d - d_0)^3} \qquad \text{Eq. 1}$$

$$E_R = [\frac{1 - v_s^2}{E_s} + \frac{1 - v_{tip}^2}{E_{tip}}]^{-1} \qquad \text{Eq. 2}$$

In these expressions, R is the tip end radius, $F - F_{adh}$ is the force on the cantilever minus the adhesion force, $d - d_0$ is the sample deformation, and E_R is the reduced modulus which can be derived from fitting a slope to the unloading curve. Then Young's modulus E_s can be derived from Eq. 2 assuming that the tip modulus E_{tip} is infinite. 30% - 90% of the retracting curves (red circles) were used to calculate the Young's modulus. As the tip moves along the polymer-substrate interface, detailed information of local modulus gradient in the interphase region is obtained. Modulus values are normalized to that obtained in a bulk sample with a modulus of ~2.7 GPa.

5.3.2 Stiffness Gradients in Confined Polymer Model Nanocomposites: Perturbations to Stiffness from Two Substrate Interfaces

Figure 5-4 shows fluorescence I_1/I_3 values as a function of total thickness, H, for single-

layer and trilayer confined model nanocomposites. Single-layer model nanocomposites, which provide the cumulative response across the whole film thickness, exhibit an incipient deviation from bulk behavior at an onset thickness of 266 nm, with the average value outside the range of bulk response and the associated error just overlapping with the range of bulk response. Major enhancements in I_1/I_3 are evident when $H \le 156$ nm. These results indicate that single-layer confined PS model nanocomposites exhibit enhanced caging and hence stiffness-confinement effects at overall thicknesses of roughly a couple hundred nanometers.

In trilayer model nanocomposites, the reporting layer is a 20-nm-thick MPy-PS layer located at the center of the sample. That is, when $H = 520$ nm, the 20-nm-thick MPy-PS layer is sandwiched between two identical neat PS layers, each 250 nm thick. As shown in Figure 5-4, in sufficiently thick model nanocomposites (*e.g.*, $H = 520$ nm), both single-layer and trilayer samples exhibit bulk response within error. In contrast, in sufficiently confined model nanocomposites ($H \le 266$ nm), the center 20-nm-thick layer exhibits enhancements in I_1/I_3 over bulk response, just above bulk when $H = 266$ nm and much more significantly enhanced when $H = 60$ or 156 nm. In order for the center layers of 60-, 156-, and 266-nm-thick model nanocomposites to exhibit stiffening based on fluorescence characterization relative to bulk response, the stiffness gradient in a confined model nanocomposite must be exhibiting a major enhancement from bulk response at a distance of ~80 nm and a perceptible enhancement at a distance of ~135 nm from each substrate interface.

Figures 5-5A and 5-5B show normalized modulus values from AFM as a function of distance in confined model nanocomposites. Data were obtained via nanoindentation across the entire thickness of the model nanocomposite sample from one substrate interface to the other for the same trilayer model nanocomposites characterized in Figure 5-4. Information regarding both the functional form of the stiffness gradient as well as the length scale can be obtained using AFM. Stiffness gradients in model nanocomposites are observed to be approximately symmetric
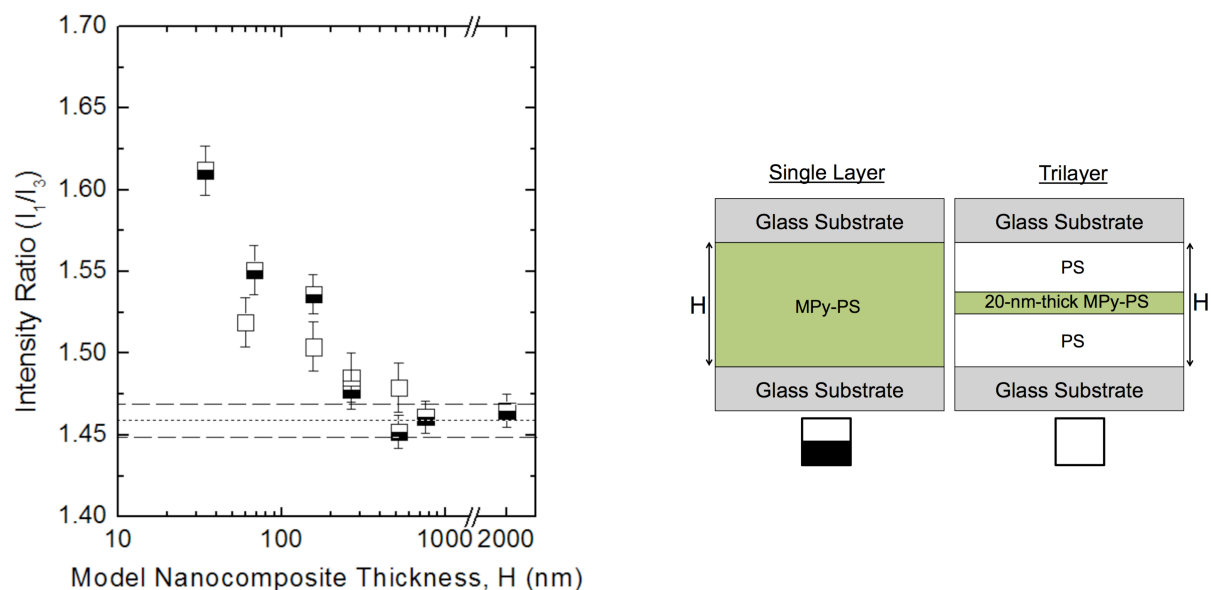
Figure 5-4: Fluorescence I_1/I_3 values as a function of thickness, H, for single-layer model nanocomposites (half-open symbols) and trilayer model nanocomposites (open symbols) at 25 °C. Measurements were taken at 25 °C for comparison with AFM results. Trilayer model nanocomposites are composed of 20-nm-thick MPy-PS layers located at the center of the samples. Dotted and dashed lines represent bulk I_1/I_3 values determined from the average of the three thickest model nanocomposite samples.
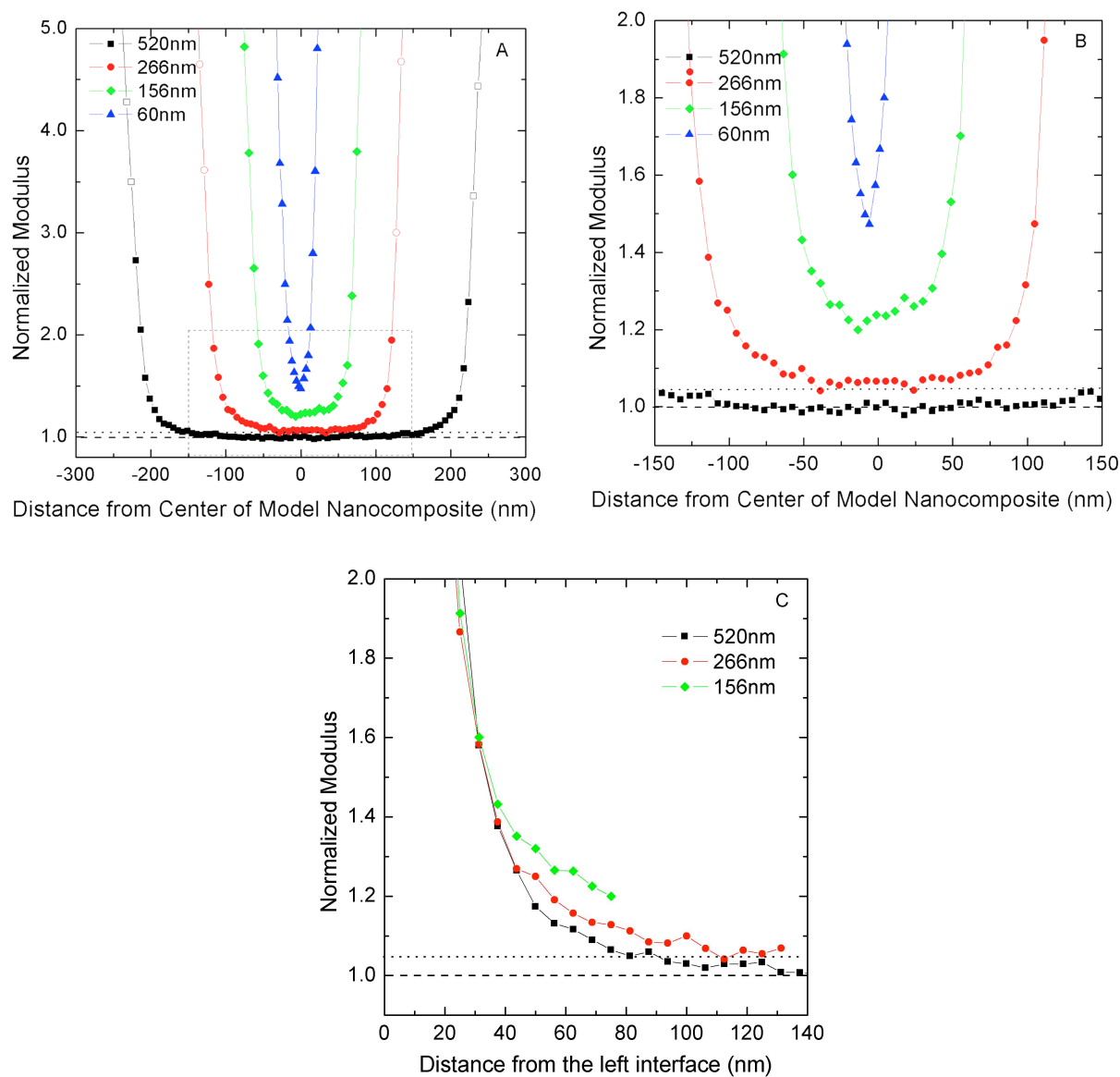
Figure 5-5: A shows normalized modulus as a function of distance from the center of model nanocomposites. The thicknesses indicated in the legends correspond to trilayer model nanocomposites (Figure 5-4, open symbols). B shows the same data as in A but truncated for visual clarity. C shows the same data plotted as a function of distance from one substrate interface. Dashed lines correspond to normalized modulus value of 1.0 determined from a bulk sample. The dotted lines correspond a 5% enhancement relative to bulk modulus.

(see Figure 5-A2 in Appendix A). This result is one internal validation of the method, as the two polymer-substrate interfaces are identical and should perturb the polymer in identical ways. We note that the lack of any change in modulus across the center of the 520-nm-thickt trilayer model nanocomposite demonstrates that the multilayer films were healed properly and that the presence of trace pyrenyl label does not impact the polymer modulus.

In order to identify a stiffness gradient length scale from AFM results, we must identify the level of deviation from bulk response, which we deem to indicate a significant change in modulus. Dotted lines in Figure 5-5 represent a 5% change in normalized modulus (relative to bulk response) determined via AFM; deviations exceeding 5% denote significant changes from bulk behavior.

In the 520-nm-thick model nanocomposite, the polymer exhibits bulk-like behavior near the center of the sample in a region spanning ~300 nm where normalized modulus values are equal to unity. Enhancements in modulus are present only in ~80-nm-thick regions next to the substrate interfaces. When the model nanocomposite is 266-nm-thick, the center of the sample exhibits a quasi-flat middle region spanning ~100 nm. In contrast to the flat region in the 520-nm-thick sample, the average normalized modulus value in the quasi-flat region in the 266-nm-thick sample lies just above the line denoting a 5% change. This demonstrates that the 266-nm-thick sample is sufficiently thin to experience stiffening across the entire thickness due to perturbations originating from both substrates. For model nanocomposites with $H = 156$ nm, the flat middle region present in thicker model nanocomposites largely disappears; all regions of the $H = 156$ nm film exhibit modulus enhancements greater than 20% relative to bulk, thus reflecting the combined perturbations originating from both substrate interfaces. The effects are even stronger in the 60-nm-thick model nanocomposite, with the center of the film exhibiting a ~50% enhancement in modulus relative to bulk.

Figure 5-5C provides results critical to demonstrating that the observed stiffness enhancements in confined model nanocomposites with $H \leq 266$ nm derive from perturbations to

stiffness from each substrate that extend more than half the distance across the film. In particular, relative to the 520-nm-thick model nanocomposite, the 266-nm-thick model nanocomposite exhibits identical stiffness enhancements within error up to 45 nm from a substrate interface. At greater distances from the substrate interface, the 266-nm-thick model nanocomposite exhibits greater normalized modulus values. Similar behavior is observed with the 156-nm-thick model nanocomposite, where enhanced stiffness is observed relative to both the 266- and 520-nm-thick model nanocomposites at distances at least 35 nm from a substrate interface. These results may be understood by considering that perturbations to stiffness propagating from a substrate interface decay as a function of distance from the interface. The decaying function from one interface is negligibly small in comparison to the function from the second interface at distances of several tens of nanometers from the second substrate interface. Thus, within 30 nm of an interface, there is little or no difference in stiffness enhancement as a function of the overall confinement thicknesses in Figure 5-5C. However, the contribution to enhanced stiffness is significant from both interfaces at greater distances from an interface, as much as ~200 nm away from either substrate interface in the case of the 266-nm-thick model nanocomposite.

The combined perturbations from both substrate interfaces also provide an explanation for interesting behavior shown in Figure 5-5B, where the middle ~100 nm region of the 266-nm-thick model nanocomposite exhibits nearly constant modulus enhancement of just above 5% relative to bulk. This behavior can result when the two identical decaying functions expressing how modulus is perturbed as a function of distance from a single substrate interface sum to an approximately identical value in the middle portion of the nanocomposite.

5.3.3 Stiffness Gradients in Bulk Polymer Model Nanocomposites: Perturbations to Stiffness from One Substrate Interface

In this subsection, we extend our characterization to bulk model nanocomposites. In contrast with our confined model nanocomposites described above, the overall thickness of the

PS film located between the two substrates exceeds 1500 nm for all bulk model

nanocomposites. Thus, the measured enhancements in stiffness at a given distance from a

substrate interface is the result of perturbations caused by the near substrate interface; in

addition, these perturbations originating at the substrate interface may be damped or suppressed

by the bulk layer of PS on the other side of the region being interrogated by fluorescence or

AFM.

Figure 5-6A shows I_1/I_3 values determined using fluorescence spectroscopy in 20-nm-

thick layers as a function of distance, h, from the substrate interface in bulk model

nanocomposites. I_1/I_3 values are invariant within error at distances of 170 nm and greater from

the substrate interface and elevated within 80 nm of the substrate interface. These results indicate

that in bulk model nanocomposites the stiffness gradient length scale extends at least 80 nm from

the substrate and are in accord with AFM results for the 520-nm-thick bulk-like model

nanocomposite described in subsection 3.2

Figure 5-6B shows normalized modulus as a function of distance from the substrate

interface, h, obtained from AFM. The error bars represent the standard deviation for at least three

samples. (The shaded region from 0 to 10 nm, *i.e.*, a distance within 10 nm from the substrate

interface, represents the region in which the modulus is significantly overestimated due to the

presence of the adjacent substrate, as determined from a refined 3D Finite Element Model.

Modulus values in the 10 nm region adjacent to the substrate are not reliable. See additional

information in Appendix A, Figures 5-A3, 5-A4, and 5-A5). The data show that modulus

increases from the bulk value with decreasing distance from the glass substrate interface, which

is in agreement with Figure 5-6A. The dashed and dotted lines in the zoomed-in plot represent

the normalized bulk modulus values of unity and a 5% enhancement in normalized modulus, the

latter indicating the condition we employ to indicate a significant change in modulus from bulk

response. Based on the 5% criterion, the stiffness gradient length scale determined using AFM
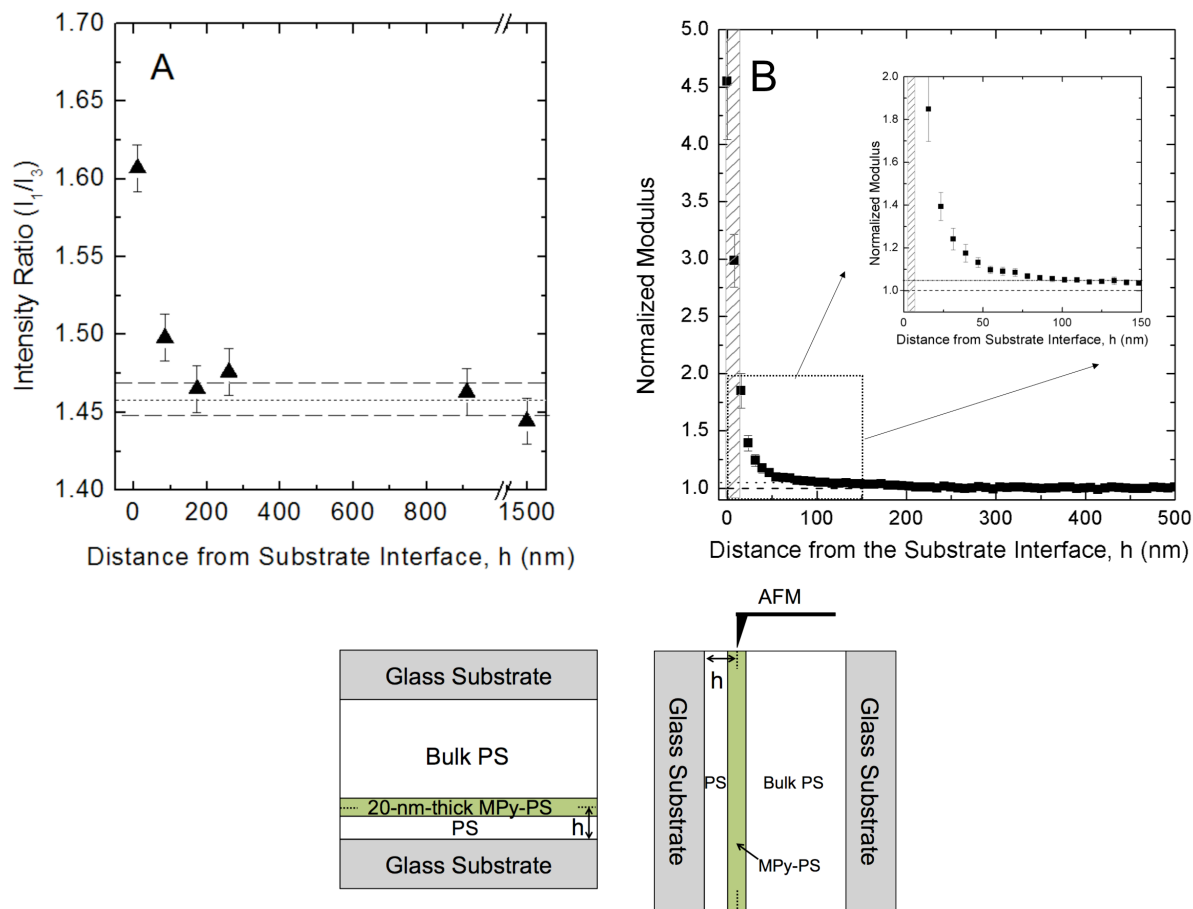
Figure 5-6: (A) I_1/I_3 values as a function of distance from the polymer-substrate interface, h, determined using trilayer model nanocomposites (see schematic) at 25 °C. Dotted and dashed lines correspond to bulk I_1/I_3 determined from the average values of single-layer model nanocomposites with thicknesses exceeding 520 nm (see Figure 5-4). (B) Normalized modulus as a function of distance from the polymer-substrate interface in the bulk PS polymer model nanocomposite (the thickness of the film is ~4 um) determined using nanoindentation via AFM. Dotted lines show normalized modulus values associated with unity and a 5% change.

extends 70 – 85 nm from the substrate interface. This length scale is in good agreement with length scales determined using fluorescence (Figure 5-6A) and also with the AFM determination on the 520-nm-thick bulk-like model nanocomposite in subsection 3.2. Given the agreement in the stiffness gradient length scales determined by both fluorescence and AFM, it can be concluded that, at room temperature, stiffness gradients extend ~80 nm into bulk PS supported on a glass substrate. This gradient length scale is also in good accord with those more roughly determined via fluorescence at 60 and 100 °C from bulk, bilayer PS films supported on glass (Askar 2016). (We note that the stiffness gradient length scale in our model nanocomposites has no bearing on the length scales associated with T_g-confinement effects for supported PS films with one free surface (Keddie 1994a, Keddie 1994b, Ellison 2003, Askar 2015). Also, as characterized by Sharp and Forrest (Sharp 2003), PS model nanocomposites exhibit no T_g-confinement effect down to a thickness of 8 nm, so our determined stiffness-confinement effects are also not attributable or related to any effect of confinement on T_g in model nanocomposites.)

Comparisons of the results from the confined model nanocomposites (Figures 5-4 and 5-5) and bulk model nanocomposites (Figure 5-6) reveal subtle differences. In the confined model nanocomposites, stiffness perturbations from a substrate interface were determined to extend up to ~200 nm from the interface (Figure 5-5C), with slightly enhanced stiffness relative to bulk being evident in the center of 266-nm-thick model nanocomposites (Figures 5-4 and 5-5B). In contrast, in bulk model nanocomposites as well as the 520-nm-thick bulk-like model nanocomposite described in subsection 3.2, stiffness gradients were observed via fluorescence and AFM to extend ~80 nm from the substrate interface under the specific thermal history conditions employed here. (The effects of thermal history on stiffness gradients are investigated in Chapter 6 of this dissertation.) The difference in the length scales associated with perturbed stiffness or the stiffness gradient in confined and bulk model nanocomposites can be attributed to differences in the sample geometries. At a particular location in the confined samples with thicknesses at or below 266 nm, the polymer experiences perturbations to stiffness on each side

over length scales of up to ~200 nm from each interface. In contrast, at a particular location in bulk model nanocomposites, the polymer experiences perturbations to stiffness from one substrate interface on one side, which can be modified, *i.e.*, damped or suppressed, by the presence of bulk polymer on the other side.

Modification or damping of perturbations caused by free surfaces and substrate interfaces has been observed in a number of studies investigating T_g-confinement effects in multilayer polymer films (Ellison 2003, Roth 2007a, Baglay 2015, Evans 2015). In particular, studies of multilayer films of two different, immiscible polymers have shown that the T_gs of nanoscale layers can be tuned by some tens of degrees via adjacent layers. For example, Roth *et al*. demonstrated that "strong reductions in T_g relative to $T_{g,bulk}$ at the free surface of certain types of films can be virtually eliminated" (Roth 2007a) with judicious choice and thickness of the supporting underlayer.

5.3.4 Commentary on the Comparison between Fluorescence Spectroscopy and AFM in Characterizing Stiffness-Confinement Effects

As applied to model nanocomposites, the fluorescence technique is a non-contact method of analysis that interrogates caging and hence stiffness behavior in a nanolayer or across the whole film thickness in such a way that there is no impact of free surfaces on the measurement. In contrast, AFM is a contact method, with the film being indented as a function of distance from a substrate interface, with the indentations always being made on a free surface. (See Figure 5-1.) The differences, non-contact vs. contact and measurement far away from a free surface vs. measurement on a free surface, naturally raised concerns at the onset of this investigation as to whether the results from the two methods could be rationally compared. The evidence provided from our model nanocomposite studies described above indicates that the fluorescence and AFM results on stiffness gradients from a substrate interface are in good qualitative and quantitative agreement. Thus, the differences in the two methods, as practiced and interpreted in our study, do not lead to substantial differences in measured response or apparent behavior. Consequently,

the results of this investigation indicate that fluorescence and AFM, whether employed singly or as complementary techniques, can be used with confidence in appropriately designed studies to characterize stiffness-confinement behavior.

Given the good qualitative and quantitative agreement found between fluorescence and AFM results, further comparisons of the data can be considered. Figure 5-7 shows normalized modulus values from AFM plotted as a function of I_1/I_3 values from fluorescence; these data were obtained from Figures 5-4 and 5-5 where the same confined model nanocomposite samples were characterized using both techniques. Even accounting for the significant error bars associated with I_1/I_3 values, results for the four samples (with total thicknesses of 60 nm, 156 nm, 266 nm, and 520 nm) are consistent with a monotonic relationship between increasing modulus values determined via AFM, up to a 50% increase over bulk modulus, and increasing I_1/I_3 values determined via fluorescence. The relationship shown in Figure 5-7 between normalized modulus and I_1/I_3 values is specific to the conditions tested here because the temperature dependences of normalized modulus and I_1/I_3 values in bulk PS are not identical. This means that the relationship in Figure 5-7 could be used to characterize and understand stiffness-confinement behavior in real nanocomposites at the same temperature condition. Similar relationships but at different temperatures could be developed to characterize and understand stiffness-confinement effects in real nanocomposites at different conditions. For instance, fluorescence could be used to obtain I_1/I_3 values in real nanocomposites as a function of filler loading and temperature that could then be related to modulus values. Yet other studies could be conducted on real nanocomposites that contain nanofiller modified with grafted brushes or hairs, ostensibly to achieve compatibilization. Stiffness gradients within such compatibilized nanocomposites could be characterized by fluorescence data from pyrenyl dye labels located on brush or hair chains (Lan 2015) at a specific distance or number of repeat units from the nanofiller interface and compared to results obtained from dye labels located on polymer chains forming the nanocomposite matrix.
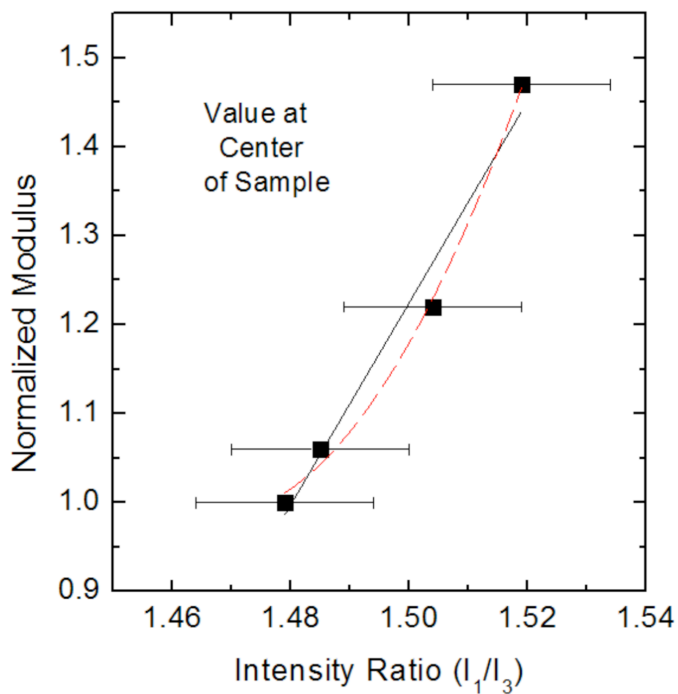
Figure 5-7: Normalized modulus values obtained using AFM plotted as a function of I_1/I_3 values obtained using fluorescence spectroscopy. Data represent normalized modulus and I_1/I_3 values determined from the center of the same polymer model nanocomposites shown in Figures 5-4 & 5-5. The solid line corresponds to a linear best fit and the dashed red line corresponds to a quadratic fit.

The fluorescence/trilayer approach can also be extended to characterize stiffness gradients near free-surface interfaces providing information that contact-based approaches cannot. In addition, as demonstrated in bilayer films in Chapter 4 (Askar 2016), fluorescence is a particularly convenient method to characterize stiffness-confinement effects over a range of temperatures in the polymer rubbery and glassy states. Such characterization by AFM would require the modification of the AFM equipment as a function of temperature.

Although fluorescence can be exploited to investigate a range of polymer systems under different conditions, many tens of samples would be required to obtained detailed information as a function of distance from a substrate interface, such as that provided relatively easily by AFM in Figure 5-5C or Figure 5-6B. In fact, the AFM approach is a particularly convenient method to obtain densely detailed spatial information from a single sample under a particular set of environmental conditions. Another major advantage of the AFM technique over fluorescence is that quantitative modulus values can be obtained, which allows for direct quantitative comparison with other experimental methods.

Regardless of whether results are obtained by one or both methods employed here, the ability to provide detailed characterization of stiffness-confinement behavior in model nanocomposites will be useful for comparison to simulation, thereby providing better fundamental understanding of these important confinement effects. As well, the results from model nanocomposite studies and additional experimental studies on real nanocomposites via fluorescence and/or AFM can be useful not only from a basic scientific standpoint, but also in practical design of real nanocomposites and polymer films leading to optimal properties.

5.4 Conclusions

This study is the first to directly characterize and compare stiffness gradient length scales near substrate interfaces using the complementary approaches of fluorescence spectroscopy, which exhibits sensitivity to stiffness based on changes in spectral shape of fluorescence

emission spectra (I_1/I_3) with molecular caging, and AFM, which yields quantitative determination of modulus. In confined model nanocomposites, the polymer region being interrogated locally via fluorescence or AFM is subject to perturbations originating from two, flat substrate interfaces. In a 266-nm-thick PS model nanocomposite, AFM reveals that perturbations to stiffness extend ~200 nm inside the film from each substrate interface. As revealed by both fluorescence and AFM, the combined effects from each substrate cause the midpoint of the 266-nm-thick nanocomposite to exhibit a small enhancement in modulus relative to bulk, just above 5% as determined by AFM. Fluorescence and AFM results indicate that significantly larger enhancements in stiffness are present at the midpoints of thinner model nanocomposites, with AFM revealing 20-25% and 50% enhancements in modulus relative to bulk in 156-nm-thick and 60-nm-thick nanocomposites, respectively.

In a bulk PS model nanocomposite, with overall thickness substantially exceeding 266 nm, stiffness gradients from a substrate interface are caused by perturbations propagating from the near substrate interface; these perturbations may be damped or suppressed by the bulk layer of PS on the other side of the local region being interrogated. As determined by fluorescence and AFM, stiffness gradients in bulk PS model nanocomposites extend ~80 nm from a glass substrate interface; at significantly greater distances, both methods indicate that local stiffness is equivalent to that of bulk PS. Thus, these two experimental techniques, which are correlated via an increasing monotonic relationship between I_1/I_3 and normalized modulus, provide good qualitative and quantitative agreement regarding stiffness gradient length scales in polymers due to interfacial effects from substrates. Use of fluorescence and AFM, whether singly or in tandem, will lead to improved understanding of how to design polymer nanocomposites and nanostructured polymer films with desired mechanical properties, which is important for a range of technological applications from electronics and healthcare to structures.

5.5 Appendix A – Supporting Materials Pertaining to AFM Characterization of Stiffness

Figure 5-A1 depicts the ion-milling procedure to prepare samples for AFM characterization. Figure 5-A2 compares stiffness gradients characterized from each substrate interface in the model nanocomposites. The functional forms of the stiffness gradients show excellent overlap.

In order to describe the relationship between polymer modulus and its distance to the substrate from the AFM results, it is important to determine the precise location of the boundary between the two domains and also explore the influence of adjacent substrate on polymer modulus. Here, we adopted a 3D finite element analysis (FEA) to locate the boundary position by mimicking the indentation as shown in Figure 5-A3. The geometry of the beam, tip and sample was explicitly sketched and meshed by 3D elements. Oscillatory displacement boundary condition was assigned to the beam, driving the tip to contact with the sample for $5 - 8$ nm indentation depth. The sample was comprised of two layers: silica substrate (73 GPa) and bulk polymer (~2.7 GPa).

During the simulation, the tip moved across the sample and made indents on different sections. At the same time, the reaction force of the film, the bending of the beam, and the displacement of tip were recorded and then extracted from the output of ABAQUS. Elastic moduli at different indent positions were then calculated using the same equations as in the AFM and the result was shown in Figure 5-A4. The output modulus recovers the input modulus, which also validates the model itself. In this simulation, we illustrated that the inflection point was a good choice as the boundary between substrate and polymer films. Also, since this is a model with no interphase presented, the influence of adjacent substrate on the polymer modulus can be
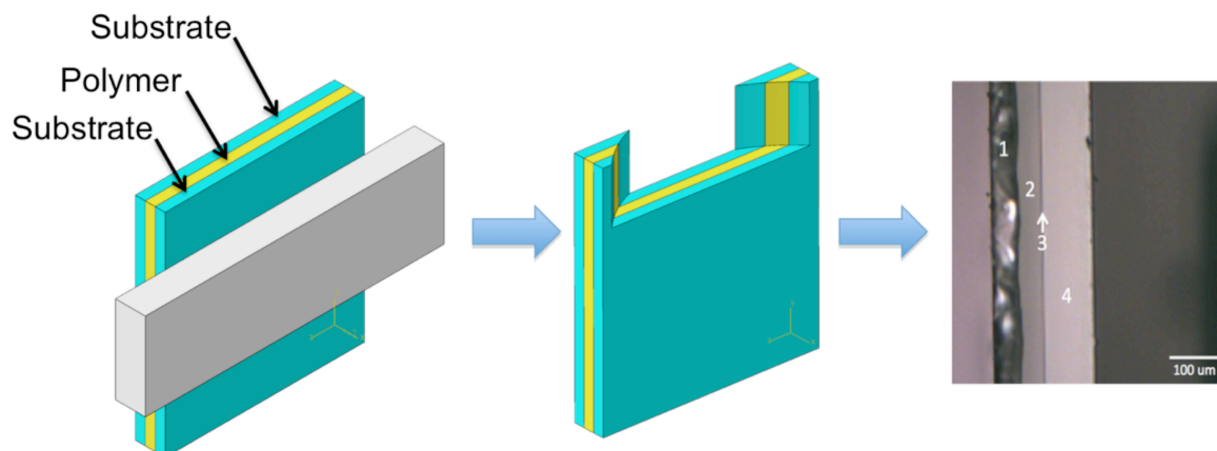
Figure 5-A1: Schematic for the ion-milling procedure (left) and the real optical image of an ion-milled surface (right). The optical image of the model nanocomposite is comprised of four surfaces: (1) un-milled cover glass, (2) milled portion of the same cover glass as (1), (3) polymer, and (4) milled surface of the second cover glass. The thin polymer layer is difficult to discern because of its thickness is very small compared to the scale bar (100 μm).
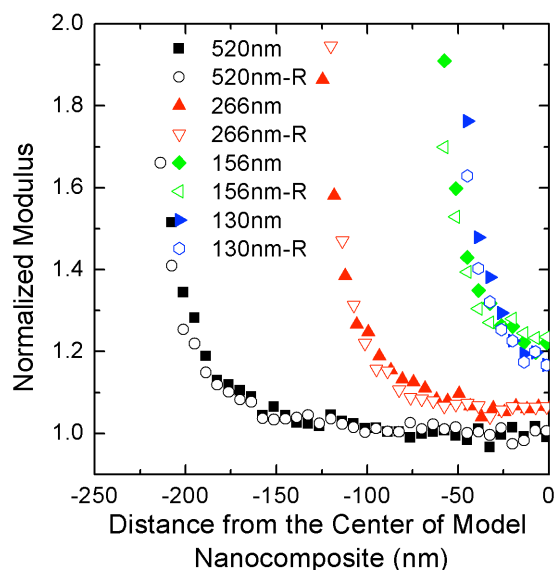
Figure 5-A2: Normalized modulus value as a function of distance from the center of the model nanocomposite. The close and open data points represent the modulus value of left half and right half (reversed) of the film. This mirror image analysis shows that the influence of the substrate on both left and right side are symmetrical as expected.
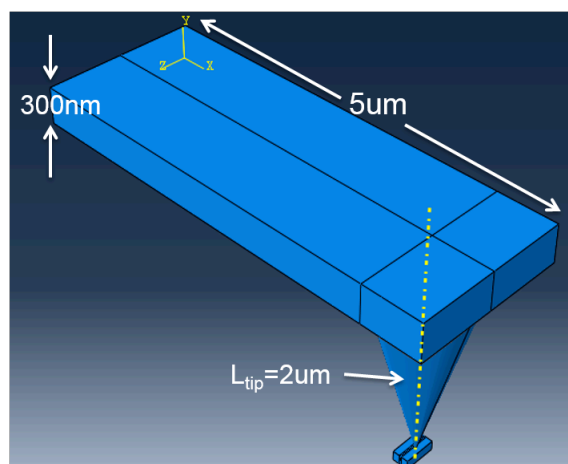
Figure 5-A3: A 3D dynamic model that mimics the AFM mechanical measurement on polymer-substrate system samples was built with Abaqus Finite Element Modeling. The model was comprised with 2 parts: an AFM probe (cantilever and tip) and sample system with polymer and substrate phase.
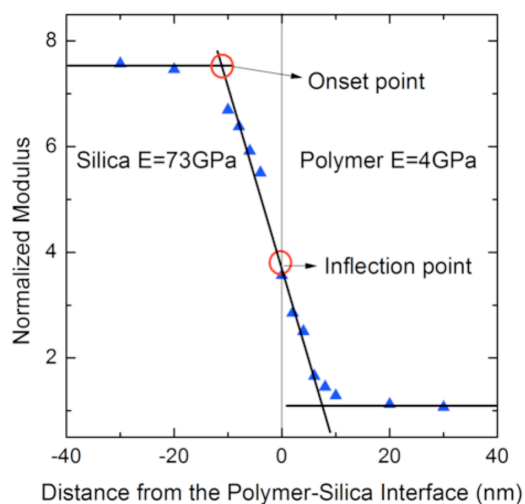
Figure 5-A4: The blue triangle data is the normalized modulus of the simulation result versus distance from the interface between polymer and silica. No interphase is presented in this model. The vertical solid line indicates the boundary between polymer and silica phase. The bold black lines are linear fit for the silica/polymer/boundary regions.

directly captured. Figure 5-A5 below shows the stress field distribution of the interphase

region between glass and polymer, for indentation at 10 nm and 20 nm away from the polymer-

substrate interface. The indentation depth was ~5.5 nm for both cases. From Figure 5-A5A, the

stress field interacts with the substrate region slightly, but the influence is insignificant since

most of the stress concentrated in the polymer. When indenting on the polymer that is 20 nm

away from the substrate (Figure 5-A5B), there is no stress interaction in the glass region. Thus,

paired with the modulus output results from Figure 5-A4, we can summarize that the influence of

adjacent substrate in the modulus of the polymer region becomes insignificant from 10 -15 nm

away from the substrate.
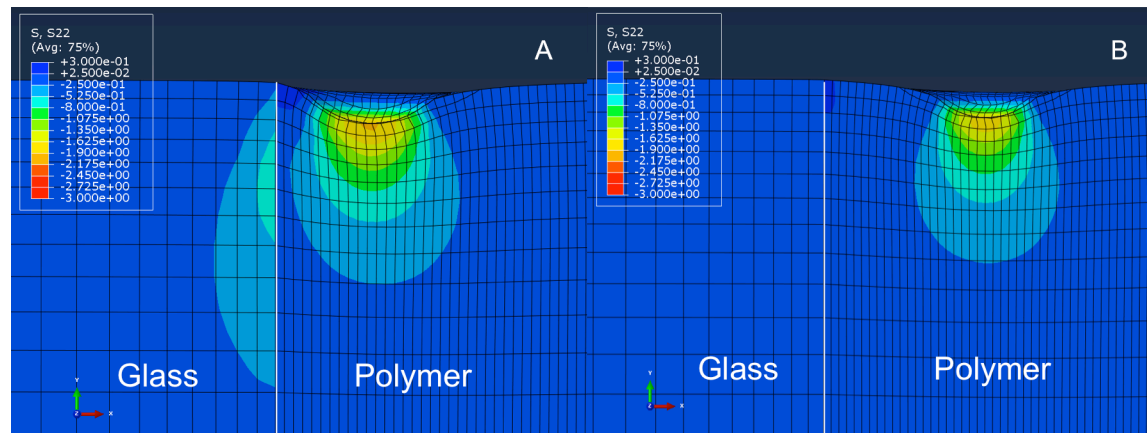
Figure 5-A5: X-Y plane cut of the 3D stress field for the glass-polymer interphase in finite element analysis (FEA). Plot A and B are showing indentations located at 10 nm and 20 nm away from the polymer-substrate interface with an indentation depth of ~5.5 nm.

CHAPTER 6

Effects of Thermal History on Stiffness Gradient Length Scales Extending from a

Polymer-Substrate Interface: Characterization via Fluorescence Spectroscopy

Chapter 5 focused on characterizing stiffness gradients of confined and bulk model

nanocomposites under a specific thermal history. This chapter focuses on characterizing and

understanding how thermal history impacts stiffness gradients in bulk model nanocomposites.

6.1 Introduction

Stiffness-confinement effects in polymer films have been investigated using a range of

techniques (Lee 1996, Briscoe 1998, Forrest 1998, Soles 2002, Hartschuh 2004, Stafford 2004,

Hartschuh 2005, Inoue 2005, O'Connell 2005, Yoshimoto 2005, Inoue 2006, Stafford 2006,

Cheng 2007, Tweedie 2007, Stoykovich 2008, Gomopoulos 2009, Delcambre 2010,

Gomopoulos 2010, Xu 2010, Arinstein 2011, Watcharotone 2011, Batistakis 2012, Evans 2012a,

Torres 2012, Batistakis 2014, Chung 2014, Askar 2015, Cheng 2015, Chung 2015, Li 2015c, Liu

2015, Xia 2015c, Xia 2015b, Ye 2015, Askar 2016, Brune 2016, Chung 2016, Nguyen 2016,

Zhang 2017). Results from our previous study as well as careful consideration of the research

literature on polystyrene (PS) films reveals general trends regarding stiffness-confinement

behavior (Askar 2016). PS films supported on rigid substrates exhibit stiffening with

confinement, and PS films supported on non-rigid substrates as well as free-standing PS films

exhibit reductions in stiffness with confinement (Stafford 2004, Inoue 2006, Stafford 2006,

Cheng 2007, Gomopoulos 2009, Torres 2012, Askar 2015, Liu 2015, Askar 2016). Such

qualitative trends demonstrate that interfaces play a major role in stiffness-confinement behavior.

To achieve a better understanding of stiffness-confinement behavior near interfaces, it is

imperative that length scales associated with stiffness perturbations, *i.e.*, stiffness gradients, are

investigated. The only two experimental techniques that have been used to characterize stiffness

gradients in polymer films and model nanocomposites are nanoindentation via atomic force

microscopy (AFM) and fluorescence spectroscopy (Askar 2015, Cheng 2015, Askar 2016, Brune

2016, Zhang 2017). The fluorescence technique that we have developed relies on the sensitivity of a pyrenyl label, 1-pyrenylmethyl methacrylate (MPy), to local molecular caging. Changes in caging affect the ~nanosecond-time-scale molecular vibrations that are related to the modulus of materials (Sperling 2006). Enhancements in a fluorescence measurable I_1/I_3 indicate enhancements in the local caging around excited-state dyes via enhanced stress and stiffness (Askar 2015, Askar 2016, Zhang 2017). Direct comparisons between AFM and fluorescence have revealed good qualitative and quantitative agreement regarding stiffness gradient length scales characterized near a polymer-substrate interface (Zhang 2017). In that study, comparisons of stiffness gradient length scales determined using AFM and fluorescence were conducted on PS model nanocomposites at room temperature, and we found that stiffness gradients extend ~80 nm near the PS-glass interface in bulk cases. Making direct comparisons between other studies in literature are difficult because of various factors that must be considered such as polymer species, substrate rigidity, free-surface effects, temperature, etc. We note that there is no study that has directly investigated the impact of thermal history on the stiffness-confinement behavior of polymers, leaving a gap in the understanding of how thermal history impacts length scales associated with stiffness-confinement effects as well as understanding differences between studies that may have been done on a number of systems but with different thermal histories prior to measurement.

Here, we provide the first direct demonstration of the impact of thermal history on stiffness gradient length scales in polymer, in this particular case involving characterization in bulk polymer model nanocomposites at room temperature. Model nanocomposites are a useful geometry with which to gain understanding of confinement length scales in real nanocomposites. This has been previously demonstrated with regard to T_g-confinement studies (Rittigstein 2007). Results of this study are compared to those obtained in our previous report (Zhang 2017) on stiffness gradients from a rigid glass substrate obtained in model PS nanocomposites at room temperature; these results are also in good accord with results for bulk PS films supported on one

side by a rigid glass substrate (Askar 2016). The impacts of thermal history investigated in this study have implications for studies in literature that seek to compare length scales associated with stiffness-confinement effects.

6.2 Experimental Methods

6.2.1 Materials

Polystyrene (Pressure Chemical, synthesized by anionic polymerization) with nominal molecular weight of 400 kg/mol and dispersity = 1.06 was used as received. Using azobisisobutyronitrile (Aldrich, under the name 2,2'-azobis(2-methylpropionitrile)) as initiator, 1-pyrenylmethyl methacrylate (MPy) (Toronto Research Chemicals) was copolymerized at very low levels with styrene (SigmaAldrich) at 70 °C via bulk free radical polymerization to yield MPy-labeled polystyrene (MPy-PS). MPy-PS polymer was dissolved in toluene and precipitated in methanol seven times to remove unreacted MPy or styrene monomer. The washed polymer was placed in a vacuum oven for 3 days at 105 °C prior to use. Gel permeation chromatography (Waters 2410, calibrated with PS standards in tetrahydrofuran, refractive index detector) was used to determine that the washed MPy-PS sample had M_n = 370 kg/mol, with dispersity = 1.7. UV-vis absorbance spectroscopy (Perkin Elmer Lambda 35) was used to determine MPy-PS contains 0.6 mol% pyrene label. Bulk T_g was determined via differential scanning calorimetry (Mettler Toledo DSC822e, second-heat T_g onset method at 10 °C/min heating rate): T_gs were 102 °C for 400 kg/mol PS and 101 °C for 370 kg/mol MPy-PS.

6.2.2 Sample Preparation

In this study, trilayer model nanocomposites are used to characterize stiffness gradient magnitudes and length scales. Trilayer model nanocomposites are composed of two unlabeled PS layers and one 20-nm-thick MPy-PS layer in between the unlabeled layers. For each model nanocomposite, the two unlabeled layers (one of varying thickness and the other with a thickness of 1500 nm) are spin-coated onto two cover glass slides (FisherBrand) from toluene

(SigmaAldrich) solutions containing 0.5 to 9.0 wt% PS with spin speeds ranging from 1500

to 3000 rpm. The 20-nm-thick MPy-PS layer is spin-coated from a 0.5 wt% solution of MPy-PS

in toluene onto freshly cleaved mica. The cover-glass-supported PS films and the mica-supported

MPy-PS films were then annealed under vacuum at 120 °C for 3 h. After annealing, mica-

supported films were transferred at room temperature onto one of the substrate supported films

by a water transfer technique (Forrest 1997b). Residual water was evaporated overnight under

ambient conditions. The cover-glass-supported layers were then brought together with the

polymer in the middle to form trilayer model nanocomposites. Trilayer model nanocomposites

were annealed in a vacuum oven at 120 °C for 3 h prior to fluorescence measurements. These

annealing conditions ensured that the trilayers healed into consolidated films without substantial

interlayer diffusion (Whitlow 1991, Ellison 2003, Kim 2011).

6.2.3 Ellipsometry

To measure film thickness, PS and MPy-PS films were first spin-coated onto silicon

slides with a native silicon oxide layer from the same solutions with the same spin speeds at the

same time as the films spin-coated onto the glass slides. Measurements were performed at room

temperature using spectroscopic ellipsometry (J. A. Woollam Co. M-2000D over a range of

wavelengths from 400 to 1000 nm). The ellipsometric angles (ψ and Δ) of incident light reflected

off silica-supported PS or MPy-PS films were measured and fitted to a Cauchy layer model to

determine thickness. The Cauchy layer model included a PS layer atop a silicon substrate

containing a 2-nm-thick silicon oxide surface layer. Film thickness was determined by fitting ψ

and Δ to the PS layer in the Cauchy model.

6.2.4 Fluorescence

Fluorescence was used to characterize I_1/I_3 values as a function of temperature, which

yield information regarding molecular caging and hence stiffness in MPy-PS (Askar 2015, Askar

2016, Zhang 2017); these measurements also yield characterization of T_g (Kim 2008, Kim 2011,

Askar 2015, Evans 2015). After spin coating and annealing films (see section 2.2) emission

spectra were collected (Photon Technology International fluorimeter in front-face geometry) at wavelengths from 370 to 405 nm (0.5 nm increment, 1 s integration), with excitation at 324 nm. Excitation and emission slit widths were 0.5 mm (1 nm bandpass). Spectra were used to determine the ratio of the first vibronic band peak intensity to the third vibronic band peak intensity (I_1/I_3) of the pyrene-labeled polymer. Peak intensities were calculated from an average of five data points spanning a 2 nm window: I_1 was an average of points between 376 and 378 nm and I_3 an average of points between 387 and 389 nm.

Two separate temperature profiles were used to characterize the model nanocomposites. In one, samples were cooled from 140 °C to 25 °C at 1 °C/min. In another, samples were cooled from 140 °C to 60 °C at 1 °C/min followed by taking a final spectrum after rapidly quenching the sample to 25 °C with the aid of liquid nitrogen. For the purposes of this study, data are only shown at 25 °C. Once spectra were collected, background noise was measured by acquiring the spectra of unlabeled PS films of thickness similar to the MPy-PS films and subtracted from the spectra. Values of I_1/I_3 at 25 °C were used to gather stiffness information for the model nanocomposites subjected to the two different thermal history conditions.

6.3 Results and Discussion

Figure 6-1 shows typical fluorescence emission spectra for 20-nm-thick MPy-PS layers located directly adjacent to the substrate interface, *i.e.*, $h = 10$ nm (the center of the 20-nm-thick MPy-PS layer lies 10 nm from the polymer-substrate interface). The plot shows the locations of the first and third vibronic band peak intensities, I_1 and I_3, associated with the spectra for 20-nm-thick substrate-adjacent MPy-PS layers. Spectra were normalized to I_1 for comparison. The spectra shown in Figure 6-1 correspond to samples that are characterized at 25 °C but have different thermal histories. The solid black curve is the spectrum for a model nanocomposite sample that was cooled from 140 °C (40 °C above T_g) to 25 °C at 1 °C/min. The dashed curve is the spectrum for a model nanocomposite sample that was cooled from 140 °C to 60 °C at 1
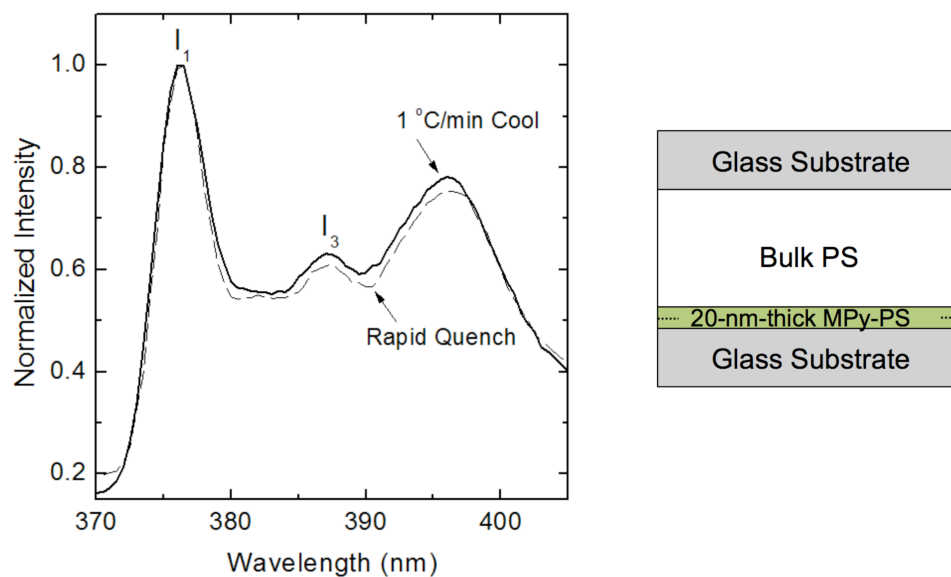
Figure 6-1: Fluorescence emission spectra from 20-nm-thick MPy-PS layers within model nanocomposites at 25 °C (see schematic). Spectra were collected from two samples with differing thermal histories: one cooled from 140 to 25 °C at 1 °C/min (solid black line) and one cooled from 140 °C to 60 °C then rapidly quenched to 25 °C (dashed red line). Locations of the first and third vibronic band peak intensities, I_1 and I_3, are shown. Bulk PS layer has thickness of 1500 nm.

°C/min then rapidly quenched to 25 °C with the aid of liquid nitrogen. We observe from the red dashed line that the rapidly quenched sample exhibits reductions in I_3 relative to the sample cooled from 140 °C to 25 °C at 1 °C/min. The peak intensity values are obtained by averaging the intensities associated with a 2 nm window spanning five data points for both I_1 and I_3. For the spectra shown, I_1/I_3 values are 1.61 for the sample cooled slowly to 25 °C and 1.69 for the sample quenched rapidly to 25 °C. The enhancement in I_1/I_3 in the quenched sample indicates that the sample experiences greater molecular caging and hence greater stress or stiffness (Askar 2015, Askar 2016, Zhang 2017) compared to the sample cooled slowly.

Figure 6-2 shows I_1/I_3 values at 25 °C as a function of distance from the polymer-substrate interface, h. The data were obtained using bulk-like trilayer model nanocomposites, which are composed of 20-nm-thick MPy-PS layers located between two unlabeled PS layers. This fluorescence/trilayer approach has been used previously to characterize stiffness gradients extending from a substrate interface (Zhang 2017). Black triangles correspond to model nanocomposites that were cooled from 140 °C to 25 °C at 1 °C/min, and red squares correspond to model nanocomposites that were cooled from 140 °C to 60 °C at 1 °C/min then rapidly quenched to 25 °C. Comparisons may be made regarding both the magnitude and length scale associated with perturbations to stiffness near the substrate interface. With decreasing distance from the substrate interface, I_1/I_3 values for the rapidly quenched samples increase more significantly than those for the samples cooled slowly. As indicated in Figure 6-1, directly adjacent to the substrate, samples cooled at 1 °C/min to 25 °C exhibit I_1/I_3 values of 1.61, whereas samples quenched to 25 °C exhibit I_1/I_3 values of 1.69.

In a previous study (Zhang 2017), we compared I_1/I_3 values from fluorescence spectroscopy and normalized modulus values from AFM characterized using bulk model nanocomposites at room temperature. Using fluorescence, we found that I_1/I_3 values increased from ~1.50 to ~1.61 (total increase of ~0.11) at distances of 80 nm and 10 nm from the substrate interface, respectively. Using AFM over the same range of distances from the substrate interface,
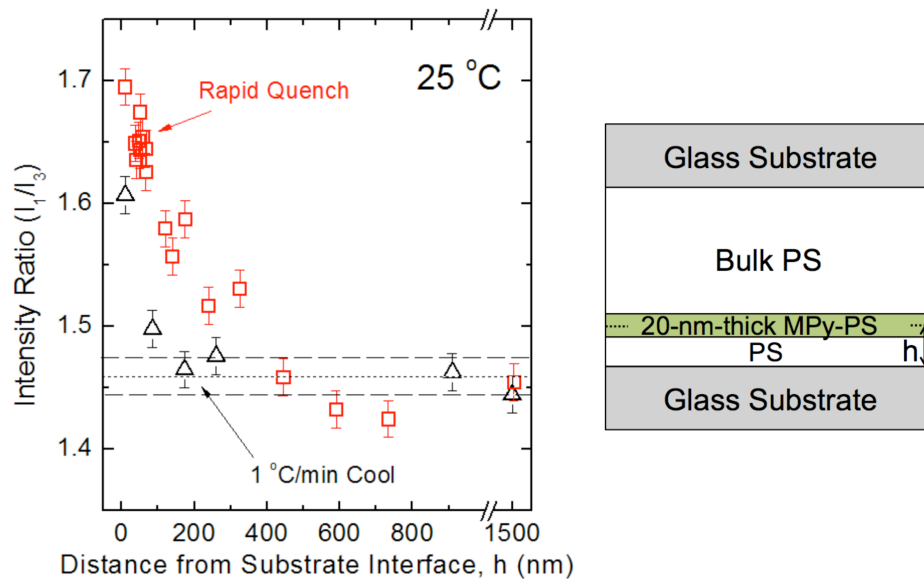
Figure 6-2: I_1/I_3 values as a function of distance from the substrate interface, h, determined using trilayer model nanocomposites at 25 °C. Red squares represent data collected for samples that were quenched rapidly and black triangles represent data for samples that were cooled at 1 °C/min. Dotted and dashed lines correspond to bulk I_1/I_3 values determined from the average values of single-layer model nanocomposites with thicknesses exceeding 1500 nm.

we found that normalized modulus increased by a factor of ~3 (Zhang 2017). Based on the results shown in Figure 6-2, at distances of 80 nm and 10 nm from the substrate interface the quenched samples exhibit I_1/I_3 values that are ~0.10 higher than the slowly cooled samples, indicating that modulus values in quenched samples are approximately a factor of 3 greater than those in slowly cooled samples within 80 nm of the substrate interface. Figure 6-2 also shows that at a distance of ~250 nm from the substrate interface, the quenched samples exhibit I_1/I_3 values that are ~0.05 higher than the slowly cooled samples indicating that modulus values are approximately a factor of 1.5 greater in the quenched samples. This demonstrates that with decreasing distance from the substrate interface, the impacts of thermal history on stiffness become stronger.

In addition to the differences in magnitude, stiffness gradient length scales are also perturbed by thermal history. The sample cooled at 1 °C/min exhibits invariance in I_1/I_3 down to 170 nm and enhancements at 80 nm and below. These data are re-plotted from a previous study investigating bulk PS model nanocomposites at 25 °C (Zhang 2017). The ~80 nm stiffness gradient length scale was determined using both fluorescence and AFM measurement techniques (Zhang 2017). By contrast, the rapidly quenched sample exhibits invariance in I_1/I_3 down to 445 nm and enhancements at 325 nm and below. The ~325 nm length scale in the quenched sample is significantly larger than what was observed for previous AFM and fluorescence results for model nanocomposites for which cooling was done at 1 °C/min down to 25 °C (Cheng 2015, Askar 2016, Zhang 2017), indicating that thermal history plays a major role in impacting the length scale associated with stiffness perturbations near a substrate interface.

The greater magnitude and length scale associated with stiffness perturbations near the substrate for model nanocomposites that were cooled at 1 °C/min from 140 to 60 °C/min and then rapidly quenched to 25 °C can be attributed to additional stresses that are imparted on the samples that were quenched to 25 °C. One source of enhanced stress can be attributed to differences in the thermal expansion coefficients between the rigid glass substrate and PS

(Beaucage 1993, Zoetelief 1996, Zhao 2000, Richardson 2003, Chung 2009, Thomas 2011b).
The thermal expansion coefficient (α) is ~2 x 10^{-4}/K for glassy-state PS (Meng 2009) and ~5 x 10^{-7}/K for silica glass (Roy 1989). As the model nanocomposite is cooled, there is a greater driving force for PS to undergo densification relative to the glass substrate, which generates stresses within the polymer (Beaucage 1993, Zhao 2000, Richardson 2003, Chung 2009, Thomas 2011b).

A second source of enhanced stress in the rapidly quenched samples can be attributed to the inability for the polymer to relax after quenching. This can be rationalized in the following manner. Two major contributors to structural relaxation behavior below T_g include the driving force to achieve equilibrium specific volume (or specific enthalpy) set by the relative difference in temperature between the sample temperature and its T_g as well as the mobility of the polymer at a certain temperature. For example, compared with a polymer at a temperature far below its T_g, a polymer just below its T_g has a relatively higher degree of mobility for structural relaxation, but a small driving force to achieve equilibrium specific volume. A polymer deep below its T_g has a strong driving force to achieve equilibrium specific volume, but significantly reduced mobility. This is why PS exhibits a maximum structural relaxation rate at 60 °C ($T_{g,bulk} - 40$ °C) (Baker 2009). At 25 °C, there is a significant driving force, but suppressed mobility for structural relaxation in both sets of data shown in Figure 6-2. However, the polymer in the slowly cooled sample is afforded some time in which to structurally relax since the cooling rate is 1 °C/min. In the rapidly quenched sample, the polymer experiences a sudden increase in the driving force to achieve equilibrium specific volume coupled with a sudden decrease in the ability to relax, which stresses the polymer to a greater extent. These sources of stress could account for why greater magnitude and length scales associated with stiffness perturbations near a rigid substrate are observed in the quenched sample relative to the sample cooled slowly.

Results from this study have implications for others investigating stiffness-confinement behavior in polymers. Studies investigating stiffness-confinement effects have reported at a

variety of temperatures, yet none of those reports in the literature have addressed differences in thermal history as an important factor. From Figure 6-2, it is apparent that thermal history significantly affects both the magnitude and length scale associated with stiffness gradients from a substrate interface. This result has important implications regarding the ability to rationally compare results in the research literature for similar polymeric systems that have different thermal histories prior to characterization. Future reports on stiffness behavior should clearly describe the thermal histories imparted on the polymers during characterization of confinement effects to enable better comparisons across experimental techniques. In addition, future work should include studies on the effect of thermal history on stiffness gradients extending from the free surface (polymer-air interface) in polymer films.

6.4 Conclusions

This study provides the first demonstration that thermal histories used to prepare samples have impacts on stiffness-confinement effects. These effects are investigated by characterizing both the magnitude and length scales associated with stiffness gradients within room-temperature bulk model PS nanocomposites. Using fluorescence, we observe that both the magnitude and length scales of the perturbations to stiffness near a PS-substrate interface increases in rapidly quenched model nanocomposites compared to model nanocomposites that are cooled slowly. With regard to the length scale, slowly cooled PS samples exhibit stiffening within ~80 nm of a glass substrate interface and rapidly quenched samples exhibit stiffening within ~325 nm of a glass substrate interface at room temperature. The enhancements in stiffness perturbations are attributed to additional stresses that are present in quenched samples. Those stresses originate from two sources: the mismatch in the thermal expansivities between the rigid substrate and polymer as well as the inability of the polymer to relax when quenched to 25 °C. These results indicate that it is necessary for reports in literature to clearly describe the thermal histories used to characterize stiffness-confinement behavior.

CHAPTER 7

Stiffness Gradient Length Scales for

Thin Supported Polystyrene Films and Model Nanocomposites:

Temperature Dependence above and below T_g Characterized by Fluorescence

7.1 Introduction

Stiffness-confinement effects in polymer films have been investigated using a range of techniques for a variety of polymer/substrate pairs and free-standing polymer films (Lee 1996, Briscoe 1998, Forrest 1998, Soles 2002, Hartschuh 2004, Stafford 2004, Hartschuh 2005, Inoue 2005, O'Connell 2005, Yoshimoto 2005, Inoue 2006, Stafford 2006, Cheng 2007, Tweedie 2007, Stoykovich 2008, Gomopoulos 2009, Delcambre 2010, Gomopoulos 2010, Xu 2010, Arinstein 2011, Watcharotone 2011, Batistakis 2012, Evans 2012a, Torres 2012, Batistakis 2014, Chung 2014, Askar 2015, Cheng 2015, Chung 2015, Li 2015c, Liu 2015, Xia 2015c, Xia 2015b, Ye 2015, Askar 2016, Brune 2016, Chung 2016, Nguyen 2016, Xia 2016, Zhang 2017). Among these studies, it has been reported that polymer films exhibit enhancements, reductions, and invariance in stiffness with decreasing thickness. To address the apparent differences in qualitative behavior, we previously utilized a fluorescence technique to determine general trends regarding stiffness-confinement effects in PS films supported on a rigid, glass substrate (Askar 2016). In agreement with the trends reported in Chapter 4, a careful review of previous reports on PS films reveals that the vast majority (Stafford 2004, Inoue 2006, Stafford 2006, Cheng 2007, Gomopoulos 2009, Torres 2012, Askar 2015, Liu 2015, Askar 2016) indicate that with sufficiently reduced thickness, PS films supported on rigid substrates exhibit enhanced stiffness relative to bulk, whereas PS films supported on soft substrates and free-standing PS films exhibit reduced stiffness. These general trends make evident that perturbations to stiffness originating from substrates and free-surface interfaces play key roles in the stiffness-confinement behavior of polymers.

The vast majority of experimental techniques used to characterize stiffness in polymer

films are only capable of characterizing average stiffness-confinement effects as a function of overall film thickness. In addition to characterizing average effects, our fluorescence approach is capable of characterizing stiffness gradients in polymers (Askar 2016, Zhang 2017). This approach relies on the sensitivity of a fluorescence measurable of a pyrenyl dye label (1-pyrenylmethyl methacrylate) (MPy) to changes in local molecular caging (Compared to MPy labels, 1-pyrenylbutyl methacrylate (BPy) labels exhibit reduced sensitivity of I_1/I_3 to local rigidity. Our group has noted the reduction in sensitivity with increasing linkage distance previously (Kim 2008, Evans 2012b).) The fluorescence technique relies on a measurable I_1/I_3 that increases in caged and hence stiff environments. Details regarding principles of fluorescence spectroscopy and motivation for its use to characterize stiffness are provided in the Background and Chapter 3.

The only other experimental technique described in literature that is capable of characterizing stiffness gradients in polymers involves nanoindentation via atomic force microscopy (AFM) (Cheng 2015, Brune 2016, Zhang 2017). Chapter 5 directly compared stiffness gradient length scales characterized using both AFM and fluorescence on the same confined and bulk PS model nanocomposite samples (Zhang 2017). That combined study demonstrated that fluorescence and AFM yield consistent results indicating that room-temperature PS model nanocomposites exhibit stiffening from a glass substrate interface over length scales of ~80 to ~200 nm, with subtle but important differences in length scales over which stiffness is perturbed depending on whether the system is a confined model nanocomposite or a bulk model nanocomposite. The previous characterization was done on PS model nanocomposites at a single temperature (Zhang 2017). More information is required to gain a deeper understanding of stiffness-confinement behavior since many technological applications require the use of polymer nanocomposites at a wide range of temperatures spanning rubbery and glassy states. In addition, Chapter 5 was limited to characterization of stiffness gradients near substrate interfaces. There is no report in literature directly characterizing

stiffness gradients near a free-surface interface.

Here, we utilize our fluorescence technique to understand stiffness-confinement behavior in new ways. First, we characterize polymer model nanocomposites in the glassy state (60 °C), near T_g (100 °C), and in the rubbery state (140 °C). (Given the ~200 ns excited-state lifetime of the pyrenyl dye (Mundra 2007b), yielding a response that is akin to a high frequency measurement, we interpret that the stiffness being probed by the fluorescence method at temperatures some tens of degrees above T_g is akin to a high frequency modulus.) Polymers utilized in coatings, nanostructured films used in manufacture of microelectronics, or nanocomposites are used at a variety of temperatures and the results of this study have implications for stiffness gradient length scales at different temperatures. Second, we characterize stiffness gradients using trilayer films supported on glass to enable characterization of stiffness gradient length scales near the substrate and, for the first time, free-surface interfaces. Third, trilayers provide direct determinations of stiffness gradient length scales that can be compared to previous results (Askar 2016, Zhang 2017).

7.2 Experimental Methods

7.2.1 Materials

Polystyrene (Pressure Chemical, synthesized by anionic polymerization) with nominal molecular weight of 400 kg/mol and dispersity = 1.06 was used as received. Using azobisisobutyronitrile (Aldrich, under the name 2,2'-azobis(2-methylpropionitrile)) as initiator, 1-pyrenylmethyl methacrylate (MPy) (Toronto Research Chemicals) was copolymerized at very low levels with styrene (SigmaAldrich) at 70 °C via bulk free radical polymerization to yield MPy-labeled polystyrene (MPy-PS). The MPy-PS polymer was dissolved in toluene and precipitated in methanol seven times to remove unreacted MPy or styrene monomer. The washed polymer was placed in a vacuum oven for 3 days at 105 °C prior to use. Gel permeation chromatography (Waters 2410, calibrated with PS standards in tetrahydrofuran, refractive index

detector) was used to determine that the washed MPy-PS sample had M_n = 370 kg/mol, with dispersity = 1.7. UV-vis absorbance spectroscopy (Perkin Elmer Lambda 35) was used to determine that MPy-PS contains 0.6 mol% pyrene label, or one label per ~ 170 repeat units. Bulk T_g was determined via DSC (Mettler Toledo DSC822e, second-heat T_g onset method at 10 °C/min heating rate): T_gs were 102 °C for 400 kg/mol PS and 101 °C for 370 kg/mol MPy-PS.

7.2.2 Sample Preparation

In this study, single-layer model nanocomposites are used to characterize cumulative stiffness-confinement behavior across the model nanocomposite thickness. Single-layer model nanocomposites are composed of two MPy-PS layers of equal thickness that are healed together into one consolidated single-layer film. This was achieved by spin coating two MPy-PS layers of equal thickness onto two cover glass slides (FisherBrand) from toluene (SigmaAldrich) solutions containing 0.5 to 7.0 wt% MPy-PS with spin speeds ranging from 1500 to 3000 rpm. After annealing the glass-supported MPy-PS layers under vacuum at 120 °C for 3 h, the layers were brought together so that the MPy-PS layers were supported on both sides with cover glass. The samples were then annealed under vacuum at 120 °C for 3 h to heal the polymer layers into a single-layer model nanocomposite prior to fluorescence measurements.

Trilayer model nanocomposite and trilayer films are used to characterize stiffness gradients. The trilayers are composed of two unlabeled PS layers as well as a 20-nm-thick MPy-PS layer placed between the unlabeled layers. Trilayer model nanocomposites were prepared by first spin coating two unlabeled PS layers onto cover glass slides. The 20-nm-thick MPy-PS layers were spun onto freshly cleaved mica and annealed under vacuum at 120 °C for 2 h. After annealing, mica-supported films were transferred at room temperature onto one of the glass-substrate supported films by a water transfer technique (Forrest 1997b). Residual water was evaporated overnight under ambient conditions. The cover-glass-supported layers were then brought together to form trilayer model nanocomposites supported on both sides with cover glass. With trilayer films, the first unlabeled layer was spin coated directly onto green glass

slides (SigmaAldrich). Glass substrates were thoroughly cleaned by etching in 1.0 M

hydrochloric acid, rinsing with water, and drying prior to submerging in base solution (10 wt%

sodium hydroxide/20 wt% water/70 wt% ethanol). Substrates were rinsed with water and dried

prior to use. The second layer (20-nm-thick MPy-PS) followed by the third layer (unlabeled PS

of varying thickness) was placed atop the first using the water transfer technique above. Residual

water was evaporated under ambient conditions overnight. Both trilayer films and trilayer model

nanocomposites were annealed in a vacuum oven at 120 °C for 3 h before fluorescence

measurement. These annealing conditions ensured that the trilayers healed into a consolidated

film without substantial interlayer diffusion (Whitlow 1991, Ellison 2003, Kim 2011).

7.2.3 Ellipsometry

To measure film thickness, PS and MPy-PS films were first spin coated onto silicon

slides with a native silicon oxide layer from the same solutions with the same spin speeds at the

same time as the films that were spin coated onto the glass slides. Measurements were performed

at room temperature using spectroscopic ellipsometry (J. A. Woollam Co. M-2000D over a range

of wavelengths from 400 to 1000 nm). The ellipsometric angles (ψ and Δ) of incident light

reflected off silica-supported PS or MPy-PS films were measured and fitted to a Cauchy layer

model to determine thickness. The Cauchy layer model included a PS layer atop a silicon

substrate containing a 2-nm-thick silicon oxide surface layer. Film thickness was determined by

fitting ψ and Δ to the PS layer in the Cauchy model.

7.2.4 Fluorescence

Fluorescence was used to characterize I_1/I_3 values, which reflect molecular caging and

hence are related to stiffness, of MPy-PS layers as a function of temperature; these

measurements are also able to yield characterization of T_g (Kim 2008, Kim 2011, Askar 2015,

Evans 2015). After spin coating and annealing films, emission spectra were collected (Photon

Technology International fluorimeter in front-face geometry) at wavelengths from 370 to 405 nm

(0.5 nm increment, 1 s integration), with excitation at 324 nm. Excitation and emission slit

widths were 0.5 mm (1 nm bandpass). Spectra were used to determine the ratio of the first to the third vibronic band peak intensity (I_1/I_3) of the pyrene-labeled polymer. Peak intensities were calculated from an average of five data points spanning a 2 nm window: I_1 was an average of points between 376 and 378 nm and I_3 an average of points between 387 and 389 nm.

Fluorescence spectra were collected after heating the samples to 140 °C and holding for 5 min and then cooling in steps from 140 °C to 60 °C in 5 °C decrements. Before collecting a spectrum, films were held for 5 min at each temperature to enable temperature equilibration. Once spectra were collected, background noise was measured by acquiring the spectra of unlabeled PS films of thickness similar to the MPy-PS films; the background noise was then subtracted from the fluorescence spectra of the MPy-PS films. The resulting spectra were used to determine the ratio of the first vibronic band peak intensity to the third vibronic band peak intensity (I_1/I_3) of the pyrene-labeled polymer. Values of I_1/I_3 at particular temperatures were used to characterize stiffness for each film in the rubbery and glassy states and near T_g.

7.3 Results and Discussion

Figure 7-1 shows a representative fluorescence emission spectrum at 60 °C of a bulk 2000-nm-thick single-layer MPy-PS model nanocomposite supported with two glass substrates. Arrows indicate the locations of the first and third vibronic band peak intensities, I_1 and I_3, respectively. As described in previous reports (Askar 2015, Askar 2016, Zhang 2017), changes in the relative peak intensities I_1/I_3 indicate changes in molecular caging experienced by excited-state pyrenyl dyes. In a more caged environment, *i.e.*, one that is more rigid or stiff, suppression of non-radiative pathways of energy decay cause enhancements in high-energy transitions of electrons from the excited state to the ground state. This is manifested as enhancements in I_1 at the expense of other peak intensities including I_3. Thus, I_1/I_3 increases in stiff environments and decreases in less stiff environments (Askar 2015, Askar 2016, Zhang 2017).

Figure 7-2 shows I_1/I_3 values as a function of total model nanocomposite thickness, H, for
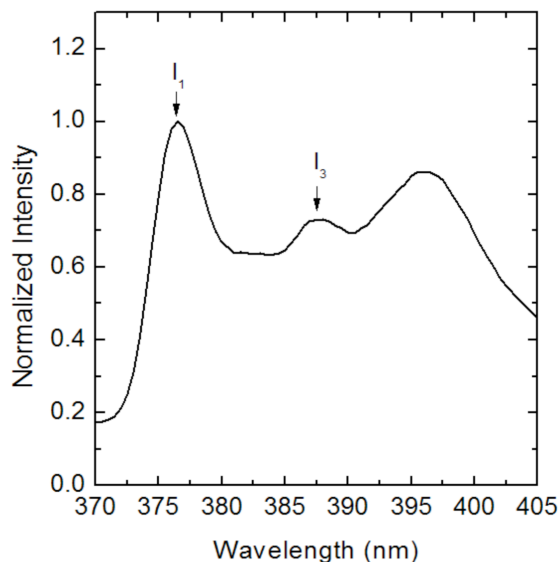
Figure 7-1: Representative fluorescence emission spectrum of a 2000-nm-thick single-layer MPy-PS model nanocomposite 60 °C. Down arrows indicate the positions of the first vibronic band peak intensity (I_1) and the third vibronic band peak intensity (I_3).
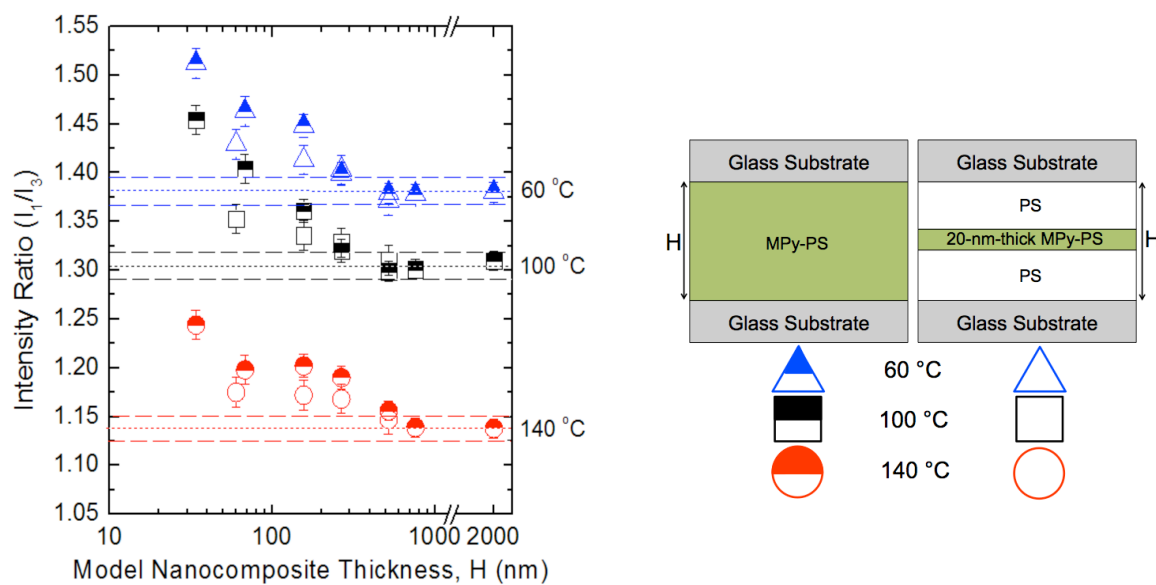
Figure 7-2: I_1/I_3 values as a function of thickness for single-layer model nanocomposites (half-open symbols) and trilayer model nanocomposites (open symbols). Dotted lines correspond to the average values of I_1/I_3 for the three thickest single-layer model nanocomposites and represent bulk values. Dashed lines and error bars indicate the variation in I_1/I_3 associated with slight position changes in the film.

single-layer and trilayer confined model nanocomposites at 60, 100, and 140 °C. The thermal

history used in this chapter involved cooling the samples from 140 to 60 °C at ~1 °C/min. At 60

and 100 °C, single-layer model nanocomposites (half-open symbols), which provide the

cumulative response across the whole film thickness, exhibit an incipient deviation from bulk

behavior at an onset thickness of 266 nm, with the average value just outside the range of bulk

response. Major enhancements in I_1/I_3 are evident when $H \leq 156$ nm. These results indicate that

single-layer, glassy-state confined PS model nanocomposites exhibit enhanced caging and

stiffness-confinement effects at total thicknesses of about a couple hundred nanometers. The

results for the glassy-state samples are in good accord with previous results (Zhang 2017)

obtained in single-layer confined model nanocomposites characterized at 25 °C.

At 140 °C, single-layer model nanocomposites exhibit an incipient deviation from bulk

behavior at an onset thickness of 520 nm. Major enhancements in I_1/I_3 are evident when $H \leq 266$

nm. These results demonstrate that perturbations to stiffness originating from both substrate

interfaces is stronger in the rubbery state relative to the glassy state. This indicates that the rigid

substrate more strongly impacts rubbery-state PS (with lower modulus) compared to glassy-state

PS (with higher modulus).

In trilayer model nanocomposites (open symbols), the reporting layer is a 20-nm-thick

MPy-PS layer located at the center of the sample. That is, when $H = 520$ nm, the 20-nm-thick

MPy-PS layer is sandwiched between two identical neat PS layers, each 250 nm thick. In

sufficiently confined model nanocomposites ($H \leq 266$ nm), the center 20-nm-thick layer exhibits

enhancements in I_1/I_3 over bulk response, just above bulk when $H = 266$ nm and much more

significantly enhanced when $H = 60$ or 156 nm. In order for the center layers of 60-, 156-, and

266-nm-thick model nanocomposites to exhibit stiffening based on fluorescence characterization

relative to bulk response, the stiffness gradient in a confined model nanocomposite must be

exhibiting a major enhancement from bulk response at a distance of ~80 nm and a perceptible

enhancement at a distance of ~135 nm from each substrate interface. More densely detailed

AFM results previously obtained in our combined fluorescence-AFM study demonstrated that stiffness gradients extend ~200 nm from each substrate interface in confined model nanocomposites with overall thickness of 266 nm (Zhang 2017).

Figure 7-3 shows I_1/I_3 values as a function of distance, h, from the polymer-substrate interface characterized using bulk trilayer model nanocomposites at 60 °C, 100 °C, and 140 °C. In contrast with our confined model nanocomposites described above, the overall thickness of the bulk PS model nanocomposites exceeds 1500 nm for all samples. Thus, the measured enhancements in stiffness at a distance h from a substrate interface is the result of perturbations caused by the near substrate interface; in addition, these perturbations originating at the substrate interface may be damped or suppressed by the bulk layer of PS on the other side of the 20-nm-thick reporting layer (Zhang 2017). Under the thermal history conditions employed, stiffness gradients from a substrate interface are observed to extend 80 – 120 nm at 60 and 100 °C and 240 – 325 nm at 140 °C. In our previous report which characterized bulk model nanocomposites at 25 °C, it was found using both AFM and fluorescence that stiffness gradients extend ~80 nm from the substrate interface in bulk PS model nanocomposites (Zhang 2017). This length scale is in good agreement with the present observations in bulk model nanocomposites at 60 °C and 100 °C. The ~80 nm length scale observed for bulk model nanocomposites is shorter than that in confined model nanocomposites. The difference in the length scales associated with stiffness gradients in confined and bulk model nanocomposites can be attributed to sample geometry. At a particular location in the confined samples with thicknesses at or below 266 nm, the polymer experiences perturbations to stiffness on each side over length scales of up to ~200 nm from each interface (Zhang 2017). In contrast, at a particular location in bulk model nanocomposites, the polymer experiences perturbations to stiffness from one substrate interface on one side, which can be modified, *i.e.*, damped or suppressed, by the presence of bulk polymer on the other side.

Modification or damping of perturbations caused by free surfaces and substrate interfaces has been observed in previous studies investigating T_g-confinement effects in multilayer polymer
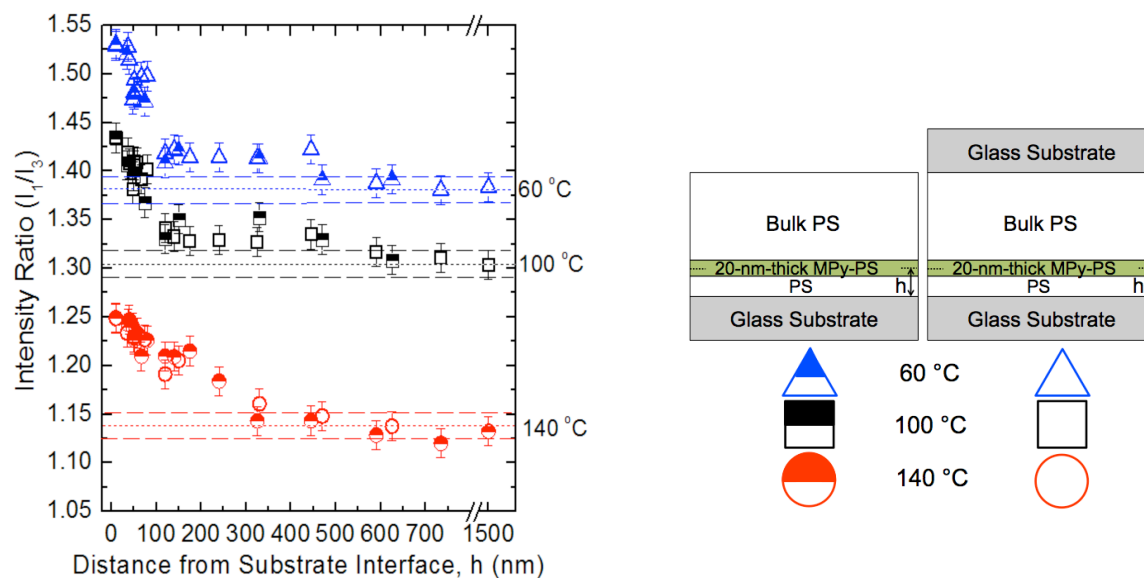
Figure 7-3: I_1/I_3 values as a function of distance from the substrate interface in supported trilayer films (half open symbols) and trilayer model nanocomposites (open symbols). The dotted lines correspond to bulk values of I_1/I_3 determined in Figure 7-2.

films (Ellison 2003, Roth 2007a, Baglay 2015, Evans 2015). In particular, multilayer film studies of two different, immiscible polymers have shown that the T_gs of nanoscale layers can be tuned by tens of degrees via adjacent layers. For example, Roth *et al*. found that "strong reductions in T_g relative to $T_{g,bulk}$ at the free surface of certain types of films can be virtually eliminated" (Roth 2007a) depending on the polymer species and thickness of the supporting underlayer.

Also included in Figure 7-3 are data obtained for bulk trilayer films (with a free surface in addition to a substrate interface) at 60 °C, 100 °C, and 140 °C. For bulk trilayer films, stiffness gradients from a substrate interface extend 75 – 120 nm at 60 °C and 100 °C and 150 – 320 nm at 140 °C. These stiffness gradient length scales are in excellent agreement with those from bulk trilayer model nanocomposites when using the same thermal history conditions, which indicates that the perturbations to stiffness as a function of distance from one substrate interface are the same in bulk films and bulk model nanocomposites. This outcome derives from the fact that the bulk polymer layer separating the region being interrogated from the second interface ensures that the perturbation from that interface, whether a free surface or a substrate, does not extend to the region being interrogated by the dye-labeled layer. The enhancement in stiffness gradient length scale from the substrate in the rubbery state relative to that in the glassy state can be attributed to a greater difference in modulus between the rigid substrate and rubbery-state PS compared to the rigid substrate and glassy-state PS (Askar 2016).

A major advantage of using trilayer films is that it allows for the direct characterization of stiffness gradient length scales near a free-surface interface. Such characterizations are currently not possible using other experimental approaches, including AFM. Figure 7-4 shows I_1/I_3 values as a function of distance, h, from the free-surface interface determined using bulk trilayer films. The I_1/I_3 values decrease with decreasing h, indicating that caging and hence stiffness is reduced at and near the free-surface interface, which is in qualitative agreement with previous fluorescence experiments on bilayer films (Askar 2016). Stiffness gradients are
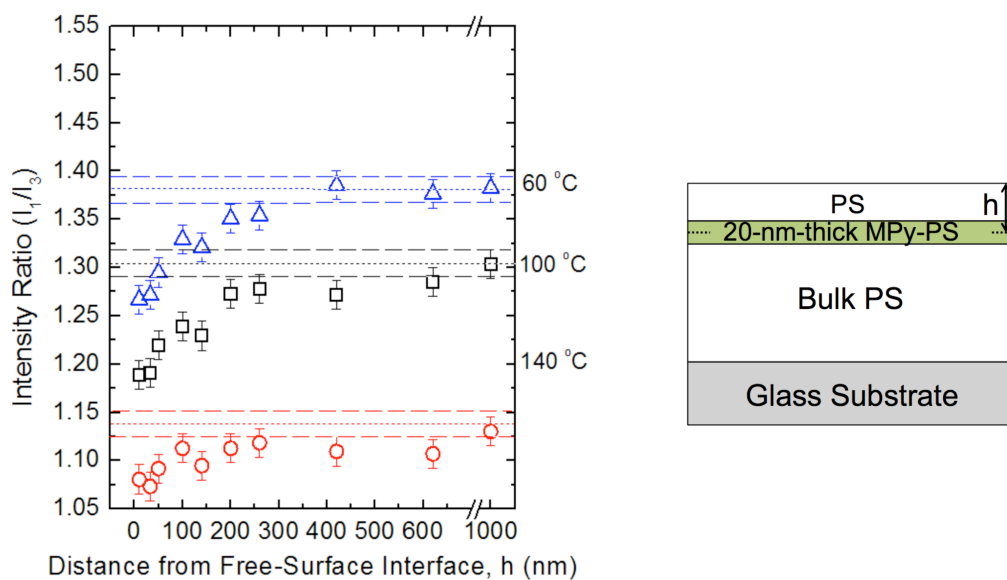
Figure 7-4: Intensity ratio (I_1/I_3) values plotted as a function distance, h, from the free-surface interface. Stiffness gradient length scales associated with the free-surface interface are determined via 20-nm-thick MPy-PS layers within trilayer films. The dotted lines correspond to bulk values of I_1/I_3 determined in Figure 7-2.

observed to extend 140 – 200 nm at 60 and 100 °C and 50 – 100 nm at 140 °C. The greater

stiffness gradient length scale at 60 and 100 °C relative to that at 140 °C, can be rationalized by

the fact that the free surface more greatly perturbs the higher modulus, glassy-state PS than the

lower modulus, rubbery-state PS.

A previous study of single-layer PS films has demonstrated that sufficiently thin films

reflect the combined perturbations to stiffness originating from both the substrate and free-

surface interfaces (Askar 2016). The data obtained in Figures 7-3 and 7-4 can be compared to

understand average stiffness-confinement effects in polymer films. Interestingly, stiffness

gradient length scales near the free surface at 60 °C and 100 °C (140 – 200 nm) are greater than

those near the substrate at 60 °C and 100 °C (75 – 120 nm). From just the length scales, one

might conclude that stiffness reductions would therefore be observed in sufficiently thin films.

However, it is important to note that the magnitude of the perturbations near the substrate is

significantly greater than that near the free surface, and thus overall stiffening is observed across

sufficiently thin polymer films despite the larger length scale associated with free-surface

perturbations to stiffness in glassy-state films. Thus, results from Figures 7-3 and 7-4

demonstrate that both magnitudes and length scales of stiffness gradients as a function of

temperature must be taken into account when considering the origins of cumulative or average

stiffness-confinement behavior.

Length scales associated with stiffness gradients characterized using bilayer films (from

Chapter 4), trilayer films, and trilayer model nanocomposites are summarized in Table 7-1. A

comparison between length scales characterized using trilayer films and bilayer films reveals that

near the substrate, stiffness gradient length scales determined using trilayer films are overlapping

with, yet on average larger than, those estimated using bilayer films. In contrast, near the free

surface, trilayer films yield greater stiffness gradient length scales than those estimated in

Chapter 4 using bilayer films. The reason for the difference can be attributed to how length

scales are obtained using each approach: trilayer films and nanocomposites yield direct

Table 7-1: Stiffness gradient length scales determined using bulk bilayer films, trilayer films, and trilayer model nanocomposites at 140 °C, 100 °C, 60 °C, and 25 °C.

Approximate Stiffness Gradient Length Scales Determined via Fluorescence				
		Bulk Bilayer Films* (nm)	Bulk Trilayer Films (nm)	Bulk Trilayer Model Nanocomposites (nm)
Substrate Interface	140 °C	85 - 200	150 - 320	240 - 325
	100 °C	45 - 85	75 - 120	80 - 120
	60 °C	45 - 85	75 - 120	80 - 120
	25 °C	-	-	~80**
Free-Surface Interface	140 °C	≤ 20	50 - 100	-
	100 °C	35 - 85	140 - 200	-
	60 °C	35 - 85	140 - 200	

*Stiffness gradient length scales estimated using bilayer films are from a previous study (Askar 2016) and involved making inferences to estimate the length scales. In contrast, the trilayer films and nanocomposites employed allow direct characterization of length scales.

**Stiffness gradient length scales determined using bulk trilayer model nanocomposites at 25 °C were obtained in a previous study using both fluorescence and AFM (Zhang 2017).

characterization as a function of length scale whereas inferences must be made to estimate the length scales associated with stiffness gradients in bilayer films.

The data summarized in Table 7-1 demonstrate the impact of temperature on stiffness gradient length scales originating from substrate and free-surface interfaces. We find that near a rigid substrate interface, the stiffness gradient length scale increases when PS is in the rubbery state relative to the glassy state. This can be attributed to the greater difference in modulus between the substrate and rubbery PS relative to the substrate and glassy PS. Near a free-surface interface, the stiffness gradient length scale increases when the PS is in the glassy state relative to the rubbery state, demonstrating that rubbery PS is less susceptible to stiffness perturbations originating from the free-surface interface compared to glassy PS. The results of this study help to understand how the important factors of temperature (related to whether polymer is in a glassy or rubbery state) and type of interface (rigid substrate vs. free surface) impact stiffness-confinement behavior in polymeric materials.

7.4 Conclusions

This study is the first to directly characterize how temperature affects stiffness gradients near substrate and free-surface interfaces in supported polymer model nanocomposites and films supported on glass substrates. Experiments were conducted on both confined and bulk model nanocomposites using a fluorescence methodology that is sensitive to molecular caging and hence to stiffness. At the center of confined model nanocomposites, major enhancement in stiffness relative to bulk response was observed at a distance of ~80 nm and a perceptible enhancement was observed at a distance of ~135 nm from each substrate interface at 60 and 100 °C, conditions at which PS is glassy. In bulk model nanocomposites, stiffness gradients extended ~80 nm from the substrate interface at 60 and 100 °C. The results obtained at 60 and 100 °C were found to be in good agreement with those previously obtained in a fluorescence and AFM study characterizing confined model nanocomposites at room temperature (Zhang 2017). At 140

°C, stiffness gradients were observed to extend 240 – 325 nm from the substrate interface, demonstrating that rigid substrates more strongly perturb rubbery-state PS relative to glassy-state PS.

Bulk trilayer films were used to directly characterize stiffness gradient length scales near substrate and free-surface interfaces. Near a substrate interface, bulk films and bulk model nanocomposites yielded the same stiffness gradient length scales within error, indicating that the perturbations to stiffness as a function of distance from one substrate interface are the same in bulk samples because the bulk polymer layer separating the region being interrogated ensures that the perturbation from the other interface, whether from a free surface or a substrate interface, does not extend to the region being interrogated by the dye-labeled layer. Trilayer films were also used to characterize stiffness gradient length scales near a free-surface interface for the first time. Stiffness gradients extended 140 – 200 nm from the free-surface interface at 60 and 100 °C and 50 – 100 nm from the free-surface interface at 140 °C, demonstrating that the free-surface interface more strongly perturbs glassy-state PS relative to rubbery-state PS. Results of this study help to understand how different interfaces impact the polymer in the rubbery and glassy states. A polymer in its glassy state is more susceptible to stiffness perturbations from a free surface interface or a soft substrate and exhibits stiffness reductions near the interface. A polymer in its rubbery state is more susceptible to stiffness perturbations from a rigid substrate and exhibits stiffness enhancements near the interface. The overall stiffness-confinement behavior of a polymer film reflects the combined perturbations to stiffness originating from both interfaces.

CHAPTER 8

Tuning Stiffness-Confinement Behavior in Supported Polystyrene Films Using Plasticizers: Characterization via Fluorescence Spectroscopy

Previous chapters in this dissertation focus on the stiffness-confinement behavior of neat PS films. The focus of this chapter is to characterize and understand the tunability of stiffness-confinement behavior via addition of plasticizer in glassy- and rubbery-state PS films.

8.1 Introduction

Stiffness-confinement effects in polymer films have been studied using a range of techniques for a variety of neat polymer/substrate pairs (Lee 1996, Briscoe 1998, Forrest 1998, Soles 2002, Hartschuh 2004, Stafford 2004, Hartschuh 2005, Inoue 2005, O'Connell 2005, Yoshimoto 2005, Inoue 2006, Stafford 2006, Cheng 2007, Tweedie 2007, Stoykovich 2008, Gomopoulos 2009, Delcambre 2010, Gomopoulos 2010, Xu 2010, Arinstein 2011, Watcharotone 2011, Batistakis 2012, Evans 2012a, Torres 2012, Batistakis 2014, Chung 2014, Askar 2015, Cheng 2015, Chung 2015, Li 2015c, Liu 2015, Xia 2015c, Xia 2015b, Ye 2015, Askar 2016, Brune 2016, Chung 2016, Nguyen 2016, Xia 2016, Askar 2017a, Askar 2017b, Zhang 2017), yet there is only one experimental report that has characterized the stiffness-confinement effect in thin polymer films containing plasticizers (Torres 2010). The relative lack of basic characterization and understanding of the tunability of stiffness-confinement effects in polymers containing small-molecule diluents has significant technological ramifications. For instance, polymers containing small-molecule photoacid generators are important in the production of microelectronic devices with feature sizes under 100 nanometers (Pohlers 1997, Shirai 1998, Wallraff 1999, Tegou 2004, Chochos 2009).

Several studies have investigated the tunability of glass transition temperature (T_g)-confinement effects in thin polymer films containing plasticizers (Ellison 2004b, Mundra 2007b, Kim 2010). Impacts of plasticizer addition on T_g-confinement behavior have been observed using fluorescence spectroscopy in polystyrene (PS) (Ellison 2004b) and poly(methyl

methacrylate) (PMMA) (Mundra 2007b) films containing dioctyl phthalate (DOP). With decreasing thickness, neat PS films supported on glass or silica substrates exhibit reductions in T_g and neat PMMA films exhibit enhancements in T_g relative to bulk response. T_g-confinement effects in both PS and PMMA are eliminated with the addition of 4 wt% DOP (Ellison 2004b, Mundra 2007b). This tunability was rationalized by the fact that DOP reduces requirements for cooperative motions associated with T_g. Suppression of T_g-confinement effects was also observed via ellipsometry in poly(vinyl acetate) films that absorbed ~0.7 wt% water (Kim 2010).

There is only one experimental report characterizing the effect of plasticizer addition on the stiffness or modulus of nanoconfined polymer thin films. Torres *et al.* (Torres 2010) used a film-wrinkling technique to investigate the modulus of neat PS and PS containing DOP in films supported on low-modulus cross-linked poly(dimethyl siloxane) (PDMS) substrates at room temperature. They reported that neat PS films exhibited reductions in modulus with decreasing thickness. (Torres *et al.* (Torres 2010) did not comment on the impact of the non-rigid PDMS substrate on the stiffness-confinement behavior of the PS films, but other studies investigating stiffness-confinement behavior of polymer films supported on soft substrates report reductions in stiffness with confinement (Stafford 2004, Stafford 2006, Torres 2012). In contrast, studies of polymer films on rigid substrates report increases in stiffness with confinement.) With the addition of 5 wt% DOP, stiffness-confinement behavior was eliminated within error (Torres 2010).

The impacts of plasticizer addition on stiffness behavior in non-thin-film geometries have also been investigated in a few reports. For instance, Sanz *et al.* (Sanz 2008) characterized the stiffness of bulk PS/C_{60} nanocomposites via changes in mean-squared displacement, $<u^2>$, in the glassy and rubbery states. (Vibrational dynamics associated with $<u^2>$ have been correlated with polymer modulus in incoherent neutron scattering studies (Soles 2002, Inoue 2005). At sufficiently low temperatures, $<u^2>$ is inversely proportional to the harmonic force (Soles 2002) or spring constant (Inoue 2005), which scale with polymer modulus. With reduced $<u^2>$,

modulus or stiffness increases.) Due to plasticization from C_{60}, they observed greater enhancements in bulk $<u^2>$ (and hence greater reductions in stiffness (Soles 2002, Inoue 2005, Inoue 2006, Sanz 2008, Askar 2015, Xia 2015b, Ye 2015, Askar 2016)) in the glassy state relative to the rubbery state. However, they did not investigate the impact of temperature on stiffness-confinement behavior of PS films. Whereas plasticizers reduce both T_g and modulus of bulk polymers, anti-plasticizers reduce T_g and enhance modulus of bulk polymers (Riggleman 2007). Delcambre *et al.* (Delcambre 2010) investigated the impacts of anti-plasticizer content on stiffness-confinement behavior of lithographically designed PMMA nanobeams. They observed that adding 5 wt% tris(2-chloropropyl) phosphate maximized the apparent modulus of the nanobeams indicating that small-molecule diluents are effective in tuning the mechanical properties of polymers. Here, we use fluorescence spectroscopy to investigate the tunability of stiffness-confinement behavior of PS films both as a function of DOP content and temperature for films supported on a rigid glass substrate. Detailed explanation for the sensitivity of fluorescence to local changes in molecular caging and hence stiffness is given in the Background and Chapter 3. (Given the ~200 ns excited-state lifetime of the pyrenyl dye (Mundra 2007b), yielding a response that is akin to a high frequency measurement, we interpret that the stiffness being probed by the fluorescence method at temperatures some tens of degrees above T_g is akin to a high frequency modulus.)

8.2 Experimental Methods

8.2.1 Materials

Using azobisisobutyronitrile (Aldrich, under the name 2,2'-azobis(2-methylproprionitrile)) as initiator, 1-pyrenylmethyl methacrylate (MPy) (Toronto Research Chemicals) was copolymerized at very low levels with styrene (SigmaAldrich) at 70 °C via bulk free radical polymerization to yield MPy-labeled polystyrene (MPy-PS). The MPy-PS product was washed by dissolving in toluene and precipitating in methanol seven times to remove all

unreacted MPy or styrene monomer. The washed polymer was placed in a vacuum oven at 105 °C for 3 days prior to use. As determined by gel permeation chromatography (Waters 2410, calibrated with PS standards in tetrahydrofuran, refractive index detector), the washed MPy-PS sample had M_n = 370 kg/mol, with dispersity = 1.7. As determined by UV-vis absorbance spectroscopy (Perkin Elmer Lambda 35), MPy-PS contains 0.6 mol% pyrene label. The bulk T_g was determined via differential scanning calorimetry (Mettler Toledo DSC822e, second-heat T_g onset method at 10 °C/min heating rate): T_g = 101 °C for 370 kg/mol MPy-PS. Dioctyl phthalate (Aldrich) and toluene (SigmaAldrich) were used as received.

8.2.2 Film Preparation

Films of neat MPy-PS or MPy-PS containing DOP were spin coated onto green glass slides from toluene solutions containing 0.5 to 7.0 wt% MPy-PS with spin speeds ranging from 1500 to 3000 rpm. Glass slides were cleaned by etching in 1.0 M hydrochloric acid, rinsing with water, and drying prior to submerging in base solution (10 wt% sodium hydroxide/20 wt% water/70 wt% ethanol). Substrates were rinsed with water and dried prior to use. After spin coating prior to characterization, films were annealed under vacuum at 120 °C for 6 h.

8.2.3 Ellipsometry

To measure film thickness, MPy-PS or MPy-PS containing DOP were first spin coated onto silicon slides with a native silicon oxide layer from the same solutions with the same spin speeds at the same time as the films spin coated onto the glass slides. Measurements were performed at room temperature using spectroscopic ellipsometry (J. A. Woollam Co. M-2000D over a range of wavelengths from 400 to 1000 nm). The ellipsometric angles (ψ and Δ) of incident light reflected off silica-supported PS or MPy-PS films were measured and fitted to a Cauchy layer model to determine thickness. The Cauchy layer model included a PS layer atop a silicon substrate containing a 2-nm-thick silicon oxide surface layer. Film thickness was determined by fitting ψ and Δ to the PS layer in the Cauchy model.

8.2.4 Characterization of T_g and Stiffness via Fluorescence Spectroscopy

Fluorescence was used to characterize I_1/I_3 values, which reflect molecular caging and hence are related to stiffness, of neat MPy-PS films and MPy-PS films containing DOP as a function of temperature. This approach can also be used to obtain measurements of T_g (Kim 2008, Kim 2011, Askar 2015, Evans 2015). After spin coating and annealing films, spectra were collected (Photon Technology International fluorimeter in front-face geometry) at wavelengths from 370 to 405 nm (0.5 nm increment, 1 s integration), with excitation at 324 nm. Excitation and emission slit widths were 0.5 mm (1 nm bandpass). Spectra were used to determine the ratio of the first to the third vibronic band peak intensity (I_1/I_3) of MPy-PS. Peak intensities were calculated from an average of five data points spanning a 2 nm window: I_1 was an average of points between 376 and 378 nm and I_3 an average of points between 387 and 389 nm.

Fluorescence spectra were collected from 140 °C to 60 °C in 5 °C decrements. Before collecting an emission spectrum, films were held for 5 min at each temperature to enable temperature equilibration. Once spectra were collected, background noise was subtracted by acquiring the spectra of unlabeled PS films of thickness similar to the MPy-PS films. Values of I_1/I_3 at specific temperatures were used to characterize stiffness for each film in rubbery and glassy states and near T_g. Lines were fitted to the rubbery and glassy temperature dependences of I_1/I_3 to determine T_g (Kim 2008, Kim 2011, Askar 2015, Evans 2015).

8.3 Results and Discussion

Figure 8-1A shows typical fluorescence emission spectra for neat 1-pyrenylmethyl methacrylate-labeled polystyrene (MPy-PS) at 140 °C, 100 °C, and 60 °C (bottom to top). (Figure 8-1A is re-plotted from Chapter 4 (Askar 2015).) The locations of the first vibronic band peak intensity (I_1) and third vibronic band peak intensity (I_3) are indicated by arrows. The plot shows that the overall intensities of the fluorescence spectra increase with decreasing temperature. As the polymer cools to the rigid, glassy state, vibrational mobility is reduced causing enhancements in fluorescence, with greater enhancements in I_1 at the expense of other
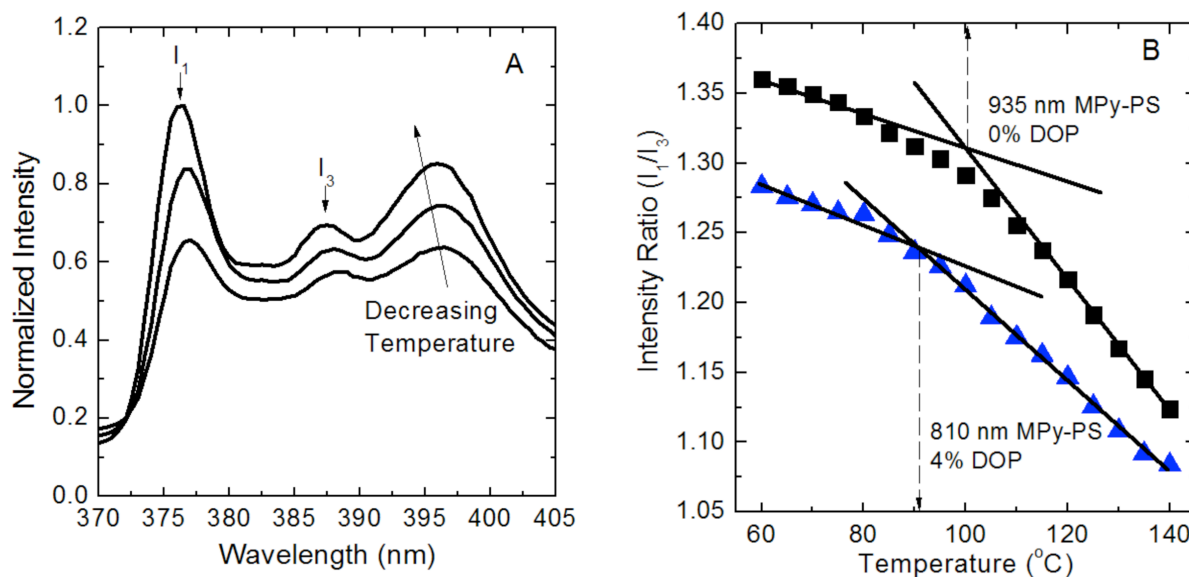
Figure 8-1: (A) shows typical fluorescence emission spectra for a 935-nm-thick MPy-PS film supported on glass at 140 °C, 100 °C, and 60 °C (bottom to top). Arrows indicate the locations of the first (I_1) and third (I_3) vibronic band peak intensities. (B) shows I_1/I_3 values as a function of temperature for a neat, 935-nm-thick MPy-PS film (black squares) and a 810-nm-thick MPy-PS film doped with 4 wt% DOP (blue triangles). Spectra in (A) and black squares in (B) are reproduced from Chapter 4 (Askar 2016).

peaks such as I_3. Thus, the ratio of peak intensities I_1/I_3 increases upon cooling (Askar 2016).

Figure 8-1B shows I_1/I_3 values as a function of temperature for two bulk PS films supported on glass. Plots are shown for a neat, 935-nm-thick MPy-PS film and an 810-nm-thick MPy-PS film containing 4 wt% dioctyl phthalate (DOP). The T_g values of the films are determined by the intersection of lines fitted through the rubbery and glassy temperature dependences of I_1/I_3 (Kim 2008, Kim 2011, Askar 2015, Evans 2015, Askar 2016). (Although T_g values can be determined using intensity ratio values, a more precise approach is to use the temperature dependence of overall integrated intensity. The intensity ratio method is used in this work to gather additional information regarding the polymer stiffness in addition to T_g.) The neat MPy-PS film exhibits $T_{g,bulk} = 101 \pm 1$ °C, in agreement with DSC measurements. The 810-nm-thick MPy-PS film containing 4 wt% DOP exhibits $T_{g,bulk} = 91 \pm 1$ °C, in agreement with both DSC measurements and the $T_{g,bulk}$ value determined in the T_g-confinement study by Ellison *et al.* (Ellison 2004b) (Although not shown in Figure 8-1B, a bulk MPy-PS film doped with 2 wt% DOP exhibits $T_{g,bulk} = 96 \pm 1$ °C.)

Figure 8-1B also shows that the addition of DOP impacts the bulk stiffness of supported PS. Relative to a 935-nm-thick neat PS film, the 810-nm-thick film containing 4 wt% DOP exhibits reduced I_1/I_3 values at all temperatures indicating that caging and hence stiffness is reduced in the plasticized PS. Although not shown, a bulk film containing 2 wt% DOP shows I_1/I_3 values intermediate to those shown in Figure 8-1B. These results are consistent with the notion that molecular caging and hence stiffness are tunable in bulk PS by addition of DOP as plasticizer.

It is important to address other factors that could contribute to I_1/I_3 values obtained from this fluorescence approach. The sensitivity of pyrene molecules to local environments originates from molecular caging around excited-state dyes. In addition to the stiffness or rigidity of the polymer, polarity could also impact caging around the dyes. For instance, seminal studies (Kalyanasundaram 1977, Dong 1984) have shown that increasing solvent polarity causes

enhancements in I_1/I_3 values for pyrenyl dye dissolved in low molecular weight solvent. The molecular caging experienced by the excited-state pyrene molecules originates from an induced dipole-dipole coupling mechanism. With greater coupling in high-polarity solvents, suppression of nonradiative forms of energy decays causes enhancements in I_1 at the expense of other peaks such as I_3 (Kalyanasundaram 1977). In benzene, DOP has a dipole moment of 2.839 D (Yaws 2014), and PS has a dipole moment of 0.36 D (Krigbaum 1959), so the addition of DOP to PS has the potential to increase the overall polarity and cause enhancements in I_1/I_3 (Kalyanasundaram 1977, Dong 1984). However, the results of this study demonstrate that polarity is not impacting the I_1/I_3 values and that the changes in I_1/I_3 reflect changes in stiffness.

Figure 8-2 shows $T_{g,film} - T_{g,bulk}$ values as a function of film thickness for neat PS and PS containing 2 or 4 wt% DOP. These results were used as a control to compare against T_g values reported in the research literature for the same polymer/plasticizer pair (Ellison 2004b). In Figure 8-2, T_g values and experimental error bars are determined from plots like Figure 8-1B. The results indicate that while the $T_{g,bulk}$ values decrease (96 °C for PS with 2 wt% DOP and 91 °C for PS with 4 wt% DOP), T_g-confinement effects can be suppressed and even eliminated with the addition of 4 wt% DOP, in agreement with Ellison *et al.* (Ellison 2004b) It is important to note that the study conducted by Ellison *et al.* (Ellison 2004b) utilized the temperature dependence of overall integrated intensity, whereas this study utilizes the temperature dependence of I_1/I_3. The good accord with the results from Ellison *et al.* (Ellison 2004b) indicates that the intensity ratio method is effective in characterizing the tunability of polymer properties with the addition of DOP as a plasticizer.

Figure 8-3 shows I_1/I_3 values for bulk PS films as a function of DOP content and temperature. Data are shown for films at 60 °C, 100 °C, and 140 °C (for the thermal history described in the experimental section). The dotted and dashed lines correspond to the I_1/I_3 values determined for a bulk PS film containing 30 wt% DOP and represent a case in which the impact
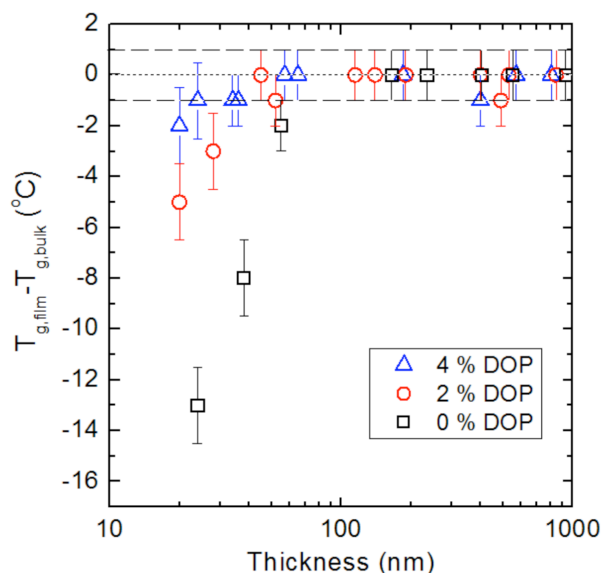
Figure 8-2: $T_{g,film} - T_{g,bulk}$ values as a function of thickness for supported MPy-PS films doped with 4 wt% DOP (blue triangles), 2 wt% DOP (red circles), and 0 wt% DOP (black squares). $T_{g,bulk}$ values for MPy-PS doped with 4 wt%, 2 wt%, and 0 wt% DOP are 91 °C, 96 °C, and 100 °C. Error bars are determined from the range of plausible values for T_g determined using plots like Figure 8-1B.
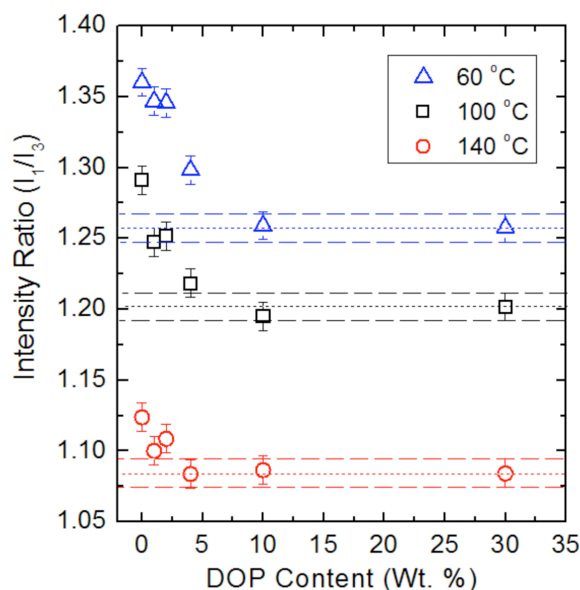
Figure 8-3: I_1/I_3 values as a function of DOP content for bulk single-layer films of MPy-PS with film thicknesses exceeding 800 nm. Data are shown 60 °C (blue triangles), 100 °C (black squares), and 140 °C (red circles). Dotted and dashed lines are shown for the I_1/I_3 values of bulk MPy-PS doped with 30 wt% DOP. Data points overlapping with the dotted and dashed lines indicate the DOP concentrations at which I_1/I_3 values (and thus stiffness) saturate.

of DOP is saturated. At all tempeatures, I_1/I_3 values decrease with increasing DOP content then reach plateau values. The reductions in I_1/I_3 values indicate reductions in molecular caging and hence stiffness. In agreement with Figure 8-1B, I_1/I_3 values decrease with increasing DOP concentration demonstrating that DOP polarity is not playing a major role in the reported values (which would lead to I_1/I_3 values increasing with increasing DOP content). Figure 8-3 also shows that whether the polymer is in the glassy or rubbery state affects how strongly DOP modifies polymer stiffness. For instance, I_1/I_3 values become invariant with DOP content between 10 wt% and 30 wt% DOP at 60 °C and between $1 - 2$ wt% and 30 wt% DOP at 140 °C. These results indicate that added DOP has less impact on molecular caging in the rubbery state relative to the glassy state in bulk polymer. At 140 °C, the excited-state pyrenyl labels experience the least caging (lowest I_1/I_3) for the three temperature studied and are therefore are the least susceptible to further reduction in caging by the addition of DOP as a plasticizer. Conversely, at 60 °C the excited-state pyrenyl labels experience the greatest caging (highest I_1/I_3) and are the most susceptible to reductions in caging from DOP. These results are in agreement with an incoherent neutron scatting study (Sanz 2008) of $<u^2>$ in PS containing C_{60}. Sanz *et al*. (Sanz 2008) found greater enhancements in $<u^2>$ (and thus greater reductions in stiffness (Soles 2002, Inoue 2005, Inoue 2006, Sanz 2008, Askar 2015, Xia 2015b, Ye 2015, Askar 2016)) in the glassy state relative to the rubbery state for PS containing up to 4 wt% C_{60}.

We investigated PS films at up to 30 wt% DOP content to study an extreme case and to observe the DOP content at which invariance in the value I_1/I_3, and hence in caging and stiffness, occurs with increasing DOP content. Related behavior is evident in the film-wrinkling study of room-temperature, PDMS-supported bulk PS films conducted by Stafford *et al*. (Stafford 2004) They observed a sigmoidal decrease in bulk polymer modulus with increasing DOP content up to 40 wt% with reductions in modulus values saturating or exhibiting a near invariance with increasing DOP content at $30 - 40$ wt% DOP in the room-temperature films.

The tunability of stiffness-confinement effects on glass-supported PS films is illustrated

in Figure 8-4, which shows I_1/I_3 values as a function of thickness. The neat PS case shown in Figure 8-4A is re-plotted from Chapter 4 (Askar 2016). As reported previously for neat PS films (Askar 2016), at 60 °C and 100 °C, I_1/I_3 values are invariant down to film thicknesses of 63 nm and are elevated at thicknesses of 36 nm and below. At 140 °C, I_1/I_3 values are invariant down to film thicknesses of 240 nm and elevated at thickness of 165 nm and below. The greater stiffness-confinement length scale in rubbery-state PS films was attributed to greater perturbations to caging originating from the substrate in the rubbery-state PS relative to the glassy-state PS, which is associated with the greater difference in modulus between the rigid glass substrate and a rubbery-state PS film relative to the rigid glass substrate and a glassy-state PS film.

Figure 8-4 also shows that length scales for single-layer film thickness associated with stiffness-confinement effects decrease with increasing DOP content. At 140 °C, PS with 2 wt% DOP exhibits an invariance in molecular caging and hence stiffness down to a film thickness of 115 nm and stiffening for thicknesses at or below 52 nm, and PS with 4 wt% DOP exhibits an invariance in stiffness down to a thickness of 57 nm and stiffening for thicknesses at or below 38 nm. The stiffness-confinement length scales for polymers at the three different temperatures are summarized in Table 8-1. Figure 8-4 and Table 8-1 show that while there are reductions in the critical length scales associated with stiffness-confinement effects at 60 °C and 100 °C, the greatest reduction in critical length scale is observed at 140 °C. It is possible that the enhanced tunability observed at 140 °C arises from the fact that the stiffness-confinement length scale is the largest at that temperature. At 60 °C and 100 °C, the critical length scales are relatively short, thereby limiting the effects of plasticization with the addition of DOP. Nevertheless, it is clear that the suppression of the stiffness-confinement effect in polymer films supported on rigid substrates occurs for rubbery-state and glassy-state polymer when plasticizer is added at low levels.

Another possible explanation for the tunability of stiffness-confinement length scale can
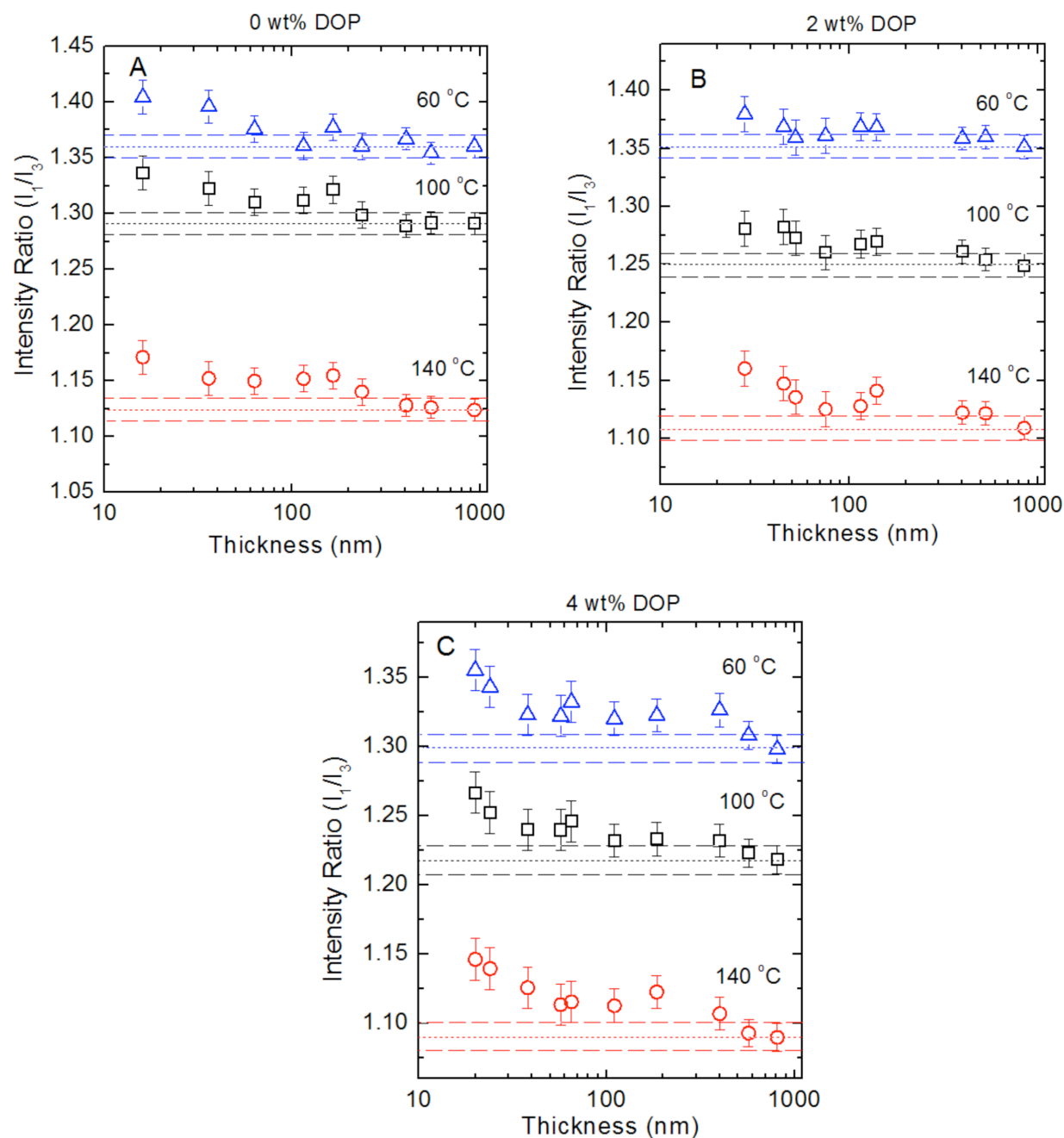
Figure 8-4: I_1/I_3 values as a function of film thickness for neat MPy-PS films (top left) as well as MPy-PS films doped with 2 wt% DOP (top right) and 4 wt% DOP (bottom). I_1/I_3 values are shown at 60 °C (blue triangles), 100 °C (black squares), and 140 °C (red circles). Dotted and dashed lines indicate the values of I_1/I_3 for the thickest films in each data set. Data shown for neat MPy-PS were obtained from Chapter 4 (Askar 2016).

Table 8-1: Summary of stiffness-confinement length scales for neat MPy-PS (Askar 2016) and MPy-PS doped with 2 wt% and 4 wt% DOP.

DOP Content (wt%)	Stiffness-Confinement Length Scale (nm)		
	60 $^{\circ}$C	100 $^{\circ}$C	140 $^{\circ}$C
0	36 - 63	36 - 63	165 - 240
2	28 - 45	45 - 52	52 - 115
4	24 - 38	24 - 38	38 - 57

be attributed to how effectively DOP impacts the perturbations to caging originating from the interfaces. We have demonstrated in Chapter 4 and 7 (Askar 2016, Askar 2017b) that perturbations to caging and hence stiffness are greater at the substrate than at the free-surface interface. In sufficiently thin neat PS films, the critical length scales associated with substrate perturbations were determined to be significantly greater than those associated with free-surface perturbations at 140 °C, which accounts for why the critical stiffness-confinement length scale in single-layer PS films supported on rigid substrates is 165 – 240 nm at 140 °C compared to 36 – 63 nm at 60 °C and 100 °C (Askar 2016). Relative to neat PS, we find that the thickness length scale decreases most significantly at 140 °C with the addition of DOP at 4 wt%. The reduction in the length scale to 38 – 57 nm at 140 °C suggests that plasticization impacts the perturbations to stiffness originating from the substrate. Further investigation into how plasticization impacts stiffness perturbation length scales from substrate and free-surface interfaces is warranted using multilayer films in which only one of the layers is labeled with trace levels of the pyrenyl dye.

Comparisons from this study may be made with a study by Torres *et al*. (Torres 2010) who reported modulus-confinement results from film-wrinkling experiments for room-temperature, PDMS-supported PS films containing 1 wt%, 3 wt%, and 5 wt% DOP. Although the PS films in that study exhibited reductions in modulus with decreasing film thickness due to perturbations from the soft (rather than rigid) crosslinked PDMS substrate, comparisons may be made regarding the tunability of stiffness-confinement behavior. They found that 1 wt% and 3 wt% DOP concentrations were sufficient to tune stiffness-confinement effects, and that 5 wt% DOP was sufficient to eliminate stiffness-confinement effects within error down to thicknesses of ~10 to 20 nm. Our results are in reasonable agreement, with addition of 4 wt% DOP nearly eliminating stiffness-confinement behavior in PS films on rigid substrates at 60 and 100 °C. Interestingly, our results indicate that despite the reduction in the critical thickness length scale, stiffening still persists in the thinnest films for PS supported on a rigid glass substrate. Our results further suggest that while DOP can reduce the perturbation length scale associated with

the rigid interface, the perturbation is not completely eliminated. Further studies investigating the impact of DOP in tuning the magnitude of stiffness perturbation in polymer films near various substrates, including soft substrates, are warranted as well as studies extending conditions to room temperature.

Finally, we note that in contrast to plasticizers, like DOP, that reduced stiffness in polymer films, anti-plasticizers have the potential to enhance the molecular caging and hence stiffness in the glass-supported PS films. Delcambre *et al*. (Delcambre 2010) have demonstrated that adding 5 wt% of an anti-plasticizer tris(2-chloropropyl) phosphate (TCPP) into poly(methyl methacrylate) maximizes the modulus of lithographically designed nanobeams. Future fluorescence-based studies investigating the tunability of molecular caging and hence stiffness in polymers films containing anti-plasticizers supported on glass substrates are warranted.

8.4 Conclusions

We investigated the tunability of stiffness-confinement behavior of glass-supported PS films as a function of DOP plasticizer content as well as temperature utilizing a fluorescence approach. As applied to single-layer PS films, this fluorescence technique can be used to measure average T_g as well as characterize the cumulative polymer stiffness across the film thickness via the sensitivity to caging of a measurable intensity ratio, I_1/I_3. It was demonstrated that DOP addition causes reductions in bulk T_g and eliminates T_g-confinement effects at 4 wt% DOP content, in agreement with reports in literature. At 60 °C, reductions in caging and hence stiffness associated with DOP addition saturated at 10 wt% DOP content, whereas at 140 °C, the reductions in caging and hence stiffness saturated at $1 - 2$ wt% DOP content. This temperature dependence was attributed to the enhanced ability of DOP to impact caging when the polymer is glassy rather than when it is rubbery. Stiffness-confinement behavior was studied by varying the thickness of PS films containing up to 4 wt% DOP. With increasing DOP content, the critical thickness at which supported PS films stiffen decreases, with the greatest impact occuring for

rubbery-state films. The tunability of stiffness-confinement effects was found to be in reasonable agreement with a previous study (Torres 2010) of PDMS-supported PS films even though the presence of the soft PDMS substrate led to a reduction in stiffness with confinement rather than an increase in stiffness with confinement. Our results indicate that plasticizers such as DOP are effective in mediating perturbations to stiffness associated with interfaces.

CHAPTER 9

Fluorescence Sensitivity of Vibronic Coupling Dyes to Molecular Caging:

Demonstration in Polymers Near the Glass Transition

Fluorescence research presented in Chapters 3 – 8 utilize a pyrenyl dye label to characterize stiffness-confinement effects. In this chapter, we extend the fluorescence technique by assessing the ability to use other fluorophores to characterize polymer properties.

9.1 Introduction

Fluorescent probes or fluorophores have been used for decades to characterize material properties such as solvent polarity (Kalyanasundaram 1977, Dong 1984, Nakashima 1993), micelle formation (Kalyanasundaram 1977, Nakashima 1993), polymer gelation (Loutfy 1981, Loutfy 1986), glass transition temperature (Frank 1975, Ellison 2002a, Ellison 2002b, Ellison 2003, Ellison 2004a, Ellison 2004b, Mundra 2007b, Priestley 2007, Kim 2008, Kim 2009, Evans 2011, Kim 2011, Evans 2012b, Evans 2012c), physical aging (Priestley 2005a), stress relaxation (Askar 2015), Debye-Waller factor (Cicerone 2011, Qian 2015) (related to mean-squared displacement), and stiffness (Askar 2016). In general, the use of such probes relies on characterizing changes in fluorescence emission spectra, which could be manifested as shifts in spectral emission wavelengths, changes in total intensity, or a combination of both. Many probes exhibit specific peaks in the fluorescence emission spectra, which correspond to particular transitions of electrons from the vibrational levels of excited states to those of the ground state. For example, the fluorescence spectrum of pyrene has five peaks corresponding to different fluorescence emission pathways. Changes in the relative intensities indicate changes in fluorescence emission pathways (Kalyanasundaram 1977).

The process of fluorescence begins with excitation of electrons from the vibrational levels of the ground state to those of the excited states. The structure of different fluorophores such as the molecular symmetry impacts such excitation pathways (Valeur 2001). Examples of some polyaromatic hydrocarbons that have a high degree of molecular symmetry include pyrene,

benzene, triphenylene, naphthalene, and coronene, and the electrons in these dyes, generally exhibit very weak transitions of electrons from the ground state (S_0) to the first excited singlet state (S_1) (Valeur 2001). Instead, the electrons are primarily promoted from the ground state into the second excited singlet state (S_2) or others. Interestingly, the general phenomenon of a weakly allowed $S_0 \Leftrightarrow S_1$ transition does not apply to all symmetric dyes. Notable exceptions include anthracene and perylene, which are symmetric but exhibit strong $S_0 \Leftrightarrow S_1$ transitions (Valeur 2001). The reason why some dyes such as pyrene experience weakly allowed $S_0 \Leftrightarrow S_1$ transitions and strongly allowed $S_0 \rightarrow S_2$ transitions originates from the fact that the vibrational levels of the excited-state energy levels overlap, and dyes exhibiting this behavior belong to a class known as vibronic coupling dyes.

Seminal studies (Kalyanasundaram 1977, Dong 1984) have demonstrated that the relative peak intensities of pyrene change depending on solvent polarity. In high polarity solvents, the fluorescence intensity associated with the first vibronic band peak of pyrene denoted as I_1 increases at the expense of other peak intensities. This was observed most dramatically in a ratio of the first to third vibronic band peak intensities (I_1/I_3). The enhancements in I_1, corresponding to transitions of electrons from $S_1 \rightarrow S_0$, indicate that solvent polarity enhances $S_0 \Leftrightarrow S_1$ transitions, by mediating or separating the overlapping excited-state energy levels. This phenomenon is known as the Ham effect. Karpovich and Blanchard (Karpovich 1995) investigated the Ham effect in pyrene and provided a physical basis for how solvent polarity mediates vibronic coupling. The fundamental origin of pyrene sensitivity to solvent polarity is by induced dipole-dipole interactions between excited-state pyrene dyes and solvent molecules (Kalyanasundaram 1977, Karpovich 1995). With increasing solvent polarity the induced dipole-dipole interactions become stronger and effectively mediate the vibronic coupling in pyrene. This causes enhancements in $S_1 \rightarrow S_0$ transitions observed as enhancements in I_1, due to a reduction in non-radiative energy decay pathways (Karpovich 1995). Other examples of vibronic coupling dyes which have a weakly allowed $S_0 \Leftrightarrow S_1$ transition but a strongly allowed $S_0 \rightarrow S_2$

transition and therefore exhibit solvent polarity dependence include benzene, coronene, benzo[e]pyrene, benzo[g,h,i]perylene, triphenylene, and phenanthrene (Durocher 1966, Cundall 1973, Acree 1990, Nakashima 1993, Karpovich 1995). Dyes that have a strongly allowed $S_0 \Leftrightarrow$ S_1 transition that do not exhibit solvent polarity dependence, *i.e.*, do not exhibit the Ham effect, include perylene, benzo[a]pyrene, dibenzo[a,e]pyrene, and anthracene (Durocher 1966, Acree 1990, Karpovich 1995).

We have previously demonstrated that pyrene fluorescence monitored using the intensity ratio I_1/I_3 is sensitive to other properties in addition to solvent polarity. By utilizing 1-pyrenylmethyl methacrylate (MPy) labels on polystyrene (PS) chains, we have characterized polymer properties such as stress relaxation, T_g, and stiffness by monitoring changes in I_1/I_3 (Askar 2015, Askar 2016, Askar 2017b, Askar 2017a, Zhang 2017). The ability to characterize a variety of properties suggested that pyrene fluorescence is sensitive to a more general phenomenon of molecular caging, and the sensitivity to solvent polarity is just one example of how pyrene is sensitive to caging. In highly caged environments, such as those with enhanced stress or stiffness, excited-state pyrene molecules experience behavior akin to the Ham effect. With greater caging, we observe enhancements in I_1 at the expense of other peaks as a result of the mediation of vibronic coupling in pyrene.

Here, we test the ability to use other fluorophores to characterize polymer properties such as stress relaxation and T_g. Phenanthrene was chosen since it is a vibronic coupling dye that has known sensitivity to solvent polarity. For comparison, we chose anthracene, which does not exhibit sensitivity to solvent polarity. Phenanthrene and anthracene are used as labels covalently attached to PS chains, and we compare our results with those obtained previously using MPy-PS. Results from this study demonstrate that the sensitivity of vibronic coupling dye fluorescence to local environments is due to the more general phenomenon of molecular caging and have the potential to be used to characterize a variety of material properties such as stiffness. The potential to use different fluorescent dyes to characterize stiffness could be important in

advancing our understanding of stiffness-confinement effects (Lee 1996, Briscoe 1998, Forrest 1998, Soles 2002, Hartschuh 2004, Stafford 2004, Hartschuh 2005, Inoue 2005, O'Connell 2005, Yoshimoto 2005, Inoue 2006, Stafford 2006, Cheng 2007, Tweedie 2007, Stoykovich 2008, Gomopoulos 2009, Delcambre 2010, Gomopoulos 2010, Xu 2010, Arinstein 2011, Watcharotone 2011, Batistakis 2012, Evans 2012a, Torres 2012, Batistakis 2014, Chung 2014, Askar 2015, Cheng 2015, Chung 2015, Li 2015c, Liu 2015, Xia 2015c, Xia 2015b, Ye 2015, Askar 2016, Brune 2016, Chung 2016, Nguyen 2016, Xia 2016, Zhang 2017).

9.2 Experimental Methods

9.2.1 Materials

Terminal phenanthrene-end labeled polystyrene (TPPS) was produced via anionic polymerization of styrene followed by reaction of a phenanthrene-labeled terminator. Using azobisisobutyronitrile (Aldrich, under the name 2,2'-azobis(2-methylpropionitrile)) as initiator, 1-pyrenylmethyl methacrylate (MPy) (Toronto Research Chemicals) or vinyl anthracene (Aldrich) was copolymerized at very low levels with styrene (SigmaAldrich) at 70 °C via bulk free radical polymerization. Labels of MPy or anthracene were incorporated randomly along the PS chains to produce MPy-labeled PS (MPy-PS) or anthracene-labeled PS (RAPS). The MPy-PS and RAPS products were dissolved in toluene and precipitated in methanol seven times to remove unreacted monomer. The washed polymers were placed in a vacuum oven for 3 days at 105 °C prior to use. Gel permeation chromatography (Waters 2410, calibrated with PS standards in tetrahydrofuran, refractive index detector) was used to determine that the washed MPy-PS, TPPS, and RAPS have $M_n = 370$ kg/mol (dispersity = 1.7), 125 kg/mol (dispersity = 1.2), and 259 kg/mol (dispersity = 1.7), respectively. UV-vis absorbance spectroscopy (Perkin Elmer Lambda 35) was used to determine that MPy-PS, TPPS, and RAPS contain less than 1 mol% label. Bulk T_g was determined via differential scanning calorimetry (Mettler Toledo DSC822e, second-heat T_g onset method at 10 °C/min heating rate): T_gs were 101 °C for MPy-PS, 100 °C

for TPPS, and 102 °C for RAPS.

9.2.2 Film Preparation

Films were spin-coated onto glass slides from toluene (SigmaAldrich) solutions containing 1.0 – 7.0 wt% polymer with spin speeds ranging from 2000 to 3000 rpm. Glass slides were thoroughly cleaned by etching in 1.0 M hydrochloric acid, rinsed with water and dried prior to submerging in base solution (10 wt% sodium hydroxide/20 wt% water/70 wt% ethanol). Substrates were rinsed and dried prior to use.

9.2.3 Ellipsometry

To measure thickness, films were first spin-coated onto silicon slides with a native silicon oxide layer from the same solutions with the same spin speeds at the same time as the films spin-coated onto the glass slides. Measurements were performed at room temperature using spectroscopic ellipsometry (J. A. Woollam Co. M-2000D over a range of wavelengths from 400 to 1000 nm). The ellipsometric angles (ψ and Δ) of incident light reflected off silica-supported TPPS and RAPS films were measured and fitted to a Cauchy layer model to determine thickness. The Cauchy layer model included a PS layer atop a silicon substrate containing a 2-nm-thick silicon oxide surface layer. Film thickness was determined by fitting ψ and Δ to the PS layer in the Cauchy model.

9.2.4 Fluorescence

Two sets of fluorescence experiments were conducted on TPPS and RAPS films. The first set involved characterization of residual stress relaxation. After spin coating, bulk TPPS and RAPS films were annealed at 60 °C for 12 h prior to fluorescence measurements. Samples were then transferred to a heating stage at either 120 °C or 140 °C. Emission spectra were collected (Photon Technology International fluorimeter in front-face geometry) every 30 min for 14 h. For TPPS, emission spectra were collected at wavelengths from 340 to 410 nm (excitation at 300 nm). For RAPS, emission spectra were collected at wavelengths from 385 to 455 nm (excitation at 370 nm). Spectra for both TPPS and RAPS were obtained in 0.5 nm increments and 1 s

integration with excitation and emission slit widths set to 0.5 mm (1 nm bandpass). The spectra were used to characterize intensity ratios (I_1/I_3 for TPPS and I_1/I_2 for RAPS) as a function of time to characterize stress relaxation behavior. Peak intensities were calculated from an average of five points spanning a 2 nm window.

The second set involved characterizing both T_g- stiffness-confinement effects. After spin-coating samples were annealed at 120 °C for 12 h prior to fluorescence measurements. Emission spectra for TPPS and RAPS films were collected in 2.5 °C decrements upon cooling from 145 °C to 60 °C at 1 °C/min. Lines were fitted to the rubbery and glassy temperature dependences of the intensity ratios and the intersection was taken as T_g. The spectra were collected under the same fluorimeter conditions and the intensity ratio values were used to determine changes in stiffness.

9.3 Results and Discussion

Figure 9-1 shows typical fluorescence emission spectra for 1-pyrenylmethyl methacrylate PS (MPy-PS), phenanthrene-end-labeled PS (TPPS) and anthracene-labeled PS (RAPS) in bulk films with thicknesses exceeding 900 nm. The spectra shown in Figure 9-1 correspond to fluorescent labels that are covalently attached to PS chains. Covalent attachment of fluorescent labels to polymers is known to affect the spectral shape of the fluorescence emission relative to free dyes (Ellison 2004a, Askar 2015). The peaks designated in Figure 9-1 are assigned based on the free-dye fluorescence spectral emissions. Previous fluorescence studies have utilized the sensitivity of pyrene to local environmental changes by monitoring changes in the ratio of peak intensities I_1/I_3, which increases in highly caged environments such as those with enhanced stress or stiffness and allows for characterization of T_g, stress relaxation, and stiffness (Askar 2015, Askar 2016, Askar 2017b, Askar 2017a, Zhang 2017). Here, we additionally compare the fluorescence behavior of phenanthrene and anthracene labels in providing sensitivity to stress relaxation and T_g in polymer films. Like pyrene, phenanthrene belongs to the class of dyes known as vibronic coupling dyes (Hochstrasser 1966), whereas anthracene does not.
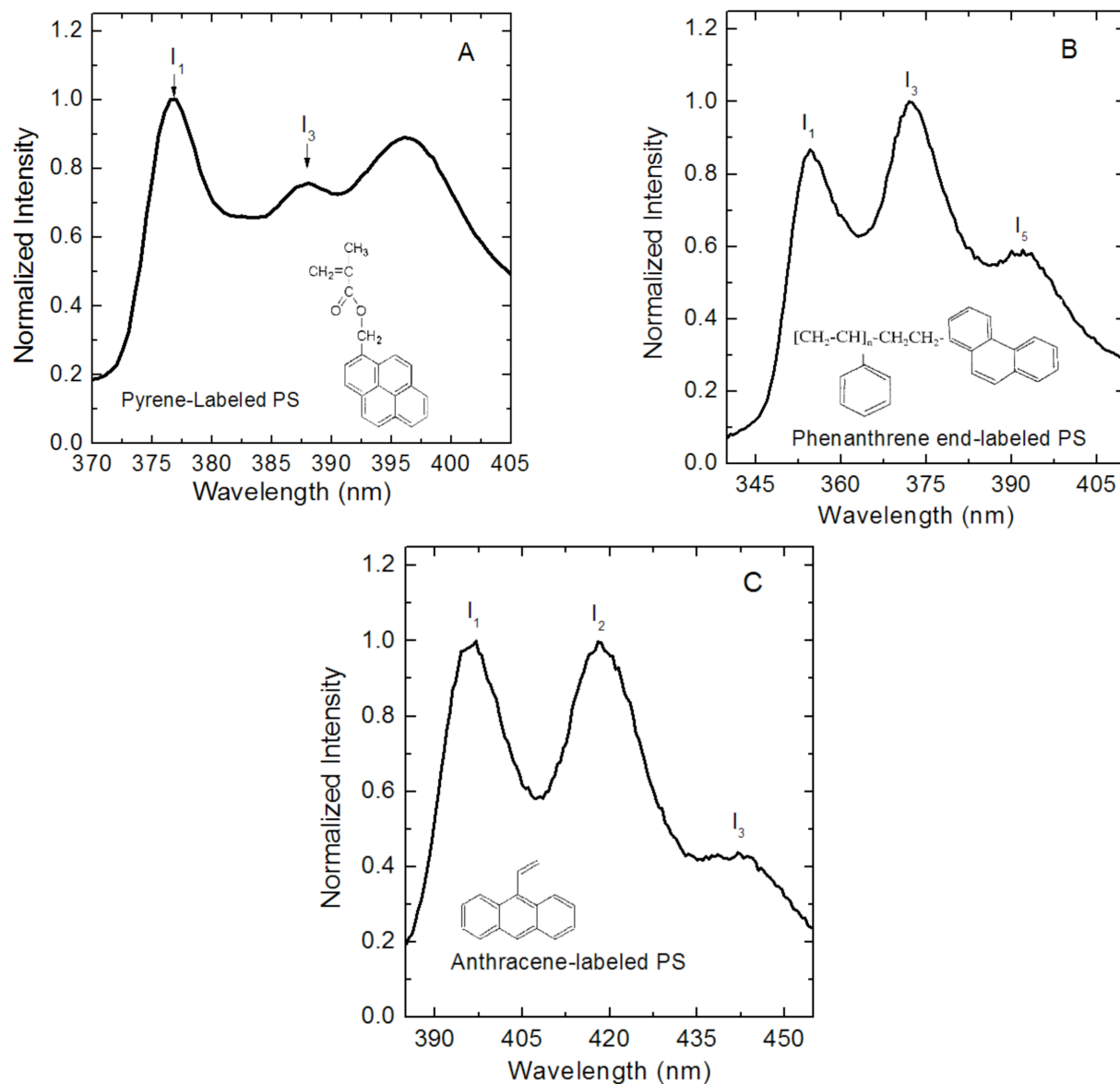
Figure 9-1: Normalized intensity as a function of wavelength for bulk films of pyrene-labeled (A), phenanthrene-end-labeled (B), and anthracene-labeled (C) PS at 100 °C. The spectra are normalized to the maximum peak intensity in each case.

Figure 9-2 shows intensity ratio values as a function of stress relaxation time at 120 °C for bulk films of MPy-PS, RAPS, and TPPS (from top to bottom) supported on glass slides. Stress relaxation data for MPy-PS has been re-plotted from our previous fluorescence study (Askar 2015). The intensity ratio values for MPy-PS were observed to decrease with increasing time at 120 °C then reach apparent steady state values. The reduction in I_1/I_3 values indicated that molecular caging was reduced and thus stresses were being relaxed (Askar 2015). Intensity ratio values for TPPS also decrease with time, which is consistent with stress relaxation. In contrast, RAPS does not exhibit any reduction in intensity ratio values over time. These results demonstrate that pyrenyl and phenanthryl dyes exhibit fluorescence sensitivity to stress relaxation due to their vibronic coupling nature, but the anthryl dye does not.

The ability to use intensity ratio values to measure bulk polymer T_g using the different dyes is investigated in Figure 9-3. Intensity ratios are plotted as a function of temperature for MPy-PS, TPPS, and RAPS. MPy-PS data are re-plotted from a previous fluorescence study (Askar 2016). Bulk T_g values are measured by the intersection of lines fitted to the rubbery and glassy temperature dependences of I_1/I_3. For MPy-PS, the clear change in temperature dependence enables accurate measurements of T_g. Data for TPPS indicates that the phenanthryl dye provides sensitivity to T_g by exhibiting changes in the temperature dependences of I_1/I_3 values similar to the pyrenyl dye, but with greater noise. The enhanced noise associated with the phenanthryl dye can be attributed to the fact that phenanthrene absorbs and fluoresces much less effectively than pyrene. By contrast, the non-vibronic coupling anthryl dye does not exhibit a clear change in temperature dependence of I_1/I_2 values. The noise in the data exceeds the total change in I_1/I_2 over the entire temperature range thus preventing accurate determinations of T_g. The results from Figure 9-3 show that the two vibronic coupling dyes can be used to measure bulk T_g, whereas non-vibronic coupling dyes cannot.

We note that the Torkelson research group has used several analysis methods to obtain T_g values from temperature-dependent fluorescence responses. Integrated fluorescence intensity
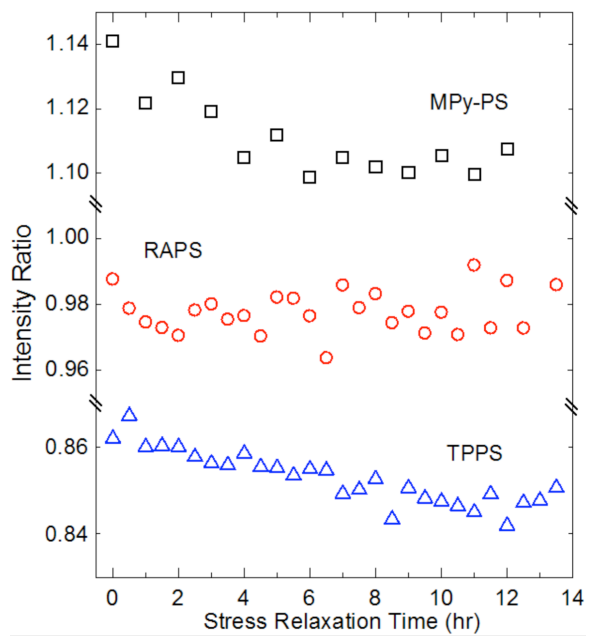
Figure 9-2: Intensity ratio as a function of stress relaxation time for bulk films of MPy-PS, TPPS, and RAPS at 120 °C. Data correspond to I_1/I_3 for MPy-PS and TPPS and I_1/I_2 for RAPS.
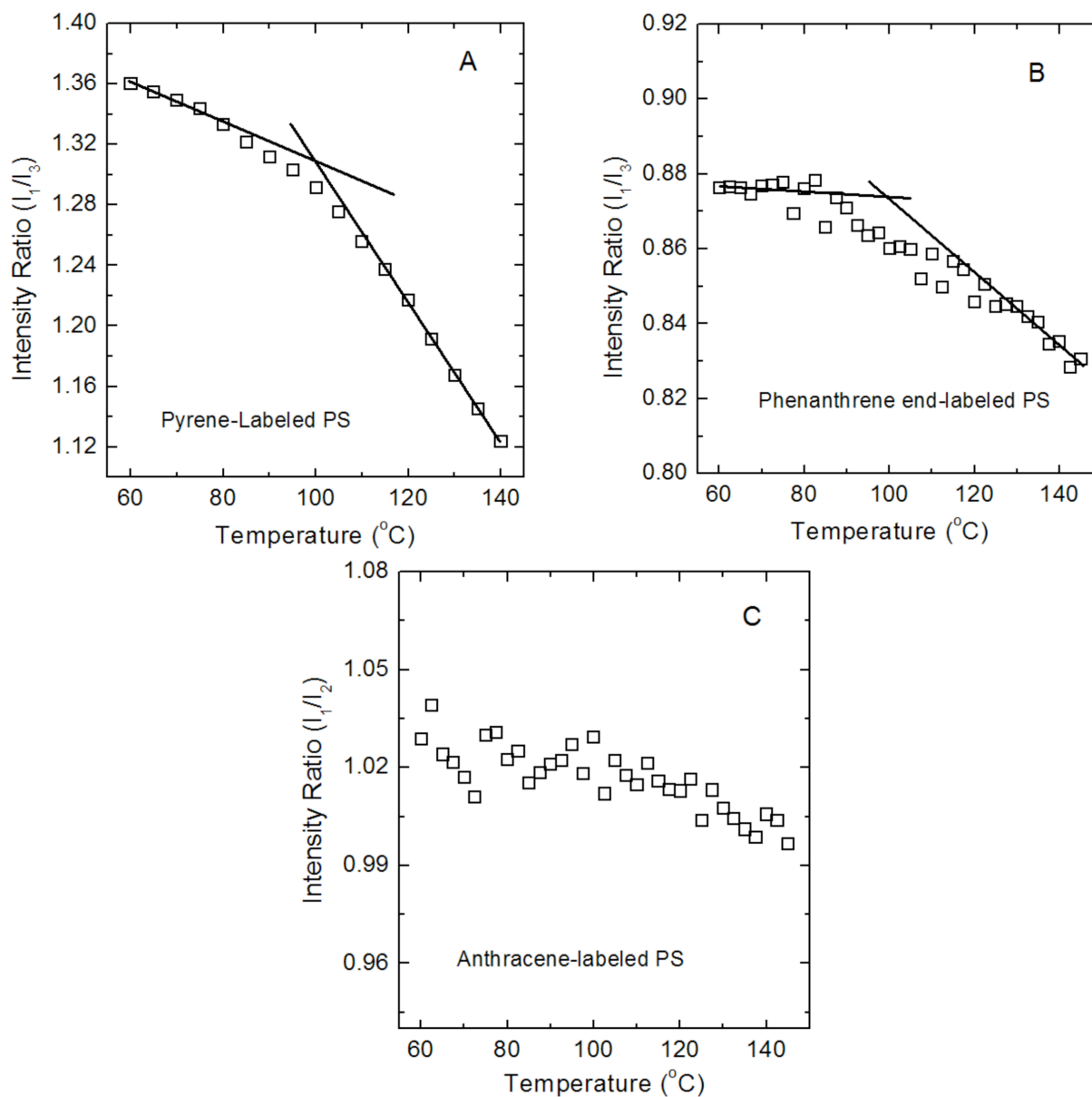
Figure 9-3: Intensity ratio values as a function of temperature for bulk films of MPy-PS (A), TPPS (B), and RAPS (C). Lines were fitted to the rubbery and glassy temperature dependences of the intensity ratio values to determine T_g.

method (over a broad range of wavelengths) as a function temperature with pyrenyl dye dopants or labels (with 1-pyrenylbutyl methacrylate) is generally preferred, because it yields highly-reproducible data subject to little intrinsic error or noise. However, in freestanding film studies, the preferred method does not provide data of sufficient quality to yield accurate and precise T_g values; this has been explained by presumed film rippling on cooling, which leads to changes in the film surface area being exposed to the fluorescence excitation light. Hence, in freestanding film studies, a self-referencing method involving an intensity ratio (I_1/I_3) is employed, which eliminated any issues associated with fluctuations in the surface area being exposed to excitation light. However, because the I_1/I_3 data result from a ratio of intensities with each intensity averaged over only 2 nm of emission, there is more error inherent in the use of I_1/I_3 data than in integrated fluorescence data. The quality of the I_1/I_3 data is sufficient to yield good determinations of T_g but insufficient to comment with confidence on issues such as glass transition breadth, which can be quantified with confidence using temperature-dependent integrated fluorescence intensity data.

Results from Figures 9-2 and 9-3 show that vibronic coupling dyes other than pyrene, such as phenanthrene, are sensitive to stress relaxation and T_g in bulk polymers. Therefore, vibronic coupling dyes are sensitive to local environmental changes via changes in molecular caging. The ability to characterize stress relaxation and bulk T_g using pyrenyl and phenanthryl labels demonstrates how the sensitivity of vibronic coupling dyes to molecular caging can be utilized in polymers. We have previously demonstrated that this sensitivity can be extended to characterize stiffness in bulk and nanoconfined polymer films and model nanocomposites using MPy-PS (Askar 2015, Askar 2016, Askar 2017b, Askar 2017a). Results from this study suggest that other vibronic coupling dyes could be utilized to characterize polymer properties such as stiffness (Durocher 1966, Cundall 1973, Acree 1990, Nakashima 1993, Karpovich 1995). But it is important to note that many factors must be considered when using dyes to characterize polymers. For instance, factors such as quantum yield, photobleaching, and photooxidation,

would lead some vibronic coupling dyes to be better suited to characterize polymer properties than others. While pyrene is not the only dye capable of characterizing stress relaxation and stiffness, it is generally preferred due to its stability and high quantum yield.

9.4 Conclusions

Here, we assess the ability to use a broader class of fluorophores known as vibronic coupling dyes to characterize polymer properties such as stress relaxation and T_g. We compare the fluorescence behavior of phenanthryl and anthryl labels to previously observed behavior of pyrenyl labels in providing sensitivity to stress relaxation and T_g in polymer films. Like pyrene, phenanthrene belongs to the class of dyes known as vibronic coupling dyes, whereas anthracene does not. It is demonstrated that phenanthryl and pyrenyl labels exhibit similar sensitivities to stress relaxation and T_g, whereas anthryl labels do not. The similarities between pyrene and phenanthrene can be attributed to the fact that the two dyes are vibronic coupling dyes whose spectra are sensitive to changes in local molecular caging. In contrast, the anthryl label did not exhibit sensitivity to stress relaxation or T_g because it does not exhibit vibronic coupling behavior. The results from this study open the possibility for a more general class of fluorophores to characterize other polymer properties such as stiffness.

III. DETERMINATION OF T_g-CONFINEMENT BEHAVIOR IN POLYMER BRUSHES AND SUPPORTED NANORODS

CHAPTER 10

Polystyrene-Grafted Silica Nanoparticles: Investigating the

Molecular Weight Dependence of Glass Transition and Fragility Behavior

10.1 Introduction

Nanofillers are commonly added to polymers to yield nanocomposites with enhanced thermal, optical, and mechanical properties relative to neat polymer (Krishnamoorti 1996, Starr 2002, Bockstaller 2005, Lin 2005, Zhu 2005, Balazs 2006, Moniruzzaman 2006, Oberdisse 2006, Rong 2006, Schadler 2007b, Vaia 2007, Winey 2007, Goncalves 2010, Jancar 2010, Milano 2011, Ndoro 2011, Du 2012, Tang 2012, Kango 2013, Kumar 2013, Park 2013, Song 2013, Holt 2014, Wang 2015, Davris 2016, Hu 2016, Salavagione 2016, Khani 2017). Many of the property enhancements associated with nanocomposites have been explained as arising from how interphase regions of polymer located nanofiller interfaces are perturbed by the nanofiller (Porter 2002, Rittigstein 2007, Harton 2010, Holt 2013, Cheng 2016). Such interfacial perturbations are also considered to be an origin of confinement effects, *i.e.*, when polymers are confined to nanoscale dimensions as in supported thin films or nanotubes (Keddie 1994a, Tan 2016). A critical consideration in optimizing and understanding nanocomposite behavior is that significant nanoparticle aggregation may hinder property enhancements associated with the presence of nanofillers. One approach to improve particle dispersion involves utilizing polymer-grafted nanoparticles or hairy nanoparticles, which in certain instances can exhibit enhanced compatibility with the surrounding polymer matrix (Savin 2002b, Rong 2006, Akcora 2009b, Pietrasik 2011, Voudouris 2011, Dang 2013, Fernandes 2013, Fernandes 2014, Kim 2015a, Koerner 2016). Polymer-grafted nanoparticles themselves have exhibited interesting self-healing behavior and enhanced mechanical properties (Choi 2012, Williams 2015, Dreyer 2016).

Many reports in literature have investigated the glass transition temperature (T_g) behavior of nanocomposites containing polymer-grafted nanoparticles within a polymer matrix (Bansal 2006, Oh 2009, Avolio 2010, Jancar 2010, Parker 2010, Kim 2012, Chandran 2013, Chen 2013,

Antonelli 2015, Mangal 2015). However, under conditions of dense grafting, polymer-grafted nanoparticles exhibit interesting T_g behavior themselves (Savin 2002b, Pietrasik 2011, Voudouris 2011, Choi 2012, Dang 2013, Fernandes 2013, Fernandes 2014, Kim 2015a, Koerner 2016). Savin *et al.* (Savin 2002b) reported reductions in T_g of polystyrene-grafted silica nanoparticles (Si-PS) with decreasing graft molecular weight (MW). In particular, $T_g = 101 \pm 1$ °C for Si-PS with graft MWs between 32.7 and 15.0 kg/mol and 94 ± 1 °C for Si-PS with graft $M_n = 5.2$ kg/mol. In agreement with Savin *et al.* (Savin 2002b), Dang *et al.* (Dang 2013) reported reductions in T_g from 105.5 °C to 94 °C in Si-PS with reductions in graft MW from ~200 kg/mol to ~10 kg/mol, respectively. Kim *et al.* (Kim 2015a) investigated the T_g behavior of *cis*-1,4-polyisoprene-grafted silica nanoparticles (Si-PI). Although they did not specifically comment on the MW dependence of T_g in Si-PI samples, their data indicate that T_g decreases with decreasing MW. These reports are in agreement that at the same MW, grafted polymers exhibit an enhanced T_g relative to free polymer chains (Savin 2002b, Dang 2013, Kim 2015a, Koerner 2016).

In addition to brushes grafted from spherical nanoparticles, brushes may also be grafted from flat silica substrates (Lan 2015, Ugur 2016). Lan and Torkelson (Lan 2015) demonstrated via ellipsometry that dense PS brushes grown from flat silica substrates exhibit no MW dependence of average T_g down to 23 kg/mol. Interestingly, T_g breadth (as measured by ellipsometry) increased from 20 °C to 35 °C with decreasing brush MW from 170 kg/mol to 23 kg/mol (Lan 2015). With decreasing brush molecular weight, the enhancement in T_g breadth coupled with the lack of change in average T_g across the length of the dense brushes indicates that the overall average T_g is a reflection of the combined perturbation to local T_g originating from grafted and free chain ends. We note that there is no published report on the T_g breadth of polymer-grafted nanoparticles as a function of graft MW.

Nanocomposite fragility can be affected by the addition of bare nanofillers (Sanz 2008, Ding 2009, Wong 2010, Betancourt 2013, Sanz 2015). Using simulations, Betancourt *et al.* (Betancourt 2013) have reported that in the case of bare nanoparticles, attractive interactions

with the polymer matrix cause enhancements in fragility and non-attractive interactions with the polymer matrix cause reductions in fragility (Betancourt 2013). Only one experimental report Oh 2009 has investigated the impact of polymer-grafted nanoparticles on the fragility of nanocomposites, in particular, PS grafted onto gold nanoparticles (Au-PS) dispersed in a PS matrix. Although the reported changes were small, the data suggested that the grafted nanoparticles caused reductions in fragility relative to neat PS and that the fragility of Au-PS exhibited MW dependence (Oh 2009). There is no published report of fragility in polymer-grafted nanoparticles without a host matrix.

Here, we investigate glass transition behavior of Si-PS nanoparticles without a host matrix. T_g measurements are obtained as a function of graft MW and are compared with other reports in the research literature. We also provide the first characterization of T_g breadth in polymer-grafted nanoparticles as a function of MW and compare our results with those from PS brushes grown from flat substrates. Fluorescence spectroscopy is also used to investigate local T_g as a function of distance from the grafting interface. The MW dependence of fragility in Si-PS is investigated using differential scanning calorimetry (DSC).

10.2 Experimental Methods

10.2.1 Materials

Styrene monomer (Sigma, 99.9%) was deinhibited using calcium hydride (Sigma, 90%) and inhibitor remover (Sigma, 311340) before polymerization. Toluene (Fisher, 99.5%) and dimethylformamide (Fisher, 99.9%) were dried over activated molecular sieves (Sigma, 208574) before use. Silica nanoparticles (Nissan Chemical, MEK-ST) with reported particle diameters of 10 – 15 nm were obtained as a dispersion (30 wt% in methyl ethyl ketone) and re-suspended in dry toluene via solvent exchange. 1-pyrenylbutyl methacrylate monomers were synthesized as described by Ellison and Torkelson (Ellison 2002b). An anionically synthesized PS standard (Polymer Science, 400 kg/mol, dispersity = 1.06), (3-aminopropyl)triethoxysilane (Sigma, 98%),

triethylamine (Sigma, 99%), α-bromoisobutyryl bromide (Sigma, 98%), tris(2-pyridylmethyl)amine (Sigma, 98%), copper(II) bromide (Sigma, 99%), methyl α-bromoisobutyrate (Sigma, 99%), methanol (Fisher), and tetrahydrofuran (Fisher) were used as received.

10.2.2 Surface Functionalization of Silica Nanoparticles with Initiator

(3-Aminopropyl)triethoxysilane (0.40 mL) was added dropwise to a mixture of silica nanoparticles (3.0 g) and dry toluene (10.0 mL) that was subjected to rigorous mixing and maintained under a nitrogen atmosphere. The mixture was then heated to reflux temperature (60 °C) and reacted for 12 h. To purify, the amine-functionalized silica nanoparticles were centrifuged and re-suspended in toluene three times. Under rigorous mixing, the atom transfer radical polymerization (ATRP) initiator (α-bromoisobutyryl bromide) (4.0 mL) was added drop-wise to a solution containing amine-functionalized silica nanoparticles (2.0 g), triethylamine (4.0 mL), and dry toluene (30.0 mL) at 0 °C. The resulting mixture was sealed and reacted ~12 h under ambient conditions. To purify, the ATRP initiator-grafted nanoparticles were recovered via centrifugation and re-suspended in ethanol three times.

10.2.3 Synthesis of Polymer Brushes

Dense PS brushes were synthesized using activator regenerated by electron transfer (ARGET) ATRP (Matyjaszewski 2007). Functionalized silica nanoparticles (0.2 g) were dispersed into a solution containing tris(2-pyridylmethyl)amine (3.0 mg), copper(II) bromide (0.5 mg in 0.2 mL dimethylformamide), methyl α-bromoisobutyrate (3.0 μL), styrene (5.0 mL), dimethylformamide (2.0 mL) and tin(II) 2-ethylhexanoate (60 mg). The mixtures were purged using nitrogen for 20 min prior to polymerization at 85 °C for various times. After polymerization, the mixtures were immediately precipitated into excess methanol. The Si-PS samples were recovered via centrifugation and washed with toluene at least three times to remove ungrafted PS chains.

In some cases, PS brushes were also labeled for fluorescence measurements at various

distances from the particle interface. Labeling was achieved by adding trace amounts of 1-pyrenylbutyl methacrylate (BPy) into styrene before ARGET ATRP. Two labeled samples were polymerized via chain extension where in one, the fluorescent label was located within 8 kg/mol of the graft interface (total brush M_n = 54 kg/mol), and in the other the label was located within 14 kg/mol of the free chain ends (total brush M_n = 93 kg/mol). This labeling was achieved via the following chain extension procedure. Brushes were first grown from the nanoparticle surfaces for the desired length of time. After polymerization, the grafted nanoparticles were precipitated in methanol and purified via centrifugation and re-suspension in toluene three times. After removing unreacted monomer and ungrafted chains, the grafted nanoparticles were used as macro-initiators to perform chain extension through ARGET ATRP for the desired length of time. A similar chain extension procedure was used for brushes grafted to flat silica substrates (Lan 2015). The resulting polymer-grafted nanoparticles were again recovered and purified via centrifugation. As determined via UV/Vis absorbance spectroscopy (Perkin-Elmer), the label contents are 0.9 or 1.1 mol% within the labeled portions of the brushes with M_n = 8 kg/mol or 14 kg/mol, respectively, as determined from the unattached labeled chains.

10.2.4 Characterization of Si-PS samples

Gel permeation chromatography (GPC) (Waters 2410, light scattering detector (Wyatt)) was used for characterizing MW and dispersity of free polymer chains. (We note that free initiator methyl α-bromoisobutyrate was used to polymerize ungrafted PS chains simultaneously with the grafted chains. This was done for MW characterization of grafted chains. It has been reported previously that the number-average MWs (M_n)s of free and grafted chains are equal (Ohno 2005, Matyjaszewski 2007).) The M_n values ranged from 12 kg/mol to 98 kg/mol with an average dispersity = 1.1 ± 0.1. All M_n values of polymers reported in this study were determined via light scattering detection (using dn/dc = 0.184 for PS in tetrahydrofuran). Thermogravimetric analysis was used to determine the graft density of the PS brushes on silica nanoparticles. The portion of PS in Si-PS samples decreases from 96 wt% to 55 wt% in Si-PS with reductions in

graft M_n from 98 kg/mol to 12 kg/mol. On average, the graft density was determined to be

0.34 ± 0.04 chains/nm^2, which indicates that these are densely grafted (Savin 2002b, Lan 2015).

10.2.5 Differential Scanning Calorimetry Measurements

DSC (Mettler-Toledo 822) was used to characterize T_g, T_g breadth, and fragility of PS

and Si-PS samples. Samples were first annealed for 10 min above bulk T_g at 140 °C and then

cooled to 40 °C at a cooling rate of -40 °C/min. T_g values were determined by the onset upon

heating at a rate of 10 °C/min from 40 °C to 140 °C.

T_g breadth values were determined from first derivative heat flow curves, which involved

taking the derivative of heat capacity curves with respect to temperature (Kim 2006, Mok 2009,

Jin 2015). Fragility values were determined from the cooling rate dependence of fictive

temperature (T_f) using rates ranging from -0.4 to -40 °C/min followed by heating at 10 °C/min

(Simon 1997, Robertson 2000, Wang 2002, Dalle-Ferrier 2009, Evans 2013a, Zhang 2013b); T_f

was evaluated using the Richardson method (Richardson 1975). The fragility, m, can be

determined from Equation 1 (Robertson 2000, Wang 2002):

$$\log(Q/Q_s) = m - m(T_f^s/T_f) \tag{1}$$

where Q is the cooling rate, Q_s is a standard cooling rate of 10 °C/min, and T_f^s is the fictive

temperature for the standard cooling rate. The reported errors for fragility are standard deviations

from at least three determinations.

10.2.6 Fluorescence Measurements

The T_g values of labeled Si-PS samples were characterized via fluorescence spectroscopy

(Photon Technology International). Si-PS samples were suspended in toluene and drop-cast onto

glass slides. After allowing excess toluene to evaporate under ambient conditions, labeled Si-PS

samples were annealed at 120 °C for 3 h prior to fluorescence measurements. Samples were then

transferred to a heating stage at 145 °C and held for 20 min. Emission spectra were collected

from 370 to 405 nm (excitation at 324 nm, 1 s integration time) using 0.5 mm slit widths (1 nm

bandpass). Samples were cooled from 145 to 60 °C at 1 °C/min, and spectra were collected every

2.5 °C. Normalized integrated intensity was plotted as a function of temperature, and the T_g was determined by the intersection of lines fitted through the rubbery and glassy temperature dependences of normalized intensity (Ellison 2003, Rittigstein 2006, Priestley 2007, Roth 2007c, Evans 2013a, Lan 2015). The best-fit lines were obtained by fitting data in the glassy and rubbery regimes beginning with the lowest and highest temperature values. Points were added to the fits until the fit lines no longer passed through the data points, *i.e.*, $R^2 < 0.990$.

10.2.7 Scanning Electron Microscopy

PS-grafted nanoparticles were dispersed in toluene and then drop casted on an alumina scanning electron microscopy stage. The samples were then dried in vacuum overnight before characterization. A Hitachi SU8030 scanning electron microscope equipped with a cold field emission gun was used to characterize the microstructure of Si-PS samples.

10.3 Results and Discussion

Figure 10-1 shows a typical field-emission scanning electron microscopy (SEM) image of PS-grafted silica nanoparticles with graft $M_n = 12$ kg/mol; the schematic on the right illustrates the molecular details of how PS is linked to the silica nanoparticle surface. In the SEM image, dark spheres represent silica nanoparticles and the lighter-color spacing between the particles indicates the presence of PS separating the nanoparticles. In a study by Savin *et al*. (Savin 2002b), transmission electron microscopy (TEM) images were presented for Si-PS samples of varying graft MW (unmodified silica nanoparticles were obtained from the same provider as employed here, Nissan Chemical, and had a reported average measured diameter of 20 nm (Savin 2002b)). In particular, the TEM image for Si-PS with graft $M_n = 15$ kg/mol from Savin *et al*. (Savin 2002b) appears nearly identical to Figure 10-1 indicating that successful grafting was achieved in this study. Figure 10-1 also shows that the interparticle spacing between silica spheres is $\lesssim 20$ nm and thus the PS grafts are nanoconfined.

DSC is used to investigate T_g behavior of Si-PS samples. Figure 10-2A shows scaled heat
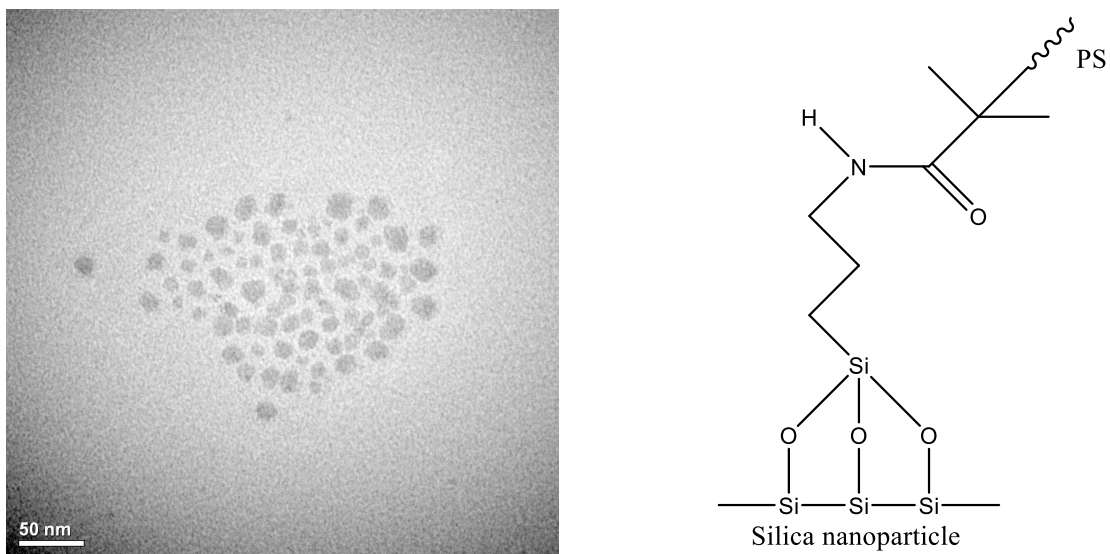
Figure 10-1: Scanning electron micrograph of PS-grafted nanoparticles with a brush molecular weight of 12 kg/mol (left) and the chemical structure of the attachment (right). Silica nanoparticles have diameters of 10 – 15 nm. The scale bar in the SEM image is 50 nm.
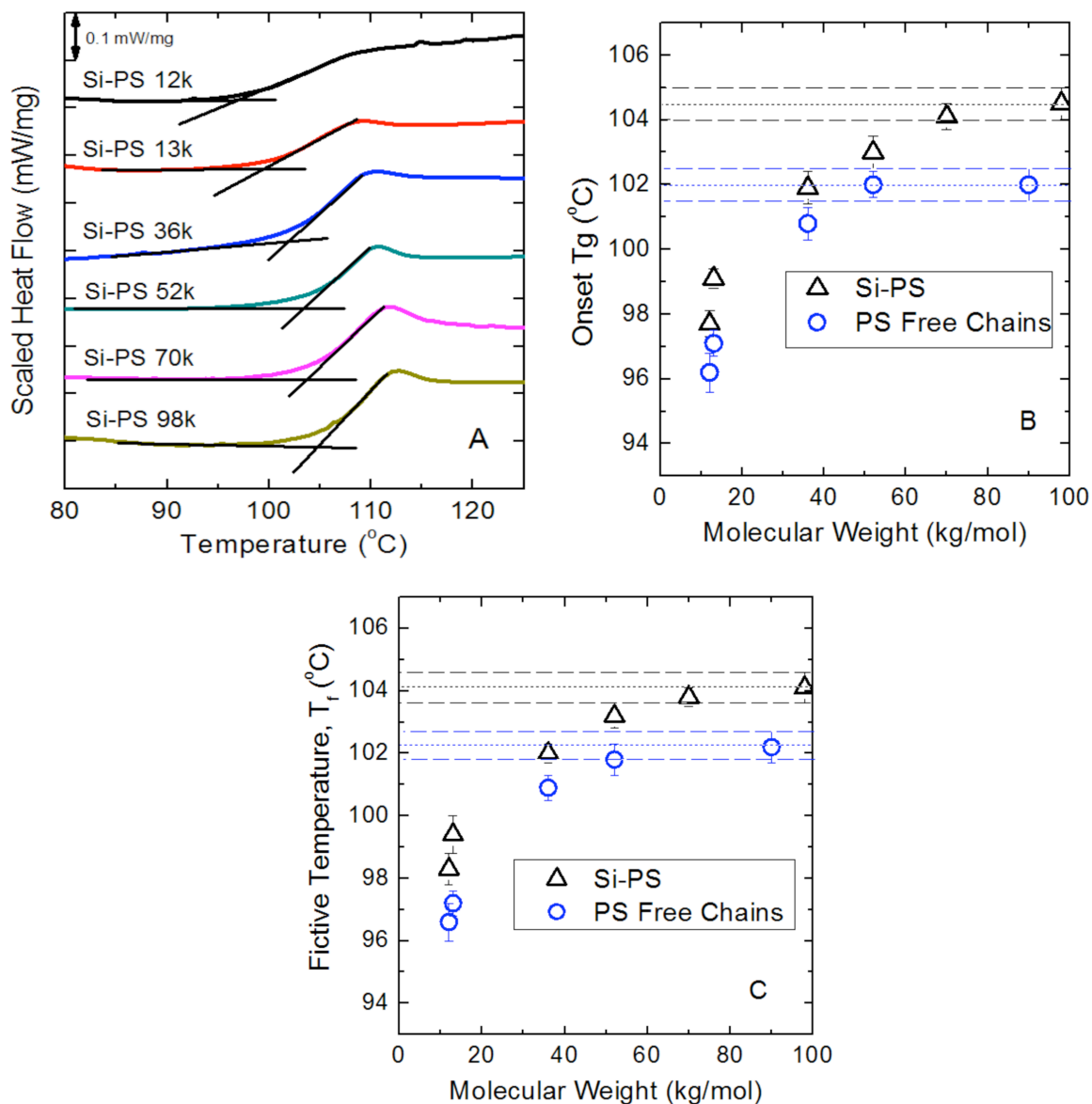
Figure 10-2: (A) Scaled heat capacity as a function of temperature for PS-grafted silica nanoparticles (Si-PS) with graft molecular weights ranging from 12 kg/mol to 98 kg/mol. The heat capacities were divided by the mass of polymer in the samples. (B) Onset T_g values as a function of molecular weight for Si-PS samples (closed triangles) and PS free chains (open circles). $T_{g,onset}$ values were determined by intersection of lines shown in A. (C) shows T_f values for the same samples shown in B. T_f values were determined by the Richardson method after cooling the samples at -40 °C/min and heating at 10 °C/min.

flow as a function of temperature for Si-PS with varying brush MW. The scaled heat flow is calculated by dividing the temperature-dependent heat capacity curves by the mass of PS in the Si-PS samples. Figure 10-2A shows that $T_{g,onset}$ values decrease as graft MW decreases. In particular, the Si-PS samples exhibit reductions in $T_{g,onset}$ from 104.5 ± 0.5 °C to 97.7 ± 0.4 °C with reductions in graft M_n from 98 kg/mol to 12 kg/mol. (Our $T_{g,onset}$ data are summarized in Table 10-1.) Savin *et al*. (Savin 2002b) report $T_g = 101 \pm 1$ °C for Si-PS with graft MWs between 32.7 and 15.0 kg/mol and 94 ± 1 °C for Si-PS with graft $M_n = 5.2$ kg/mol. (Savin *et al*. (Savin 2002b) used the Richardson method (Richardson 1975) to measure fictive temperature (T_f) values from DSC heat flow curves, which they report as T_g values. The fictive temperature is defined as the point at which a glass would transition to a rubbery equilibrium state upon sufficiently rapid heating from the nonequilibrium glassy state (Tool 1946, Evans 2013a).) In addition, Dang *et al*. (Dang 2013) report reductions in T_g from 105.5 °C in Si-PS 200 kg/mol to 94 °C in Si-PS 10 kg/mol. (Dang *et al*. (Dang 2013) measured $T_{g,onset}$ values from DSC heat flow curves).

Figure 10-2A also indicates that for the lowest MW brushes in this study (Si-PS 12 & 13 kg/mol), the step change in heat capacity (ΔC_p) is smaller than that in higher MW brushes. This contrasts with PS free chains, which exhibit no reduction in ΔC_p within error with decreasing MW for the MW range studied. We note that ΔC_p values for PS free chains are within error equal to those for Si-PS with sufficiently high MW. (See Table 10-1.) Reductions in ΔC_p with decreasing MW have been noted in other reports of bare silica nanoparticles within a polymer matrix (Mizuno 2011, Holt 2014). With increasing silica content, the reduction in ΔC_p in such nanocomposites has been attributed to the immobilization of polymer in the interfacial region near the nanofiller, which restricts participation in the glass transition. This description may also apply to our two lowest MW Si-PS systems, where a sizable fraction of the PS brushes do not apparently participate in the glass transition.

Figures 10-2B and 10-2C show in full detail how $T_{g,onset}$ and T_f values decrease with

Table 10-1: Property Summary for PS-Grafted Silica Nanoparticles and PS Free Chains as a Function of Molecular Weight

Brush M_n (kg/mol)	$\Delta C_{p,brush}$ (J/gK)	Brush $T_{g,onset}$ (°C)	Brush T_g breadth (°C)	Brush T_f* (°C)	Brush Fragility, m
12	0.10 ± 0.03	97.7 ± 0.4	16.0 ± 0.5	98.3 ± 0.5	119 ± 9
13	0.19 ± 0.02	99.1 ± 0.3	15.3 ± 0.4	99.4 ± 0.6	121 ± 7
36	0.20 ± 0.01	101.9 ± 0.5	13.4 ± 0.6	102.0 ± 0.3	130 ± 5
52	0.24 ± 0.02	103.0 ± 0.5	12.4 ± 0.5	103.2 ± 0.4	144 ± 9
70	0.24 ± 0.01	104.1 ± 0.4	13.4 ± 0.3	103.8 ± 0.3	148 ± 8
98	0.24 ± 0.01	104.5 ± 0.5	12.7 ± 0.5	104.1 ± 0.5	156 ± 9
Free Chain M_n (kg/mol)	$\Delta C_{p,free\ chain}$ (J/gK)	Free Chain $T_{g,onset}$ (°C)	Free Chain T_g breadth (°C)	Free Chain T_f* (°C)	Free Chain Fragility, m
12	0.23 ± 0.02	96.2 ± 0.6	12.3 ± 0.5	96.6 ± 0.6	140 ± 7
13	0.25 ± 0.02	97.1 ± 0.4	12.7 ± 0.6	97.2 ± 0.4	143 ± 9
36	0.25 ± 0.01	100.8 ± 0.5	12.5 ± 0.4	100.9 ± 0.4	150 ± 6
52	0.27 ± 0.01	102.0 ± 0.4	12.7 ± 0.4	101.8 ± 0.5	157 ± 8
90	0.28 ± 0.02	102.0 ± 0.5	12.9 ± 0.6	102.2 ± 0.4	158 ± 8
400**	0.26 ± 0.01	102.0 ± 0.5	12.6 ± 0.5	102.3 ± 0.4	163 ± 10

*T_f values were determined from the Richardson method. Samples were characterized after cooling at -40 °C/min and heating at 10 °C/min, identical to the method used to determine $T_{g,onset}$ values.

**Anionically synthesized PS standard.

decreasing MW for both Si-PS and PS free chains. The MW dependence observed in our study is in major agreement with both Savin *et al*. (Savin 2002b) and Dang *et al*. (Dang 2013) Reductions in T_g can be attributed to enhanced influence from free chain ends at low MW. Zhang and Torkelson (Zhang 2016) recently stated that "the role of chain ends in providing a greater degree of conformational freedom is central to the MW dependence of T_g." This is because free chain ends enhance free volume and configurational entropy of the polymer chains (Roland 1996, Rizos 1998, Ellison 2005, Miwa 2005, Miwa 2015, Zhang 2016). As MW decreases, enhanced configurational freedom provided by free chain ends reduces requirements for cooperative mobility and hence T_g decreases. In the case of Si-PS, one end of the chains is immobilized. The immobilization causes an enhancement in T_g relative to PS free chains of the same MW. These results are in agreement with reports in literature (Savin 2002b, Dang 2013, Kim 2015a, Koerner 2016), which indicate that tethering and chain confinement cause elevated T_g in the grafted chains relative to free chains. In understanding the MW dependence of T_g, one might simply compare the T_g of grafted chains with the T_g of free chains with twice the MW since the concentration of free chain ends would be the same. However, such a simplistic comparison does not capture differences in chain end effects associated with Si-PS and unattached PS. In the case of Si-PS, the free chain ends are concentrated away from the grafting interfaces of the nanoparticles, whereas in the case of unattached PS, the free chain ends are evenly dispersed throughout the polymer. The influence of free chain ends on cooperative mobility and packing efficiency is investigated further in a later discussion of fragility results.

The breadth of the glass transition is also investigated using DSC. Figure 10-3A shows scaled first derivative heat flow curves as a function of temperature for Si-PS with varying brush MW. These curves are obtained by taking the derivative (with respect to temperature) of the heat flow curves shown in Figure 10-2A. T_0 values are determined by the onset of deviations from baseline behavior of the scaled first derivative heat flow curves, and T_e values are determined
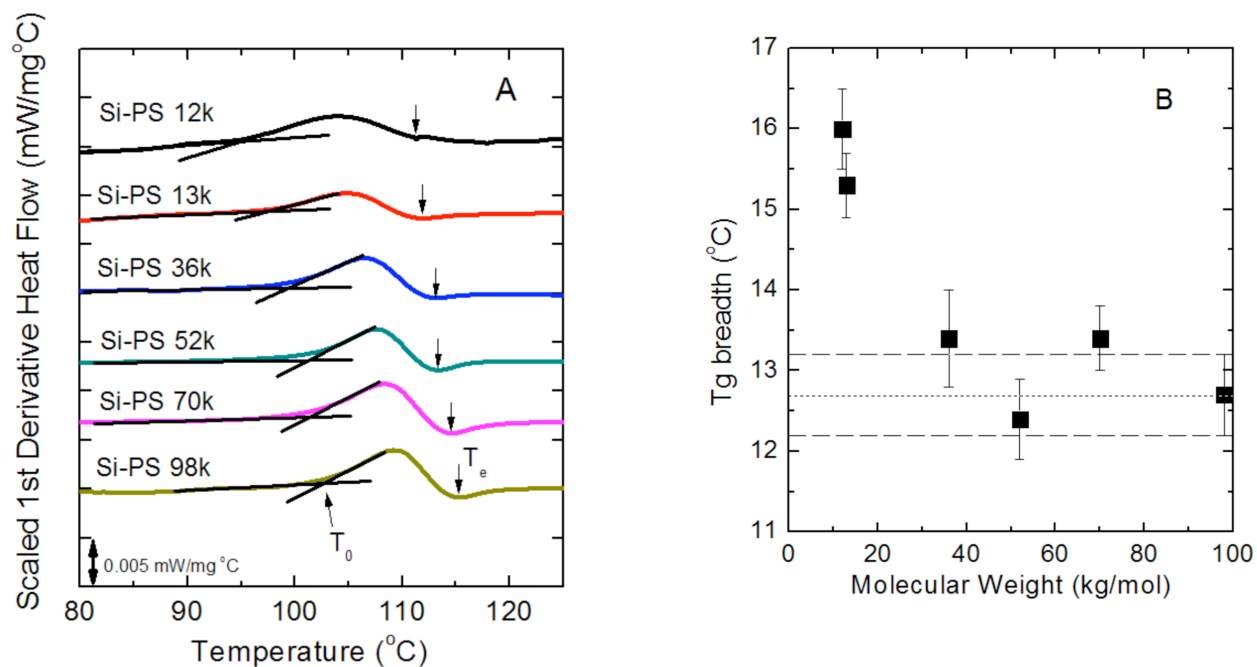
Figure 10-3: A: Scaled first derivative heat flow as a function of temperature for Si-PS samples with graft molecular weights ranging from 12 kg/mol to 98 kg/mol. T_0 values are shown by the intersection of lines depicting deviation from baseline behavior, and T_e values are indicated by down arrows. B: T_g breadth as a function of graft molecular weight. T_g breadths were calculated via $T_e - T_0$ from A.

from temperatures at which minima are observed in the first derivative heat flow curves after the transition (Kim 2006, Mok 2009, Jin 2015). The T_g breadth is determined from $T_e - T_0$ and the values associated with Si-PS samples are plotted in Figure 10-3B. Relative to Si-PS 98 kg/mol, which exhibits a breadth of $12.7 \pm 0.5\ °C$, T_g breadth remains invariant with graft MW down to 36 kg/mol and increases to $15.3 \pm 0.4\ °C$ and $16.0 \pm 0.5\ °C$ for graft MWs of 13 kg/mol and 12 kg/mol, respectively. While both T_0 and T_e values decrease in the lowest MW Si-PS samples, the enhancement in T_g breadth in such cases can be attributed to greater reductions in T_0 values relative to T_e values. This suggests that as brush MW decreases, enhancements in configurational freedom provided by the high concentration of free chain ends in regions away from the nanoparticle interface becomes stronger. For unattached PS, T_g breadths are invariant with MW for the MW range studied and identical within error to the T_g breadth of high MW Si-PS. (See Table 10-1 for a summary of T_g breadth data.)

Results for T_g breadth of PS brushes grafted from silica nanoparticles may be compared with those of PS brushes grafted from flat silica substrates (Lan 2015). Using ellipsometry, Lan and Torkelson (Lan 2015) reported that T_g breadth of PS grafts increased from 20 °C to 35 °C with reduced graft M_n from 170 kg/mol to 23 kg/mol. The results of the present study are in agreement that the T_g breadth increases with decreasing graft MW.

Quantitative differences in the results can be attributed to differences in geometry between brushes on highly curved spherical nanoparticles and flat substrates. (They cannot be attributed to the different measurement methods, because the T_g breadths for 470 kg/mol PS as measured by DSC and ellipsometry were reported to be the same within error (Jin 2015).) For instance, in the spherical geometry, polymer grafts experience greater conformational freedom with increasing distance from the interface. The influence of the substrate is apparent until the polymer grafts exhibit random coil-like conformations far from the grafting interface. In contrast, the influence of the substrate extends to greater lengths along the polymer chains in brushes grafted from flat substrates. This is why Lan and Torkelson (Lan 2015) observed greater T_+

values (from ellipsometry) compared to T_e values (from DSC) in this study. Geometry also impacts the influence of free-surface effects on T_g behavior. In Si-PS, there are no true free surfaces. Thus, reductions in T_0 as observed via DSC are associated only with free chain-end effects. In contrast, in the case of brushes on a flat substrate, free chain ends are in contact with or very close to a free surface. As MW decreases, free-surface effects coupled with the enhanced conformational freedom provided by free chain ends cause substantial reductions in T_- as observed via ellipsometry. The enhancement in T_+ relative to T_e and reduction in T_- relative to T_0 due to sample geometry explains the greater T_g breadth observed in brushes on flat substrates than in brushes on spherical nanoparticles.

Fluorescence spectroscopy is used to investigate local T_g values in dense Si-PS brushes with high molecular weight. Figure 10-4 shows the normalized integrated intensity as a function of temperature for two samples. Lines fitted to the rubbery and glassy temperature dependences of integrated intensity yield T_g (Ellison 2003, Rittigstein 2006, Priestley 2007, Roth 2007c, Evans 2013a, Lan 2015). Open squares represent the data for grafted PS chains where the 1-pyrenylbutyl methacrylate (BPy) label is incorporated in trace amounts within 8 kg/mol of the graft interface (total graft M_n = 54 kg/mol), with local T_g = ~116 °C. Open triangles represent the data for grafted PS chains where the BPy label is incorporated within 14 kg/mol of the free chain ends (total graft M_n = 93 kg/mol), with local T_g = ~102 °C. The fluorescence approach yields local T_g values that agree quantitatively with T_0 and T_e values determined via DSC for Si-PS with high brush MW (Figure 10-3A). Based on Figure 10-2A, the Si-PS 54 kg/mol and Si-PS 93 kg/mol samples would be expected to yield the same overall average T_g to within 1 °C, with $T_g \approx$ 104 °C. This suggests that in high MW cases, the fraction of PS chains with enhanced local T_g near the graft interface is small relative to the fraction of PS chains exhibiting bulk-like behavior. In low MW brush cases, reductions in average T_g as observed by DSC can be attributed to increasing influence of free chain end effects.

The fluorescence results may be compared with those from Lan and Torkelson
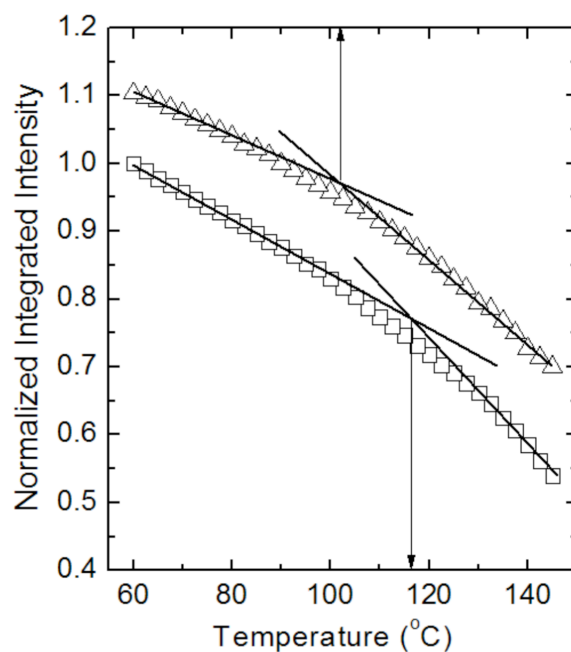
Figure 10-4: Normalized integrated intensity as a function of temperature for end-labeled Si-PS. Intensity values were normalized to the maximum intensity value and shifted arbitrarily for clarity. Open triangles represent Si-PS with 1-pyrenylbutyl methacrylate (BPy) labeling within 14 kg/mol of the free chain ends (total brush $M_n = 93$ kg/mol). Open squares represent Si-PS with BPy labeling within 8 kg/mol of the graft interface (total brush $M_n = 54$ kg/mol). Arrows indicate the location of T_g determined by the intersection of lines fitted to the rubbery and glassy temperature dependences of intensity.

(Lan 2015) who conducted similar experiments on PS grafted from flat silica substrates. They observed T_g = 136 °C near the graft interface and T_g = 86 °C near the free chain ends. The higher T_g near the flat substrate relative to that near the nanoparticle can be attributed to brush geometry. As mentioned in the discussion of Figure 10-3, the impact of dense grafting is retained to greater lengths along brushes in the case of flat substrates (relative to spherical nanoparticles) since polymer chains do not experience a large change in local conformation as a function of distance from the graft interface. The lower T_g in the free chain ends associated with a flat substrate relative to that in nanoparticles can be attributed to free-surface effects. In the case of flat substrates, the free chain ends are in contact with or very near a free surface whereas in the case of nanoparticles, there is no true free surface. These results demonstrate that grafting geometry impacts local T_g behavior.

Fragility behavior of Si-PS without a host matrix is also investigated using DSC. Figure 10-5A shows $\log(Q/Q_s)$ as a function of T_f^s/T_f for a 400 kg/mol PS standard and Si-PS 12 kg/mol. The cooling rates (Q) are -40, -20, -10, -4, -1, and -0.4 °C/min, and the standard cooling rate Q_s = -10 °C/min. Fictive temperature values are determined via DSC using the Richardson method (Richardson 1975), and T_f^s corresponds to the fictive temperature after cooling at the standard rate. The negative of the slope of a best-fit line in Figure 10-5A is the fragility (see Eqn. 1 in Experimental Section). For the two examples shown, fragility values are 160 and 110 for a 400 kg/mol PS standard and Si-PS 12 kg/mol sample, respectively. Plots like Figure 10-5A are used to determine fragility values for all samples in this study. Each sample is measured at least three times to obtain averages and standard deviations.

Figure 10-5B shows fragility as a function of MW for Si-PS and PS free chains determined via DSC. (Results are also summarized in Table 10-1.) The dotted line corresponds to the average fragility value of a 400 kg/mol PS standard. In PS free chains, fragility decreases from 163 ± 10 in 400 kg/mol PS to 140 ± 7 in 12 kg/mol PS. The reduction in fragility with decreasing MW in PS free chains is in agreement with values in literature (Santangelo 1998). In
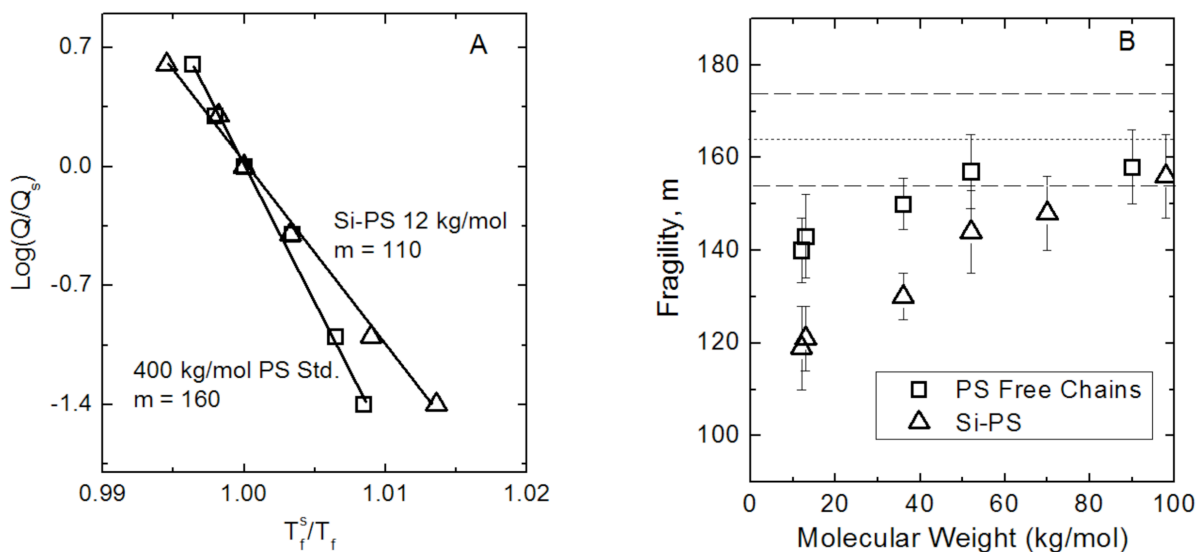
Figure 10-5: A: Log(Q/Q_s) as a function of T_f^s/T_f for 400 kg/mol PS and Si-PS 12 kg/mol. The negative of the slope is fragility (Eqn. 1). B: Fragility as a function of molecular weight for PS free chains (open squares) and Si-PS (closed triangles). The dotted and dashed lines correspond to the average fragility and standard deviation of a 400 kg/mol PS standard. The data points denote average values from three sample determinations of m, and error bars are associated with the standard deviation of three trials for each sample.

Si-PS, fragility decreases from 156 ± 9 in Si-PS 98 kg/mol to 119 ± 9 in Si-PS 12 kg/mol. Thus, the fragility of Si-PS 98 kg/mol is within error the same as that of high MW PS free chains. A comparison of 52 kg/mol Si-PS and PS free chains reveals that they both exhibit the same fragility values within experimental error. At 36 kg/mol, Si-PS exhibits significantly reduced fragility relative to PS free chains with the latter exhibiting no change within error from 400 kg/mol PS samples. At 13 kg/mol and 12 kg/mol, both Si-PS and PS free chains exhibit reduced fragility (outside error) relative to 400 kg/mol PS free chains, with Si-PS exhibiting greater reductions.

The data in Figure 10-5B indicate that grafting from spherical nanoparticles plays an important role in fragility behavior. In Si-PS, the free chain ends are concentrated in the spacing between neighboring Si-PS particles (Green 2011). As MW decreases, free chain ends influence chain packing to a greater extent. As mentioned in the discussion of Figure 10-2, reduction in MW introduces free volume and conformational mobility via free chain-end effects. Enhancements in conformational freedom allow chains to pack more efficiently, which reduces fragility (Dudowicz 2005a, Dudowicz 2005b, Kunal 2008, Zhang 2016). Figure 10-5B shows that PS free chains exhibit a weaker MW dependence of fragility than Si-PS. This can be attributed to the fact that free chain ends are randomly dispersed throughout the polymer in unattached PS. While a reduction in MW enhances the concentration of free chain ends, the impact on conformational freedom in unattached PS is less than that in Si-PS. We also note that stronger glass formation and reduced T_g in Si-PS is indicative of anti-plasticization behavior as indicated by other reports (Riggleman 2007, Oh 2009).

Although this is the first experimental characterization of fragility in Si-PS without a host matrix, comparisons may be made with reports on polymer-grafted nanoparticles within a host matrix. Oh and Green (Oh 2009)) used DSC to measure fragility of PS nanocomposites containing Au-PS nanoparticles. They investigated two Au-PS samples with graft MWs of 1 kg/mol and 48 kg/mol. In nanocomposites using Au-PS with 1 kg/mol grafts, fragility decreased

from 106 in neat PS to ~82 at 0.5 wt% Au-PS in PS. In nanocomposites using Au-PS with 48 kg/mol grafts, fragility decreased to ~99 at 1.5 wt% Au-PS in PS (Oh 2009). It is important to note that in their study the matrix PS had a MW of 5 kg/mol, so the reported fragility of the neat PS is 106. Although the fragility of the nanocomposites exhibited small reductions, their data may suggest that Au-PS nanoparticles themselves exhibited reduced fragility relative to PS free chains and also that fragility in PS-grafted nanoparticles decreased with decreasing MW. The interpretation agrees qualitatively with results in Figure 10-5B.

The results of this study may be compared with simulations of nanocomposites. Betancourt *et al*. (Betancourt 2013) used molecular dynamics simulations to investigate the impact of attractive and non-attractive interactions on T_g and fragility in nanocomposites containing bare nanoparticles. They reported enhancements in T_g and fragility for particle/matrix pairs with attractive interactions and reductions in T_g and fragility for particle/matrix pairs with non-attractive interactions. Based on these predictions, the Si-PS samples (without a matrix) exhibit T_g and fragility behavior that is consistent with non-attractive particle/matrix pairs. This result suggests that covalent attachment of chain ends to nanoparticles is not analogous to particle/matrix pairs that exhibit attractive interactions. This is in agreement with results of Akcora *et al*. (Akcora 2009a, Akcora 2010) who have indicated that the "dislike" between PS grafts and the nanoparticle cores is retained despite covalent attachment.

A comparison of the fragility results from Si-PS may be made to those from brushes on flat silica substrates. Using ellipsometry, Lan and Torkelson (Lan 2016) reported that fragility is independent of dense brush thickness down to 27 nm (M_n = 45 kg/mol). In this range, reducing the thickness and hence MW "does not significantly alter packing frustration in dense PS brushes." (Lan 2016) The results in this study are in agreement, where significant changes in fragility are only observed for brush MWs at 36 kg/mol and below. For sufficiently low MW brushes in Si-PS, the impact of free chain ends in enhancing conformational mobility increases. This enables more efficient packing and thus reduced fragility in the low MW polymer chains

grafted from spherical nanoparticles.

10.4 Conclusions

Glass transition behavior of PS-grafted silica nanoparticles without a host polymer matrix is investigated by DSC. T_g values (both $T_{g,onset}$ and T_f) decrease as a function of decreasing graft MW, in agreement with reports in literature (Savin 2002b, Dang 2013, Kim 2015a). Reductions in T_g are attributed to the impact of free chain ends in enhancing conformational mobility of polymer chains. At the same MW, Si-PS exhibited greater T_g relative to PS free chains due to chain tethering. DSC is also used to determine that T_g breadth is invariant within error with decreasing graft MW down to 36 kg/mol and increases for graft MWs of 12 and 13 kg/mol. The enhanced T_g breadth of low MW Si-PS can be understood to arise from greater reduction in local T_g associated with the free chain ends relative to the local T_g associated with the grafted ends. Using fluorescence spectroscopy, we find that T_g is ~116 °C within 8 kg/mol of the graft interface (total brush M_n = 54 kg/mol) and is ~102 °C within 14 kg/mol of the free chain ends (total brush M_n = 93 kg/mol). The MW dependence of fragility in Si-PS without a host matrix is investigated for the first time using DSC. With reductions in graft MW, fragility of Si-PS decreases to a greater extent than in unattached PS. This result is attributed to the enhanced ability of free chain ends to impact chain packing in Si-PS relative to unattached PS and is in contrast to results on densely grafted PS brushes on flat silica substrates, which who show no MW dependence to brush fragility for the brush MWs under investigation.

CHAPTER 11

Molecular Weight Dependence of the Intrinsic Size Effect on T_g in

AAO Template-Supported Polymer Nanorods: A DSC Study

11.1 Introduction

The effects of nanoscale confinement on the glass transition temperature (T_g) of amorphous polymers and low molecular weight (MW) glass formers have been heavily studied over the past twenty-five years (Jackson 1991, Keddie 1994b, Forrest 1997a, Grohens 1998, Fukao 2000, Kim 2000, Mattsson 2000, Dalnoki-Veress 2001, Kawana 2001, Tsui 2001, Grohens 2002, Xie 2002, Ellison 2003, Sharp 2003, Ellison 2005, Fakhraai 2005, Roth 2006, Seemann 2006, Mundra 2007b, Rittigstein 2007, Roth 2007a, Roth 2007c, Torres 2009, Dion 2010, Glynos 2011, Kim 2011, Baeumchen 2012, Evans 2013a, Gao 2013, Zhang 2013a, Lan 2014, Vignaud 2014, Baglay 2015, Evans 2015, Geng 2015, Glor 2015, Glynos 2015, Kanaya 2015, Kawaguchi 2015, Li 2015a, Priestley 2015, Zhang 2015, Geng 2016, Jin 2016, Lan 2016, Liu 2016, Shin 2016, Tan 2016). The interest in this topic arises from important scientific questions related to both confinement effects (Forrest 2001, Alcoutlabi 2005, Peter 2006, Riggleman 2006, Ediger 2014, Mirigian 2014, White 2015, Xia 2015a, Xie 2015, Ngai 2016, Simmons 2016) and the underlying nature of the glass transition itself (Anderson 1995) as well as to the significance of nanoconfined polymers in advanced technological applications ranging from nanolithography to nanocomposites. Most typically, T_g-confinement effects have been studied for linear polymers confined in supported thin films with one free surface (Keddie 1994b, Grohens 1998, Fukao 2000, Kim 2000, Kawana 2001, Tsui 2001, Grohens 2002, Xie 2002, Ellison 2003, Sharp 2003, Ellison 2005, Fakhraai 2005, Seemann 2006, Mundra 2007b, Rittigstein 2007, Roth 2007a, Roth 2007c, Torres 2009, Dion 2010, Glynos 2011, Kim 2011, Baeumchen 2012, Evans 2013a, Lan 2014, Vignaud 2014, Baglay 2015, Evans 2015, Geng 2015, Glor 2015, Glynos 2015, Kanaya 2015, Kawaguchi 2015, Li 2015a, Priestley 2015, Zhang 2015, Geng 2016, Jin 2016, Lan 2016, Liu 2016, Shin 2016, Tan 2016) and, to a lesser extent, in

free-standing films with two free surfaces (Forrest 1997a, Mattsson 2000, Dalnoki-Veress 2001, Roth 2006, Kim 2011, Gao 2013). As generally characterized by (pseudo-)thermodynamic methods which measure transitions over a small range near T_g, including ellipsometry, fluorescence, capacitive dilatometry, etc., T_g decreases with decreasing thickness in the absence of attractive polymer-substrate interactions but increases with decreasing thickness in the presence of sufficiently strong attractive polymer-substrate interactions, *e.g.*, hydrogen bonds. Anionically polymerized polystyrene (PS) has no potential to undergo hydrogen bonding and exhibits the same reduction in T_g with nanoscale film thickness on substrates that have different levels of hydroxyl groups on the substrate surface, *e.g.*, Si/SiO$_x$ and alumina (Tan 2016).

Differences in the quantitative strength of the T_g-confinement effect have been noted as a function of polymer species for supported polymer films lacking attractive polymer-substrate interactions. One explanation of the polymer species dependence of the T_g-confinement effect in such supported films relates to the fragility (*m*) of the polymer and the extent to which *m* can be perturbed by confinement, *e.g.*, by the presence of free surfaces in supported films and free-standing filmsn (Evans 2013a, Jin 2016, Lan 2016). Fragility, which is related to the extent of cooperativity required for α-relaxation dynamics associated with T_g as well as the breadth of the α-relaxation distribution, is quantitatively defined by the slope of the logarithm of the α-relaxation time in the liquid state as a function of temperature ($m = d[\log \tau_\alpha]/d[T_g/T]$) in the limit $T = T_g$ (Angell 1985, Angell 1991, Bohmer 1992, Bohmer 1993, Dudowicz 2005a, Evans 2013a). It reflects the structure and dynamics of a glass formerAngell 1985 as well as chain packing frustration, with greater packing frustration being associated with higher fragility values (Dudowicz 2005a). The explanation of the polymer species dependence of the T_g-confinement effect in supported films lacking attractive polymer-substrate interactions posits that, with few exceptions, linear polymers with greater bulk fragility values and thereby greater cooperativity of α-relaxation dynamics undergo greater perturbations of fragility associated with free surfaces and thus exhibit larger T_g-confinement effects (Evans 2013a, Jin 2016). Experimental support for

this explanation has been provided by several studies (Evans 2013a, Jin 2016, Lan 2016).

Whereas some polymer species (*e.g.*, poly(methyl methacrylate) (PMMA) and poly(α-methyl styrene)) exhibit a MW dependence of the T_g-confinement effect in supported films even when samples of different MW have identical tacticity (Grohens 1998, Kim 2000, Dion 2010, Lan 2014, Geng 2015, Geng 2016), studies have indicated that there is little or no MW dependence of the T_g-confinement effect in supported PS films (Keddie 1994b, Kawana 2001, Ellison 2003, Ellison 2005, Seemann 2006, Lan 2014, Zhang 2015). In contrast, at sufficiently high MW, free-standing PS films exhibit MW dependence of T_g-confinement effects (Forrest 1997a, Mattsson 2000, Dalnoki-Veress 2001, Kim 2011), the cause of which remains in question.

Although the seminal study on the T_g-confinement effect was done via differential scanning calorimetry (DSC) on low MW, non-polymeric glass formers confined within a nanoporous glass and thus with no free surface (Jackson 1991), relatively few studies have employed DSC to characterize T_g-confinement effects in polymers confined in (quasi-)nanoporous substrates (Shin 2007, Duran 2009, Giussi 2013, Li 2014, Sha 2014, Zhao 2014, Li 2015b, Lopez 2015, Reid 2015, Tan 2016, Wang 2016a). Anodic aluminum oxide (AAO) templates with cylindrical nanopores of various sizes make such studies possible. DSC offers a simple assessment of T_g and is the most common method to characterize bulk T_g in both academic and industrial environments. As a result, DSC characterization of polymer confined within AAO templates provides an important avenue for advancing studies of confinement effects on T_g and physical aging. We recently compared DSC characterization of T_g-confinement effects for PMMA nanotubes (with a free surface) supported within the cylindrical nanopores of AAO templates with ellipsometry characterization of T_g-confinement effects for PMMA thin films supported on alumina substrates (Tan 2016). We obtained excellent agreement between the two confinement effects (Tan 2016).

Here, we examine intrinsic size effects in the absence of free surfaces or attractive

polymer-substrate interactions by using DSC to characterize the T_g of PS nanorods confined within unmodified, cylindrical nanopores present in AAO templates. We vary PS MW and nanorod diameter and demonstrate MW dependence at high MW of the quantitative perturbation of T_g caused by intrinsic size effects. Notably, intrinsic size effects on T_g are evident only when $d \leq \sim 2R_g$, where d is the nanorod diameter and R_g is the bulk polymer radius of gyration. We explain why such intrinsic size effects do not contradict previous reports (Keddie 1994b, Kawana 2001, Ellison 2003, Ellison 2005, Seemann 2006, Lan 2014, Zhang 2015) indicating that the T_g-confinement effect exhibits little or no MW dependence in supported PS films and offer a potential explanation for the origin of the intrinsic size effects observed in our study.

11.2 Experimental Methods

11.2.1 Materials

High MW, anionically synthesized PS samples of various nominal MW were from Pressure Chemical Co. and Toyo Soda Manufacturing. We characterized the absolute number-average molecular weight (M_n) and weight-average molecular weight (M_w) of these as-received samples by gel permeation chromatography (GPC, Waters Breeze instrument) in tetrahydrofuran (THF) solvent with a multiangle laser light-scattering detector (mini Dawn, Wyatt Technologies) and K-5 flow cell. We employed a differential index of refraction (dn/dc) value of 0.184 mL/g for PS in THF (HPLC grade, Sigma-Aldrich). The results, which are summarized in Table 11-S1, show substantial agreement between nominal MWs reported by the suppliers and our absolute M_n and M_w values at low to moderate MW. However, for PS samples with reported MW of 900 kg/mol or higher, the MWs reported by the suppliers substantially exceed the GPC/light scattering determined values of absolute M_n and M_w.

Anodic aluminum oxide templates of various nominal pore diameters were obtained from Puyuan Nano with reported diameters of 20, 40, 70, 100, and 200 nm and used without any chemical modification of the template surfaces. Figure 11-S1 shows scanning electron

microscopy images (top view and cross section) of the as-received, nominally 20 and 70 nm diameter AAO templates. To obtain these images, the AAO templates were mounted onto carbon tape. A 5-nm-thick layer of gold was sputtered onto the surface to prevent charging, and a Hitachi SU 4800 scanning electron microscope was used. (A limited set of measurements resulting in the determination of a single fragility value used an AAO template from a different source [Anopore Inorganic Membranes, with reported diameter of 200 nm] that was described in Tan and Torkelson (Tan 2016).)

11.2.2 Methods to Produce AAO Template-Supported PS Nanorods

Polymer films were produced by casting concentrated polymer solutions (typically ~15 wt% in toluene) onto degreased Kapton paper. The films were held at ambient conditions for several hours and then placed in a vacuum oven at 140 °C overnight. After cooling, films were collected by carefully peeling the PS from the Kapton paper.

These films were employed in two separate procedures for producing template-supported PS nanorods. For the three higher MW samples, nanorods were produced by placing a bulk film atop a bare template and melt infiltrating at 250 °C for 90 min under flowing nitrogen. (Thermogravimetric analysis demonstrated that there was no mass loss within error at such heating conditions.) Samples were then cooled to room temperature at -40 °C/min. With lower MW samples, annealing at 250 °C for 90 min results in nanotubes (Tan 2016) rather than nanorods. For the as-received PS sample with measured $M_n = 182$ kg/mol and $M_w = 190$ kg/mol, nanorods were produced by placing a polymer film atop a bare template and annealing at 150 °C for 72 h under vacuum. A measurement of T_g was also done for nanorods in a nominally 20 nm diameter AAO template with an as-received PS sample with measured $M_n = 30.1$ kg/mol and $M_w = 30.2$ kg/mol. This nanorod sample was prepared by annealing at 140 °C for 48 h. In all cases, excess polymer left atop the template after melt infiltration was removed by polishing with SiC grit paper (Tan 2016).

11.2.3 Size and Morphological Characterization of PS Nanorods

Nanorods were first released from the template by taking a piece of infiltrated template and immersing it in 2 M sodium hydroxide that dissolves the template. Rods were collected and rinsed in distilled water before mounting onto carbon tape. A thin layer of osmium was sputtered onto the surface to prevent charging. A Hitachi SU 4800 SEM was used to obtain images. The size distribution was determined by measuring the diameters of 50 to 100 nanorods using ImageJ software. Measurements were done only on areas where there was no overlap with other rods; each rod was measured only once along its entire length. The mass-average diameter (d_m) and number-average diameter (d_n) of the nanorods were determined for each template size using one of the higher MW PS samples; rod diameters were nearly monodisperse with differences being noted from the nominal template diameters reported by the supplier. We employ d_m values in our quantitative characterization of T_g-confinement effects since T_g was measured by DSC, which is sensitive to mass of rods of particular diameters as opposed to number of rods of particular diameters. (Given the very small differences in d_m and d_n values, the conclusions reached from our study would be the same regardless of whether values of d_m or d_n are used.)

11.2.4 Thermal Characterization of AAO Template-Supported PS Nanorods

The T_g values were obtained using a Mettler Toledo 822e differential scanning calorimeter. T_g values were determined via the onset method, $T_{g,onset}$, and by use of the Richardson method (Richardson 1975) to obtain fictive temperature, T_f. In limited samples, T_f were also obtained by the Moynihan method (Moynihan 1976). Although the T_f determined by Richardson method and Moynihan method is not exactly the same, the results were reasonably close (see Table 11-S2 in section 11.5). The Richardson method was used to determine T_f values in this study. A DSC sample was created by placing a small piece of infiltrated template into a 40 µl aluminum DSC pan. Each sample was first annealed in the DSC at 130 °C (~30 °C above the bulk T_g) for 10 min and then cooled to 30 °C at a rate of -40 °C/min. Measurements of T_g were obtained on second heat from 30 at a rate of 10 °C/min. Some second heats were terminated at

140 °C whereas many others were terminated at 160 °C or higher, with results in excellent agreement without regard to the ending temperature. Reported T_g values are averages of at least three measurements with associated errors being standard deviations. (The protocol used to measure fictive temperatures for fragility determination is described in Results and Discussion.)

11.2.5 Molecular Weight Characterization of PS in the Nanorods after Melt Infiltration into the AAO Templates

After DSC characterization, template-supported PS nanorods were added to HPLC-grade THF and allowed to sit at room temperature for 24 h in order for the PS to fully dissolve. The solution was then filtered with 0.2 μm PTFE syringe filter and characterized by GPC using the light-scattering detector as described in section A above. For each PS sample, we characterized the absolute M_n and M_w values of 24 nm, 63 nm, and 210 nm PS nanorods, which had values that were identical within error for a given PS sample. Table 11-1 lists absolute M_n and M_w values for each PS sample before and after melt infiltration.

11.3 Results and Discussion

11.3.1 Size, Morphology, and MW Characterization of PS Nanorods after Melt Infiltration

Figure 11-1 provides a schematic representation of the procedure used to produce template-supported PS nanorods by capillary filling in the melt state. For the three higher MW PS samples, melt infiltration from a polymer film set atop a template was done under flowing nitrogen at 250 °C for 90 min. An attempt to use this protocol to produce template-supported nanorods of PS with an extraordinarily high, nominal MW of 23,000 kg/mol (as reported by the supplier, Polysciences, Inc.) was unsuccessful, possibly associated with the ultrahigh viscosity of this PS sample (Zhang 2006). The use of this protocol at 250 °C for 90 min with an anionically polymerized PS standard with nominal MW = 190 kg/mol, as reported by the supplier, led to formation of nanotubes (Tan 2016) rather than nanorods for some template diameters. For this PS sample, an alternative melt infiltration condition involving annealing at 160 °C for 72 h under

Table 11-1: Molecular weight of PS characterized by GPC before and after infiltration

Sample Name	Before infiltration			After infiltration		
	M_n (kg/mol)	M_w (kg/mol)	PDI	M_n (kg/mol)	M_w (kg/mol)	PDI
30.0/30.1	30.1	30.2	1.01	30.0	30.1	1.01
175/182 PS	182	190	1.05	175	182	1.04
326/498 PS	548	655	1.19	326	498	1.52
959/1260 PS	1,480	1,580	1.07	959	1,260	1.30
929/1420 PS	2,880	3,070	1.06	929	1,420	1.53
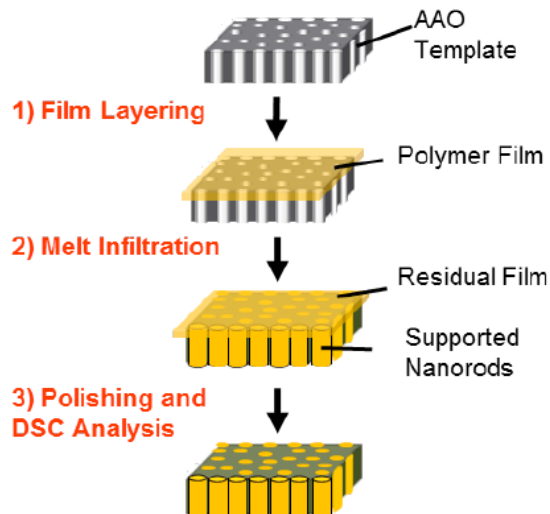
Figure 11-1: Schematic for producing template-supported PS nanorods. After melt infiltration, templates are polished of excess polymer in preparation for DSC analysis.

vacuum led to nanorods. Finally, template-supported PS nanorods were also made for the smallest rod diameter (nominally 20 nm) using an anionically polymerized PS standard with nominal MW of 30 kg/mol by annealing at 140 °C for 48 h under vacuum.

Figure 11-2 shows scanning electron micrograph images of bare, unsupported PS nanorods after removal of the template by dissolution in a 2 M sodium hydroxide solution. These nanorods were made in nominally 100-nm-diameter AAO templates (as reported by the supplier) using PS with M_n = 959 kg/mol and M_w = 1260 kg/mol as determined after melt infiltration. The images show that nanorods made using our melt infiltration method are continuous and defect-free. Detailed characterization of nanorods in Figure 11-2 and similar images using ImageJ software indicates that the mass-average diameter is 86 nm and the number- average diameter is 84 nm. (Nanorod length (L) is generally in the tens of microns, so $L >> d$.) Thus, although the nanotube diameters are nearly uniform, the measured diameter differs by about 15% from the nominal template pore diameter reported by the supplier. Related analyses were performed on nanotubes made from each template with differently sized cylindrical nanopores. Values of d_m and d_n for each template size are given in Table 11-2. (The bare, unsupported PS nanorods are used here only for characterization of nanorod uniformity and diameters. Thermal analysis by DSC was done exclusively on template-supported nanorods.)

Table 11-1 shows the absolute M_n and M_w values measured by GPC with light-scattering detection for the four PS samples used for the whole range of available AAO templates. Measurements are provided before infiltration (as-received samples) and after melt infiltration and DSC characterization of T_g. (See Table 11-S1 in section 11.5 for absolute MW characterization of a range of as-received PS standards, showing that results exhibit excellent accord between reported and experimentally determined MWs for samples with reported MW $\leq$ 290 kg/mol but substantial differences for samples with reported MW $\geq$ 900 kg/mol.) Table 11-1 also provides an explanation for our sample naming convention. For example, the sample named 175/182 PS has absolute M_n and M_w equal to 175 kg/mol and 182 kg/mol, respectively, *after*
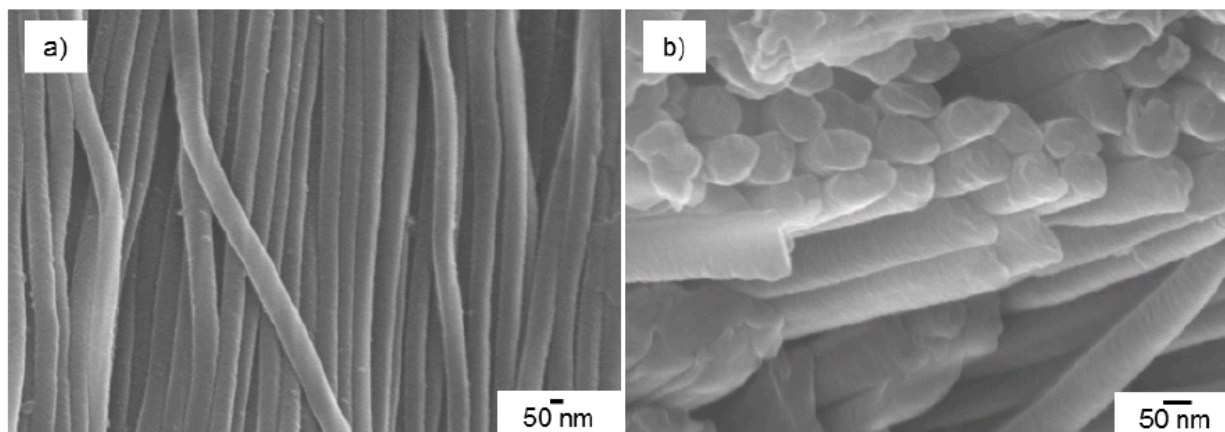
Figure 11-2: Scanning electron micrograph images of 959.1260 PS nanorods produced using melt infiltration into AAO templates. SEM images were taken on unsupported nanorods by dissolving the AAO template in 2 M NaOH solution. a) Side view of nanorods with a $d_m = 86$ nm. b) End view of the same nanorods as in (a).

Table 11-2: Summary of $T_{g,onset}$ and T_f values for the PS nanorods as a function of mass-average rod diameter, number-average rod diameter, and molecular weight.

Mass-Avg. Diameter, d_m (nm)	Number-Avg. Diameter, d_n (nm)	$T_{g,onset}$ /T_f 175/182 PS (°C)	$T_{g,onset}$ /T_f 326/498 PS (°C)	$T_{g,onset}$ /T_f 959/1260 PS (°C)	$T_{g,onset}$ /T_f 929/1420 PS (°C)
Bulk	Bulk	101.6 ± 0.3/ 102.8 ± 0.4	104.5 ± 0.3/ 104.9 ± 0.3	103.8 ± 0.3/ 104.1 ± 0.3	103.3 ± 0.1/ 104.4 ± 0.4
210	190	101.7 ± 0.2/ 102.8 ± 0.2	--	103.9 ± 0.8/ 104.3 ± 1.0	102.5 ± 0.3/ 103.1 ± 0.3
86	84	101.7 ± 0.6/ 103.1 ± 0.4	105.2 ± 1.0/ 105.3 ± 1.0	102.4 ± 0.9/ 102.8 ± 0.5	101.5 ± 0.7/ 102.2 ± 0.9
63	61	102.8 ± 0.4/ 103.5 ± 0.4	104.0 ± 0.4/ 105.0 ± 0.6	101.6 ± 1.0/ 102.9 ± 0.2	100.9 ± 0.4/ 101.3 ± 1.0
33	32	101.1 ± 0.7/ 102.5 ± 0.5	103.9 ± 0.4/ 104.7 ± 0.9	100.2 ± 1.0/ 100.8 ± 0.8	98.5 ± 0.4/ 97.6 ± 0.9
24	24	99.1 ± 1.0/ 100.8 ± 0.6	101.3 ± 1.0/ 103.3 ± 1.0	97.1 ± 0.9/ 98.4 ± 0.3	95.9 ± 0.9/ 96.2 ± 1.2

*Note: 326/498 PS cannot be made into 210 nm nanorods with high temperature procedure.

melt infiltration. For the 175/182 PS sample, there is very little reduction (~4%) in MW values after melt infiltration relative to before melt infiltration. However, for the three higher MW samples, there are substantial reductions in MWs after melt infiltration, *e.g.*, 20-24% reductions in M_w for 326/498 PS and 959/1260 PS. A part of these reductions could arise for from the different wetting transition temperatures and melt viscosities as a function of MW, which led Zhang et al. (Zhang 2006) to exploit these effects in cylindrical alumina nanopores to fractionate PS with different MW. No evidence of mass loss is observed by thermogravimetric analysis at the annealing conditions employed in our study. We do not discount the possibility of extremely small levels of chain scission occurring at the annealing conditions employed in our study that could contribute to the observed MW reductions after melt infiltration. However, we note that "bulk T_g behavior (T_g and apparent T_g breadth) of neat PS are unaffected after thermal annealing at 250 °C for 90 min under dry nitrogen" (Jin 2016).

11.3.2 T_g as a Function of Nanorod Diameter and PS Molecular Weight

Figure 11-3 shows representative DSC heat flow curves as a function of temperature for template-supported nanorods, which contain 175/182 PS (Figure 11-3A) and 959/1260 PS (Figure 11-3B). Values of bulk T_g ($T_{g,bulk}$) for these samples are 104.5 ± 0.3 °C (175/182 PS) and 103.8 ± 0.3 °C (959/1260 PS), within error identical to the values obtained for the template-supported PS nanorods with $d_m = 210$ nm. See Table 11-2 for a summary of T_g values for template-supported PS samples as a function d_m and d_n for each PS sample.

As shown in Figure 11-3A and Table 11-2, T_g remains invariant within error with respect to bulk T_g for 175/182 PS with decreasing nanorod diameter down to $d_m = 33$ nm and exhibits a 2 °C reduction when $d_m = 24$ nm. In contrast, as shown in Figure 11-3B and Table 11-2, confinement effects outside the range of experimental error are evident with 959/1260 PS when $d_m \leq 63$ nm, with $T_{g,rod} - T_{g,bulk} = \sim$ -6 °C in 24-nm-diameter nanorods. A slightly larger T_g depression is evident in 24-nm-diameter nanorods made with 929/1420 PS, with $T_{g,rod} - T_{g,bulk} = \sim$ -8 °C. If we define significant intrinsic size effects as cases in which $|T_{g,rod} - T_{g,bulk}| > 2.0$ °C,
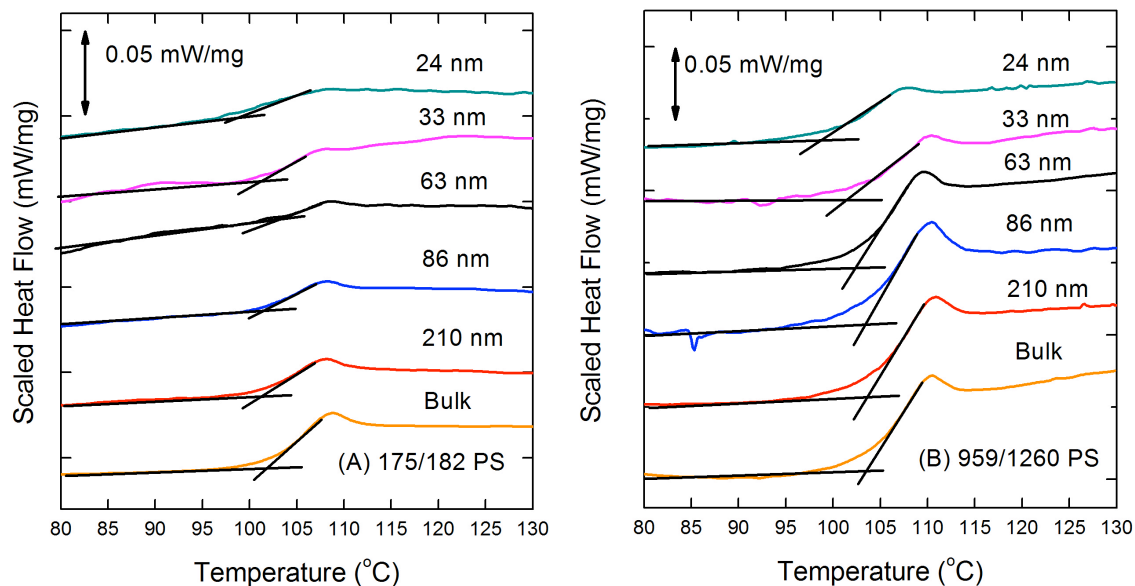
Figure 11-3: Scaled DSC heat flow curves for template-supported PS nanorods of varying diameter. Plots are shown for 175/182 PS nanorods (A) and 959/1260 PS nanorods (B). The curves are vertically shifted in an arbitrary manner to avoid overlapping. (Note: the units on the y-axis are reported as mW/mg, where the mg refers to the total mass of the polymer rods and AAO template in the DSC sample. We caution the reader in making comparisons between the heat capacity changes between A & B.)

then such effects are also evident in 326/498 PS for $d_\mathrm{m} = 24$ nm and 929/1420 PS for $d_\mathrm{m} \leq 63$ nm. Finally, we note that DSC characterization was also done on a 30.0/30.1 PS sample in the template yielding $d_\mathrm{m} = 24$ nm. As shown in Figure 11-S2 (in section 11.5), the T_g data (both $T_\mathrm{g,onset}$ and T_f) for this sample exhibit no reduction in the nanorod relative to bulk PS.

In addition to T_g values, we also characterized the heat capacity jump, ΔC_p, at T_g in the 929/1420 PS sample as a function of d_m. As shown in Table 11-S3 (in section 11.5), when taking an error of 0.01 J/(gK), ΔC_p is unchanged from its bulk value of 0.27 J/(gK) with decreasing nanorod diameter down to 63 nm. The strength of the glass transition as characterized by ΔC_p decreases to 0.23 and 0.21 J/(gK) in nanorods with $d_\mathrm{m} = 33$ and 24 nm, respectively.

Figure 11-4A shows values of $T_\mathrm{g,rod} - T_\mathrm{g,bulk}$ (where T_gs are onset values) and Figure 11-4B show values of $T_\mathrm{f,rod} - T_\mathrm{f,bulk}$ as a functions of d_m and PS MW and demonstrate that there is a MW dependence of the intrinsic size effect on T_g. The nanorod diameters at which intrinsic size effects become evident in these samples are of the order of the bulk-state radius of gyration, R_g, of the polymer chains. Previous studies have reported the following relationship between R_g and the MW of bulk, nearly monodisperse PS (Schmidt 1981, Hayward 1999):

$$R_\mathrm{g} = 0.029(\mathrm{MW})^{0.50} \qquad (1)$$

where R_g has units of nm and MW has units of g/mol. To simplify comparison in the text and figures, in characterizing R_g values we have taken MW to be the M_w value determined for each melt-infiltrated nanorod sample. (We provide similar plots in Figure 11-S3 in section 11.5 where we have characterized R_g using the M_n value for each melt-infiltrated sample.)

Although the $T_\mathrm{g,onset}$ data in Figure 11-4C apparently collapse to a single curve when plotted as a function of $d_\mathrm{m}/(2R_\mathrm{g})$, there is a small difference in the T_f data plotted in Figure 11-4D, with the two data points for the 326/498 PS sample being ~1.5 °C above the other data points at $d_\mathrm{m}/(2R_\mathrm{g})$ values of ~0.6 and ~0.8. Related behavior is apparent when data are plotted in the same format but with R_g determined using the M_n for each melt-infiltrated nanorod sample. (See Figure 11-S3 in section 11.5.) Future work is warranted, possibly with a greater number of MWs of PS
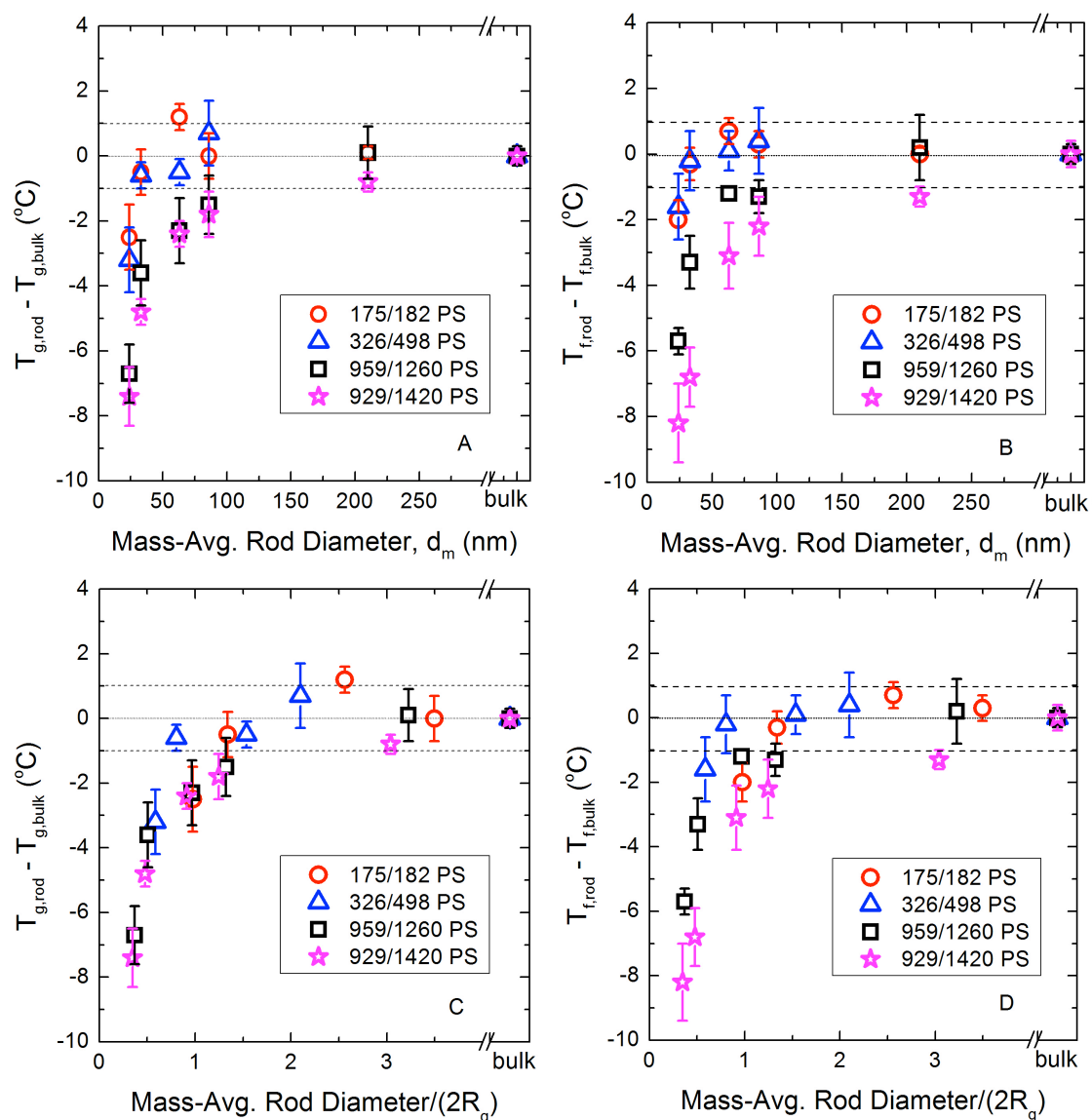
Figure 11-4: $T_{g,rod} - T_{g,bulk}$ (A) and $T_{f,rod} - T_{f,bulk}$ (B) for template-supported PS nanorods of varying molecular weight plotted as a function of rod diameter. $T_{g,rod} - T_{g,bulk}$ (C) and $T_{f,rod} - T_{f,bulk}$ (D) for template-supported PS nanorods of varying molecular weight plotted as a function of rod diameter/$(2R_g)$. R_g of each sample set is calculated from M_w in (C) and (D). Error bars represent the standard deviation of T_g and T_f values.

extending to higher MW as well as with other linear polymer species that do not exhibit significant attractive interactions with alumina substrates, to determine whether plotting data in the form of Figures 11-4C and 11-4D (and Figure 11-S3) leads to a collapse of data to single, (quasi-)universal curve.

11.3.3 Intrinsic Size Effect on Fragility as a Function of Nanorod Diameter

In order to demonstrate that intrinsic size effects on T_g in supported PS nanorods are accompanied by intrinsic size effects on fragility, the cooling-rate dependence of fictive temperature was measured on 959/1260 PS nanorods, with analysis as follows (Robertson 2000, Wang 2002):

$$\log_{10} (Q/Q_{std}) = m - m (T_{f,std}/T_f) \qquad (2)$$

Here, Q and Q_{std} are cooling rate and the standard cooling rate and $T_{f,std}$ is the fictive temperature at the standard cooling rate. Figure 11-5 shows DSC heat flow curves obtained on heating at a rate of 20 °C/min after cooling at various rates for bulk PS and 33-nm-diameter template-supported PS nanorods. The Richardson method (Richardson 1975) was used to determine T_f for each cooling rate.

Figure 11-6A is a plot of log (Q/Q_{std}) as a function of $T_{f,std}/T_f$ for a set of five diameters of template-supported 959/1260 PS nanorods. (Data at some cooling rates for the 24-nm-diameter nanorods were of insufficient quality to obtain a well justified determination of fragility; a fifth set of nanotubes was prepared with another AAO template described by Tan and Torkelson (Tan 2016), leading to a measured d_m value of 370 nm where a bulk response is anticipated.) In Figure 11-6A, Q_{std} is taken to be -20 °C/min. The m values were determined from slopes and intercepts of the lines in Figure 11-6A, which represent best fits to the data.

Figure 11-6B shows the intrinsic size effect on m of template-supported 959/1260 PS nanorods. Assuming that positive identification of a m-confinement effect requires a greater than 10% deviation in m from m_{bulk} (m_{bulk} = 169 as characterized by DSC on a bulk sample, in reasonable agreement with values reported for PS in other studies
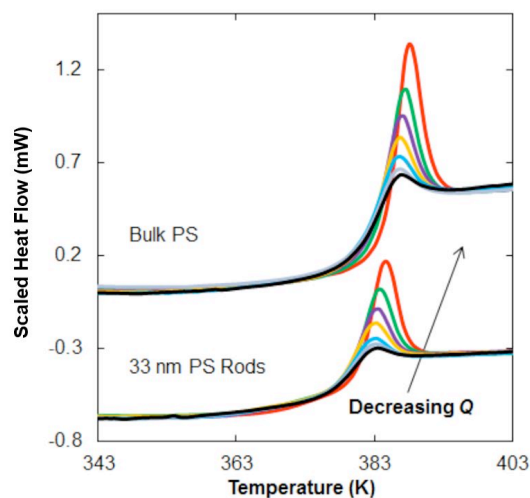
Figure 11-5: Enthalpy relaxation curves for bulk PS and 33-nm-diameter template-supported 959/1260 PS nanorods. DSC heat flow curves were obtained upon heating at a rate of 20 °C/min after cooling at rates of -0.4, -1, -2, -4, -10, -20, and -40 °C/min.
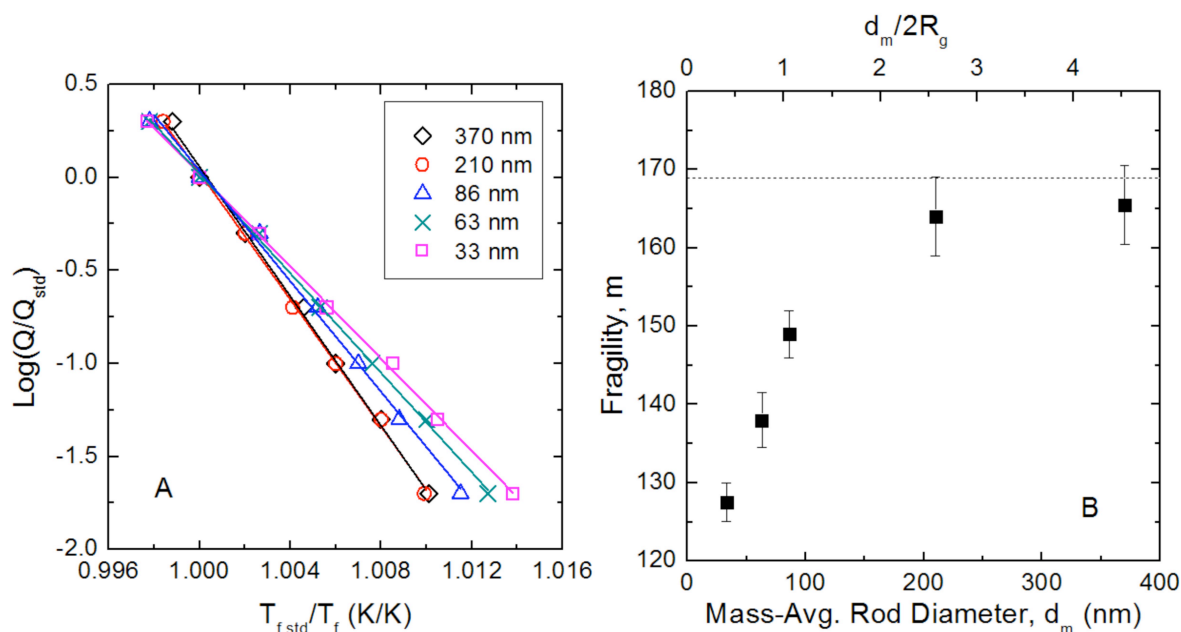
Figure 11-6: (A) Plot of log (Q/Q_{std}) as a function of ($T_{f,std}/T_f$) for template-supported PS nanorods for various mass-average rod diameters, d_m. Data are shown for 959/1260 PS. Fragility values are determined by the slopes in (A). (B) Fragility values as a function of d_m and characteristic length. Error bars correspond to the standard deviations. The dotted line corresponds to bulk fragility ($m = 169$).

(Dalle-Ferrier 2009, Evans 2013a, Zhang 2013b, Evans 2015, Jin 2016, Lan 2016)), we observe m-confinement effects for $d_m \leq 86$ nm, with 12, 18, and 24% reductions from m_{bulk} in 86-, 63-, and 33-nm-diameter nanorods, respectively. In order to ascertain whether the intrinsic size effect on fragility has a MW dependence similar to that on T_g, characterization of m-intrinsic size effects of other MW samples of template-supported PS nanorods is warranted.

Results provided in Figures 11-4 and 11-6 as well as Table 11-2 for 959/1260 PS indicate that the onset of intrinsic size effects occurs at d_m values slightly above 86 nm for fragility but at 63 nm $< d_m < 86$ nm for T_g. Studies on supported polymer films and silica-capped nanospheres have similarly reported that the measurable onset of m-confinement effects occurs at larger length scales compared to the onset of T_g-confinement effects (Zhang 2013c). One factor that may contribute to the different length scales is the fact that, as reported in the literature, T_g-confinement effects in films are commonly measured with T_g determined upon cooling at a single rate, often -1 °C/min. However, determination of m-confinement effects involves measuring the cooling rate dependence of T_g or T_f. Thus, the larger length scale associated with m-confinement effects may reflect a larger length scale of T_g-confinement effects at lower cooling rate. Future study is warranted to determine the extent to which other possible factors may also contribute to these different, apparent confinement length scales.

11.3.4 Comparisons with Previously Reported Studies

Our study focuses on the effect of polymer MW and bulk polymer R_g on the intrinsic size effect of PS nanorods that are infiltrated into unmodified AAO templates with cylindrical pores. Here we limit comparison of experimental studies to ones that have focused on AAO template-supported polymeric PS nanorods where the template surface was not chemically modified. For example, we note that Alexandris et al. (Alexandris 2016) recently reported on the glass temperature of PS confined in nanoporous alumina using dielectric relaxation spectroscopy. However, their PS sample was dimeric/trimeric styrene and not polymeric PS, as M_n was reported to be 266 g/mol (with $T_{g,bulk} = -174$ °C by DSC and -170 °C by dielectric relaxation

spectroscopy) (Alexandris 2016). As the sample studied by Alexandris et al. (Alexandris 2016) could be described to be a low MW glass former rather than a polymer, we defer further discussion.

The results shown in Figures 11-3 and 11-4 differ from those reported in 2007 by Shin et al. (Shin 2007) who performed DSC characterization of T_g of six MWs (with reported MWs ranging from 115 to 1210 kg/mol) of PS confined in nanoporous alumina with $d \sim 15$ nm. They prepared the nanorods by melt infiltration via an annealing process. Each "sample was heated to 190 °C under vacuum" (Shin 2007), but no information was provided on the time scale or whether the time varied with MW. They also did not characterize the PS MWs after melt infiltration as we did in our current study. They reported data taken upon heating at a rate of 30 °C/min after physically aging the samples at 60 °C for 18 h. Neither the use of physical aging prior to heating nor the 30 °C heating rate is part of a typical method for DSC measurement of T_g. However, both the physical aging and the more rapid than standard heating rate should accentuate the ability to discern the presence of a glass transition by DSC, if it difficult to discern the glass transition using more standard heat/cool/heat approaches for determination of T_g values by DSC.

Heat flow DSC curves reported by Shin et al. (Shin 2007) showed that a bulk sample of 1210 kg/mol PS exhibited an enthalpy relaxation peak, which was absent in all of their PS samples confined within the nanoporous alumina. They also commented, "The glass-transition region of polystyrene in the nanoporous alumina… showed little dependence on the molecular weight" (Shin 2007). Given eqn. (1) (which indicates that Shin et al.'s PS samples may have had R_g values ranging from 9.8 to 31.9 nm) and our results shown in Figures 11-4C and 11-4D, with use of a DSC protocol like that in our study each of Shin et al.'s template-supported samples with $d \sim 15$ nm would be expected to exhibit discernable T_g reduction relative to $T_{g,bulk}$. In particular, the 1210 kg/mol PS sample used in Shin et al.'s study would be expected to exhibit $T_{g,rod} - T_{g,bulk} = \sim$ -7 °C.

Shin et al. also noted that "the glass-transition region of polystyrene in nanoporous alumina was broader than that of bulk" (Shin 2007). Using first-derivative DSC heat flow curves (Mok 2009), we determined values of apparent T_g breadth for 959/1260 PS in bulk and confined to AAO cylindrical nanopores and obtained values of 13 to 14 °C in all cases, indicating that confinement in the AAO templates employed in our study had little or no effect on apparent glass transition breadth as measured by DSC.

Further study of the apparent differences between the results of our study and those of Shin et al. (Shin 2007) are warranted. Unfortunately, it is not possible to prepare template-supported PS nanorods following the exact protocol of Shin et al. (Shin 2007) as they did not provide the time frame(s) associated with annealing used to achieve melt infiltration. Perhaps the more extreme absolute confinement in cylindrical nanopores with $d \sim 15$ nm is a source of the difference, especially given the weaker apparent glass transitions shown in our 24 nm diameter PS nanorod samples as compared with our nanorod samples with $d_m \geq 63$ nm. Differences are evident from the data given in Figure 11-3 and well as in the DSC-determined ΔC_p values for our 959/1260 PS nanorods as a function of d_m in Table 11-S3. We also note that when amorphous polymer experiences very extreme confinement by being intercalated in $1.5 - 2.0$ nm layers between (albeit organically modified) layered silicates, signatures of a glass transition near the bulk T_g are absent as characterized by dielectric spectroscopy (Anastasiadis 2000) and positron lifetime annihilation spectroscopy (Olson 1997). Instead, the bulk polymer α-relaxation is replaced by a much faster relaxation mode with a much weaker temperature dependence.Olson 1997 (The 1.5 to 2.0 nm intercalation length scale is even smaller than the length scales commonly associated with cooperatively rearranging regions present in bulk amorphous polymers near T_g (Anastasiadis 2000, Reinsberg 2002, Ellison 2005).)

Finally, Marvin et al. (Marvin 2014) used simulations to study T_g- and m-confinement effects of free-standing films. In agreement with experimental results represented by the current study as well as experimental results reported on free-standing films (Forrest 1997a, Mattsson

2000, Dalnoki-Veress 2001, Roth 2006, Kim 2011), they concluded that free-surface effects have a much larger influence on T_g-confinement behavior than intrinsic size effects. However, they reported that free-surface effects increase m but intrinsic size effects decrease m to a larger extent, resulting in an overall decrease of m in supported polymer films with confinement. Our experimental results on intrinsic size effects reported here on template-supported PS nanorods and m-confinement effect results by our group and others (Glor 2015, Jin 2016, Lan 2016) on supported films of linear PS indicate that free-surface effects have a greater influence on m-confinement behavior than intrinsic size effects. In turn, this implies that the fragility of linear polymer is reduced rather than increased near free surfaces.

11.3.5 Cause of the MW Dependence of the T_g-Intrinsic Confinement Effect in Nanorods

Our study provides the first report of a polymer MW dependence of the T_g-intrinsic confinement effect in which free-surface effects, significant attractive polymer-substrate interactions, and surface modifications with highly mobile monolayers are absent. Our results reveal a simple, apparent relationship between the length scale associated with confinement (d_m in supported nanorods) and a size scale associated with the diameter of the volume pervaded by a linear polymer coil in bulk ($2R_g$). We note that a significant MW dependence of the T_g-confinement effect has been documented in several studies of free-standing PS films (Forrest 1997a, Mattsson 2000, Dalnoki-Veress 2001, Kim 2011) (with no polymer-substrate interface) but that little or no MW dependence of the effect is apparent in substrate-supported PS films (Keddie 1994b, Kawana 2001, Ellison 2003, Ellison 2005, Seemann 2006, Lan 2014, Zhang 2015). The underlying cause for the difference in the MW dependences of T_g-confinement effects in free-standing and substrate-supported PS films has not been resolved, although a potential theoretical argument (de Gennes 2000) has been experimentally disproven (Kim 2011).

In particular, our research group has previously made the case that there is little or no apparent MW dependence of the T_g-confinement effect in supported PS films with MW ranging from 2 to 3000 kg/mol (Ellison 2005, Lan 2014, Zhang 2015). Thus, it is important for us to

consider why we observe a MW dependence of intrinsic confinement effects in supported PS nanorods (with no free surface) but previously observed little or no dependence in substrate-supported PS films (with a free surface). In order to compare intrinsic size effects measured on supported PS nanorods with confinement effects reported for supported PS films (with a free surface), we recalculate T_g-confinement effects as a function of a characteristic length scale (t^*), defined as the ratio of volume to relevant surface area. For template-supported nanorods, the volume and relevant surface area are $\pi d_m^2 L/4$ and $\pi d_m L$, respectively, where L is rod length. Thus, $t^*_{rod} = d_m/4$. In the case of a supported thin film in which the main driving force for confinement effects is the free surface, the relevant volume and surface area are hyz and yz, where h is the thickness and x and y are the film width and length. (Note: yz is the free-surface area.) This implies that $t^*_{film} = h$.

The 63-nm-diameter template-supported PS nanorods have $t^*_{rod} = 15.8$ nm and exhibit no intrinsic size effect on $T_{g,rod} - T_{g,bulk}$ within error for the 175/182 PS and 326/498 PS samples and only $\sim$ -2 °C effects for the 959/1260 PS and 929/1420 PS samples. As determined via ellipsometry, supported PS films with $h = 16$ nm (recall $h = t^*_{film}$), $T_{g,film} - T_{g,bulk} = \sim$ -19 °C.Keddie 1994b (16 nm is close to the minimum film thickness used in many literature studies of T_g-confinement effects in supported PS films.) Thus, any contribution of intrinsic size effects (which exhibit a MW dependence at high PS MW) to confinement effects in supported PS films is either absent within error or very small in comparison to commonly reported results in such films. (Our smallest PS nanorods with $d_m = 24$ nm would have $t^*_{rod} = 6$ nm. Data have rarely been reported in the literature on T_g-confinement effects for 6-nm-thick supported PS films. Caution should be applied regarding ellipsometry-based characterization of such thin films as Keddie and Jones warned that "measuring T_g in films below a thickness of 8 nm or so is approaching the experimental limits of the technique" (Keddie 1995).) Consequently, our results on the MW dependence of the T_g-intrinsic size effects in PS in no way contradict the apparent lack of a significant MW dependence on the T_g-confinement effect in supported PS films

reported in the literature.

Still unresolved is the underlying cause of the observed MW dependence of the intrinsic size effect on T_g in our template-supported PS nanorods. Although we do not totally discount an effect of a PS-AAO template interface (which lacks attractive interactions) in reducing requirements for cooperativity near the interface, this effect would not be expected to exhibit a significant dependence on MW for the PS MWs considered in our study. One possible explanation that would account for a MW dependence is suggested by the small-angle neutron scattering (SANS) characterization of AAO template-supported PS nanorods by Shin et al. (Shin 2007) They characterized 30-nm-diameter nanorods made from a ~528 kg/mol deuterated PS/~591 kg/mol hydrogenous PS mixture, which based on eqn. (1) would indicate that $d =$ ~$1.4R_g$. Their SANS results indicated that the chains were not stretched relative to bulk polymer in the axial direction, *i.e.*, "along the chain axis, the chain (was) unperturbed" (Shin 2007). However, they indicated that when the chains were confined within nanorods with $d = 1.4R_g$, the chains were compressed in the radial direction. From this observation, we may infer that there is a difference in the packing frustration of polymer chain segments confined to supported nanorods and those in bulk polymer, which in turn implies that there would be a difference between fragility in confined nanorods with $d < 2R_g$ and fragility in bulk polymer. This inference and implication provide an explanation for the observed MW dependence of the T_g-intrinsic size effect. Furthermore, the results shown in Figure 11-6B are consistent with this implication, although the effect on m may be evident at a slightly larger length scale than the effect on T_g. Previous studies have indicated that fragility-confinement effects may form the underlying physical basis for T_g-confinement effects (Evans 2013a, Lan 2016). This potential explanation is in accord with such a conclusion.

This explanation would obviously not extend in a simple manner to T_g-intrinsic confinement effects of cross-linked polymers, which have been shown to be substantial in a study by Lopez and Simon (Lopez 2015) of simultaneously in situ polymerized and cross-linked

networks in nanoporous glasses. Future DSC studies are warranted to address how cross-linking linear polymer can modify intrinsic confinement effects in AAO templates by taking advantage of approaches recently described by Jin and Torkelson (Jin 2016) that allow for direct comparison of confinement effects exhibited by cross-linked polymers and their linear polymer precursors. Additionally, DSC analysis of polymer nanorods confined within AAO templates will also allow for novel characterization of intrinsic size effects on physical aging as well as the role MW distribution in modifying intrinsic size effects on T_g, fragility, and physical aging. Finally, a film-based analog of the nanorod intrinsic confinement effects characterized by DSC would involve fluorescence characterization of intrinsic confinement effects in nanoscale-thick PS films confined on both sides between silica or glass slides. Such a system was exploited a decade ago in model nanocomposite studies (Rittigstein 2007) to characterize the impact of attractive polymer-substrate interactions (hydrogen bonding) in modifying T_g- and physical aging-confinement effects in several-hundred-nanometer-thick films of poly(2-vinyl pyridine) and PMMA confined between substrates with surfaces containing hydroxyl groups. Extension of this approach to several-tens-of nanometers thick films of PS confined between similar substrates and comparison with results of the current study could allow for determination of any effect of dimensionality of confinement on intrinsic confinement effects. Related investigations are underway in our laboratory.

11.4 Conclusions

Values of T_g and fragility of PS nanorods supported in AAO templates were characterized via DSC. Using differently sized templates, nanorod d_m values were varied from 24 to 210 nm, thus allowing determination of intrinsic size effects in the absence of free surfaces or significant polymer-substrate attractive interactions. Four PS samples were employed for the range of available templates. For a fifth, lowest MW PS sample with MW = 30 kg/mol, PS nanorods were melt infiltrated in only the template that resulted in the smallest d_m value of 24 nm, with the T_g of

the nanorods exhibiting no change from $T_{g,bulk}$. However, T_g-intrinsic size effects are observed for PS nanorods with M_n and $M_w \geq$ ~180 kg/mol, with effects increasing with increasing MW up to $T_{g,rod} - T_{g.bulk}$ = ~ -8 °C for 929/1420 PS in 24-nm-diameter nanorods. In general, $T_{g,rod} - T_{g,bulk}$ data for AAO-template supported nanorods exhibit intrinsic-size-effect reductions when $d_m/(2R_g) \leq$ ~1. Thus, T_g-intrinsic size effects, which are much smaller than T_g-confinement effects observed in the presence of free surfaces, are observed in nanorods when d_m is smaller than the diameter ($2R_g$) of the volume pervaded by a coil in bulk. Based on these results and complementary results by Shin et al. (Shin 2007), we hypothesize that the T_g reduction caused by intrinsic size effects occurs when chain segment packing frustration is sufficiently perturbed by nanorod confinement. Measurements of fragility reduction with nanorod confinement support this explanation.

The MW dependence of the small T_g-intrinsic size effect observed in PS nanorods in no way contradicts past reports that the T_g-confinement effect in supported PS films with one free surface exhibits little or no MW dependence. This point can be understood by comparing nanorod and thin film T_g reductions at a similar characteristic length scale, t^*. For PS nanorods with d_m = 63 nm or t^* = 15.8 nm, as measured by DSC there is no reduction in T_g relative to bulk response when M_n and $M_w \leq$ ~500 kg/mol, and $T_{g,rod} - T_{g,bulk}$ = ~ -2 °C for 959/1260 PS and 929/1420 PS samples. As determined by ellipsometry, supported PS films with thickness of 16 nm (t^* = 16 nm) exhibit $T_{g,film} - T_{g,bulk}$ = ~ -19 °C (Keddie 1994b). Thus, at MWs of PS most commonly used in studies of T_g-confinement effects in the presence of a free surface, intrinsic size effects contribute nothing within error to the measured effect; at extremely high PS MW, the contribution of intrinsic size effects is only a very small percentage of the reported T_g reduction.

11.5 Supplementary Information – Molecular Weight and Glass Transition Characterization of Supported PS Nanorods

Presented below are additional tables and figures referenced in sections 11.3 and 11.4.

Table 11-S1: Molecular weight of as received PS standards characterized by GPC using a light scattering detector

Nominal MW (kg/mol)	Manufacturer	Lot Number	M_n (kg/mol)	M_w (kg/mol)	PDI
30	Pressure Chemical	80314	30.1	30.2	1.00
186	Toyo Soda Manufacturing Co.	TS-17	177	185	1.05
290	Pressure Chemical	70114	281	283	1.01
900	Pressure Chemical	80303	548	655	1.19
1800	Pressure Chemical	14a	1,330	1,580	1.18
2000	Pressure Chemical	61111	1,480	1,580	1.07
3840	Toyo Soda Manufacturing Co.	TS-34	2,880	3,070	1.06

Note: Samples with nominal molecular weights of 290 and 1800 kg/mol were only used for molecular weight characterization and were not made into PS nanorods. Nominal MW values are the values reported by the supplier.

Table 11-S2: T_g determined by onset method, T_f determined by Richardson method and Moynihan method

Sample Name	$T_{g,onset}$ (°C)	T_f (°C) Richardson method	T_f (°C) Moynihan method
Bulk 326/498 PS	104.3	104.9	104.7
Bulk 959/1260 PS	103.6	104.3	104.5
Bulk 929/1420 PS	103.4	104.6	105.3

Note: $T_{g,onset}$ and T_f values determined Richardson and Moynihan methods are determined from the same DSC curve.

Table 11-S3: $T_{g,onset}$, ΔC_p, T_g breadth and fragility of template-supported 959/1260 PS nanorods.

Mass-Avg. d_m (nm)	Number-Avg. d_n (nm)	$T_{g,onset}$ (°C)	ΔC_p (J/gK)	T_g breadth (°C)	Fragility
Bulk	Bulk	103.8 ± 0.3	0.27	13	169 ± 5
370	320	103.5 ± 0.3	0.27	14	165 ± 5
210	190	103.9 ± 0.8	0.27	13	164 ± 5
86	84	102.4 ± 0.9	0.27	13	149 ± 3
63	61	101.6 ± 1.0	0.25	13	139 ± 4
33	32	100.2 ± 1.0	0.23	14	128 ± 3
24	24	97.1 ± 0.9	0.21	14	-
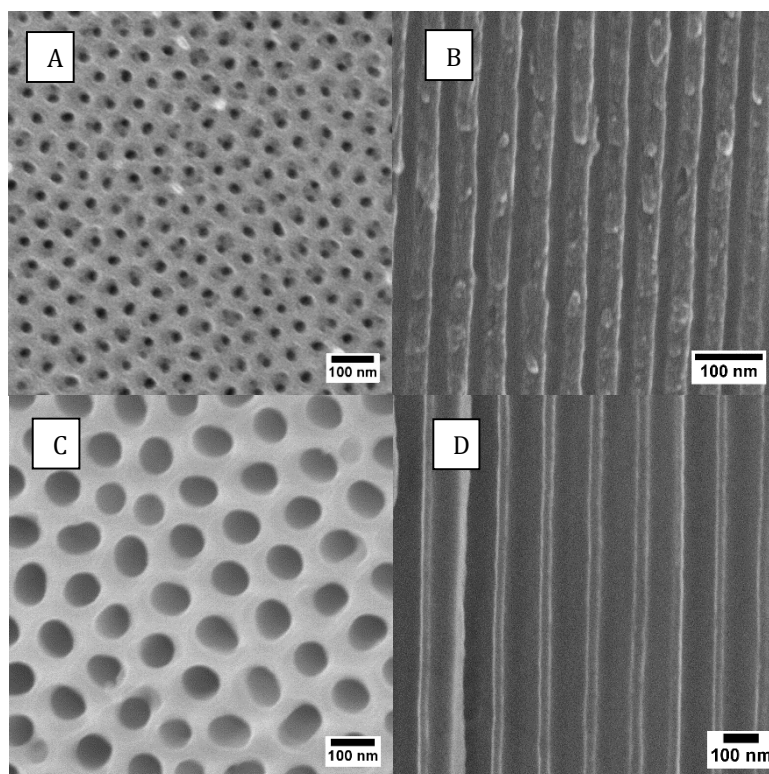
Figure 11-S1: SEM images of AAO templates with nominal diameter of 20 nm (A: top view, B: cross section) and 70 nm (C: top view, D: cross section).
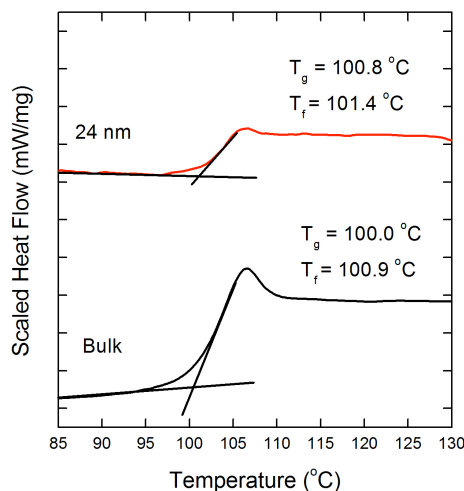
Figure 11-S2: Scaled DSC heat flow curves for bulk 30 kg/mol PS standard (R_g = 5 nm) and template-supported PS nanorods. The curves are vertically shifted in an arbitrary manner to avoid overlapping.
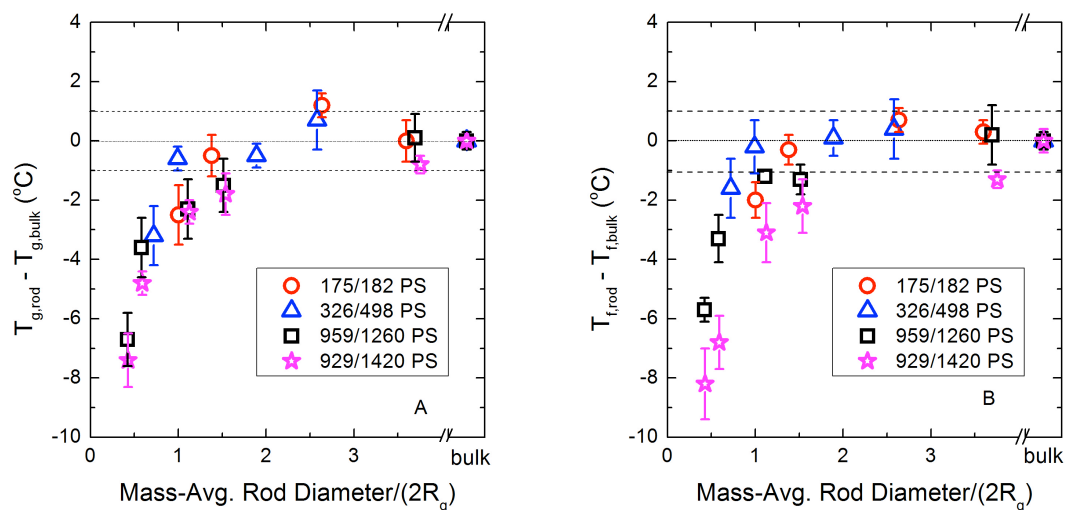
Figure 11-S3: $T_{g,rod} - T_{g,bulk}$ (A) and $T_{f,rod} - T_{f,bulk}$ (B) for template-supported PS nanorods of various molecular weight plotted as a function of rod diameter/($2R_g$). R_g of each sample set is calculated from M_n in (A) and (B). T_g values are $T_{g,onset}$. Error bars represent the standard deviation of T_g and T_f values.

ACKNOWLEDGMENTS

IV. SUMMARY

CHAPTER 12

Conclusions and Recommendations for Future Research

This thesis has investigated the physics of polymers in a number of geometries with the goal of advancing a fundamental understanding of stress relaxation, T_g, and stiffness above and below T_g. The focus of Section II was to characterize and understand stiffness of polymers when confined to nanoscale dimensions. The focus of Section III was to study T_g behavior in complex geometries such as polymer brushes and supported nanorods. The key findings in each chapter are summarized and recommendations for future research are offered.

In Chapter 3, ellipsometry and fluorescence were used to characterize residual stress relaxation in PS films using non-contact (and hence non-perturbative) experimental methods. Both techniques showed that residual stress relaxation occurred over a period of hours despite the PS films being $15 - 40$ °C above the film glass transition temperature (T_g). Both techniques also showed that film T_g was unaffected by stress relaxation, even when stress relaxation was accompanied by measurable changes in thickness. Fluorescence showed that stress relaxation time followed an Arrhenius temperature dependence with an activation energy of ~110 kJ/mol, which was consistent with stress relaxation occurring via β-relaxation. Using a fluorescence/bilayer technique with bulk bilayer films, it was observed by I_1/I_3 measurements that a 30-nm-thick MPy-PS layer located at a glass substrate interface was stiffer than a 30-nm-thick MPy-PS layer located at a free surface. Over a 20 to 400 nm thickness range, fluorescence of MPy-PS films showed a significant effect of substrate on molecular caging and hence stiffness, with stiffness increasing in the following order: free-standing films (no substrate) < films supported on a PDMS (soft) substrate < films supported on a glass (hard) substrate.

In Chapter 4, the fluorescence approach was used to characterize stiffness-confinement effects in supported PS films. Near T_g at 100 °C and in the glassy state at 60 °C, molecular caging and hence stiffness in single-layer films was independent of thickness down to 63 nm and increased with decreasing thickness at 36 nm and below. In contrast, at 140 °C, molecular caging

and hence stiffness in single-layer PS films supported on silica was independent of thickness down to 240 nm and increased with decreasing thickness at 165 nm and below. In bulk bilayer films, perturbations originating at the substrate interface (free-surface interface) caused major enhancements (reductions) in caging and hence stiffness in 20-nm-thick substrate-adjacent (free-surface-adjacent) layers. In contrast, in 40-nm-thick bilayer films, the 20-nm-thick substrate-adjacent and free-surface-adjacent layers exhibited little difference in caging and stiffness. Thus, the gradient in stiffness from a film interface depends significantly on confinement, which was attributed to the combined length scales over which free-surface and substrate perturbations propagate inside the film. Bulk bilayer films were used to investigate the length scales associated with interfacial perturbation, and this study provided the first characterization of stiffness gradients near a free-surface interface. At 100 °C and 60 °C, stiffness-gradient length scales were estimated to extend ~45 – 85 nm from the substrate and ~35 – 85 nm from the free surface. At 140 °C, the stiffness-gradient length scales were estimated to extend ~85 – 200 nm from the substrate and $\lesssim$ 20 nm from the free surface.

Chapter 5 describes the first comparison of stiffness gradient length scales in polymeric materials characterized by two techniques, fluorescence spectroscopy and AFM. Characterization was done at room temperature on model nanocomposites in which a PS film was supported on both sides by glass substrates after being cooled from 140 °C (40 °C above T_g to 25 °C at 1 °C/min cooling rate). In confined model nanocomposites with the previously described thermal history, the local stiffness enhancement relative to bulk was the result of perturbations from both substrate interfaces. In a 266-nm-thick PS model nanocomposite, perturbations to modulus extended ~200 nm inside the film from each interface. Both methods indicated that a small (>5%) stiffness enhancement was evident at the midpoint of a 266-nm-thick model nanocomposite; the midpoint modulus enhancement increased with confinement and was an order of magnitude greater at the midpoint of a 60-nm-thick model nanocomposite. In bulk PS model nanocomposites, stiffness gradients resulted from perturbations propagating from

a single substrate interface that were damped by the bulk layer of polymer, and both fluorescence and AFM indicated that stiffness gradients extended ~80 nm from an interface. The two techniques showed good qualitative and quantitative agreement regarding stiffness gradient length scales and were correlated via a simple monotonic relationship between the fluorescence measurable and normalized modulus under a specific thermal history condition.

Chapter 6 provided the first demonstration that thermal histories used to prepare samples have impacts on stiffness-confinement effects. These effects were investigated by characterizing both the magnitude and length scales associated with stiffness gradients within room-temperature bulk model PS nanocomposites. Using fluorescence, we observed that both the magnitude and length scales of the perturbations to stiffness near a PS-substrate interface increased in model nanocomposites that were rapidly quenched from 60 to 25 °C compared to model nanocomposites that were cooled slowly (1 °C/min). With regard to the length scale, slowly cooled PS samples exhibited stiffening within ~80 nm of a glass substrate interface and rapidly quenched samples exhibited stiffening within ~325 nm of a glass substrate interface at room temperature. The enhancements in stiffness perturbations were attributed to additional stresses that were present in quenched samples. Those stresses originated from two sources: the mismatch in the thermal expansivities between the rigid substrate and polymer as well as the inability of the polymer to relax when quenched to 25 °C. These results indicate the very important role of thermal history in the stiffness-confinement behavior of polymer nanocomposites as well as the necessity for reports in literature to clearly describe the thermal histories used in samples to characterize stiffness-confinement effects.

Chapter 7 extends the fluorescence technique to study stiffness-confinement behavior in a number of new ways. It is the first to directly characterize how temperature affects stiffness gradients near substrate and free-surface interfaces in supported polymer model nanocomposites and films supported on glass substrates. At the center of confined model nanocomposites that were cooled from 140 °C to 60 °C at 1 °C/min, major enhancement in stiffness relative to bulk

response was observed at a distance of ~80 nm and a perceptible enhancement was observed at a distance of ~135 nm from each substrate interface at 60 and 100 °C, conditions at which PS is glassy. In bulk model nanocomposites, stiffness gradients extended ~80 nm from the substrate interface at 60 and 100 °C. The results obtained at 60 and 100 °C were found to be in good agreement with those previously obtained in Chapter 5. In contrast, at 140 °C, stiffness gradients were observed to extend 240 – 325 nm from the substrate interface, demonstrating that rigid substrates more strongly perturb rubbery-state PS relative to glassy-state PS. Bulk trilayer films were used to directly characterize stiffness gradient length scales near substrate and free-surface interfaces. Near a substrate interface, bulk films and bulk model nanocomposites yielded the same stiffness gradient length scales within error, indicating that the perturbations to stiffness as a function of distance from one substrate interface were the same in bulk samples because the bulk polymer layer separating the region being interrogated ensured that the perturbation from the other interface, whether from a free surface or a substrate interface, did not extend to the region being interrogated by the dye-labeled layer. Trilayer films were also used to characterize stiffness gradient length scales near a free-surface interface for the first time. Stiffness gradients extended 140 – 200 nm from the free-surface interface at 60 and 100 °C and 50 – 100 nm from the free-surface interface at 140 °C, demonstrating that the free-surface interface more strongly perturbs glassy-state PS relative to rubbery-state PS. Results in Chapter 7 help to understand how different interfaces impact the polymer in the rubbery and glassy states. A polymer in its glassy state is more susceptible to stiffness perturbations from a free surface interface or a soft substrate and exhibits stiffness reductions near the interface. A polymer in its rubbery state is more susceptible to stiffness perturbations from a rigid substrate and exhibits stiffness enhancements near the interface. The overall stiffness-confinement behavior of a polymer film reflects the combined perturbations to stiffness originating from both interfaces.

Chapter 8 is the first study to investigate the tunability of stiffness-confinement behavior by plasticizer addition to polymer films supported on a rigid substrate. Fluorescence results

demonstrated that there was temperature dependence to the reduction in caging for bulk PS films with increasing DOP content. For glassy-state PS at 60 °C, I_1/I_3 values and hence caging saturated at DOP concentrations at or above 10 wt%; for rubbery-state bulk PS films at 140 °C, I_1/I_3 values saturated at or above 1 – 2 wt% DOP. The tunability of stiffness-confinement behavior was investigated in PS films containing up to 4 wt% DOP. With decreasing thickness below a critical value, I_1/I_3 increased with decreasing thickness; hence, caging and stiffness increased with confinement. With increasing DOP content, the critical thickness at which single-layer PS films exhibited deviations from bulk response decreased, with much larger reductions in critical thickness occurring at 140 °C than at 100 °C or 60 °C. The impact of DOP addition was described in terms of the ability of plasticizers to mediate perturbations to stiffness near a rigid substrate.

The research in Chapters 3 – 8 involved using pyrene fluorescence to characterize the polymer properties. Chapter 9 demonstrated that the ability to characterize polymer stress relaxation and T_g is not limited to just pyrene and that a broader class of vibronic coupling dyes can be used. Comparisons were made between the fluorescence behavior of phenanthryl and anthryl labels to previously observed behavior of pyrenyl labels in providing sensitivity to stress relaxation and T_g in polymer films. Like pyrene, phenanthrene belongs to the class of dyes known as vibronic coupling dyes, whereas anthracene does not. It was demonstrated that phenanthryl and pyrenyl labels exhibited similar sensitivities to stress relaxation and T_g, whereas anthryl labels did not. The similarities between pyrene and phenanthrene were attributed to the fact that the two dyes are vibronic coupling dyes, the spectra of which are sensitive to changes in local molecular caging. In contrast, the anthryl label did not exhibit sensitivity to stress relaxation or T_g because it did not exhibit vibronic coupling behavior. The results from Chapter 9 open the possibility for a more general class of fluorophores to characterize other polymer properties such as stiffness.

The research in Section II significantly advances understanding of stiffness-confinement

behavior and provides consensus among reports in the research field. By investigating factors affecting polymer stiffness, general trends associated with stiffness-confinement behavior can be obtained. For instance, factors such as interfacial perturbations, temperature, substrate stiffness, gradient length scale, and thermal history have been shown to impact stiffness-confinement behavior. With the research in this dissertation and careful consideration of the various subtleties associated with stiffness-confinement behavior, significant agreement can be found among reports in the research community.

The research in Section III involved characterizing T_g-confinement behavior in more complex geometries using an established experimental approach in differential scanning calorimetry. In Chapter 10, polystyrene-grafted silica nanoparticles (Si-PS) were synthesized via ARGET ATRP, achieving the densely grafted state. Using DSC, brush molecular weight (MW) dependence of T_g, T_g breadth, heat capacity jump (ΔC_p), and fragility from 12 to 98 kg/mol was investigated. Compared with free PS chains of the same MW, brush T_g increased by $1 - 2$ °C, brush T_g breadth remained unchanged within error down to 36 kg/mol and increased by $3 - 4$ °C at brush MWs of 12 and 13 kg/mol, and brush ΔC_p and fragility remained unchanged within error down to 52 kg/mol and then decreased with decreasing MW. Evidence of a significant T_g gradient from near the nanoparticle graft interface to near the free chain end was obtained via fluorescence of a pyrenyl dye labeled at specific regions along the brush chain length. In relatively high MW brushes, $T_g = $ ~116 °C near the graft interface, and $T_g = $ ~102 °C near the chain end. Comparisons were made to results recently reported for similar PS brushes densely grafted to a flat substrate, which indicated that a larger T_g gradient was evident in a grafting geometry involving a flat interface as compared with a spherical nanoparticle interface. Results of Chapter 10 help to better understand nanocomposites and tailor them for optimal properties.

In Chapter 11, values of T_g and fragility of PS nanorods supported in AAO templates were characterized via DSC. Four PS samples were employed for the range of available templates. T_g-intrinsic size effects are observed for PS nanorods with M_n and $M_w \geq$ ~180 kg/mol,

with effects increasing with increasing MW up to $T_{g,rod} - T_{g.bulk} = \sim$ -8 °C for 929/1420 PS in 24-nm-diameter nanorods. In general, $T_{g,rod} - T_{g,bulk}$ data for AAO-template supported nanorods exhibit intrinsic-size-effect reductions when $d_m/(2R_g) \leq \sim 1$. Thus, T_g-intrinsic size effects are observed in nanorods when d_m is smaller than the diameter $(2R_g)$ of the volume pervaded by a coil in bulk. It is hypothesized that the T_g reduction caused by intrinsic size effects occurs when chain segment packing frustration is sufficiently perturbed by nanorod confinement. Measurements of fragility reduction with nanorod confinement support this explanation. The MW dependence of the small T_g-intrinsic size effect observed in PS nanorods in no way contradicts past reports that the T_g-confinement effect in supported PS films with one free surface exhibits little or no MW dependence. This point can be understood by comparing nanorod and thin film T_g reductions at a similar characteristic length scale, t^*. For PS nanorods with $d_m = 63$ nm or $t^* = 15.8$ nm, as measured by DSC there is no reduction in T_g relative to bulk response when M_n and $M_w \leq \sim 500$ kg/mol, and $T_{g,rod} - T_{g,bulk} = \sim$ -2 °C for 959/1260 PS and 929/1420 PS samples. As determined by ellipsometry, supported PS films with thickness of 16 nm ($t^* = 16$ nm) exhibit $T_{g,film} - T_{g,bulk} = \sim$ -19 °C (Keddie 1994b). Thus, at MWs of PS most commonly used in studies of T_g-confinement effects in the presence of a free surface, intrinsic size effects contribute nothing within error to the measured effect; at extremely high PS MW, the contribution of intrinsic size effects is only a very small percentage of the reported T_g reduction.

The research presented in this dissertation can be extended in a number of ways to further an understanding of stress, stiffness, and T_g behavior in polymers. Recommendations for future research are provided in the paragraphs that follow.

Future research into stress relaxation should seek to characterize behavior in confined polymer films to understand the role of confinement in impacting stress relaxation. In addition, other polymers containing different side groups should be tested to understand the tunability of stress relaxation behavior by impacting β-relaxation.

Stiffness-confinement behavior in polymer films can also be investigated in a number of

ways. Future research should focus on characterizing various polymer/substrate pairs at a variety of temperatures. Examples could include pairs where there are attractive interactions between a polymer the substrate such as poly(methyl methacrylate) or poly(2-vinyl pyridine) supported on silica or alumina. Such experiments would provide insight into how perturbations to stiffness originating from the interfaces impact average stiffness-confinement behavior in the glassy and rubbery states. Future research should further an understanding of thermal history effects on stiffness in polymers supported on soft substrates or near free surfaces. Research into the tunability of stiffness-confinement behavior can be extended to characterizing polymers containing anti-plasticizers or nanoparticles. The fluorescence technique itself can also be further developed by identifying and utilizing other vibronic coupling dyes that can be used to characterize polymer properties.

The research in Chapters 3 – 8 gave insight into the stiffness-confinement length scales in polymer films and model nanocomposites. Future work should advance knowledge of stiffness gradient length scales in real nanocomposites. A relationship was developed in Chapter 5 that enabled quantitative comparisons between fluorescence I_1/I_3 values and normalized modulus values. Similar relationships but at different temperatures could be developed to characterize and understand stiffness-confinement effects in real nanocomposites at different conditions. For instance, fluorescence could be used to obtain I_1/I_3 values in real nanocomposites as a function of filler loading and temperature that could then be related to modulus values. Yet other studies could be conducted on real nanocomposites that contain nanofiller modified with grafted brushes or hairs to achieve compatibilization. Stiffness gradients within such nanocomposites could be characterized by fluorescence data from pyrenyl dye labels located on brush or hair chains at a specific distance from the nanofiller interface and compared to results obtained from dye labels located on polymer chains forming the nanocomposite matrix.

Research into T_g-confinement effects in more complex geometries can be extended to gain a deeper understanding. Future work should focus on utilizing fluorescence approaches to

characterize T_g-confinement length scales in polymer-grafted nanoparticles. By incorporating dyes at particular distances from nanofiller interfaces, T_g gradient length scales in real nanocomposites can be characterized. Further research utilizing nanorods should also focus on polymer blends of high and low molecular weight chains where molecular weight and/or dispersity of the resulting mix can be altered. In addition, polymer systems may be investigated where there are attractive interactions between the polymer and nanorod template. Studies involving non-linear polymers would also help to understand intrinsic size effects on T_g-confinement behavior.

REFERENCES

Acree, W. E.; Tucker, S. A.; Zvaigzne, A. I.; Street, K. W.; Fetzer, J. C.; Grutzmacher, H.-F., *Appl. Spectrosc.* **1990**, *44*, 477

Adam, G.; Gibbs, J. H., *J. Chem. Phys.* **1965**, *43*, 139

Akcora, P.; Kumar, S. K.; Sakai, V. G.; Li, Y.; Benicewicz, B. C.; Schadler, L., *Macromolecules* **2010**, *43*, 8275

Akcora, P.; Liu, H.; Kumar, S. K.; Moll, J.; Li, Y.; Benicewicz, B. C.; Schadler, L. S.; Acehan, D.; Panagiotopoulos, A. Z.; Pryamitsyn, V.; Ganesan, V.; Ilavsky, J.; Thiyagarajan, P.; Colby, R. H.; Douglas, J. F., *Nat. Mater.* **2009a**, *8*, 354

Akcora, P.; Liu, H.; Kumar, S. K.; Moll, J.; Li, Y.; Benicewicz, B. C.; Schadler, L. S.; Acehan, D.; Panagiotopoulos, A. Z.; Pryamitsyn, V.; Ganesan, V.; Ilavsky, J.; Thiyagarajan, P.; Colby, R. H.; Douglas, J. F., *Nat Mater* **2009b**, *8*, 354

Alcoutlabi, M.; McKenna, G. B., *J. Phys. - Condens. Mat.* **2005**, *17*, R461

Alexandris, S.; Papadopoulous, P.; Sakellariou, G.; Steinhart, M.; Butt, H.-J.; Floudas, G., *Macromolecules* **2016**,

Anastasiadis, S. H.; Karatasos, K.; Vlachos, G.; Manias, E.; Giannelis, E. P., *Phys. Rev. Lett.* **2000**, *84*, 915

Anderson, P., *Science* **1995**, *267*, 1609

Angell, C. A., *J. Non-Cryst. Solids* **1985**, *73*, 1

Angell, C. A., *J. Non-Cryst. Solids* **1991**, *13*, 131

Angell, C. A., *Science* **1995**, *267*, 1924

Angell, C. A., *Polymer* **1997**, *38*, 6261

Antonelli, C.; Serrano, B.; Baselga, J.; Ozisik, R.; Cabanelas, J. C., *Eur. Polym. J.* **2015**, *62*, 31

Arabeche, K.; Delbreilh, L.; Saiter, J. M.; Michler, G. H.; Adhikari, R.; Baer, E., *Polymer* **2014**, *55*, 1546

Arinstein, A.; Zussman, E., *J. Polym. Sci., Part B: Polym. Phys.* **2011**, *49*, 691

Arrighi, V.; McEwen, I. J.; Qian, H.; Serrano Prieto, M. B., *Polymer* **2003**, *44*, 6259

Ash, B. J.; Rogers, D. F.; Wiegand, C. J.; Schadler, L. S.; Siegel, R. W.; Benicewicz, B. C.; Apple, T., *Polym. Compos.* **2002a**, *23*, 1014

Ash, B. J.; Schadler, L. S.; Siegel, R. W., *Mater. Lett.* **2002b**, *55*, 83

Askar, S.; Evans, C. M.; Torkelson, J. M., *Polymer* **2015**, *76*, 113

Askar, S.; Torkelson, J. M., *Polymer* **2016**, *99*, 417

Askar, S.; Torkelson, J. M., *In Preparation* **2017a**

Askar, S.; Torkelson, J. M., *In Preparation* **2017b**

Avolio, R.; Gentile, G.; Avella, M.; Capitani, D.; Errico, M. E., *J. Polym. Sci. Part A: Polym. Chem.* **2010**, *48*, 5618

Baeumchen, O.; McGraw, J. D.; Forrest, J. A.; Dalnoki-Veress, K., *Phys. Rev. Lett.* **2012**, *109*, 055701

Baglay, R. R.; Roth, C. B., *J. Chem. Phys.* **2015**, *143*, 111101

Baker, E. A.; Rittigstein, P.; Torkelson, J. M.; Roth, C. B., *J. Polym. Sci., Part B: Polym. Phys.* **2009**, *47*, 2509

Balazs, A. C.; Emrick, T.; Russell, T. P., *Science* **2006**, *314*, 1107

Bansal, A.; Yang, H. C.; Li, C. Z.; Benicewicz, R. C.; Kumar, S. K.; Schadler, L. S., *J. Polym. Sci. Part B: Polym. Phys.* **2006**, *44*, 2944

Bansal, A.; Yang, H. C.; Li, C. Z.; Cho, K. W.; Benicewicz, B. C.; Kumar, S. K.; Schadler, L. S., *Nat. Mater.* **2005**, *4*, 693

Batistakis, C.; Lyulin, A. V.; Michels, M. A. J., *Macromolecules* **2012**, *45*, 7282

Batistakis, C.; Michels, M. A. J.; Lyulin, A. V., *Macromolecules* **2014**, *47*, 4690

Beaucage, G.; Composto, R.; Stein, R. S., *J. Polym. Sci., Part B: Polym. Phys.* **1993**, *31*, 319

Berriot, J.; Montes, H.; Lequeux, F.; Long, D.; Sotta, P., *Macromolecules* **2002**, *35*, 9756

Betancourt, B. A. P.; Douglas, J. F.; Starr, F. W., *Soft Matter* **2013**, *9*, 241

Blum, F. D.; Lin, W. Y.; Porter, C. E., *Coll. Polym. Sci.* **2003**, *281*, 197

Bockstaller, M. R.; Mickiewicz, R. A.; Thomas, E. L., *Adv. Mater.* **2005**, *17*, 1331

Bohmer, R.; Angell, C. A., *Phys. Rev. B* **1992**, *45*, 10091

Bohmer, R.; Ngai, K. L.; Angell, C. A.; Plazek, D. J., *J. Chem. Phys.* **1993**, *99*, 4201

Briscoe, B. J.; Fiori, L.; Pelillo, E., *J. Phys. D: Appl. Phys.* **1998**, *31*, 2395

Brune, P. F.; Blackman, G. S.; Diehl, T.; Meth, J. S.; Brill, D.; Tao, Y.; Thornton, J.,
    Macromolecules **2016**, *49*, 4909

Cangialosi, D.; Alegria, A.; Colmenero, J., *J. Phys. Rev. E* **2007**, *76*, 011514

Casalini, R.; Roland, C. M., *Macromolecules* **2016**, *49*, 3919

Chandler, D.; Garrahan, J. P., *J. Chem. Phys.* **2005**, *124*, 024906

Chandran, S.; Basu, J. K.; Mukhopadhyay, M. K., *J. Chem. Phys.* **2013**, *138*, 014902

Chandran, S.; Begam, N.; Padmanabhan, V.; Basu, J. K., *Nat. Commun.* **2014**, *5*, 3697

Chen, F.; Clough, A.; Reinhard, B. M.; Grinstaff, M. W.; Jiang, N.; Koga, T.; Tsui, O. K. C.,
    Macromolecules **2013**, *46*, 4663

Chen, P.; Tian, H. F.; Zhang, L.; Chen, Y.; Wang, X. Y.; Do, Y. M., *J. Biobased Mater.
    Bioenergy* **2008**, *2*, 248

Cheng, S. W.; Holt, A. P.; Wang, H. Q.; Fan, F.; Bocharova, V.; Martin, H.; Etampawala, T.;
    White, B. T.; Saito, T.; Kang, N. G.; Dadmun, M. D.; Mays, J. W.; Sokolov, A. P., *Phys.
    Rev. Lett.* **2016**, *116*, 038302

Cheng, W.; Sainidou, G.; Burgardt, P.; Stefanou, N.; Kiyanova, A.; Efremov, M.; Fytas, G.;
    Nealey, P. F., *Macromolecules* **2007**, *40*, 7283

Cheng, X.; Putz, K. W.; Wood, C. D.; Brinson, L. C., *Macromol. Rapid Commun.* **2015**, *36*, 391

Chochos, C. L.; Ismailova, E.; Brochon, C.; Leclerc, N.; Tiron, R.; Sourd, C.; Bandelier, P.;
    Foucher, J.; Ridaoui, H.; Dirani, A.; Soppera, O.; Perret, D.; Brault, C.; Serra, C. A.;
    Hadziioannou, G., *Adv. Mater.* **2009**, *21*, 1121

Choi, J.; Hui, C. M.; Pietrasik, J.; Dong, H. C.; Matyjaszewski, K.; Bockstaller, M. R., *Soft
    Matter* **2012**, *8*, 4072

Chowdhury, M.; Freyberg, P.; Ziebert, F.; Yang, A. C. M.; Steiner, U.; Reiter, G., *Phys. Rev. Lett.* **2012**, *109*, 136102

Chung, J. Y.; Chastek, T. Q.; Fasolka, M. J.; Ro, H. W.; Stafford, C. M., *ACS Nano* **2009**, *3*, 844

Chung, P. C.; Glynos, E.; Green, P. F., *Langmuir* **2014**, *30*, 15200

Chung, P. C.; Glynos, E.; Sakellarious, G.; Green, P. F., *ACS Macro Lett.* **2016**, *5*, 439

Chung, P. C.; Green, P. F., *Macromolecules* **2015**, *48*, 3991

Cicerone, M. T.; Zhong, Q.; Johnson, J.; Aamer, K. A.; Tyagi, M., *J. Phys. Chem. Lett.* **2011**, *2*, 1464

Cohen, Y.; Reich, S., *J. Polym. Sci., Part B: Polym. Phys.* **1981**, *19*, 599

Croll, S. G., *J. Coat. Technol.* **1978**, *50*, 33

Croll, S. G., *J. Appl. Polym. Sci.* **1979**, *23*, 847

Cundall, R. B.; Pereira, L. C., *Chem. Phys. Lett.* **1973**, *18*, 371

Dalle-Ferrier, C.; Simon, S.; Zheng, W.; Badrinarayanan, P.; Fennell, T.; Frick, B.; Zanotti, J. M.; Alba-Simionesco, C., *Phys. Rev. Lett.* **2009**, *103*, 185702

Dalnoki-Veress, K.; Forrest, J. A.; Murray, C.; Gigault, C.; Dutcher, J. R., *Phys. Rev. E* **2001**, *63*, 031801

Damman, P.; Gabriele, S.; Coppee, S.; Desprez, S.; Villers, D.; Vilmin, T.; Raphael, E.; Hamieh, M.; Al Akhrass, S.; Reiter, G., *Phys. Rev. Lett.* **2007**, *99*, 036101

Dang, A.; Hui, C. M.; Ferebee, R.; Kubiak, J.; Li, T.; Matyjaszewski, K.; Bockstaller, M. R., *Macromol. Symp.* **2013**, *331*, 9

Davris, T.; Mermet-Guyennet, M. R. B.; Bonn, D.; Lyulin, A. V., *Macromolecules* **2016**, *49*, 7077

de Gennes, P. G., *J. Chem. Phys.* **1971**, *55*, 572

de Gennes, P. G., *Eur. Phys. J. E* **2000**, *2*, 201

Debenedetti, P. G.; Stillinger, F. H., *Nature* **2001**, *410*, 259

DeFelice, J.; Milner, S. T.; Lipson, J. E. G., *Macromolecules* **2016**, *49*, 1822

Delcambre, S. P.; Riggleman, R. A.; de Pablo, J. J.; Nealey, P. F., *Soft Matter* **2010**, *6*, 2475

Dhinojwala, A.; Torkelson, J. M., *Macromolecules* **1994a**, *27*, 4817

Dhinojwala, A.; Wong, G. K.; Torkelson, J. M., *J. Chem. Phys.* **1994b**, *100*, 6046

Diez-Pascual, A. M.; Xu, C. P.; Luque, R., *J. Mater. Chem. B* **2014**, *2*, 3065

Ding, Y.; Pawlus, S.; Sokolov, A. P.; Douglas, J. F.; Karim, A.; Soles, C. L., *Macromolecules* **2009**, *42*, 3201

Dion, M.; Larson, A. B.; Vogt, B. D., *J. Polym. Sci. Part B: Polym. Phys.* **2010**, *48*, 2366

Dong, D. C.; Winnik, M. A., *Can. J. Chem.* **1984**, *62*, 2560

Dong, Y. C.; Feng, S. S., *Biomaterials* **2005**, *26*, 6068

Donth, E., *J. Polym. Sci. Part B: Polym. Phys.* **1996**, *34*, 2881

Dreyer, A.; Feld, A.; Kornowski, A.; Yilmaz, E. D.; Noei, H.; Meyer, A.; Krekeler, T.; Jiao, C.; Stierle, A.; Abetz, V.; Weller, H.; Schneider, G. A., *Nat. Mater.* **2016**, *15*, 522

Du, J. H.; Cheng, H. M., *Macromol. Chem. Phys.* **2012**, *213*, 1060

Dudowicz, J.; Freed, K. F.; Douglas, J. F., *J. Phys. Chem. B* **2005a**, *109*, 21350

Dudowicz, J.; Freed, K. F.; Douglas, J. F., *J. Phys. Chem.* **2005b**, *109*, 21285

Duran, H.; Gitsas, A.; Floudas, G.; Mondeshki, M.; Steinhard, M.; Knoll, W., *Macromolecules* **2009**, *42*, 2881

Durocher, G.; Sandorfy, C., *J. Mol. Spectrosc.* **1966**, *20*, 410

Dyre, J. C., *Rev. Mod. Phys.* **2006**, *78*, 953

Ediger, M. D.; Angell, C. A.; Nagel, S. R., *J. Phys. Chem.* **1996**, *1000*, 13200

Ediger, M. D.; Forrest, J. A., *Macromolecules* **2014**, *47*, 471

Ellison, C. J.; Kim, S. D.; Hall, D. B.; Torkelson, J. M., *Eur. Phys. J. E* **2002a**, *8*, 155

Ellison, C. J.; Miller, K. E.; Torkelson, J. M., *Polymer* **2004a**, *45*, 2623

Ellison, C. J.; Mundra, M. K.; Torkelson, J. M., *Macromolecules* **2005**, *38*, 1767

Ellison, C. J.; Ruszkowski, R. L.; Fredin, N. J.; Torkelson, J. M., *Phys. Rev. Lett.* **2004b**, *92*, 095702

Ellison, C. J.; Torkelson, J. M., *J. Polym. Sci., Part B: Polym. Phys.* **2002b**, *40*, 2745

Ellison, C. J.; Torkelson, J. M., *Nat. Mater.* **2003**, *2*, 695

Evans, C. M.; Deng, H.; Jager, W. F.; Torkelson, J. M., *Macromolecules* **2013a**, *46*, 6091

Evans, C. M.; Henderson, K. J.; Saathoff, J. D.; Shull, K. R.; Torkelson, J. M., *Macromolecules* **2013b**, *46*, 4131

Evans, C. M.; Kim, S.; Roth, C. B.; Priestley, R. D.; Broadbelt, L. J.; Torkelson, J. M., *Polymer* **2015**, *80*, 180

Evans, C. M.; Narayanan, S.; Jiang, Z.; Torkelson, J. M., *Phys. Rev. Lett.* **2012a**, *109*, 038302

Evans, C. M.; Sandoval, R. W.; Torkelson, J. M., *Macromolecules* **2011**, *44*, 6645

Evans, C. M.; Torkelson, J. M., *Polymer* **2012b**, *53*, 6118

Evans, C. M.; Torkelson, J. M., *Macromolecules* **2012c**, *45*, 8319

Fakhraai, Z.; Forrest, J. A., *Phys. Rev. Lett.* **2005**, *95*, 025701

Fang, M.; Wang, K. G.; Lu, H. B.; Yang, Y. L.; Nutt, S., *J. Mater. Chem.* **2009**, *19*, 7098

Fang, M.; Wang, K. G.; Lu, H. B.; Yang, Y. L.; Nutt, S., *J. Mater. Chem.* **2010**, *20*, 1982

Fernandes, N. J.; Koerner, H.; Giannelis, E. P.; Vaia, R. A., *MRS Commun.* **2013**, *3*, 13

Fernandes, N. J.; Wallin, T. J.; Vaia, R. A.; Koerner, H.; Giannelis, E. P., *Chem. Mater.* **2014**, *26*, 84

Ferry, J. D. *Viscoelastic Properties of Polymers, 3rd Ed.*, (John Wiley & Sons, Inc., 1980).

Forrest, J. A.; Dalnoki-Veress, K., *Adv. Colloid Interface Sci.* **2001**, *94*, 167

Forrest, J. A.; Dalnoki-Veress, K., *ACS Macro Lett.* **2014**, *3*, 310

Forrest, J. A.; Dalnoki-Veress, K.; Dutcher, J. R., *Phys. Rev. E* **1997a**, *56*, 5705

Forrest, J. A.; Dalnoki-Veress, K.; Dutcher, J. R., *Phys. Rev. E* **1997b**, *56*, 5705

Forrest, J. A.; Dalnoki-Veress, K.; Dutcher, J. R., *Phys. Rev. E* **1998**, *58*, 6109

Fotiadou, S.; Karageorgaki, C.; Chrissopoulou, K.; Karatasos, K.; Tanis, I.; Tragoudaras, D.; Frick, B.; Anastasiadis, S. H., *Macromolecules* **2013**, *46*, 2842

Francis, L. F.; McCormick, A. V.; Vaessen, D. M.; Payne, J. A., *J. Mater. Sci.* **2002**, *37*, 4717

Frank, C. W., *Macromolecules* **1975**, *8*, 305

Frank, C. W.; Rao, V.; Despotopoulou, M. M.; Pease, R. F. W.; Hinsberg, W. D.; Miller, R. D.; Rabolt, J. F., *Science* **1996**, *273*, 912

Froltsov, V. A.; Kluppel, M.; Raos, G., *Phys. Rev. E* **2012**, *86*,

Fukao, K.; Miyamoto, Y., *Phys. Rev. E* **2000**, *61*, 1743

Fukao, K.; Miyamoto, Y., *Phys. Rev. E* **2001**, *64*, 1

Fukao, K.; Terasawa, T.; Oda, Y.; Nakamura, K.; Tahara, D., *Phys. Rev. E* **2011**, *84*, 041808

Gao, S.; Koh, Y. P.; Simon, S. L., *Macromolecules* **2013**, *46*, 5620

Gebert, M. S.; Torkelson, J. M., *Polymer* **1990**, *31*, 2402

Geiser, V.; Leterrier, Y.; Manson, J. A. E., *Macromolecules* **2010**, *43*, 7705

Geng, K.; Chen, F.; Tsui, O. K. C., *J. Non-Cryst. Solids* **2015**, *407*, 296

Geng, K.; Tsui, O. K. C., *Macromolecules* **2016**, *49*, 2671

Gibson, R. F., *Compos. Struct.* **2010**, *92*, 2793

Giesa, T.; Buehler, M. J. in *Ann. Rev. Biophys.* Vol. 42 *Annual Review of Biophysics* (ed K. A. Dill) 651 (2013).

Giussi, J. M.; Blaszczyk-Lezak, I.; Cortizo, M. S.; Mijangos, C., *Polymer* **2013**, *54*, 6886

Glor, E. C.; Composto, R. J.; Fakhraai, Z., *Macromolecules* **2015**, *48*, 6682

Glynos, E.; Frieberg, B.; Chremos, A.; Sakellarious, G.; Gidley, D. W.; Green, P. F., *Macromolecules* **2015**, *48*, 2305

Glynos, E.; Frieberg, B.; Oh, H.; Liu, M.; Gidley, D. W.; Green, P. F., *Phys. Rev. Lett.* **2011**, *106*, 128301

Gomopoulos, N.; Cheng, W.; Efremov, M.; Nealey, P. F.; Fytas, G., *Macromolecules* **2009**, *42*, 7164

Gomopoulos, N.; Saini, G.; Efremov, M.; Nealey, P. F.; Nelson, K.; Fytas, G., *Macromolecules* **2010**, *43*, 1551

Goncalves, G.; Marques, P.; Barros-Timmons, A.; Bdkin, I.; Singh, M. K.; Emami, N.; Gracio,

J., *J. Mater. Chem.* **2010**, *20*, 9927

Gotze, W., *Cond. Matter Phys.* **1998**, *1*, 873

Gotze, W.; Sjogren, L., *Rep. Prog. Phys.* **1992**, *55*, 241

Green, P. F., *Soft Matter* **2011**, *7*, 7914

Grohens, Y.; Brogly, M.; Labbe, C.; David, M. O.; Schultz, J., *Langmuir* **1998**, *14*, 2929

Grohens, Y.; Hamon, L.; Reiter, G.; Soldera, A.; Holl, Y., *Eur. Phys. J. E* **2002**, *8*, 217

Guo, S.; Wan, K. T.; Dillard, D. A., *Int. J. Solids Struct.* **2005**, *42*, 2771

Hall, D. B.; Dhinojwala, A.; Torkelson, J. M., *Phys. Rev. Lett.* **1997**, *79*, 103

Harton, S. E.; Kumar, S. K.; Yang, H. C.; Koga, T.; Hicks, K.; Lee, E.; Mijovic, J.; Liu, M.;
Vallery, R. S.; Gidley, D. W., *Macromolecules* **2010**, *43*, 3415

Hartschuh, R.; Ding, Y.; Roh, J. H.; Kisliuk, A.; Sokolov, A. P.; Soles, C. L.; Jones, R. L.; Hu,
T. J.; Wu, W. L.; Mahorowala, A. P., *J. Polym. Sci. Part B* **2004**, *42*, 1106

Hartschuh, R.; Kisliuk, A.; Novikov, V.; Sokolov, A. P.; Heyliger, P. R.; Flannery, C. M.;
Johnson, W. L.; Soles, C. L.; Wu, W.-L., *Appl. Phys. Lett.* **2005**, *87*, 173121

Hayashi, T.; Fukao, K., *Phys. Rev. E* **2014**, *89*, 022602

Hayward, R. C.; Graessley, W. W., *Macromolecules* **1999**, *32*, 3502

Herminghaus, S., *Eur. Phys. J. E* **2002**, *8*, 237

Hochstrasser, R. M.; Small, G. J., *J. Chem. Phys.* **1966**, *45*, 2270

Holt, A. P.; Griffin, P. J.; Bocharova, V.; Agapov, A. L.; Imel, A. E.; Dadmun, M. D.; Sangoro,
J. R.; Sokolov, A. P., *Macromolecules* **2014**, *47*, 1837

Holt, A. P.; Sangoro, J. R.; Wang, Y. Y.; Agapov, A. L.; Sokolov, A. P., *Macromolecules* **2013**,
46, 4168

Hong, R. Y.; Qian, J. Z.; Cao, J. X., *Powder Technol.* **2006**, *163*, 160

Hu, Y.; Du, Z. S.; Deng, X. L.; Wang, T.; Yang, Z. H.; Zhou, W. Y.; Wang, C. Y.,
Macromolecules **2016**, *49*, 5660

Huang, Y.; Paul, D. R., *Macromolecules* **2006**, *39*, 1553

Inoue, R.; Kanaya, T.; Nishida, K.; Tsukushi, I.; Shibata, K., *Phys. Rev. Lett.* **2005**, *95*, 056102

Inoue, R.; Kanaya, T.; Nishida, K.; Tsukushi, I.; Shibata, K., *Phys. Rev. E* **2006**, *74*, 021801

Inoue, R.; Kawashima, K.; Matsui, K.; Kanaya, T.; Nishida, K.; Matsuba, G.; Hino, M., *Phys. Rev. E* **2011**, *83*, 021801

Inoue, R.; Nakamura, M.; Matsui, K.; Kanaya, T.; Nishida, K.; Hino, M., *Phys. Rev. E* **2013**, *88*,

Jackson, C. L.; McKenna, G. B., *J. Non-Cryst. Solids* **1991**, *131*, 221

Jancar, J.; Douglas, J. F.; Starr, F. W.; Kumar, S. K.; Cassagnau, P.; Lesser, A. J.; Sternstein, S. S.; Buehler, M. J., *Polymer* **2010**, *51*, 3321

Jin, K.; Torkelson, J. M., *Polymer* **2015**, *65*, 233

Jin, K.; Torkelson, J. M., *Macromolecules* **2016**, *49*, 5092

Ju, B. F.; Liu, K. K.; Wong, M. F.; Wan, K. T., *Eng. Fract. Mech.* **2007**, *74*, 1101

Kader, M. A.; Kim, K.; Lee, Y. S.; Nah, C., *J. Mater. Sci.* **2006**, *41*, 7341

Kalyanasundaram, K.; Thomas, J. K., *J. Am. Chem. Soc.* **1977**, *99*, 2039

Kanaya, T.; Miyazaki, T.; Watanabe, H.; Nishida, K.; Yamana, H.; Tasaki, S.; Bucknall, D. B., *Polymer* **2003**, *44*, 3769

Kanaya, T.; Ogawa, H.; Kishimoto, M.; Inoue, R.; Suter, A.; Prokscha, T., *Phys. Rev. E* **2015**, *92*, 022604

Kango, S.; Kalia, S.; Celli, A.; Njuguna, J.; Habibi, Y.; Kumar, R., *Prog. Polym. Sci.* **2013**, *38*, 1232

Karpovich, D. S.; Blanchard, G. J., *J. Phys. Chem.* **1995**, *99*, 3951

Kauzmann, W., *Chem. Rev.* **1948**, *43*, 219

Kawaguchi, D.; Tateishi, Y.; Tanaka, K., *J. Non-Cryst. Solids* **2015**, *407*, 284

Kawana, S.; Jones, R. A. L., *Phys. Rev. E* **2001**, *63*, 021501

Keddie, J. L.; Jones, R. A. L., *Isr. J. Chem.* **1995**, *35*, 21

Keddie, J. L.; Jones, R. A. L.; Cory, R. A., *Faraday Discuss.* **1994a**, *98*, 219

Keddie, J. L.; Jones, R. A. L.; Cory, R. A., *Europhys. Lett.* **1994b**, *27*, 59

Khani, M. M.; Woo, D.; Mumpower, E. L.; Benicewicz, B., *Polymer* **2017**, *109*, 339

Killgore, J. P.; Kelly, J. Y.; Stafford, C. M.; Fasolka, M. J.; Hurley, D. C., *Nanotechnology* **2011**, *22*, 175706

Kim, C.; Facchetti, A.; Marks, T. J., *Science* **2007**, *318*, 76

Kim, D.; Srivastava, S.; Narayanan, S.; Archer, L. A., *Soft Matter* **2012**, *8*, 10813

Kim, J.; Mok, M. M.; Sandoval, R. W.; Woo, D. J.; Torkelson, J. M., *Macromolecules* **2006**, *39*, 6152

Kim, J. H.; Jang, J.; Zin, W. C., *Langmuir* **2000**, *16*, 4064

Kim, S.; Hewlett, S. A.; Roth, C. B.; Torkelson, J. M., *Eur. Phys. J. E* **2009**, *30*, 83

Kim, S.; Mundra, M. K.; Roth, C. B.; Torkelson, J. M., *Macromolecules* **2010**, *43*, 5158

Kim, S.; Roth, C. B.; Torkelson, J. M., *J. Polym. Sci., Part B: Polym. Phys.* **2008**, *46*, 2754

Kim, S.; Torkelson, J. M., *Macromolecules* **2011**, *44*, 4546

Kim, S. A.; Mangal, R.; Archer, L. A., *Macromolecules* **2015a**, *48*, 6280

Kim, S. D.; Torkelson, J. M., *Macromolecules* **2002**, *35*, 5943

Kim, S. K.; Nguyen, N. A.; Wie, J. J.; Park, H. S., *Nanoscale* **2015b**, *7*, 8864

Koerner, H.; Opsitnick, E.; Grabowski, C. A.; Drummy, L. F.; Hsiao, M.-S.; Che, J.; Pike, M.; Person, V.; Bockstaller, M. R.; Meth, J. S.; Vaia, R. A., *J. Polym. Sci. Part B: Polym. Phys.* **2016**, *54*, 319

Kontou, E.; Anthoulis, G., *J. Appl. Polym. Sci.* **2007**, *105*, 1723

Krigbaum, W. R.; Roig, A., *J. Chem. Phys.* **1959**, *31*, 544

Krishnamoorti, R.; Vaia, R. A.; Giannelis, E. P., *Chem. Mater.* **1996**, *8*, 1728

Kropka, J. M.; Pryamitsyn, V.; Ganesan, V., *Phys. Rev. Lett.* **2008**, *101*, 075702

Kropka, J. M.; Putz, K. W.; Pryamitsyn, V.; Ganesan, V.; Green, P., *Macromolecules* **2007**, *40*, 5424

Kumar, S. K.; Jouault, N.; Benicewicz, B.; Neely, T., *Macromolecules* **2013**, *46*, 3199

Kunal, K.; Robertson, C. G.; Pawlus, S.; Hahn, S. F.; Sokolov, A. P., *Macromolecules* **2008**, *41*, 7232

Lakowicz, J. R. *Principles of Fluorescence Spectroscopy, 3rd Edition*. (Springer Science + Business Media, LLC, 2006).

Lan, T.; Torkelson, J. M., *Polymer* **2014**, *55*, 1249

Lan, T.; Torkelson, J. M., *Polymer* **2015**, *64*, 183

Lan, T.; Torkelson, J. M., *Macromolecules* **2016**, *49*, 1331

Lang, R. J.; Merling, W. L.; Simmons, D. S., *ACS Macro Lett.* **2014**, *3*, 758

Lang, R. J.; Simmons, D. S., *Macromolecules* **2013**, *46*, 9818

Lee, K. J.; Lee, D. K.; Kim, Y. W.; Choe, W.-S.; Kim, J. H., *J. Polym. Sci. Part B: Polym. Phys.* **2007**, *45*, 2232

Lee, Y. C.; Bretz, K. C.; Wise, F. W.; Sachse, W., *Appl. Phys. Lett.* **1996**, *69*, 1692

Lenhart, J. L.; van Zanten, J. H.; Dunkers, J. P.; Parnas, R. S., *Macromolecules* **2001**, *34*, 2225

Li, B.; Lu, X. L.; Ma, Y. H.; Han, X. F.; Chen, Z., *ACS Macro Lett.* **2015a**, *4*, 548

Li, L. L.; Chen, J.; Deng, W. J.; Zhang, C.; Sha, Y.; Cheng, Z.; Xue, G.; Zhou, D. S., *J. Phys. Chem. B* **2015b**, *119*, 5047

Li, L. L.; Zhou, D. S.; Huang, D. H.; Xue, G., *Macromolecules* **2014**, *47*, 297

Li, X.; McKenna, G. B., *Macromolecules* **2015c**, *48*, 6329

Lin, L.; Bidstrup, S. A., *J. Appl. Polym. Sci.* **1993**, *49*, 1277

Lin, Y.; Boker, A.; He, J. B.; Sill, K.; Xiang, H. Q.; Abetz, C.; Li, X. F.; Wang, J.; Emrick, T.; Long, S.; Wang, Q.; Balazs, A.; Russell, T. P., *Nature* **2005**, *434*, 55

Liu, D.; Qin, H.; Zhang, J. H.; Wang, J., *Phys. Rev. E* **2016**, *94*, 052503

Liu, R. Y. F.; Jin, Y.; Hiltner, A.; Baer, E., *Macromol. Rapid Commun.* **2003**, *24*, 943

Liu, Y.; Chen, Y.-C.; Hutchens, S.; Lawrence, J.; Emrick, T.; Crosby, A. J., *Macromolecules* **2015**, *48*, 6534

Lopez, E.; Simon, S. L., *Macromolecules* **2015**, *48*, 4692

Loutfy, R. O., *Macromolecules* **1981**, *14*, 270

Loutfy, R. O., *Pure Appl. Chem.* **1986**, *58*, 1239

Madkour, T. M.; Hagag, F. M.; Mamdouh, W.; Azzam, R. A., *Polymer* **2012**, *53*, 5788

Maillard, D.; Kumar, S. K.; Fragneaud, B.; Kysar, J. W.; Rungta, A.; Benicewicz, B. C.; Deng, H.; Brinson, L. C.; Douglas, J. F., *Nano Lett.* **2012**, *12*, 3909

Mangal, R.; Srivastava, S.; Archer, L. A., *Nat. Commun.* **2015**, *6*, 7198

Mangal, R.; Wen, Y. H.; Choudhury, S.; Archer, L. A., *Macromolecules* **2016**, *49*, 5202

Marvin, M. D.; Lang, R. J.; Simmons, D. S., *Soft Matter* **2014**, *10*, 3166

Mattsson, J.; Forrest, J. A.; Borjesson, L., *Phys. Rev. E* **2000**, *62*, 5187

Matyjaszewski, K.; Dong, H.; Jakubowski, W.; Pietrasik, J.; Kusumo, A., *Langmuir* **2007**, *23*, 4528

Meng, Y.; Bernazzani, P.; O'Connell, P. A.; McKenna, G. B.; Simon, S., *Rev. Sci. Intrum.* **2009**, *80*, 053903

Merabia, S.; Sotta, P.; Long, D., *Eur. Phys. J. E* **2004**, *15*, 189

Mijovic, J.; Lee, H. K.; Kenny, J.; Mays, J., *Macromolecules* **2006**, *39*, 2172

Milano, G.; Santangelo, G.; Ragone, F.; Cavallo, L.; Di Matteo, A., *J. Phys. Chem. C* **2011**, *115*, 15154

Mirigian, S.; Schweizer, K. S., *J Phys. Chem. Lett.* **2013**, *4*, 3648

Mirigian, S.; Schweizer, K. S., *J. Chem. Phys.* **2014**, *141*, 161103

Mirigian, S.; Schweizer, K. S., *J. Chem. Phys.* **2015**, *143*, 244705

Miwa, Y.; Urakawa, O.; Nobukawa, S.; Kutsumizu, S., *Polymer* **2015**, *59*, 194

Miwa, Y.; Yamamoto, K.; Sakaguchi, M.; Sakai, M.; Makita, S.; Shimada, S., *Macromolecules* **2005**, *38*, 832

Mizuno, M.; Nakamura, K.; Konishi, T.; Fukao, K., *J. Non-Cryst. Solids* **2011**, *357*, 594

Mok, M. M.; Kim, J.; Wong, C. L. H.; Marrou, S. R.; Woo, D. J.; Dettmer, C. M.; Nguyen, S. T.; Ellison, C. J.; Shull, K. R.; Torkelson, J. M., *Macromolecules* **2009**, *42*, 7863

Moll, J.; Kumar, S. K., *Macromolecules* **2012**, *45*, 1131

Moniruzzaman, M.; Winey, K. I., *Macromolecules* **2006**, *39*, 5194

Monteiro, D. R.; Gorup, L. F.; Takamiya, A. S.; Ruvollo, A. C.; Camargo, E. R.; Barbosa, D. B., *Int. J. Antimicrob. Agents* **2009**, *34*, 103

Moynihan, C. T.; Easteal, A. J.; Debolt, M. A.; Tucker, J., *J. Am. Ceram. Soc.* **1976**, *59*, 12

Mujtaba, A.; Keller, M.; Ilisch, S.; Radusch, H. J.; Beiner, M.; Thurn-Albrecht, T.; Saalwachter, K., *ACS Macro Lett.* **2014**, *3*, 481

Mundra, M. K.; Donthu, S. K.; Dravid, V. P.; Torkelson, J. M., *Nano Lett.* **2007a**, *7*, 713

Mundra, M. K.; Ellison, C. J.; Behling, R. E.; Torkelson, J. M., *Polymer* **2006**, *47*, 7747

Mundra, M. K.; Ellison, C. J.; Rittigstein, P.; Torkelson, J. M., *Eur. Phys. J. - Spec. Top.* **2007b**, *141*, 143

Nakashima, K.; Tanaka, I., *Langmuir* **1993**, *9*, 90

Napolitano, S.; Wubbenhorst, M., *Polymer* **2010**, *51*, 5309

Napolitano, S.; Wubbenhorst, M., *Nat. Commun.* **2011**, *2*, 1

Natarajan, B.; Neely, T.; Rungta, A.; Benicewicz, B. C.; Schadler, L. S., *Macromolecules* **2013**, *46*, 4909

Ndoro, T. V. M.; Bohm, M. C.; Muller-Plathe, F., *Macromolecules* **2012**, *45*, 171

Ndoro, T. V. M.; Voyiatzis, E.; Ghanbari, A.; Theodorou, D. N.; Bohm, M. C.; Muller-Plathe, F., *Macromolecules* **2011**, *44*, 2316

Ngai, K. L.; Prevesto, D.; Cappaccioli, S., *Philos. Mag.* **2016**, *96*, 854

Nguyen, H. K.; Fujinami, S.; Nakajima, K., *Polymer* **2016**, *105*, 64

O'Connell, P. A.; Hutcheson, S. A.; McKenna, G. B., *J. Polym. Sci., Part B: Polym. Phys.* **2008**, *46*, 1952

O'Connell, P. A.; McKenna, G. B., *Science* **2005**, *307*, 1760

Oberdisse, J., *Soft Matter* **2006**, *2*, 29

Oh, H.; Green, P. F., *Nat. Mater.* **2009**, *8*, 139

Ohno, K.; Morinaga, T.; Koh, K.; Tsujii, Y.; Fukuda, T., *Macromolecules* **2005**, *38*, 2137

Olson, B. G.; Peng, Z. L.; Srithawatpong, R.; McGervey, J. D.; Ishida, H.; Jamieson, A. M.; Manias, E.; Giannelis, E. P. in *Proceedings of the 11th International Conference on Positron Annihilation* Vol. 255 *Mater. Sci. Forum*   336 (1997).

Park, C. H.; Kim, J. H.; Ree, M.; Sohn, B. H.; Jung, J. C.; Zin, W. C., *Polymer* **2004**, *45*, 4507

Park, O. K.; Hwang, J. Y.; Goh, M.; Lee, J. H.; Ku, B. C.; You, N. H., *Macromolecules* **2013**, *46*, 3505

Parker, K.; Schneider, R. T.; Siegel, R. W.; Ozisik, R.; Cabanelas, J. C.; Serrano, B.; Antonelli, C.; Baselga, J., *Polymer* **2010**, *51*, 4891

Patel, M., *Polym. Test.* **2004**, *23*, 107

Peter, S.; Meyer, H.; Baschnagel, J., *J. Polym. Sci. Part B: Polym. Phys.* **2006**, *44*, 2951

Pietrasik, J.; Hui, C. M.; Chaladaj, W.; Dong, H. C.; Choi, J.; Jurczak, J.; Bockstaller, M. R.; Matyjaszewski, K., *Macromol. Rapid Commun.* **2011**, *32*, 295

Plazek, D. J., *J. Phys. Chem.* **1965**, *69*, 3480

Pohlers, G.; Scaiano, J. C.; Sinta, R., *Chem. Mater.* **1997**, *9*, 3222

Porter, C. E.; Blum, F. D., *Macromolecules* **2002**, *35*, 7448

Prado, E. A.; Yamaki, S. B.; Atvars, T. D. Z.; Zimerman, O. E.; Weiss, R. G., *J. Phys. Chem. B* **2000**, *104*, 5905

Pramoda, K. P.; Mya, K. Y.; Lin, T. T.; Wang, J.; He, C. B. in *Nmr Spectroscopy of Polymers: Innovative Strategies for Complex Macromolecules* Vol. 1077 *ACS Symposium Series* (eds H. N. Cheng, T. Asakura, & A. D. English) 105 (2011).

Prest, W. M.; Luca, D. J., *J. of Appl. Phys.* **1979**, *50*, 6067

Prest, W. M.; Luca, D. J., *J. Appl. Phys.* **1980**, *51*, 5170

Prest, W. M.; Roberts, F. J., *Ann. N.Y. Acad. Sci.* **1981**, *371*, 67

Priestley, R. D.; Broadbelt, L. J.; Torkelson, J. M., *Macromolecules* **2005a**, *38*, 654

Priestley, R. D.; Cangialosi, D.; Napolitano, S., *J. Non-Cryst. Solids* **2015**, *407*, 288

Priestley, R. D.; Ellison, C. J.; Broadbelt, L. J.; Torkelson, J. M., *Science* **2005b**, *309*, 456

Priestley, R. D.; Mundra, M. K.; Barnett, N. J.; Broadbelt, L. J.; Torkelson, J. M., *Aust. J. Chem.* **2007**, *60*, 765

Pryamitsyn, V.; Ganesan, V., *Macromolecules* **2010**, *43*, 5851

Pschorn, U.; Rossler, E.; Sillescu, H.; Kaufmann, S.; Schaefer, D.; Spiess, H. W., *Macromolecules* **1991**, *24*, 398

Qian, K. K.; Grobelny, P. J.; Tyagi, M.; Cicerone, M. T., *Mol. Pharmaceutics* **2015**, *12*, 1141

Ramanathan, T.; Abdala, A. A.; Stankovich, S.; Dikin, D. A.; Herrera-Alonso, M.; Piner, R. D.; Adamson, D. H.; Schniepp, H. C.; Chen, X.; Ruoff, R. S.; Nguyen, S. T.; Aksay, I. A.; Prud'homme, R. K.; Brinson, L. C., *Nat. Nanotechnol.* **2008**, *3*, 327

Ramanathan, T.; Liu, H.; Brinson, L. C., *J. Polym. Sci. Part B: Polym. Phys.* **2005**, *43*, 2269

Ramorino, G.; Bignotti, F.; Pandini, S.; Ricco, T., *Compos. Sci. Technol.* **2009**, *69*, 1206

Ree, M.; Chu, C. W.; Goldberg, M. J., *J. Appl. Phys.* **1994**, *75*, 1410

Ree, M.; Park, Y. H.; Kim, K.; Kim, S. I.; Cho, C. K.; Park, C. E., *Polymer* **1997**, *38*, 6333

Reid, D. K.; Freire, M. A.; Yao, H. Q.; Sue, H. J.; Lutkenhaus, J. L., *Acs Macro Lett.* **2015**, *4*, 151

Reinsberg, S.; Qiu, X.; Wilhelm, M.; Spiess, H. W.; Ediger, M. D., *J. Chem. Phys.* **2001**, *114*, 7299

Reinsberg, S. A.; Heuer, A.; Doliwa, B.; Zimmerman, H.; Spiess, H. W., *J. Non-Cryst. Solids* **2002**, *307*, 208

Reiter, G., *Phys. Rev. Lett.* **1992**, *68*, 75

Reiter, G., *Langmuir* **1993**, *9*, 1344

Reiter, G., *Macromolecules* **1994**, *27*, 3046

Reiter, G., *Adv. Polym. Sci.* **2013**, *252*, 29

Reiter, G.; de Gennes, P. G., *Eur. Phys. J. E* **2001**, *6*, 25

Reiter, G.; Hamieh, M.; Damman, P.; Sclavons, S.; Gabriele, S.; Vilmin, T.; Raphael, E., *Nat.*

Mater. **2005**, *4*, 754

Rharbi, Y.; Cabane, B.; Vacher, A.; Joanicot, M.; Boue, F., *Europhys. Lett.* **1999**, *46*, 472

Richardson, H.; Carelli, C.; Keddie, J. L.; Sferrazza, M., *Eur. Phys. J. E* **2003**, *12*, 437

Richardson, M. J.; Savill, N. G., *Polymer* **1975**, *16*, 753

Riggleman, R. A.; Douglas, J. F.; de Pablo, J. J., *J. Chem. Phys.* **2007**, *126*, 234903

Riggleman, R. A.; Yoshimoto, K.; Douglas, J. F.; de Pablo, J. J., *Phys. Rev. Lett.* **2006**, *97*, 045502

Rittigstein, P.; Priestley, R. D.; Broadbelt, L. J.; Torkelson, J. M., *Nat. Mater.* **2007**, *6*, 278

Rittigstein, P.; Torkelson, J. M., *J. Polym. Sci. Part B: Polym. Phys.* **2006**, *44*, 2935

Rizos, A. K.; Ngai, K. L., *Macromolecules* **1998**, *31*, 6217

Robertson, C. G.; Santangelo, P. G.; Roland, C. M., *J. Non-Cryst. Solids* **2000**, *275*, 153

Roland, C. M. *Viscoelastic Behavior of Rubbery Materials*. (Oxford University Press, 2011).

Roland, C. M.; Ngai, K. L., *Macromolecules* **1996**, *29*, 5747

Rong, M. Z.; Zhang, M. Q.; Ruan, W. H., *Mater. Sci. Technol.* **2006**, *22*, 787

Roth, C. B.; McNerny, K. L.; Jager, W. F.; Torkelson, J. M., *Macromolecules* **2007a**, *40*, 2568

Roth, C. B.; Pound, A.; Kamp, S. W.; Murray, C. A.; Dutcher, J. R., *Eur. Phys. J. E* **2006**, *20*, 441

Roth, C. B.; Torkelson, J. M., *Macromolecules* **2007b**, *40*, 3328

Roth, C. B.; Torkelson, J. M., *Macromolecules* **2007c**, *40*, 3328

Roy, R.; Agrawal, D. K.; McKinstry, H. A., *Annu. Rev. Mater. Sci.* **1989**, *19*, 59

Salavagione, H. J.; Quiles-Diaz, S.; Enrique-Jimenez, P.; Martinez, G.; Ania, F.; Flores, A.; Gomez-Fatou, M. A., *Macromolecules* **2016**, *49*, 4948

Santangelo, P. G.; Roland, C. M., *Macromolecules* **1998**, *31*, 4581

Sanz, A.; Ruppel, M.; Douglas, J. F.; Cabral, J. T., *J. Phys. - Condens. Mat.* **2008**, *20*, 104209

Sanz, A.; Wong, H. C.; Nedoma, A. J.; Douglas, J. F.; Cabral, J. T., *Polymer* **2015**, *68*, 47

Savin, D. A.; Pyun, J.; Patterson, G. D.; Kowalewski, T.; Matyjaszewski, K., *J. Polym. Sci., Part*

B: Polym. Phys. **2002a**, *40*, 2667

Savin, D. A.; Pyun, J.; Patterson, G. D.; Kowalewski, T.; Matyjaszewski, K., *J. Polym. Sci. Part B: Polym. Phys.* **2002b**, *40*, 2667

Schadler, L., *Nat. Mater.* **2007a**, *6*, 257

Schadler, L. S.; Kumar, S. K.; Benicewicz, B. C.; Lewis, S. L.; Harton, S. E., *MRS Bulletin* **2007b**, *32*, 335

Schmidt, M.; Burchard, W., *Macromolecules* **1981**, *14*, 210

Schmidt-Rohr, K.; Spiess, H. W., *Phys. Rev. Lett.* **1991**, *66*, 3020

Schweizer, K. S., *J. Chem. Phys.* **1989**, *91*, 5802

Seemann, R.; Jacobs, K.; Landfester, K.; Herminghaus, S., *J. Polym. Sci. Part B: Polym. Phys.* **2006**, *44*, 2968

Sha, Y.; Li, L. L.; Wang, X. L.; Wan, Y. X.; Yu, J.; Xue, G.; Zhou, D. S., *Macromolecules* **2014**, *47*, 8722

Shao, C.; Keten, S., *Sci. Rep.* **2015**, *5*, 16452

Sharp, J. S.; Forrest, J. A., *Phys. Rev. Lett.* **2003**, *91*, 235701

Shen, L.; Lin, Y. J.; Du, Q. G.; Zhong, W., *Compos. Sci. Technol.* **2006**, *66*, 2242

Shin, K.; Obukhov, S.; Chen, J. T.; Huh, J.; Hwang, Y.; Mok, S.; Dobriyal, P.; Thiyagarajan, P.; Russell, T. P., *Nat. Mater.* **2007**, *6*, 961

Shin, Y.; Lee, H.; Lee, W.; Ryu, D. Y., *Macromolecules* **2016**, *49*, 5291

Shirai, M.; Tsunooka, M., *Bull. Chem. Soc. Jpn.* **1998**, *71*, 2483

Simmons, D. S., *Macromol. Chem. Phys.* **2016**, *217*, 137

Simon, S. L.; Plazek, D. J.; Sobieski, J. W.; McGregor, E. T., *J. Polym. Sci. Part B: Polym. Phys.* **1997**, *35*, 929

Small, C. E.; Chen, S.; Subbiah, J.; Amb, C. M.; Tsang, S. W.; Lai, T. H.; Reynolds, J. R.; So, F., *Nat. Photonics* **2012**, *6*, 115

Soles, C. L.; Dimeo, R. M.; Neumann, D. A.; Kisliuk, A.; Sokolov, A. P.; Liu, J. W.; Yee, A. F.,

Macromolecules **2001**, *34*, 4082

Soles, C. L.; Douglas, J. F.; Wu, W. L.; Dimeo, R. M., *Phys. Rev. Lett.* **2002**, *88*, 037401

Song, G. S.; Zhang, L.; He, C. C.; Fang, D. C.; Whitten, P. G.; Wang, H. L., *Macromolecules* **2013**, *46*, 7423

Sperling, L. H. *Introduction to Physical Polymer Science*. 4th Ed. edn, (John Wiley & Sons, Inc., 2006).

Stafford, C. M.; Harrison, C.; Beers, K. L.; Karim, A.; Amis, E. J.; Vanlandingham, M. R.; Kim, H. C.; Volksen, W.; Miller, R. D.; Simonyi, E. E., *Nat. Mater.* **2004**, *3*, 545

Stafford, C. M.; Vogt, B. D.; Harrison, C.; Julthongpiput, D.; Huang, R., *Macromolecules* **2006**, *39*, 5095

Starr, F. W.; Schroder, T. B.; Glotzer, S. C., *Phys. Rev. E* **2001**, *64*, 021802

Starr, F. W.; Schroder, T. B.; Glotzer, S. C., *Macromolecules* **2002**, *35*, 4481

Stoykovich, M. P.; Yoshimoto, K.; Nealey, P. F., *App. Phys. A* **2008**, *90*, 277

Tan, A. W.; Torkelson, J. M., *Polymer* **2016**, *82*, 327

Tang, Y. J.; Chen, J.; Huang, Y. B.; Li, D. C.; Wang, S. S.; Li, Z. H.; Zhang, W. D., *J. Micromech. Microeng.* **2007**, *17*, 1923

Tang, Z. H.; Kang, H. L.; Shen, Z. L.; Guo, B. C.; Zhang, L. Q.; Jia, D. M., *Macromolecules* **2012**, *45*, 3444

Tedeschi, C.; Mohwald, H.; Kirstein, S., *J. Am. Chem. Soc.* **2001**, *123*, 954

Tegou, E.; Bellas, V.; Gogolides, E.; Argitis, P.; Eon, D.; Cartry, G.; Cardinaud, C., *Chem. Mater.* **2004**, *16*, 2567

Thomas, K. R.; Chenneviere, A.; Reiter, G.; Steiner, U., *Phys. Rev. E* **2011a**, *83*, 021804

Thomas, K. R.; Steiner, U., *Soft Matter* **2011b**, *7*, 7839

Tobolsky, A. V., *J. Appl. Phys.* **1956**, *27*, 673

Tobolsky, A. V.; Murakami, K., *J. Polym. Sci.* **1960**, *47*, 55

Tool, A. Q., *J. Am. Chem. Soc.* **1946**, *29*, 240

Torres, J. M.; Stafford, C. M.; Uhrig, D.; Vogt, B. D., *J. Polym. Sci., Part B: Polym. Phys.* **2012**, *50*, 370

Torres, J. M.; Stafford, C. M.; Vogt, B. D., *ACS Nano* **2009**, *3*, 2677

Torres, J. M.; Stafford, C. M.; Vogt, B. D., *ACS Nano* **2010**, *4*, 5357

Tracht, U.; Wilhelm, M.; Heuer, A.; Feng, H.; Schmidt-Rohr, K.; Spiess, H. W., *Phys. Rev. Lett.* **1998**, *81*, 2727

Tsui, O. K. C.; Zhang, H. F., *Macromolecules* **2001**, *34*, 9139

Tsukruk, V. V.; Sidorenko, A.; Gorbunov, V. V.; Chizhik, S. A., *Langmuir* **2001**, *17*, 6715

Tweedie, C. A.; Constantinides, G.; Lehman, K. E.; Brill, D. J.; Blackman, G. S.; Van Vliet, K. J., *Adv. Mater.* **2007**, *19*, 2540

Ugur, G.; Akgun, B.; Jiang, Z.; Narayanan, S.; Satija, S.; Foster, M. D., *Soft Matter* **2016**, *12*, 5372

Vaia, R. A.; Maguire, J. F., *Chem. Mater.* **2007**, *19*, 2736

Valeur, B. *Molecular Fluorescence: Principles and Applications*. (Wiley-VCH, 2001).

van Zanten, J. H.; Rufener, K. P., *Phys. Rev. E* **2000**, *62*, 5389

van Zanten, J. H.; Wallace, W. E.; Wu, W.-L., *Phys. Rev. E* **1996**, *53*, 2053

Vignaud, G.; Chebil, M. S.; Bal, J. K.; Delorme, N.; Beuvier, T.; Grohens, Y.; Gibaud, A., *Langmuir* **2014**, *30*, 11599

Voudouris, P.; Choi, J.; Gomopoulos, N.; Sainidou, R.; Dong, H. C.; Matyjaszewski, K.; Bockstaller, M. R.; Fytas, G., *ACS Nano* **2011**, *5*, 5746

Walheim, S.; Boltau, M.; Mlynek, J.; Krausch, G.; Steiner, U., *Macromolecules* **1997**, *30*, 4995

Wallraff, G. M.; Hinsberg, W. D., *Chem. Rev.* **1999**, *99*, 1801

Wang, H. X.; Chang, T. X.; Li, X. H.; Zhang, W. D.; Hu, Z. J.; Jonas, A. M., *Nanoscale* **2016a**, *8*, 14950

Wang, L. M.; Velikov, V.; Angell, C. A., *J. Chem. Phys.* **2002**, *117*, 10184

Wang, M.; Fan, X. S.; Thitsartarn, W.; He, C. B., *Polymer* **2015**, *58*, 43

Wang, Y.; Chen, W. C., *E-Polymers* **2012**, 012

Wang, Y. T.; Chang, T. C.; Hong, Y. S.; Chen, H. B., *Thermochim. Acta* **2003**, *397*, 219

Wang, Y. X.; Ma, R. L.; Hu, K. S.; Kim, S. H.; Fang, G. Q.; Shao, Z. Z.; Tsukruk, V. V., *ACS Appl. Mater. Interfaces* **2016b**, *8*, 24962

Wardle, B. L.; Saito, D. S.; Garcia, E. J.; Hart, A. J.; de Villoria, R. G.; Verploegen, E. A., *Adv. Mater.* **2008**, *20*, 2707

Watcharotone, S.; Wood, C. D.; Friedrich, R.; Chen, X.; Qiao, R.; Putz, K.; Brinson, L. C., *Adv. Eng. Mater.* **2011**, *13*, 400

Weir, M. P.; Johnson, D. W.; Boothroyd, S. C.; Savage, R. C.; Thompson, R. L.; King, S. M.; Rogers, S. E.; Coleman, K. S.; Clarke, N., *ACS Macro Lett.* **2016**, *5*, 430

White, R. P.; Price, C. C.; Lipson, J. E. G., *Macromolecules* **2015**, *48*, 4132

Whitlow, S. J.; Wool, R. P., *Macromolecules* **1991**, *24*, 5926

Wilhelm, M.; Zhao, C. L.; Wang, Y. C.; Xu, R. L.; Winnik, M. A.; Mura, J. L.; Riess, G.; Croucher, M. D., *Macromolecules* **1991**, *24*, 1033

Williams, G. A.; Ishige, R.; Cromwell, O. R.; Chung, J.; Takahara, A.; Guan, Z., *Adv. Mater.* **2015**, *27*, 3934

Winey, K. I.; Vaia, R. A., *MRS Bulletin* **2007**, *32*, 314

Wong, H. C.; Sanz, A.; Douglas, J. F.; Cabral, J. T., *J. Mol. Liq.* **2010**, *153*, 79

Xia, W.; Hsu, D. D.; Keten, S., *Macromol. Rapid Commun.* **2015a**, *36*, 1422

Xia, W.; Song, J.; Hsu, D. D.; Keten, S., *Macromolecules* **2016**, *49*, 3810

Xia, W. J.; Keten, S., *Extreme Mech. Lett.* **2015b**, *4*, 89

Xia, W. J.; Keten, S., *J. Mater. Res.* **2015c**, *30*, 36

Xia, W. J.; Mishra, S.; Keten, S., *Polymer* **2013**, *54*, 5942

Xie, F. C.; Zhang, H. F.; Lee, F. K.; Du, B. Y.; Tsui, O. K. C.; Yokoe, Y.; Tanaka, K.; Takahara, A.; Kajiyama, T.; He, T. B., *Macromolecules* **2002**, *35*, 1491

Xie, S. J.; Quan, H. J.; Lei, Z. Y., *J. Chem. Phys.* **2015**, *142*, 074902

Xin, H.; Kim, F. S.; Jenekhe, S. A., *J. Am. Chem. Soc.* **2008**, *130*, 5424

Xu, S.; O'Connell, P. A.; McKenna, G. B., *J. Chem. Phys.* **2010**, *132*, 184902

Yang, J.; Schweizer, K. S., *J. Chem. Phys.* **2011**, *134*, 204909

Yang, J.; Zhao, J. J.; Han, C. R.; Duan, J. F., *Compos. Sci. Technol.* **2014**, *95*, 1

Yang, Z.; Fujii, Y.; Lee, F. K.; Lam, C.-H.; Tsui, O. K. C., *Science* **2010**, *328*, 1676

Yano, O.; Wada, Y., *J. Polym. Sci., Part B: Polym. Phys.* **1971**, *9*, 669

Yaws, C. L. *Thermophysical Properties of Chemicals and Hydrocarbons, 2nd Ed.*, (Elsevier, 2014).

Ye, C.; Wiener, C. G.; Tyagi, M.; Uhrig, D.; Orski, S. V.; Soles, C. L.; Vogt, B. D.; Simmons, D. S., *Macromolecules* **2015**, *48*, 801

Yoon, H.; McKenna, G. B., *Macromolecules* **2014**, *47*, 8808

Yoshimoto, K.; Jain, T. S.; Nealey, P. F.; de Pablo, J. J., *J. Chem. Phys.* **2005**, *122*, 144712

Zachariah, A. K.; Chandra, A. K.; Mohammed, P. K.; Parameswaranpillai, J.; Thomas, S., *Appl. Clay Sci.* **2016**, *123*, 1

Zhang, C.; Boucher, V. M.; Cangialosi, D.; Priestley, R. D., *Polymer* **2013a**, *54*, 230

Zhang, C.; Guo, Y.; Shepard, K. B.; Priestley, R. D., *J. Phys. Chem. Lett.* **2013b**, *4*, 431

Zhang, C.; Priestley, R. D., *Soft Matter* **2013c**, *9*, 7076

Zhang, L.; Marsiglio, J. A.; Lan, T.; Torkelson, J. M., *Macromolecules* **2016**, *49*, 2387

Zhang, L.; Torkelson, J. M., *Polymer* **2015**, *65*, 105

Zhang, M.; Askar, S.; Torkelson, J. M.; Brinson, L. C., *In Preparation* **2017**

Zhang, M. F.; Dobriyal, P.; Chen, J. T.; Russell, T. P.; Olmo, J.; Merry, A., *Nano Lett.* **2006**, *6*, 1075

Zhang, X. H.; Yager, K. G.; Kang, S. H.; Fredin, N. J.; Akgun, B.; Satija, S.; Douglas, J. F.; Karim, A.; Jones, R. L., *Macromolecules* **2010**, *43*, 1117

Zhao, H. Y.; Yu, Z. N.; Begum, F.; Hedden, R. C.; Simon, S. L., *Polymer* **2014**, *55*, 4959

Zhao, J. H.; Kiene, M.; Hu, C.; Ho, P. S., *Appl. Phys. Lett.* **2000**, *77*, 2843

Zhu, L. L.; Wang, X. L.; Gu, Q.; Chen, W.; Sun, P. C.; Xue, G., *Macromolecules* **2013**, *46*, 2292

Zhu, Z. Y.; Thompson, T.; Wang, S. Q.; von Meerwall, E. D.; Halasa, A., *Macromolecules* **2005**, *38*, 8816

Zoetelief, W. F.; Douven, L. F. A.; Housz, A. J. I., *Polym. Eng. Sci.* **1996**, *36*, 1886